Measurement of the Proton Structure Function $F_2(x, Q^2)$ and the Gluon Density of the Proton at low x using Deep Inelastic ep Scattering at the H1 Detector

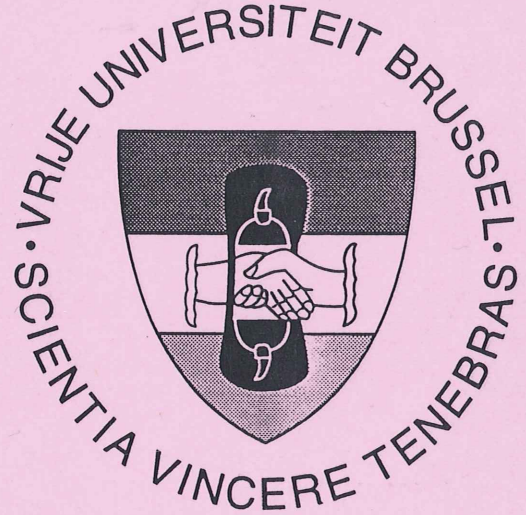

Erik Evrard

1996

Promotor: Prof. Dr. J. Lemonne

Vrije Universiteit Brussel
Pleinlaan 2
B-1050 Brussel

Proefwerk ingediend met
het oog op het behalen van
de wettelijke graad van
Doctor in de Wetenschappen.

Measurement of the Proton Structure Function $F_2(x, Q^2)$ and the Gluon Density of the Proton at low x using Deep Inelastic ep Scattering at the H1 Detector

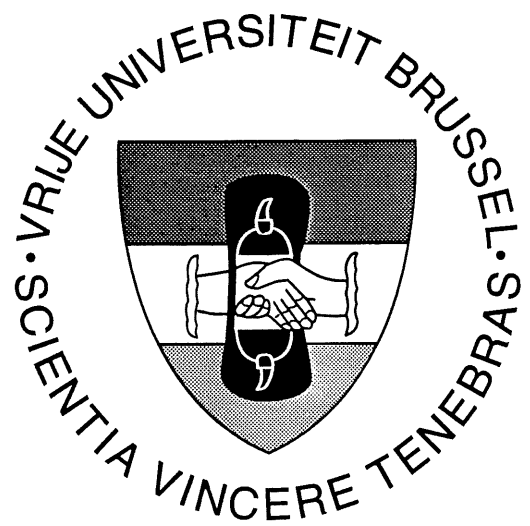

Erik Evrard

1996

Promotor: Prof. Dr. J. Lemonne

Vrije Universiteit Brussel
Pleinlaan 2
B-1050 Brussel

Proefwerk ingediend met
het oog op het behalen van
de wettelijke graad van
Doctor in de Wetenschappen.

Abstract

In 1992 the HERA collider provided the first collisions between 820 GeV protons and 26.7 GeV electrons in the H1 and Zeus detectors. In this thesis the measurement of the $F_2(x, Q^2)$ proton structure function is described, based on the H1 data which was taken in 1994. This data originated from collisions of 27.6 GeV positrons and 820 GeV protons, so that the total squared centre of mass energy was $s = 4E_eE_p \simeq 10^5$ GeV^2. The measurement covers the kinematic domain of squared momentum transfers Q^2 between 5 GeV^2 and 100 GeV^2, and Bjorken x values between 10^{-4} and 10^{-2}, which could not be accessed by previous fixed target experiments.

With an integrated luminosity of 2.5 pb^{-1} which means a tenfold higher statistics than in 1993, the observation of a rise of F_2 with decreasing x at a given Q^2 is confirmed. The gluon density is extracted from the scaling violations of F_2 by means of an approximate solution of the QCD evolution equations and is found to rise steeply with decreasing x. This result is compatible with a recent QCD analysis of the data.

Revision 1.1

Contents

Introduction

Lepton-nucleon experiments have played an important role in our understanding of the fundamental structure of matter. From such experiments we learned that there are three point-like valence *partons* in nucleons [66],[61]. Soon those partons were associated with the *quarks*, which were introduced in 1964 by Gell-Mann and Zweig as a theoretical explanation for the hadron spectroscopy. They have spin 1/2 and their charges are $\pm 1/3$ or $\pm 2/3$ of the electron charge. From further experiments one observed that only about 50% of the nucleon momentum was carried by the quarks. It was suggested that the other half is carried by *gluons*, which are the carriers of the strong force. The behaviour of this force is described by *Quantum chromodynamics (QCD)*, and lepton-nucleon experiments have significantly contributed to the development of this theory.

By the end of 1991 the electron-proton collider HERA (Hadron-Elektron Ring Anlage) became operational. HERA is the first machine in which electrons (from 1994 also positrons) and protons can be accelerated to collide. During the collisions of $\sim$ 30 GeV electrons with 820 GeV protons, four-momentum squared transfers Q^2 up to 10^5 GeV$^2/c^2$ can be reached, which allows to probe the structure of the nucleons with a resolution improved by two orders of magnitude (down to 10^{-18} m) than with earlier fixed target experiments. Therefore HERA allows to test several *QCD* predictions.

In the middle of 1992 the first data of e^-p collisions has been taken by both HERA experiments H1 and ZEUS. In the beginning the luminosity was rather small (about 22 nb^{-1}, but in 1993 already 270 nb^{-1} was achieved. In 1994 the luminosity increased even further, and also positron-proton collisions were studied for the first time ($\sim$300 nb^{-1} for e^-p, $\sim$2.5 pb^{-1} for e^+p).

In this study the 1994 data are used to determine the F_2 structure function of the proton at low values of the momentum transfer $Q^2 < 100$ GeV$^2/c^2$. The cross section of such events is dominated by scattering off partons which carry a small momentum fraction of the proton ($x \ll 1$). The theoretical interest in such experiments is very big, because—in contrast to high Q^2 scattering—there is no generally accepted theory yet which describes the physics at low values of x.

Chapter 1 summarises some theoretical aspects, which are relevant to this study.

Chapter 2 describes the fundamental parts of the H1 detector.

Chapter 3 is entirely dedicated to the data acquisition of the multiwire proportional chambers, of which the development of the first day software was my main activity for several years.

Chapter 4 is devoted to several basic aspects of the measurement of the cross section of deep inelastic scattering, such as the measurement of the kinematic variables, the various backgrounds and the radiative corrections.

Chapter 5 describes the details of the measurement of this cross section: the run and event selection, the calculation of the efficiencies, acceptances and corrections. In this chapter the measurement of F_2 is presented as a function of x and Q^2.

Chapter 6 describes the extraction of the gluon momentum density xg from the scaling violations of the structure function F_2, by using an approximate solution of the QCD evolution equations.

Chapter 1

Deep inelastic scattering at HERA

1.1 Deep inelastic scattering

The first experimental information about the structure of the nucleon has been gained in 1956 by the electron-nucleon scattering experiments of McAllister and Hofstadter in which electrons with an energy of 190 Mev were scattered off a hydrogen target. These experiments showed that protons behave like a charge distribution with a spread of 10^{-15} m. With increasing electron energy, the available resolving power increased and at an energy of 7–17 GeV the SLAC—MIT experiment of Friedman, Kendall and Taylor [67] discovered a substructure in the proton. Numerous lepton-nucleon scattering experiments, like for example CDHS and CCFR (Fermilab), CHARM, BCDMS and EMC/NMC (CERN), continued this research in the 1970s and 1980s.

In this chapter we will introduce the deep inelastic scattering process, the quark-parton model and the structure functions of the proton. Further we will present the important Altarelli-Parisi evolution equations and its limitations. Finally we will give an approximate method to solve these equations to estimate the gluon momentum density. It is not the intention of this chapter to be complete, but merely to present enough background information to understand the methods and motivations of the following chapters which describe the experimental methods and results.

1.2 The kinematic variables

We want to study the scattering process of a lepton with four-momentum k, off a nucleon of mass M and four-momentum p and where the final state contains the scattered electron with four-momentum k':

$$\begin{array}{ccccc} l + N & \longrightarrow & l + X \\ (k)\ \ (p) & & (k')\ \ (p') \end{array} \tag{1.1}$$

At sufficiently high momentum transfer, the proton breaks up and the process is said to be *inelastic.* At momentum transfers above several GeV/c, the term *deep inelastic scattering* (DIS) is used. The final hadronic system will be called X and its total four-momentum is p'. In the case of HERA, the nucleon beam consists of protons and the lepton beam of electrons or positrons.

The lowest order Feynman diagram of such an interaction is shown in figure 1.1. The intermediating particle is either a photon or a Z^0 vector boson and one talks about a *neutral current process.* The cross section with Z^0 exchange is several orders of magnitude smaller than with virtual photon (γ^*) exchange. Although at HERA one can reach sufficiently

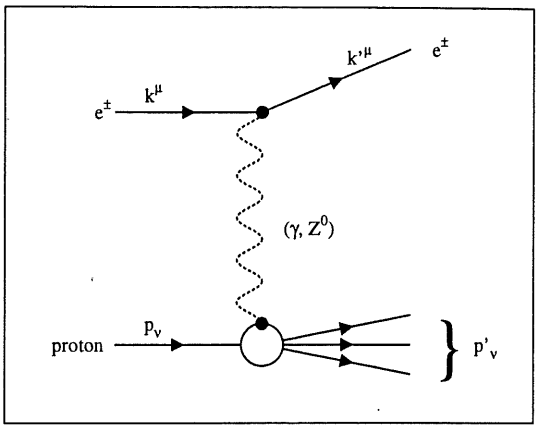

Figure 1.1: **Lowest order Feynman diagram of deep inelastic $e^{\pm}p$ scattering.** *The intermediate boson is either a photon or a Z^0. Since the collision is inelastic, the proton breaks up.*

high values of Q^2 to observe scattering events with Z^0 exchange, we will consider only the lowest order electromagnetic interaction (γ^* exchange) for the calculation of the cross section. The analysis in this document will be limited to a rather low range of momentum transfer (below 11 GeV/c) where the γ^* exchange fully dominates.

In earlier experiments, only the momentum and angle of the scattered electron was measured. Although the H1 detector (as will be shown in the next chapter) allows to measure the hadronic final state, we will calculate the *inclusive* cross section, i.e. the cross section where all the possible hadronic final states are taken into account.

In such an inclusive experiment there are only two independent kinematical variables, with which all the possible other kinematical variables can be reconstructed (on condition that p and k are given). As we will see in section 4.3 the angle θ and energy E of the scattered electron are possible candidates for this purpose. We can define the following invariants of the process (1.1):

$$s = (k+p)^2 \tag{1.2}$$
$$Q^2 = -q^2 = -(k-k')^2 \tag{1.3}$$
$$W^2 = (q+p)^2 \tag{1.4}$$
$$\nu = \frac{p\cdot q}{M}. \tag{1.5}$$

The Mandelstam variable s is the total square of the energy available in the center of mass frame, Q^2 is the square of the transferred four-vector momentum, W^2 is the invariant mass squared of the hadronic system X and ν is the transferred energy $\nu = E_e - E$ in the proton's rest frame ($E_e = k_0$, $E = k_0'$) and M is the mass of the proton.

It is common to replace ν and Q^2 by the dimensionless variables

$$x = \frac{-q^2}{2p\cdot q} = -\frac{q^2}{2M\nu} \tag{1.6}$$
$$y = \frac{p\cdot q}{p\cdot k}. \tag{1.7}$$

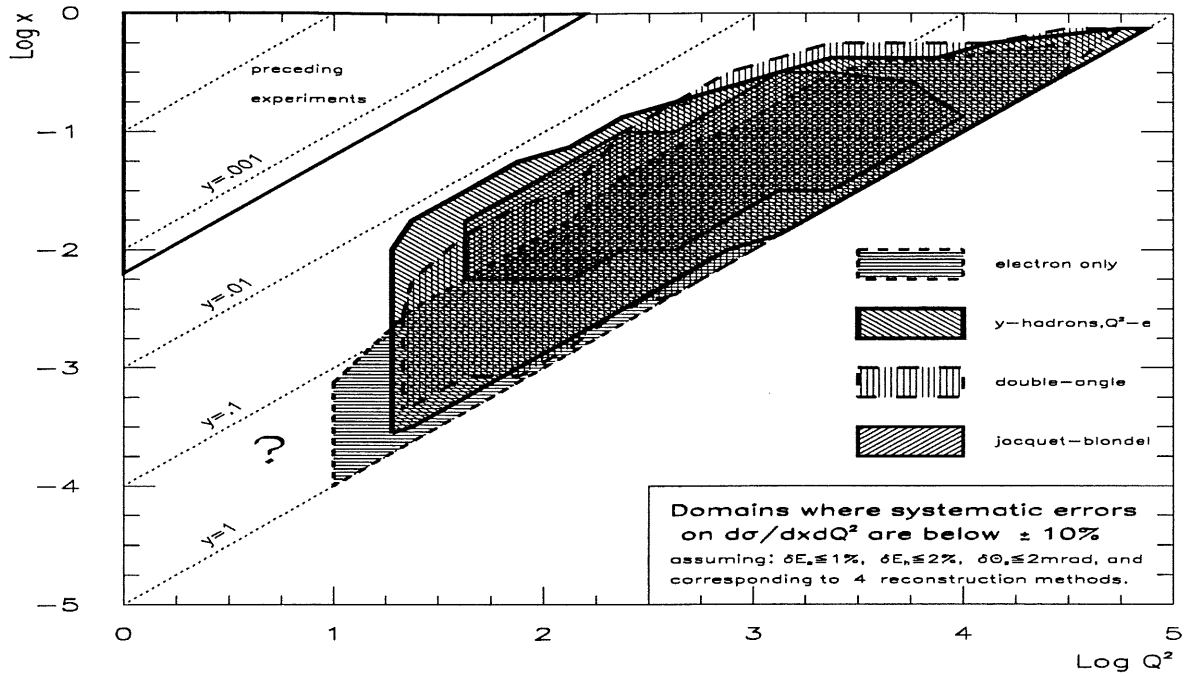

Figure 1.2: **The kinematic domains of HERA as compared to earlier fixed target DIS experiments.**
The shaded regions are the domains in which the differential cross section of DIS can be measured with a precision better than 10% (taken from a Monte Carlo study presented in [33]). The differential cross section can be measured by using several methods, each of which has its own domain in which it is most efficient. This will be explained in greater detail in chapter 4.

The following relation between x, y and Q^2 holds:

$$s\,x\,y = Q^2. \tag{1.8}$$

The allowed kinematic region for $ep \to eX$ can be shown to be confined to $0 \leq x \leq 1$, $0 \leq y \leq 1$ and $0 \leq Q^2 \leq s$. At fixed value of s, the accessible domain is thus a triangle in the (x, Q^2) domain.

As can be seen on figure 1.2, the kinematicaly accessible domain of HERA extends to Q^2 values up to 10^5 GeV^2/c^2, and down to very low values of x to 10^{-5}–10^{-4} for low Q^2 values of the order of 1–10 GeV^2/c^2. These regions have never been explored by earlier fixed target DIS experiments, which only probed Q^2 values up to 300 GeV^2/c^2 and x larger than 0.008 for Q^2 around several GeV^2/c^2. In chapter 4 the kinematics of DIS will be studied in function of the H1 detector.

1.3 Cross-section of deep inelastic scattering and structure functions

The cross section of deep inelastic scattering (figure 1.1) can be written as the contraction of the leptonic and the hadronic tensors $L^{\mu\nu}$ and $W_{\mu\nu}$:

$$d\sigma \sim L^e_{\mu\nu} W^{\mu\nu}. \tag{1.9}$$

The leptonic tensor follows from standard QED considerations and has the form:

$$L^e_{\mu\nu} \equiv \frac{1}{2} \sum_{\text{(e spins)}} [\bar{u}(k')\gamma^\mu u(k)] \, [\bar{u}(k')\gamma^\nu u(k)]^*, \tag{1.10}$$

where $J^\mu = \bar{u}(k')\gamma^\mu u(k)$ represents the lepton current. The leptonic tensor (1.10) can be exactly evaluated using the trace theorems [42]. If the proton were a point particle, then the hadronic tensor would be a similar expression. But since the proton has an internal structure, the hadronic tensor $W^{\mu\nu}$ serves to parametrise the form of the current at the other end of the propagator. The most general form of the tensor $W^{\mu\nu}$ can be constructed out of a linear combination of the independent momenta p and q ($p' = p + q$):

$$W^{\mu\nu} = c_1 g^{\mu\nu} + c_2 q^\mu q^\nu + c_3 p^\mu p^\nu + c_4(p^\mu q^\nu + q^\mu p^\nu) + c_5(p^\mu q^\nu - q^\mu p^\nu) + c_6 \epsilon_{\mu\nu\lambda\rho} p^\lambda q^\rho. \tag{1.11}$$

The c_i's are functions of the Lorentz scalar variables that can be constructed from the four-momenta at the hadronic vertex. In the case of inelastic scattering there are two degrees of freedom, and one can choose as variables q^2, $p \cdot q$ or more commonly x,Q^2 or x,y. Since the leptonic tensor $L^e_{\mu\nu}$ is symmetric for permutations of μ and ν, the antisymmetric terms of c_5 and c_6 can be omitted. Furthermore, one can show that current conservation at the hadronic vertex means that c_4 can be expressed as a function of c_3 and c_2 as a function of c_1 and c_3, so that only two terms are really independent [42]. It is common to introduce:

$$W_1 = -c_1 \quad \text{and} \quad W_2 = M^2 c_3, \tag{1.12}$$

so that equation (1.11) becomes:

$$W^{\mu\nu} = W_1 \left(-g^{\mu\nu} + \frac{q^\mu q^\nu}{q^2}\right) + W_2 \frac{1}{M^2} \left(p^\mu - \frac{p \cdot q}{q^2} q^\mu\right) \left(p^\nu - \frac{p \cdot q}{q^2} q^\nu\right). \tag{1.13}$$

This leads to an expression for the differential deep inelastic ep cross section (expressed as a function of two independent variables, the energy (E') and angle (θ) of the scattered electron):

$$\frac{d^2\sigma}{dE'\, d\Omega} = \frac{\alpha^2}{4E^2 \cos^4 \frac{\theta}{2}} \left(W_2(\nu, q^2) \cos^2 \frac{\theta}{2} + 2W_1(\nu, q^2) \sin^2 \frac{\theta}{2}\right). \tag{1.14}$$

It is customary to introduce dimensionless structure functions F_1 and F_2:

$$F_1(Q^2, x) \equiv M W_1(q^2, \nu) \tag{1.15}$$

$$F_2(Q^2, x) \equiv \nu W_2(q^2, \nu) \tag{1.16}$$

so that equation (1.14) becomes:

$$\frac{d^2\sigma}{dx\,dQ^2} = \frac{4\pi\alpha^2}{xQ^4}\left(xy^2F_1(x,Q^2) + (1-y)F_2(x,Q^2)\right) \tag{1.17}$$

$$= \frac{2\pi\alpha^2}{xQ^4}\left(1-(1-y)^2 - y^2\frac{R}{1+R}\right)F_2(x,Q^2), \tag{1.18}$$

in which

$$R = \frac{F_L(x,Q^2)}{2xF_1(x,Q^2)} \tag{1.19}$$

and

$$F_L(x,Q^2) = F_2(x,Q^2) - 2xF_1(x,Q^2). \tag{1.20}$$

From equation (1.17) we can see that in order to make model independent measurements of F_1 and F_2 for fixed values of x and Q^2, we must measure the cross section at different values of y, which according to (1.8) means at different values of s. In the course of 1994 HERA operated at a fixed value of $s \simeq 10^5$ GeV^2/c^2. However in the next section we shall see that in a simple model of the nucleon, the parton model, F_1 and F_2 are closely related, so that it will be possible to measure the structure functions for given values of s. We will also show that F_2 has a physical interpretation in this model.

1.4 Scale invariance and the quark-parton model

In the sixties a series of electron-nucleon scattering experiments at SLAC [67] resulted in a measurement of the proton struction function W_2 as a function of Q^2 and ν. It was noted that $W_2(\nu, Q^2)$ appeared to be independent of Q^2, and was hence essentially only a function of the ratio of Q^2 to ν, i.e. of x (see equation (1.6)). This effect was called *scale invariance* or *Bjorken scaling*, predicted on theoretical grounds by Bjorken in 1966 [16].

The interpretation of those first F_2 structure function measurements was made in 1969 by Feynman [30]. Feynman concluded that the proton consists of point-like particles, called partons. In a deep inelastic lepton-proton interaction, the exchanged boson interacts with one of those partons.

In this *parton model*, the masses of the partons as well as any possible interaction between the partons themselves are neglected. This is a valid assumption in a relativistic reference frame where the proton has a very large momentum ($|p| \gg M$). Such a frame is called a 'Breit' or 'brick wall' frame), and one can show that in this frame the interaction rate between the partons is slowed down and the parton, with which the virtual boson interacts, is essentially a *free* particle during the short interaction time. At large momentum transfers between the electron and the proton, the scattering between the virtual photon and the proton can be considered as the incoherent sum of elastic photon-parton sub-interactions (figure 1.3).

We can then introduce the parton momentum distribution $f_i(x)$ which describes the probability that the struck parton i carries a fraction x of the proton's momentum p. If (at large Q^2) an *inelastic* electron-proton scattering is viewed as an *elastic* scattering of the electron on a 'free' parton, the structure functions W_1 and W_2 become delta functions

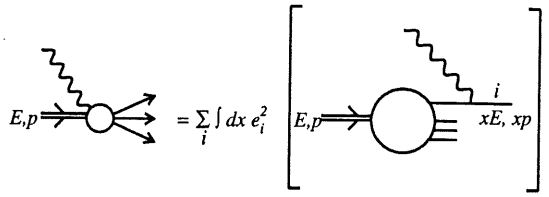

Figure 1.3: **In the parton model the γ^*-proton interaction can be considered as the incoherent sum of γ^*-parton interactions.**
Parton i carries a fraction x of the total energy E and momentum p.

(for a quark with mass $m \neq 0$):

$$2\,W_1^{point}(Q^2,\nu) = \frac{Q^2}{2m^2}\delta\left(\nu - \frac{Q^2}{2m}\right) \tag{1.21}$$

$$W_2^{point}(Q^2,\nu) = \delta\left(\nu - \frac{Q^2}{2m}\right). \tag{1.22}$$

The 'point' notation means that the quarks are considered to be structureless Dirac particles. The functions W_1^{point} and W_2^{point} are now only function of the ratio $Q^2/2m\nu$ and not of Q^2 and ν independently. If we define

$$\omega = \frac{2M\nu}{Q^2}, \tag{1.23}$$

then one can easily show that the dimensionless structure functions become:

$$F_2(\omega) = \sum_i \int dx\, e_i^2\, f_i(x)\, x\, \delta\left(x - \frac{1}{\omega}\right) \tag{1.24}$$

$$F_1(\omega) = \frac{\omega}{2} F_2(\omega), \tag{1.25}$$

where the sum runs over all the quarks i in the proton. We can then see that

$$F_2(x) = \sum_i e_i^2\, x\, f_i(x) \tag{1.26}$$

$$F_1(x) = \frac{1}{2x} F_2(x) \tag{1.27}$$

with

$$x = \frac{1}{\omega} = \frac{Q^2}{2M\nu}. \tag{1.28}$$

In the Breit frame the kinematic variable x has hence a simple interpretation: it is the momentum fraction carried by the struck parton. According to equation (1.28) this variable can be associated with the Bjorken x variable defined in equation (1.6).

Equation (1.27) is called the Callan-Gross relation. In the parton model it holds only for spin-$\frac{1}{2}$ partons. It was experimentally found to be valid, indicating that partons are indeed spin-$\frac{1}{2}$ particles. From equations (1.27) and (1.19) one can conclude that

$$R = 0. \tag{1.29}$$

One can show however that if the partons posess a transverse momentum k_T (which is indeed the case, due to their confinement), R is no longer zero. This correction becomes important for small values of Q^2:

$$R = \frac{4 < k_T^2 >}{Q^2}. \tag{1.30}$$

Soon the partons were associated with the *quarks*, which were introduced in 1964 by Gell-Mann and Zweig as a theoretical explanation for the hadron spectroscopy. Several experiments in the early seventies confirmed the correctness of this association. Theorists also proposed a 'sea' of quark-antiquark pairs, which co-exists with the original three quarks (the 'valence' quarks).

But it was found that the quarks were not the only constituents of the nucleons, since they were found to carry about only half the nucleon momentum. A first indication of the existence of *gluons* in the nucleon, came from a measurement of the momentum balance:

$$\int_0^1 dx\, F_2^{\nu N}(x) = \int_0^1 dx \sum_{f=1}^{N_f} x\,[q_f(x) + \bar{q}_f(x)] = 1 - \epsilon, \tag{1.31}$$

where N_f is the number of quark flavours. Conventionally the quark structure functions $q_f(x)$ are called $u(x)$, $\bar{u}(x)$, $d(x)$, $\bar{d}(x)$, $s(x)$, $\bar{s}(x)$, ... for all the possible quark flavours. The normalisation of the valence quark densities is determined by the counting rules: $\int(u(x)-\bar{u}(x))dx = 2$, $\int(d(x)-\bar{d}(x))dx = 1$. There are no other valence quarks than u and d, so $\int(s(x)-\bar{s}(x))dx = 0$, $\int(c(x)-\bar{c}(x))dx = 0$, $\int(b(x)-\bar{b}(x))dx = 0$, $\int(t(x)-\bar{t}(x))dx = 0$.

In 1972 is was experimentally found that $\epsilon \sim 0.5$, which means that only half of the nucleon's momentum is carried by the quarks [24]. The other half is carried by—electrically neutral—gluons, which only interact via the strong force and therefore don't contribute to the cross section.

The data of deep inelastic lepton-nucleon thus revealed the presence of point-like spin-$\frac{1}{2}$ Dirac particles inside nucleons. Those particles could be identified with the earlier postulated quarks. Despite its successes, the 'naive' quark-parton model has several disadvantages:

- The scale invariance of F_2 was broken at higher values of Q^2. This was first seen in experiments at SLAC and Fermilab in 1975 [69].
- The model does not describe the interactions between the quarks and does not explain the quark confinement.
- The total sum of the quark momenta was found to be different from the proton momentum.

The theory of Quantum Chromodynamics (QCD) allows to solve some of these problems.

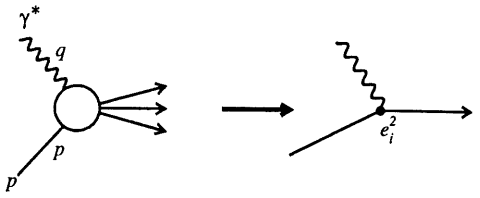

Figure 1.4: **Schematic representation of the parton model for the process** $ep \longrightarrow eX$.

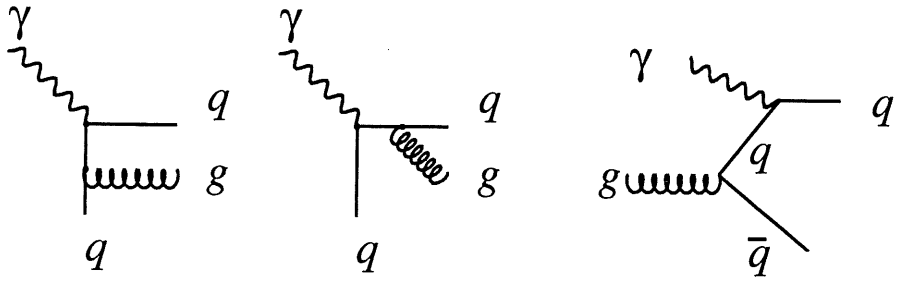

Figure 1.5: $\mathcal{O}(\alpha\alpha_s)$ **contributions to** $ep \longrightarrow eX$.

1.5 QCD and the evolution of the structure functions

Quantum chromodynamics (QCD) is an SU(3) gauge theory which introduces a 'colour charge' for quarks. In this theory hadrons appear as colour singlets and consist of 2 or 3 valence quarks. Quarks interact through gluon exchange. Gluons form an SU(3) octet of colour charge, are massless and have spin 1.

In QCD, quarks which carry a colour charge may radiate gluons ($q \longrightarrow gq$), which is analogue to photon emission from a charged particle in QED, but with a much bigger coupling strength of order α_s. But what makes QCD so distinct from QED, is that gluons are not colour-neutral and may thus also radiate other gluons ($g \longrightarrow gg$) or interact with each other ($gg \longrightarrow gg$).

The parton model, symbolically represented by figure 1.4, completely ignores the dynamical role of gluons as the carriers of the strong force associated with coloured quarks. One must for instance take into account that the quarks in figure 1.4 may radiate a gluon before or after being struck by the virtual photon γ^*. Additionally a gluon constituent in the target can contribute to DIS via $\gamma^* g \longrightarrow q\bar{q}$ pair production. These $\mathcal{O}(\alpha\alpha_s)$ processes are shown in figure 1.5. The process in figure 1.4 is a zero order process in α_s.

The inclusion of the processes of figure 1.5 has two experimentally observable consequences:

- The scaling property of the F_2 structure function will no longer be true.
- The outgoing quark (and thus the direction of its hadron jet) will no longer be collinear with the virtual photon.

QCD allows to compute the contributions from the $\mathcal{O}(\alpha\alpha_s)$ diagrams of figure 1.5 to the $\gamma^* p$ cross section, so it is possible to predict the scaling violations as well as the angular jet distributions relative to the virtual photon.

1.5.1 The leading log approximation and the splitting functions

The gluon bremsstrahlung $\gamma^* q \to qg$ process contributes to the cross section of DIS and thus to the structure function. This contribution can be calculated by using the QCD rules approximated as (*leading log (LL) approximation*):

$$\sigma\left(\gamma^* q \to qg\right)_{LL} \simeq e_i^2 \frac{4\pi^2\alpha}{\hat{s}} \left(\frac{\alpha_s}{2\pi} P_{qq}(z) \log \frac{Q^2}{Q_0^2}\right), \tag{1.32}$$

where $\hat{s}$ represents s in the γ^*-parton frame. The lower limit Q_0^2 in equation (1.32) is introduced as a cutoff, to regularise the divergence when $Q^2 \longrightarrow 0$. The functional form of $P_{qq}(z)$ is

$$P_{qq}(z) = \frac{4}{3}\left[\left(\frac{1+z^2}{1-z}\right)_+ + 2\delta(1-z)\right] \tag{1.33}$$

with

$$h_+(\alpha) = \lim_{\beta\to 0}\left[h(\alpha)\theta(1-\alpha-\beta) - \delta(1-\alpha-\beta)\int_0^{1-\beta} d\gamma\, h(\gamma)\right], \tag{1.34}$$

where θ is the heaviside function. Function $P_{qq}(z)$ is called a *splitting function* and can be physically interpreted as the probability of a quark emitting a gluon, so that the quark momentum is reduced by a fraction z.

In leading order the strong coupling factor α_s depends on Q^2 as:

$$\alpha_{LO}(Q^2) = \frac{\alpha_s(Q_0^2)}{1 + \frac{\alpha_s(Q_0^2)}{4\pi}\beta_0 \log\frac{Q^2}{Q_0^2}}, \tag{1.35}$$

with

$$\beta_0 = 11 - \frac{2}{3}n_f \tag{1.36}$$

and n_f is the number of active quark flavours. At sufficiently low Q^2, the effective coupling will become large, and it is customary to denote the Q^2 scale at which this happens by Λ^2, where

$$\Lambda^2 = Q_0^2\, e^{-4\pi/(11-\frac{2}{3}n_f)\alpha_s(Q_0^2)}, \tag{1.37}$$

so that we can write equation (1.35) as:

$$\alpha_{LO}(Q^2) = \frac{4\pi}{\beta_0 \log\frac{Q^2}{\Lambda^2}}. \tag{1.38}$$

Since the factor $\alpha_s(Q^2)\log Q^2$ of equation (1.32) is of the order one we must sum all the other contributions $\gamma^* q \longrightarrow q(ng)$, since they are all of the same order. This summation is written as $\sum_n \left[\alpha_s(Q^2)\log Q^2\right]^n$. Unfortunately, the calculation of repeated gluon emissions leads to interference terms, which render the calculation difficult. However, there exists

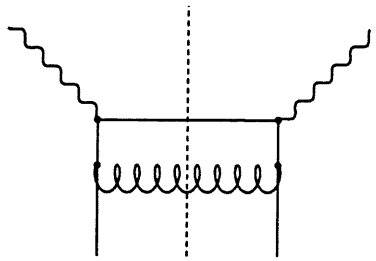

Figure 1.6: **Dominant contribution in the axial gauge.**
In the axial gauge, only the first process of figure 1.5 contributes to leading log of the cross section of repeated gluon emission $\gamma^* q \longrightarrow q(ng)$. This figure shows the square of this contribution.

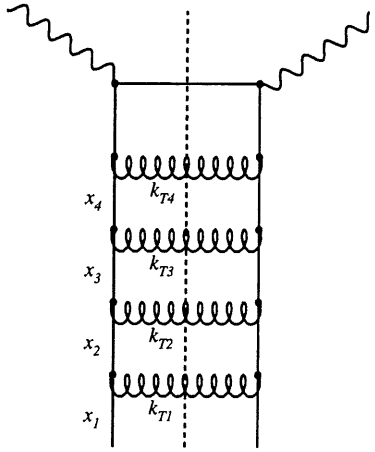

Figure 1.7: **Ladder diagram.**
Square of the amplitude for the emission of n gluons in the process $\gamma^* q \longrightarrow q(ng)$ in the leading log approximation. In an axial gauge the interference terms do not contribute to leading order and the cross section takes on a simple ladder form.

a gauge in which only one term, the interaction of a photon with a quark which has previously emitted a gluon (figure 1.6), contributes to the leading order. This gauge is called the *axial gauge*.

In the axial gauge, it now very easy to add all the terms $\sum_n [\alpha_s(Q^2) \log Q^2]^n$. The cross section for the emission of n gluons in the leading log approximation has the simple *ladder* structure shown in figure 1.7. Since after every gluon emission the quark momentum diminuishes, the following strict ordering emerges:

$$z_1 > z_2 > \ldots > z. \tag{1.39}$$

More complex types of diagrams can be considered as a cascade of four possible 'basic' vertices (figure 1.8). Each of them has an associated splitting function:

$$P_{qq}(z) = \frac{4}{3}\left[\frac{1+z^2}{(1-z)_+} + 2\delta(1-z)\right] \tag{1.40}$$

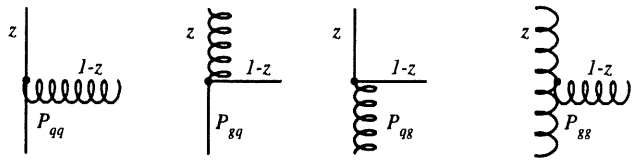

Figure 1.8: **Basic QCD vertices.**
These vertices correspond to the splitting functions P_{qq},P_{gq},P_{qg},P_{gg}.

$$P_{gg}(z) = 6\left[\frac{z}{(1-z)_+} + \frac{1-z}{z} + z(1-z) + \left(\frac{11}{12} - \frac{n_f}{18}\right)\delta(z-1)\right] \tag{1.41}$$

$$P_{qg}(z) = \frac{1}{2}\left[z^2 + (1-z)^2\right] \tag{1.42}$$

$$P_{gq}(z) = \frac{4}{3}\frac{1+(1-z)^2}{z}, \tag{1.43}$$

where the distribution $(1-z)_+$ is defined as:

$$\int_0^1 dz \frac{f(z)}{(1-z)_+} = \int_0^1 dz \frac{f(z)-f(1)}{1-z}, \tag{1.44}$$

and n_f is the number of active quark flavours.

1.5.2 The equations of Altarelli-Parisi

We can now also incorporate the quark-antiquark pair production processes of figure 1.5 by introducing the gluon distribution function $g(x,Q^2)$, which is convoluted with the P_{gq} splitting function. It is then possible to calculate the Q^2-evolution of the quark and gluon distributions as a function of $g(x,Q^2)$ and $q(x,Q^2)$:

$$\frac{dq(x,Q^2)}{d\log Q^2} = \frac{\alpha_s(Q^2)}{2\pi}\left\{P_{qq}\otimes q + P_{qg}\otimes g\right\} \tag{1.45}$$

$$\frac{dg(x,Q^2)}{d\log Q^2} = \frac{\alpha_s(Q^2)}{2\pi}\left\{P_{gg}\otimes g + P_{gq}\otimes \sum q\right\} \tag{1.46}$$

An expression such as equation (1.45) is a short notation for:

$$\frac{dq(x,Q^2)}{d\log Q^2} = \frac{\alpha_s(Q^2)}{2\pi}\int_x^1 \left\{P_{qq}(\frac{x}{y})q(y,Q^2) + g(y,Q^2)P_{qg}(\frac{x}{y})\right\}\frac{dy}{y} \tag{1.47}$$

The sum in equation (1.46) is taken over all the quark flavours. These evolution equations were first calculated by Dokshitzer, Altarelli and Parisi and by Gribov and Lipatov, and are usually referred to as the DGLAP equations [73],[32], or simply the Altarelli-Parisi equations.

The evolution of the structure function $F_2(x,Q^2)$, which can be written as

$$F_2(x,Q^2) = 2x\,F_1(x,Q^2) = \sum e_q^2\, x\left\{q(x,Q^2)+\bar{q}(x,Q^2)\right\}, \tag{1.48}$$

can then be deduced from the evolution equations of the quark and gluon densities:

$$\frac{dF_2(x,Q^2)}{d\log Q^2} = \frac{\alpha_s(Q^2)}{2\pi}\left\{\int_x^1 dy\; F_2(\frac{x}{y},Q^2)\,P_{qq}(y) + \int_x^1 dy\;\left(2\Sigma e_q^2\right)\frac{x}{y}\,g(\frac{x}{y},Q^2)\,P_{qg}(y)\right\}. \tag{1.49}$$

This equation allows to calculate the evolution of F_2 as a function of Q^2, starting from a known value $F_2(Q_0^2)$. Therefore, the DGLAP equation does not give an absolute prediction of F_2. Only the measurement of the structure function in a large x, Q^2 domain, as it is the case for HERA, allows to test the validity of this equation and the QCD principles it has been built upon. The influence of the gluons is small, except for small x ($x < 10^{-2}$).

1.6 The structure functions at low x

At present the low x physics is one of the most interesting and difficult problems in QCD. At $x \to 0$ we deal with a dense system of partons in the weak coupling limit (small values of α_s, but in which nevertheless the interactions between the partons have large effects due to their high density). With HERA it is possible to explore experimentally the region of low x down to 10^{-5}.

1.6.1 The gluon momentum distribution at low x

Gluons can be emitted by either quarks or by other gluons. In the hypothesis that at low x the contribution of the quarks to the gluon density distribution is negligable, and that thus the double log approximation (DLA) applies, equation (1.46) becomes:

$$\frac{dg(x,Q^2)}{d\log Q^2} = \frac{\alpha_s(Q^2)}{2\pi} P_{gg}\otimes g, \tag{1.50}$$

with $P_{gg}(z) \approx \frac{6}{z}$. This equation can be exactly solved, and we find the DGLAP solution for $x \to 0$:

$$xg(x,Q^2) \propto \exp\left(\sqrt{\frac{48}{\beta_0}\log\frac{1}{x}\log\log\frac{Q^2}{Q_0^2}}\right), \tag{1.51}$$

which is a quickly rising function at small x.

The leading log approximation was based on the summation of the terms in $(\alpha_s \log Q^2)^n$. This approximation is only valid for:

$$\alpha_S \log Q^2 \simeq 1 \tag{1.52}$$

$$\alpha_S \log\frac{1}{x} \ll 1 \tag{1.53}$$

$$\alpha_S \ll 1 \tag{1.54}$$

There exists another formalism which allows to sum all the terms in $(\alpha_s \log\frac{1}{x})^n$. This formalism of the leading $\log\frac{1}{x}$ approximation corresponds to an integro-differential equation by Balitsky, Fadin, Kuraev and Lipatov (BFKL equation [25],[77]). This equation

describes the evolution of the quark and gluon distributions as a function of x and is valid in an orthogonal part of the x, Q^2 domain:

$$\alpha_S \log Q^2 \ll 1 \tag{1.55}$$

$$\alpha_S \log \frac{1}{x} \simeq 1 \tag{1.56}$$

$$\alpha_S \ll 1. \tag{1.57}$$

An approximate solution of the BFKL equation also leads to a divergent behaviour of the gluon momentum distribution:

$$x\, g(x, Q^2) \propto x^{-\lambda} \tag{1.58}$$

with

$$\lambda = \frac{3\,\alpha_s}{\pi} 4 \log 2 \approx 0.5 \tag{1.59}$$

Both the DGLAP as well as the BFKL equation indicate a divergent behaviour of xg at low x. The distribution of the quarks, which are emitted by the gluons, will therefore increase at low x, and consequently F_2 will increase too. However, one must keep in mind that this divergent behaviour is only the result of approximate and asymptotic solutions of the evolution equations and that the influence of the initial values of the distributions is important. It is of great importance for QCD that experimental data of this low x region are collected. HERA offered for the first time a chance to open experimentally this interesting region.

1.6.2 Violation of the unitarity and the saturation effect

As we saw in the previous section and according to the DGLAP and BFKL equations, the asymptotic behaviour of the gluon momentum distribution function at low x is:

$$\lim_{x \to 0} xg(x, Q^2) = \infty, \tag{1.60}$$

which means that also the structure function increases to infinity at low x. As the cross section of photon-proton interactions is given by

$$\sigma_{\gamma P}(x, Q^2) \propto \frac{\alpha^2}{Q^2} F_2(x, Q^2), \tag{1.61}$$

unitarity will be violated at very small x.

The large probability of creating a parton at low x from another parton leads to the divergence of the structure function. However, this divergence is compensated by the annihilation of partons and the structure function increases less quickly than when no annihiliation would take place. If the structure function would reach a constant value for $x \longrightarrow 0$, one speaks about *saturation*. It is yet unknown whether saturation does occur or not, and if it does, at which value of x it would be experimentally detectable.

Param.	μN DIS	νN DIS	Prompt γ	Drell Yann	$W^{\pm}$,Z^0	ep DIS
MRS D^0,D^-	BCDMS NMC*	CDHSW CCFR*	WA70	E605	UA2 CDF	
MRS D'^0,D'^-	BCDMS NMC	CCFR	WA70	E605	UA2 CDF	
MRSH	BCDMS NMC	CCFR CCFR	WA70 WA70	E605	UA2 CDF	H1
GRV	-	-	-	-	-	-

Table 1.1: **Experiments used for various structure function parametrisations.** *(* preliminary results)*

1.7 Parametrisations of structure functions

In the past several deep inelastic scattering experiments have led to a more precise measurement of the structure functions of the nucleons. Many of these experiments extended the measurement to new parts of the kinematical (x,Q^2) plane. Several parametrisations of the structure functions have been proposed based on these measurements. The goal of such parametrisations is to extrapolate the measurements to yet unexplored regions of x and Q^2.

Most of the parametrisations are based on the same principle: starting from the Altarelli-Parisi evolution equation (either in leading log or next-to-leading log approximation), a hypothesis on the initial conditions is made, i.e. the quark and gluon distributions are determined experimentally at a particular value of Q_0^2. Particular constraints based on physical grounds are applied, such as quark sum rules and assumptions on the distribution of quarks. The choice of these constraints depends on the author(s) of the parametrisation. Finally, the evolution equations are applied to obtain a prediction of the quark and gluon distributions for the experimentally unexplored kinematical domain. Most parametrisations contain parameters that can be adjusted to fit the experimental results.

We will use some of these parametrisations in our experimental analysis, since they are at the basis of all Monte Carlo predictions of DIS events. In particular the detector smearing, which is an important quantity for the determination of F_2, but also for the estimation of the radiative corrections, will be influenced by the choice of parametrisation.

Many older parametrisations have been found to be incompatible with modern experimental results and only two recent parametrisations will be discussed here since they were used for our measurement of F_2 with H1.

1.7.1 Parametrisation of Martin, Roberts and Stirling D^0D^-, $D'^0D'^-$ and H

Martin, Roberts and Stirling (MRS) have proposed several sets of parametrisations in the past. One can distinguish two distinct classes, one with a quickly rising F_2 at small x (D^-), and one with a flat F_2-behaviour at small x (D^0). This different behaviour originates from different assumptions on the gluon distribution at small x. In the case of D^- $xg(x,Q^2)$ is assumed to diverge as $x^{-\frac{1}{2}}$, while for D^0 there is no such divergence. The total form of

the MRS gluon parametrisations can be written as:

$$xg(x,Q_0^2) = A_g x^{\delta_g}(1+\gamma_g x)(1-x)^{\eta_g} \tag{1.62}$$

with for D^0:

$$\delta_g = 0 \qquad \gamma_g = 0 \tag{1.63}$$

and for D^-:

$$\delta_g = -0.5 \qquad \gamma_g = 12.0 \tag{1.64}$$

In both cases the valence quark distributions were taken to be of the form:

$$xq = A_q x^{\eta_q}(1-x)^{\zeta_q}(1+\epsilon x^{\frac{1}{2}}+\gamma x). \tag{1.65}$$

The next-to-leading log Altarelli-Parisi evolution equations are used to calculate the xg and xq distributions, starting from Q_0^2=4 GeV^2. The newer parametrisations D'^0 and D'^- [5] are similar to D^0 and D^-, with the only difference that the final NMC and CCFR data, published in 1991, was used. This data caused a significant increase of the quark distributions for $x \leq 0.05$. When the first F_2 measurements by HERA were published [38] in 1992, the quick rise of F_2 at small x was confirmed and the authors modified the $MRSD'^-$ parametrisation so that the divergent term of the gluon distribution was $x^{-0.3}$. This parametrisation predicts lower values for F_2 then $MRSD'^-$. This parametrisation is called $MRSH$ (where the H stands for H1).

On figure 1.9 one can see F_2 as a function of x at $Q^2 = 10$ GeV^2 for the parametrisations $MRS\ D'^0$, D'^- and H.

1.7.2 Parametrisation of Glück, Reya and Vogt

The approach of Glück, Reya and Vogt [55] is very different from the other parametrisations. Their analysis is based on the hypothesis that at a certain low energy scale Q_0^2 of the order of several hundred MeV, the proton consists only of gluons and valence quarks and contains no sea quarks, i.e. $g(x,Q_0^2) = q_s(x,Q_0^2) = \bar{q}_s(x,Q_0^2) = 0$. Then, they postulate that at Q_0^2:

$$g(x,Q_0^2) = \frac{n_g}{3}\left(u_v(x,Q_0^2) + d_v(x,Q_0^2)\right). \tag{1.66}$$

The sum rules for the valence quarks imply that

$$\int_0^1 dx\ g(x,Q_0^2) = \frac{n_g}{3}(2+1) = n_g. \tag{1.67}$$

The parameter n_g thus appears as the number of *valence gluons*. Once the distributions of the valence quarks and the parameter n_g are fixed, all the parton distribution follow from the DGLAP evolution equations in a unique way for all values of Q^2 and x.

The authors proposed $n_g = 2$, so that the proton contains "intrinsically" two gluons. Two parametrisations have been calculated:

GRV(LO) based on the leading log approximation

GRV(HO) based on the next to leading log approximation

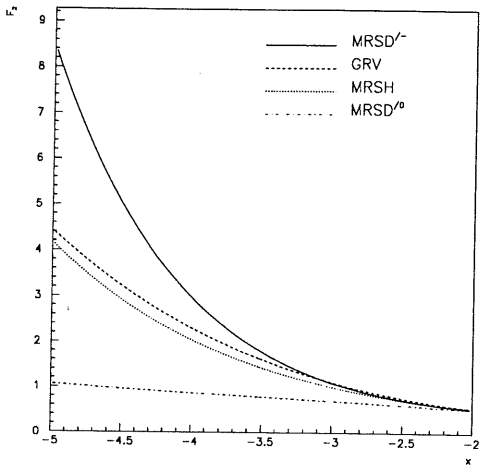

Figure 1.9: **Structure function parametrisations.**
The plot shows F_2 according to the four most relevant structure functions for this analysis (see text). For all parametrisations is $Q^2 = 10\ GeV^2$.

An interesting aspect of the GRV parametrisations is that they predict a divergent distribution of the gluon momentum density at low x, although this feature was never explicitly introduced in the scheme. According to the authors, the GRV parametrisations are valid for

$$10^{-4} \leq x \leq 1 \qquad \text{and} \qquad 0.2\,\text{GeV}^2 \leq Q^2 \leq 10^6\ \text{GeV}^2. \tag{1.68}$$

The GRV parametrisation is also shown on figure 1.9 for comparison with the others.

1.8 Extraction of the gluon momentum distribution $xg(x, Q^2)$

In this section a recently proposed approximate method by Prytz [64], [65] to estimate the gluon distribution momentum function $xg(x, Q^2)$ is discussed. This approximate method reduces the integro-differential DGLAP equations (1.45, 1.46) to simple differential equations in $\log(Q^2)$, and is based on three hypothesis:

1. The DGLAP equations stay valid up to low values of x.
2. At low x, the density of the gluons is significantly larger than the density of quarks.
3. The splitting function $P_{qg}(z)$ is symmetric around $z = \frac{1}{2}$ (this is exact in the leading log approximation, see equation (1.42)).

We will discuss the validity of the other assumptions and their implications below. Because of assumption 2, the evolution equation (1.49) of the structure function can be simplified to:

$$\frac{dF_2(x,Q^2)}{d\log Q^2} = \frac{\alpha_s(Q^2)}{2\pi}\int_x^1 dy\ \left(2\Sigma e_q^2\right)\ \frac{x}{y}g(\frac{x}{y},Q^2)\,P_{qg}(y). \tag{1.69}$$

Because of assumption 3, this can be written as:

$$\frac{dF_2(x,Q^2)}{d\log Q^2} = \frac{\alpha_s(Q^2)}{2\pi}\int_0^{1-x} dy\ \left(2\Sigma e_q^2\right)\ \frac{x}{1-y}g(\frac{x}{1-y},Q^2)\,P_{qg}(y). \tag{1.70}$$

By defining

$$g^*(x,Q^2) = xg(x,Q^2) \tag{1.71}$$

this becomes:

$$\frac{dF_2(x,Q^2)}{d\log Q^2} = \frac{\alpha_s(Q^2)}{2\pi}\int_0^{1-x} dy\ \left(2\Sigma e_q^2\right)\ g^*(\frac{x}{1-y},Q^2)\,P_{qg}(y), \tag{1.72}$$

We then define

$$G_{x,Q^2}(y) = g^*(\frac{x}{1-y},Q^2), \tag{1.73}$$

and we can now develop this new function around $y=\frac{1}{2}$ up to the first order:

$$G_{x,Q^2}(y) = G_{x,Q^2}(\frac{1}{2}) + (y-\frac{1}{2})\left.\frac{dG_{x,Q^2}}{dy}\right|_{y=\frac{1}{2}} + \mathcal{O}((y-\frac{1}{2})^2). \tag{1.74}$$

We can now insert this development into equation (1.72). The second term will vanish in view of the symmetry of P_{qg} around $y=\frac{1}{2}$, and the terms of $\mathcal{O}((y-\frac{1}{2})^2)$ and higher orders are expected to contribute little and are neglected. We then get:

$$\frac{dF_2(x,Q^2)}{d\log Q^2} = \frac{\alpha_s(Q^2)}{2\pi}g^*(2x,Q^2)\left(2\Sigma e_q^2\right)\int_0^{1-x} dy\,P_{qq}(y), \tag{1.75}$$

Since we are only interested in the low x region ($x<10^{-2}$), the upper limit of the integral in equation (1.75) can be approximated by 1 and one finds:

$$\frac{dF_2}{d\log(Q^2)} = \frac{5\alpha_s}{9\pi}\cdot\frac{2}{3}\cdot g^*(2x,Q^2). \tag{1.76}$$

The assumption that the DGLAP evolution equations stay valid for low values of x is now confirmed by H1 and Zeus data in 1992 and 1993 [38], [41], [78].

The second assumption that the gluon density is much higher than the quark density at low x is less evident. Some parametrisations such as MRS [5], suppose that the x-dependence of the sea quarks and of the gluons are identical at low x. Another series of parametrisations that we have not mentioned are the CTEQ [26] parametrisations, which include the hypothesis that the x-dependence of the sea quarks is flat and that the gluons diverge at low x. The resulting structure function F_2 behaves in a similar way for the MRS and the CTEQ parametrisations, even at low x.

The third assumption that $P_{qg}(z)$ is symmetric around $z=\frac{1}{2}$ is only true in the case of the leading log approximation. Unfortunately this approximation is not sufficient at low x. If one uses the splitting function of the next to leading log approximation, the symmetry argument to simplify the integral no longer holds.

Numerical studies have been performed to estimate the error of the approximative method which we have just described [37]. Depending on the steepness of the gluon density, the theoretical correction of the apprimation can rise up to 20%, about half of which comes from the neglect of the quark densities.

In chapter 6 we will use this method to extract the density of the gluon from the measured F_2 structure function.

Chapter 2

The experimental setup

2.1 The HERA collider

HERA (Hadron Electron Ring Anlage) is the first electron proton collider ever built. It consists of two independent accelerators, designed to store respectively 820 GeV protons and 30 GeV electrons, and to collide the two counterrotating beams head on in four interaction points, which are spaced uniformly around its 6.3 km long circumference. HERA's two main experiments, H1 and Zeus, are located at two opposed interaction points in resp. the North and the South Hall, as shown on figure 2.1. The main design parameters of the HERA rings are listed in table 2.1.

At the nominal beam energies, the center of mass energy is

$$\sqrt{s} \simeq 314 \text{ GeV},$$

which would be equivalent to the energy in a fixed target experiment using an incident beam of 51 TeV. The time interval between two bunch crossings is 96 ns.

The electrons (positrons) and protons, which enter the HERA accelerator, are preaccelerated by several other accelerators, as can be seen on figure 2.2. The maximum number of bunches for both the $e^{\pm}$ and the p beam is 210, but in 1994 HERA was operated with maximum 170 electron (or positron) bunches and 168 proton bunches, of which 153 bunches were colliding. Seventeen electron and fifteen proton bunches were unpaired and had no collision partner. In 1994, the third running year of HERA, the electron beam energy was 27.5 GeV instead of the nominal value of 30 GeV, which implies a centre of mass energy $\sqrt{s} \simeq 300$ GeV. For technical reasons, positrons were injected instead of electrons from August until November.

The length of the interaction region is determined by the proton bunch length and extends over a region of width $\sigma = 11$ cm along the beam line. The length of the electron bunches is approximately 0.8 cm.

2.2 The H1 detector

2.2.1 Detector scheme and design

The H1 detector is a general purpose detector for HERA, designed to measure with high precision the energy and momentum of particles and jets.

The detector (figure 2.3) consists of a large, fine grained calorimeter for detecting electromagnetic and hadronic particles, covering nearly 4π, and of several additional tracking and particle identification elements. Around the calorimeter is a superconducting coil, which provides a magnetic field of 1.2 Tesla. The iron yoke of the coil is instrumented

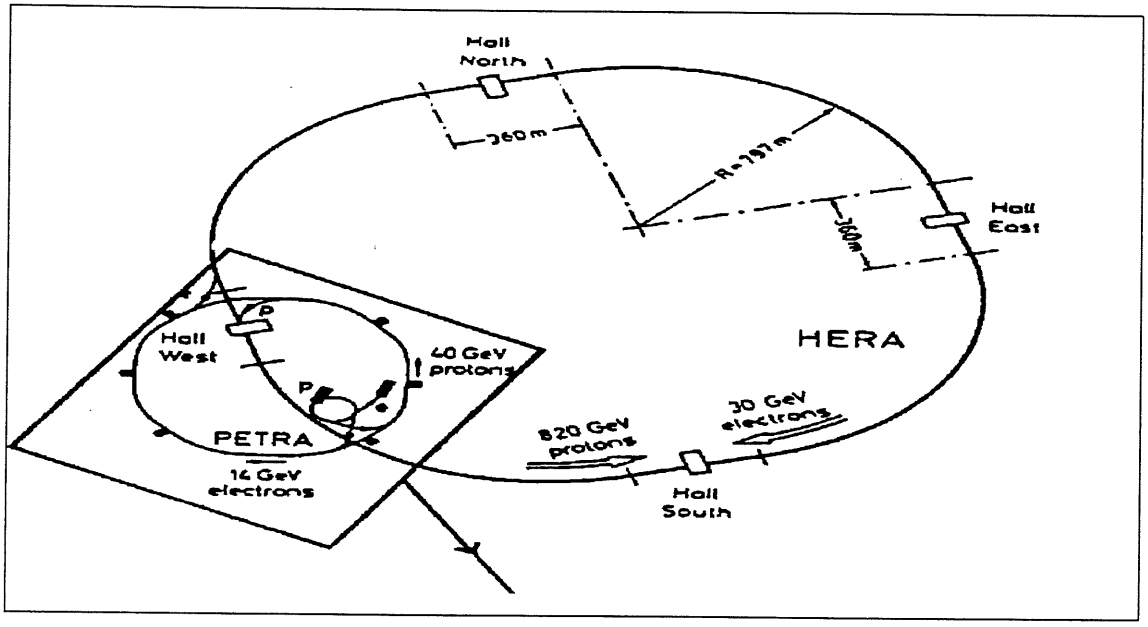

Figure 2.1: **The layout of HERA.**

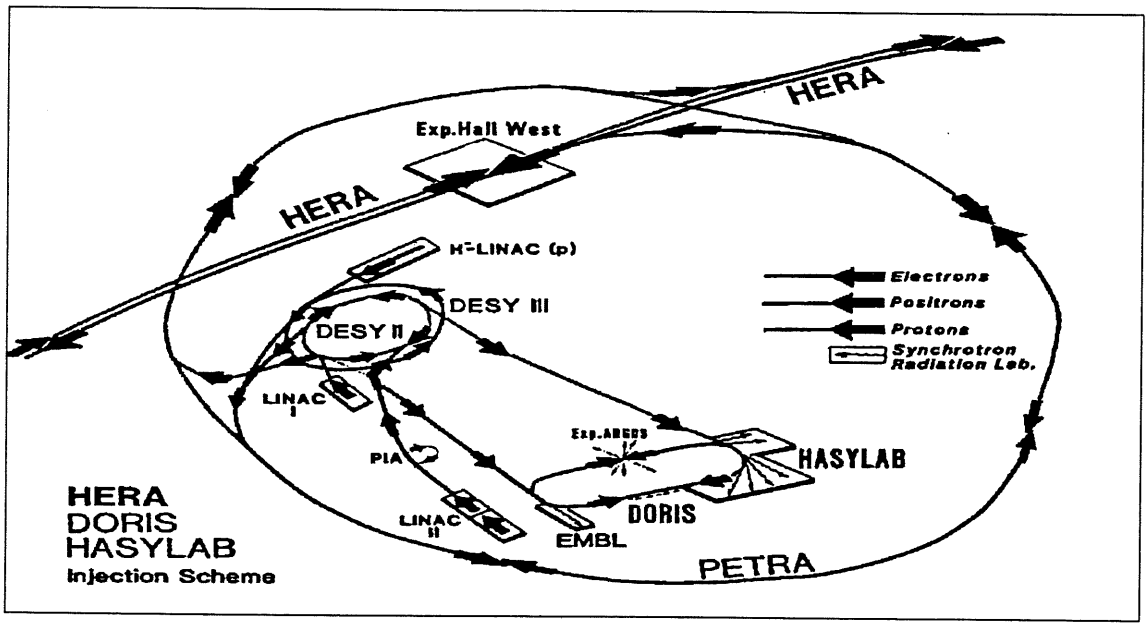

Figure 2.2: **The pre-accelerators of HERA.**
In the PETRA accelerator the 14 GeV electrons or positrons go clockwise, the 40 GeV positrons go counter-clockwise.

to detect muons, as well as hadronic particles which leak out of the calorimeter. Supplemental calorimeters are present to extend the coverage of the large calorimeter in the very forward (proton) and backward (electron) directions.

The design aspects of the H1 detector are not very different from the detectors at e^+e^- or $p\bar{p}$ colliders built in the past. Different at HERA is however the imbalance in the energy of the two colliding beams, which affects the detector geometry.

	p-ring	e-ring	units
Nominal energy	820	30	GeV
Polarisation time		28	minutes
Magnetic field	4.68	0.165	T
Number of particles	2.1	0.8	10^{13}
Number of bunches	210	210	
Injection energy	40	14	GeV
Filling time	20	15	minutes
σ_x/σ_y at I.P.	0.29/0.07	0.26/0.02	mm
σ_z	110	8.0	mm
Energy loss/turn	6.26×10^{-6}	127	MeV
RF-power	1	13.1	MW
Luminosity	1.5×10^{31}	$\mathrm{cm}^{-2}\ \mathrm{s}^{-1}$	

Table 2.1: **Nominal (design) HERA parameters.**
(The coordinates are defined as in figure 2.3.)

Due to the imbalance in the energy of the two colliding beams, the centre of mass of the ep system is boosted along the proton direction, and in that direction the H1 detector is considerably more instrumented and has a finer granularity. This asymmetry can be seen on the longitudinal view (figure 2.4) of the detector. We will frequently refer to the direction of the proton as the *forward* detector part (positive z-values relative to the center of the interaction region) and vice versa to that of the electron as the *backward* direction (negative z).

Starting from the center of the interaction region, the detector consists of a central and a forward tracking system, each containing several layers of drift chambers and proportional chambers. Those chambers are surrounded by the liquid argon cryostat, which contains an electromagnetic and a hadronic section. Around the cryostat is a superconducting cylindrical coil with a diameter of 6 m and a length of 5.75 m, which provides the magnetic induction field of 1.15 T. The return yoke of the magnet is instrumented and filled with streamer tubes, which are used to detect the small fraction of hadronic energy leaking out of the back of the calorimeter (tail catcher), but also serve as muon chambers. In the forward direction there is a supplementary toroidal magnet sandwiched between drift chambers, which allows to analyse the high momentum muon tracks in the forward direction. Since the liquid argon calorimeter doesn't cover the full polar angular range ($4° \leq \theta_{LAr} \leq 153°$), two supplementary warm calorimeters are present to extend calorimetric particle detection closely towards the beam pipe: the plug calorimeter in the very forward part and a backward electromagnetic calorimeter.

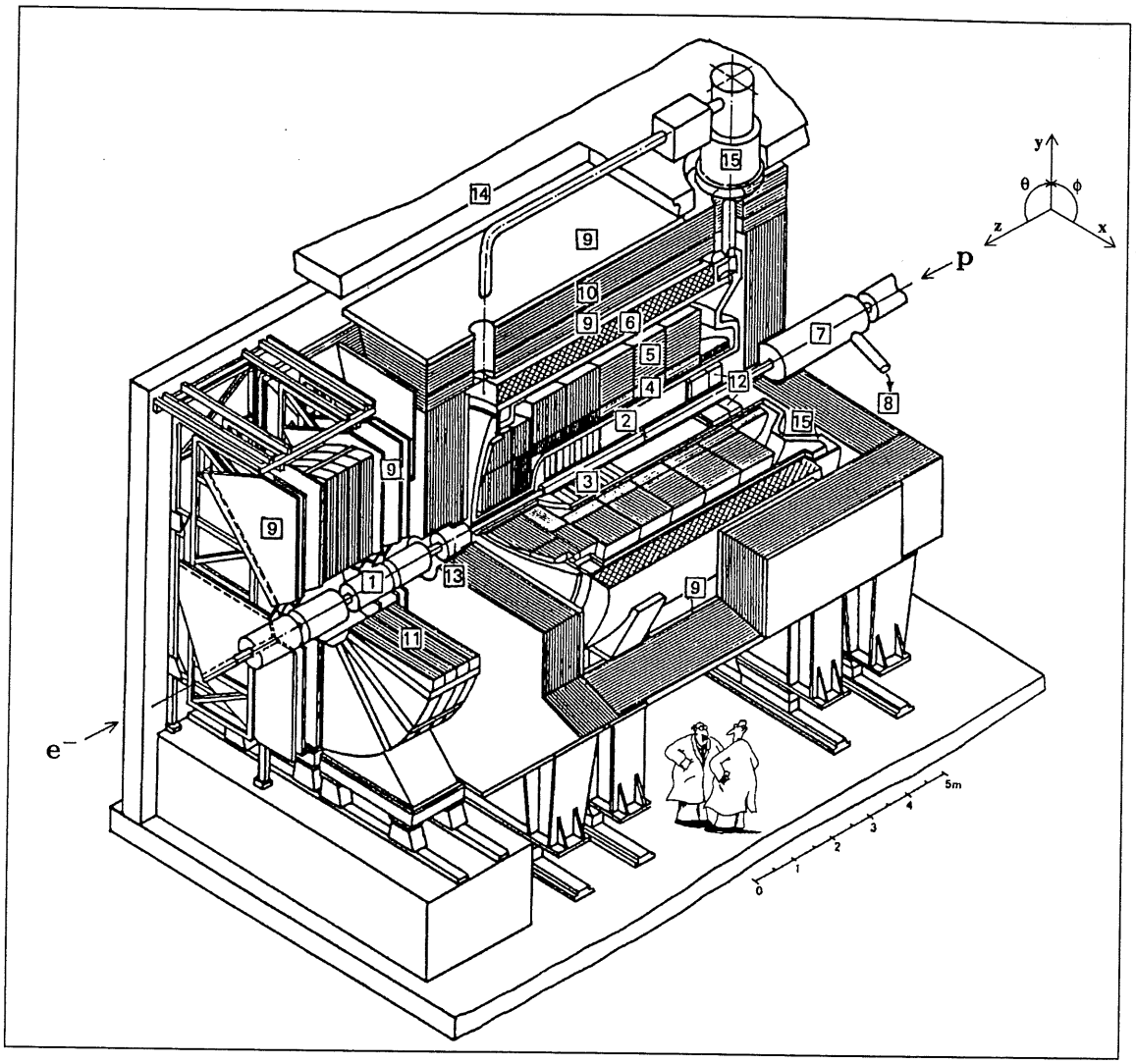

Figure 2.3: **The H1 detector.**
The H1 detector measures approx. 12 m×10 m×15 m and weighs 2800 t.
It consists of the following components:

1	Beam pipe and beam magnets	2	Central tracking chambers
3	Forward tracking chambers and Transition radiators		
4	Electromagnetic liquid argon calorimeter (lead)		
5	Hadronic liquid argon calorimeter (steel)		
6	Superconducting coil (1.15 T)	7	Compensating magnet
8	Helium cryogenics	9	Muon chambers
10	Instrumented iron (iron stabs + streamer tube detectors)		
11	Muon toroid magnet		
12	Warm electromagnetic calorimeter BEMC		
13	Plug Calorimeter	14	Concrete shielding
15	Liquid argon cryostat		

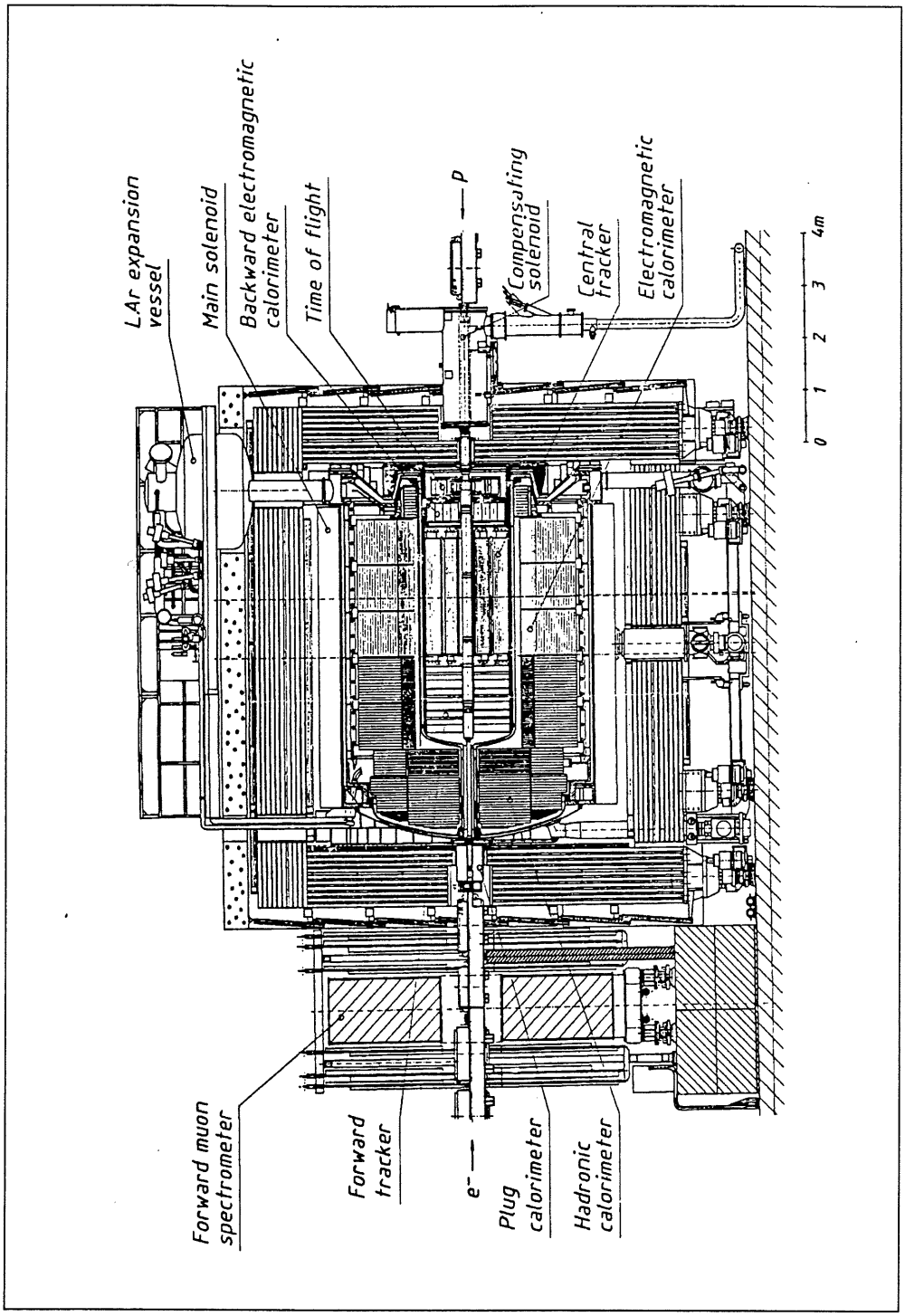

Figure 2.4: **Longitudinal cut through the H1 detector along the beam line.**

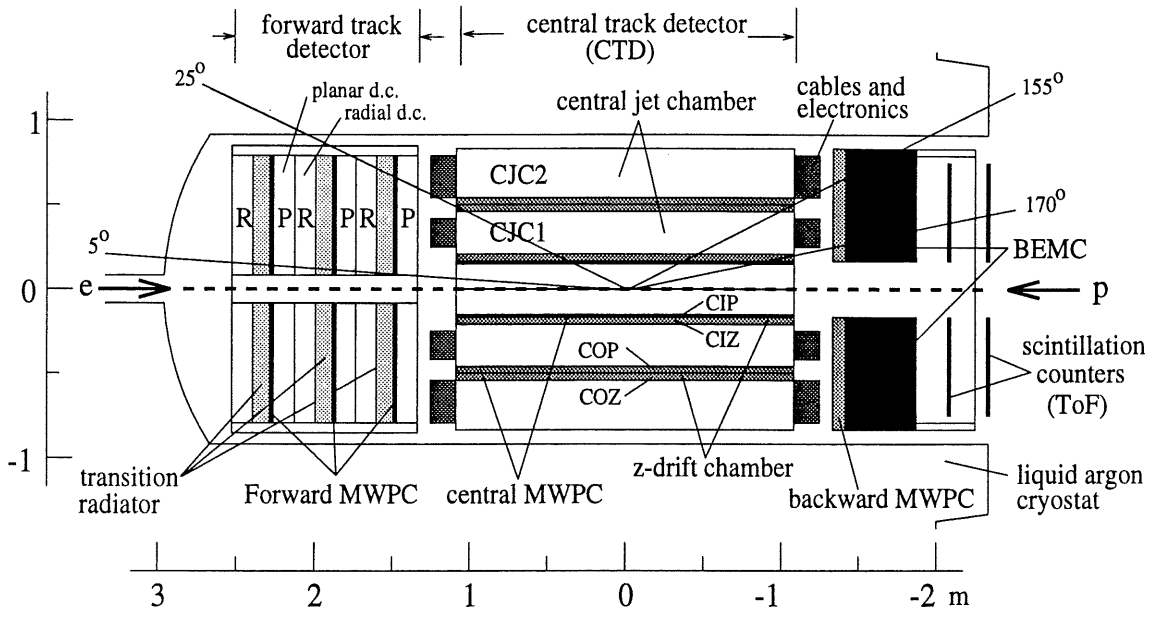

Figure 2.5: **Longitudinal view of the H1 tracking detectors.**

Two scintillator walls in the backward direction are installed to recognise background produced by the proton interactions upstream of the H1 detector.

Finally, an electron tagger at $z = -33$ m from the interaction point (not shown on figure 2.4) marks the energy of an electron with very small scattering angle. In coincidence with a photon detector at $z = -103$ m, this tagger serves to monitor the luminosity by the bremsstrahlung process. The electron tagger can also be used to study photoproduction and radiative events.

The following sections will give a more detailled description of the major detector parts. For a full description of the H1 detector we refer to [21] and [39].

2.2.2 Trackers

Introduction

The tracking system of the H1 detector provides both track triggering, reconstruction and particle identification for tracks produced by electron-proton collisions.

The central tracker detector (CTD) covers a polar angular range of 25°–175°, and consists of two large drift chambers (CJC1 and CJC2), each complemented by two thin drift chambers (CIZ and COZ) and two double layered proportional chambers (CIP and COP). The forward tracker covers an angular range of 5°–25° and consists of three identical supermodules. Each supermodule includes three different orientations of planar wire drift chambers, two multiwire proportional chambers, a transition radiatior and a radial drift chamber. Figure 2.5 shows the tracking detectors of H1. All these chambers will be briefly described in the next subsections. The basic parameters and the gas compositions of the tracking detectors are summarized in tables 2.2 and 2.3 respectively [21].

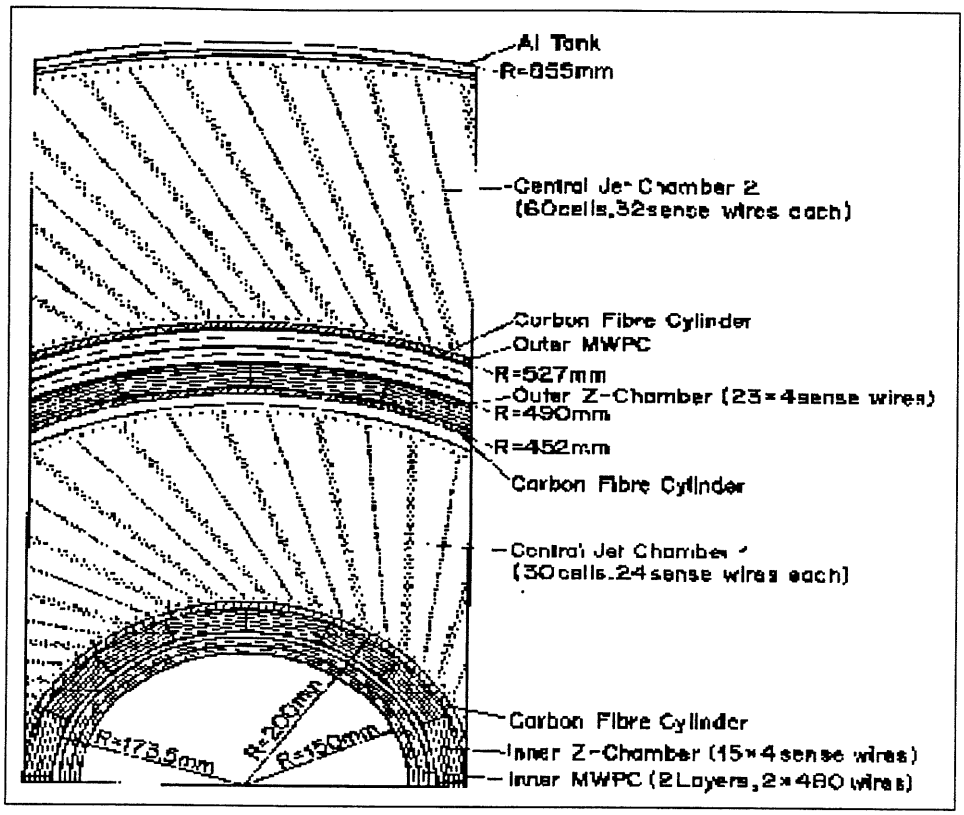

Figure 2.6: **Transverse view of the H1 central tracking detectors.**

The multiwire proportional chambers are separately described in section 2.2.3.

The central trackers CJC1 and CJC2

The central tracker is mainly based on two large concentric "jet" drift chambers, CJC1 and CJC2. The chambers have wires strung parallel to the beam axis (z-direction) with the drift cells inclined with respect to the radial direction to compensate the Lorentz angle (figure 2.6).

A space point resolution of 170 μm in the drift coordinate ($r\phi$) was measured, and it is possible to achieve a resolution of a few percent of the wire length in z (see table 2.2), by comparing signals read out at both wire ends. From the signals recorded in these chambers the transverse track momentum is determined ($\sigma_{p_T/p_T^2} \simeq 10^{-2}$ GeV). In addition the specific energy loss dE/dx can be measured with a precision of approximately 10%. Figure 2.7 shows the hits and reconstructed tracks of an electron-proton collision event, as seen in a part of the CJC.

Central z-chambers CIZ and COZ

The z-chambers allow a precise measurement of the z-coordinate of the tracks which pass through the CJC.

The central z-chambers are two thin driftchambers, and surround the inner half of the CJC1 and CJC2 respectively (figure 2.6). The sense wires are wound circumferentially

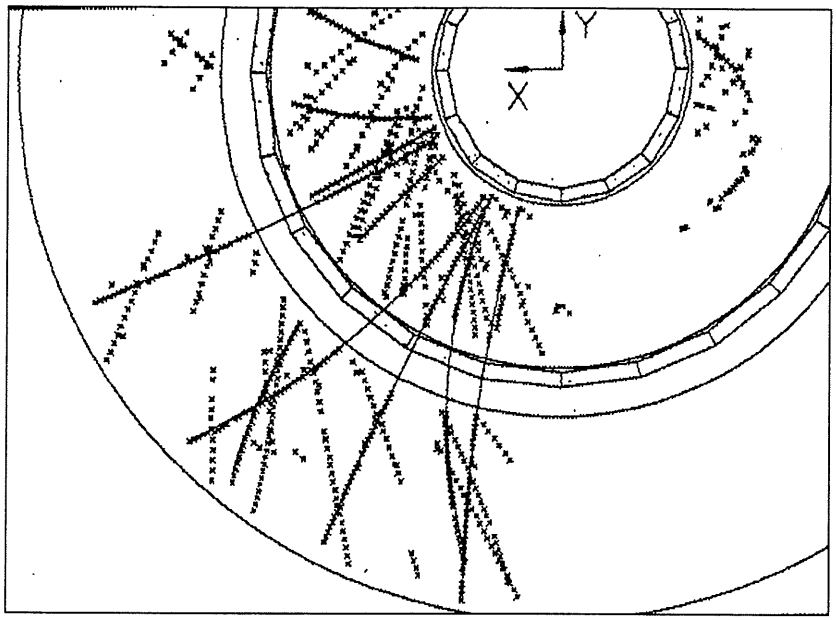

Figure 2.7: **Electron-proton scattering event as seen in the CJC showing tracks (and mirror tracks) found by the pattern recognition program.**

Chamber	r $[cm]$	z_{min} $[cm]$	z_{max} $[cm]$	$\sigma_{r\phi}$ $[mm]$	σ_z $[mm]$	σ_r $[mm]$	$\sigma_{x,y}$ $[mm]$
CIP	15.3-17.2	-112.5	106.5	-	-	-	-
CIZ	17.4-20.0	-108	72	25	0.25	-	-
CJC1, CJC2	21.5-76.9	-112.5	107.5	0.21	23.5	-	-
COZ	46-49	-110.5	105.5	58	0.34	-	-
COP	50-53	-110.7	106.5	-	-	-	-
FWR	15-75	-	-	0.17	-	29.0	-
FWP	15-75	-	-	-	-	-	0.21
BPC	13.5-65	-144	-138	-	-	-	2.0

Table 2.2: **Tracking detectors sensitive regions (r, z) and resolutions ($\sigma_{r,\phi,z,x,y}$) as obtained from the first luminosity runs at HERA.**

Chamber	Gas volume (m^3)	Gas components	Composition
Planars & FPC	~ 900	$Ar/C_3H_8/C_2H_5OH$	90/10/$\sim$1
Radials 1,2	~ 700	1: Ar/C_2H_6	48/52
		2: $Xe/C_2H_6/He/C_3H_7OH$	20/40/40/$\sim$1
Radiators	~ 500	He/C_2H_6	60/40
CJC 1,2	~ 4220	1: $Ar/CO_2/CH_4$	89.5/9.5/1
		2: $Ar/C_2H_6/H_2O$	50/50/$\sim$0.5
CIZ	~ 55	$Ar/CH_4/H_2O$	80/20/$\sim$0.2
COZ	~ 240	$Ar/C_2H_6/C_3H_7OH$	48/52/$\sim$1
CIP	~ 30	$Ar/C_2H_6/Freon_{12}/H_2O$	49.9/49.9/0.2/$\sim$0.2
COP	~ 150	$Ar/C_2H_6/Freon_{12}$	49.9/49.9/0.2
BPC	~ 120	$Ar/C_2H_6/Freon_{12}$	49.9/49.9/0.2

Table 2.3: **Composition of the gas mixtures in the tracking detectors.**

around the surface of two cylinders and are perpendicular to the beam axis, which means that the drift direction is parallel to the beam axis. The z-chambers therefore deliver track elements with a good resolution in z (typically 250 μm).

The radial, planar and transition radiation chambers

The geometrical acceptance of the CTD is limited to tracks with $\theta > 25°$ with respect to the beam axis. The forward tracking detector is aimed at providing an accurate measurement of space impact points of charged particles in the forward direction. Additionally limited particle identification by means of transition radiation is possible.

As already mentioned earlier, the forward tracking detector consists of an integrated assembly of three identical supermodules (see figure 2.8). Each supermodule includes, in increasing z: three different orientations of planar wire drift chambers designed to provide accurate θ measurements, a multiwire proportional chamber (FPC) for fast triggering, a radial wire drift chamber which provides accurate ϕ (drift coordinate) information, a moderate radial measurement by charge division and limited particle identification by measuring the transition radiation produced immediately upstream.

The planar module consists of three drift chambers each four wires deep in z and rotated at 60° in azimuth. The sense wires of the planar chambers are all parallel with respect to each other.

The radial drift chambers contain wires which are strung radially outwards from the beam pipe, perpendicular to the beam axis . Each of these chambers covers 360° of the azimuthal angle ϕ.

The transition radiatators (TR) consist of a passive array of polypropylene sheets. Passing electrons produce X-rays, which can be efficiently detected by the radial drift chambers. The combination of TR and radial chambers is designed for electron-pion discrimination, at the level of 90% electron acceptance with less than 10% pion contamination, up to 80 GeV for tracks passing through all three modules of the FTD.

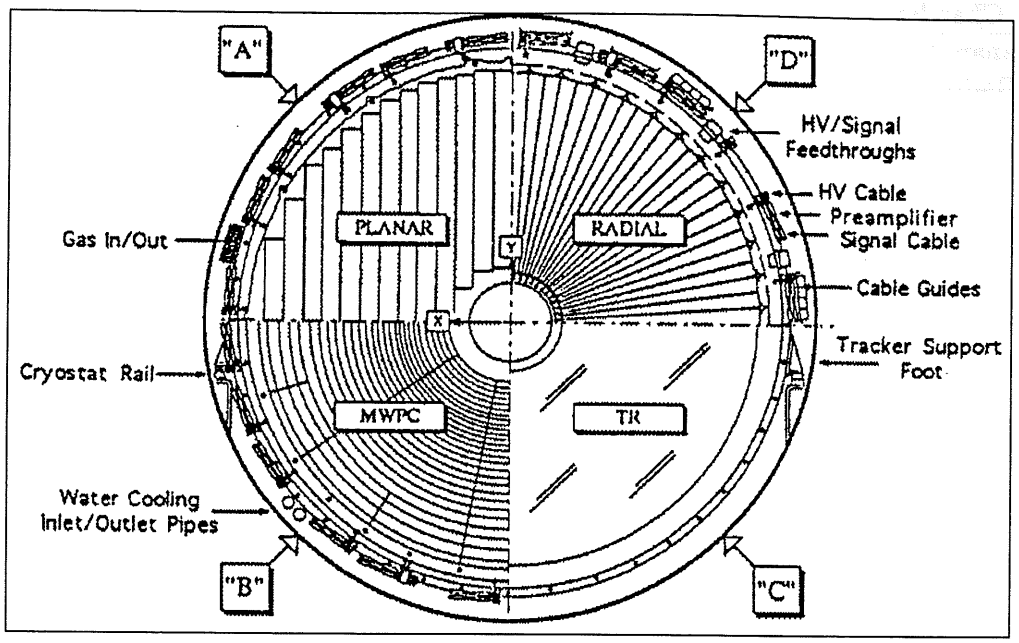

Figure 2.8: **The forward tracking detector (FTD).**

2.2.3 Multiwire proportional chambers

The polar angular range from 5° to 175° is completely covered by four different multiwire proportional chambers. They serve three different functions: they deliver a fast timing signal with a time resolution better than the time interval between two succeeding HERA *ep* bunches, they provide moderately accurate space points for charged particle track reconstruction at the first trigger level and lastly, they add an accurate track element in the backward direction, which lies outside the acceptance range of the drift chambers. As an example, figure 2.9 shows an MWPC-based z-vertex level 1 trigger.

The basic parameters and the gas compositions of the multiwire proportional detectors are summarized together with the drift chambers in tables 2.2 and 2.3 respectively [21].

The forward proportional chambers (FPC)

The planar forward proportional chambers are interspaced between different drift chambers in the forward supermodules. Each of the three forward proportional chambers consist of three cathode planes interleaved with two wire planes. Two of the cathode planes are partioned into 'sectors', which are ring shaped, and which are further divided into 'pads'. The signals of those pads are digitised and read out (yes/no information). Figure 2.8 shows the geometry of the FPC pads. In total 192 pads per plane are to be read out, resulting in 384 pads per supermodule and 1152 FPC pads in total for the three supermodules. The FPC data provides limited space point information, which is used to enhance the level 1 MWPC trigger, as can be seen on figure 2.9.

The FPC share their gas volume with the forward drift chambers and the transition radiation detectors.

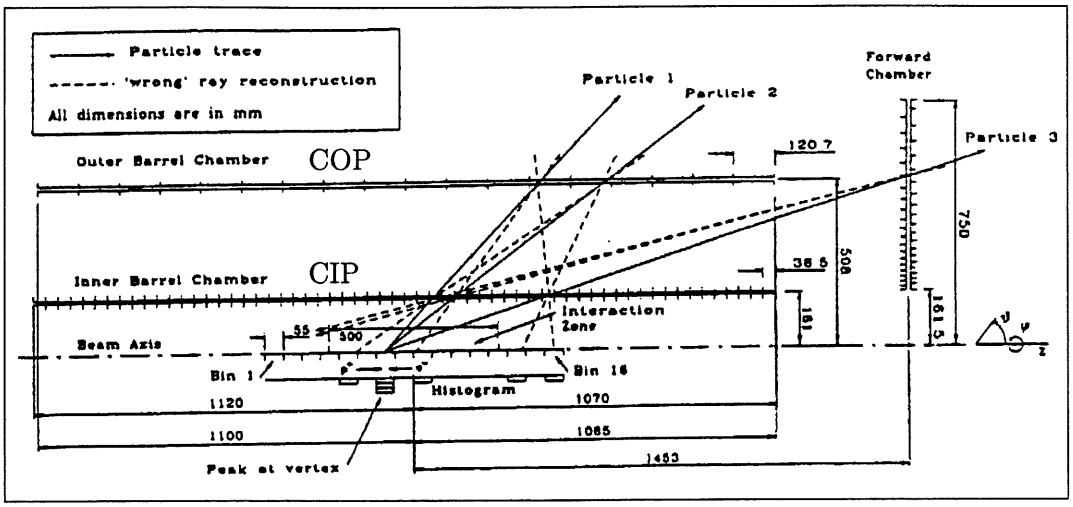

Figure 2.9: **MWPC z-vertex trigger:**
the z-vertex is reconstructed by building a histogram, which displays a peak at the true vertex location. Particles 1 and 2 pass through the CIP and COP chambers, particle 3 lies outside the geometrical acceptance of the central MWPCs and is detected by the forward proportional chambers (FPC).

The central proportional chambers (CIP and COP)

Both the central inner (CIP) as the central outer (COP) proportional chambers consist of three concentric cylinders, which are mounted around the CIZ and the COZ, respectively.

The middle cylinder forms the outer cathode of the inner cylinder and the inner cathode of the outer cylinder. An Cu/Kapton-foil on both outer and middle cylinders serves as cathode and is segmented into pads. Like the FPC, those pads are digitised and read out (yes/no information). The CIP has 60 pads in z and 8 'sectors' covering $\pi/4$ in ϕ. The pads of the inner CIP and the outer CIP are rotated by $\pi/8$, thereby doubling the azimuthal angle resolution. The COP is segmented into 18 pads in z and into 16 'sectors' in ϕ. The pads of the inner and the outer COP are located on top of each other.

This geometry allows to reconstruct a space point of charged tracks within the ep bunch crossing time interval. By combining the CIP, COP and also the FPC, a z-vertex can be reconstructed with a resolution of around 5 cm due to the pad geometry (figure 2.9).

The backward proportional chambers (BPC)

The backward proportional chamber (BPC) is mounted directly in front of the backward electromagnetic calorimeter (BEMC) at $z = -142$ cm. This detector allows to measure the impact point of charged particles which enter the BEMC and covers polar angles of $155.5° < \theta < 174.5°$.

The BPC consists of four individual planar wire chambers. There are 312 wires per plane to read out, resulting in 1248 wires in total.

In every plane the wires are strung parallel every 2.5 mm, and the wire orientations

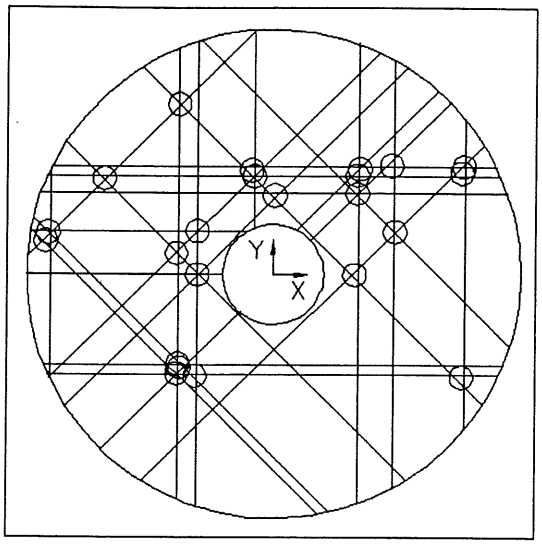

Figure 2.10: **The backward proportional chamber (BPC).**
The BPC impact points are reconstructed from the coincidence of three or four wires of different planes.

are vertical, horizontal and $\pm 45°$ for the four layers (figure 2.10). The signals from two wires each are fed to one preamplifier, resulting in an intrinsic space resolution of 1.5 mm.

The particle impact point can be reconstructed by requiring the coincidence of the four planes. The algorithm which was used to reconstruct those impact points will be described in chapter 5.

2.2.4 Calorimeters

The main calorimeter (LAC) which uses liquid argon as active material, is placed inside the large coil. This calorimeter covers the polar angular range between $\theta = 4°$ and $\theta \approx 153°$. The main reasons for choosing the liquid argon technique were good stability and ease of calibration, fine granularity for e/π separation and energy flow measurements, as well as homogeneity of response. A small Si-Cu calorimeter (PLUG) in the proton direction covers the region between the beam pipe and the liquid argon crystat ($\theta \leq 4°$) and a Pb-scintillator backward electromagnetic calorimeter (BEMC) covers the electron direction ($151° \leq \theta \leq 177°$). Finally the calorimetric coverage is completed by the tail catcher system (TC), which provides a rough calorimetric measurement of hadronic particles leaking out of the LAC or the BEMC, and is based on the analogue readout of the pads of the streamer tubes that instrument the iron yoke (the same ones as the muon chambers).

In the next sections the cryostat and the cryogenic system of the liquid argon calorimeter (LAC), the LAC itself, the BEMC, the PLUG and the TC are briefly described.

Cryostat and cryogenic system

The cryostat is made of stainless steel (some parts of aluminium alloy) to withstand a maximum pressure of 3 bars and to support the weight of the calorimeters (600 t). The

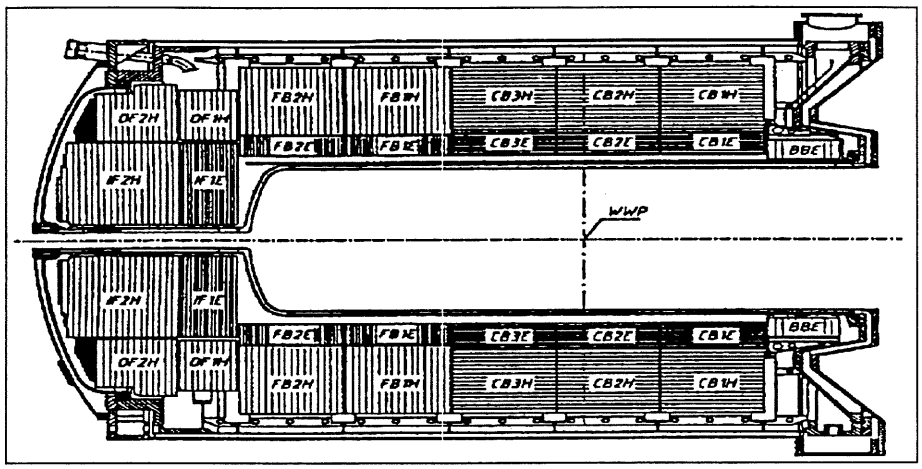

Figure 2.11: **Longitudinal view of the calorimeters.**

system is designed to allow cool-down and warm-up times less than 30 days and a transfer time of the liquid argon into the cold cryostat within 12 hours. More important, the temperature and the pressure should stay stable over several months. This is obtained by a regulated flow of liquid nitrogen through coils located within the cold and expansion vessels. The actual cooling down to liquid argon temperature is achieved by circulation of helium gas cooled in an external heat exchanger.

The liquid argon calorimeter (LAC)

The liquid argon calorimeter consist of two parts: an inner electromagnetic part (EMC) and an outer hadronic part (HAC). The segmentation along the beam axis is done in eight self supporting 'wheels' as shown in figure 2.11. There are six wheels in the barrel, and each of these is segmented in ϕ into eight identical stacks or octants. The two forward wheels are somewhat similar in principle but mechanically assembled as two half rings. This segmentation was a compromise between the requirement of minimising the dead volumes and practical building and handling. The areas between the different stacks of the calorimeter are called cracks and a great effort was made to minimise their size. The most backward wheel (BBE) is purely electromagnetic and covers the angular θ range from 143° and 152°.

Each electromagnetic stack consists of a pile of readout cells. Those readout cells are a sandwich structure, made of 2.4 mm Pb as absorber between two layers of epoxy+fiberglass and 2.35 mm liquid argon as active material with, per gap, one readout pad with copper pads and one high voltage plane. The hadronic sampling cells are made of 19 mm stainless steel with independent readout cells (with a similar structure as the electromagnetic cells), inserted between the plates. The hadronic stacks define the rigid structure on to which the corresponding electromagnetic stacks are mounted. The readout stacks are grouped into 'towers', to reduce the number of electronic channels. Those towers have a projective structure in ϕ and partially in θ (figure 2.12).

The total thickness of the electromagnetic calorimeter varies between 20 and 30 radiation lengths (X_0). This EMC has a depth of about 1 interaction length (λ_{abs}). The

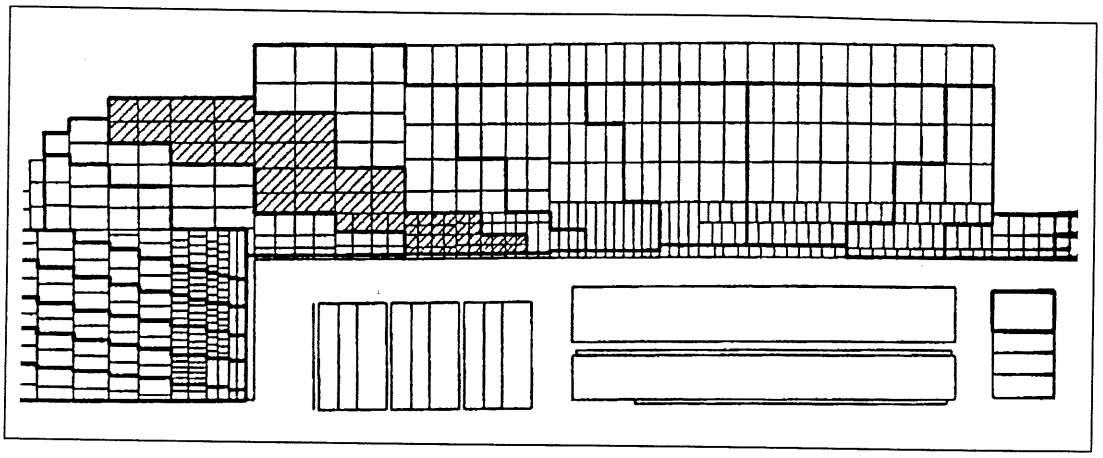

Figure 2.12: **The calorimeter towers and longitudinal segmentation.** *The structure of these towers is projective in ϕ and partially in θ and reflects the imbalance of the energies of the colliding beams.*

granularity of the of the readout cells follows from the requirements of a good separation of electromagnetic and of hadronic showers. Longitudinal segmentation is 3 to 4–fold for the EMC and 4 to 6–fold for the hadronic calorimeter (HAC). The depth of the hadronic calorimeter varies from about 5 to about 8 interaction lengths. A further constraint to the tower size is directly related to the calorimeter trigger, for which the collected energies must belong to a unique bunch crossing t_0 of the accelerator.

The number of pads is roughly 45000, and the electron drift time lies between 480 and 500 ns ($\sim$ 5 bunch crossings). Further processing of the signals takes 2.2 μs, which is approximately 22 bunch crossings.

The energy resolution of the electromagnetic calorimeter varies between $\sigma/E = 10\%/\sqrt{E}$ and $13\%/\sqrt{E}$ depending on the stack, with a constant term below 1%. The hadronic calorimeter has an energy resolution of $\sigma/E = 50\%/\sqrt{E}$ with a constant term of 2%. The major parameter which determines the time stability of the calorimeter response, is the liquid argon purity. This time stability is around 1%. The absolute energy calibration of the EMC and HAC allows to measure the energy with a precision of 2% and 7% resp.

The backward electromagnetic calorimeter (BEMC)

The backward region of the H1 detector is instrumented with a conventional electromagnetic lead-scintillator calorimeter. This Backward Electromagnetic Calorimeter (BEMC) has been designed to measure the energies of electrons scattered under small angles in the backward direction, a region which is not covered by the main liquid argon calorimeter.

The calorimeter elements (stacks) of the BEMC are mounted in an aluminium barrel with inner diameters of 21.5 cm and 23.3 cm and outer diameters of 159.0 cm and 162.1 cm, and with a length of 43.9 cm. The front face of the BEMC is located at a distance of 144 cm from the normal interaction point (IP) (figure 2.13). The BEMC covers the full azimuth and a maximum angle range from 151.4° to 176.5°. Since the accepance of the rear part of the liquid argon calorimeter starts at 153°, there is an almost continuous transition between the two calorimeter types.

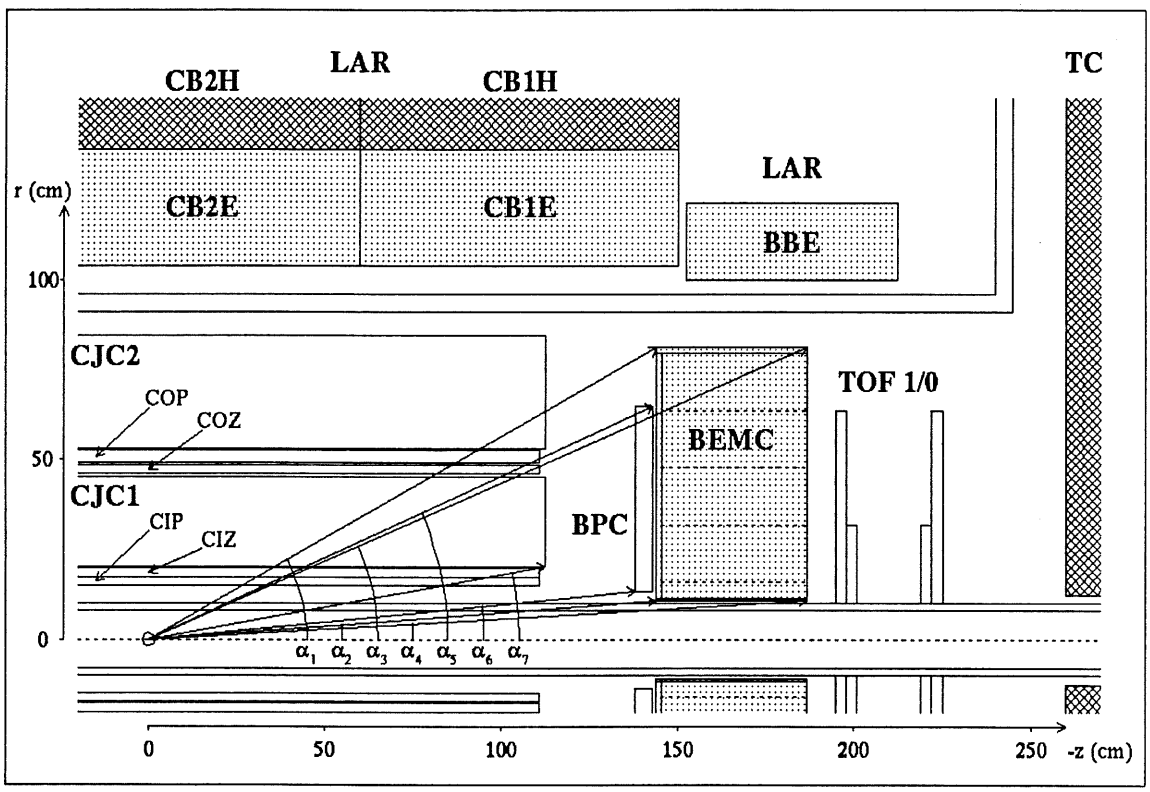

Figure 2.13: **Backward region of the H1 detectors.**
The values of the angles on the picture are:

BEMC:	$\theta_1 = 180^\circ - \alpha_1 = 150.63^\circ$	$\theta_2 = 180^\circ - \alpha_2 = 156.56^\circ$
	$\theta_3 = 180^\circ - \alpha_3 = 175.73^\circ$	$\theta_4 = 180^\circ - \alpha_4 = 176.71^\circ$
BPC:	$\theta_5 = 180^\circ - \alpha_5 = 155.56^\circ$	$\theta_6 = 180^\circ - \alpha_6 = 174.41^\circ$
CJC:	$\theta_7 = 180^\circ - \alpha_7 = 169.77^\circ$	

Granularity is provided by segmentation into 88 calorimeter stacks, which are parallel to the beam line. The stacks are multi-layer lead-scintillator sandwich structures (50 sampling layers). The produced scintillating light is read out via wavelengthshifters (WLS) extending over the full depth of the stack (long WLS). At the end of each WLS a photodiode with an active surface of 1 cm^2 is glued. The entire BEMC has an average density of 5 g/cm^3, which corresponds to a sensitive length of 22.5 electromagnetic radiation lengths (X_0) and which is equivalent to 0.97 hadronic interaction lengths (λ) for perpendicular impact. This means that the BEMC is an electromagnetic calorimeter, which is inefficient for measuring hadrons. In addition the scintillating light produced in the last 6.8 radiation lengths (15 sampling layers) is read out by separate WLS (short WLS), to measure the tail of the electromagnetic showers.

Figure 2.14 shows a tranverse view of the BEMC together with the stack structure and numbering. There are 56 so-called quadratic stacks, the remaining ones are of trapezoidal or triangular shapes.

The quadratic and trapezoidal stacks are equipped with four long WLS. The big triangular stacks also have four long WLS but the small ones only have three. All the photodiodes are read out separately in order to provide a measurement of the shower impact position using a 'center of gravity' algorithm, which will be explained in chapter 5. In total there are 472 readout channels in the BEMC.

The energy resolution of the BEMC has been determined in test beam studies carried out with electron beams ranging from 1 GeV to 80 GeV. A sampling term of $\sigma/E = 10\%/\sqrt{E}$ has been found in agreement with expectations from the mechanical design. The constant term is below 1%. In the real H1 environment the average noise per calorimeter stack was measured to be equivalent to 150 MeV. Several methods to calibrate the BEMC from H1 data have been developed and applied, and lead to the conclusion that the uncertainty of the channel-to-channel calibration is around 3%. More details of some of those methods will be given in chapter 5.

Interacting hadrons deposit typically 30% of their energy in the BEMC. About 30% of all hadrons do not interact at all. Their minimum ionising signal is about 2σ above the level of electronic noise and is very difficult to measure.

By determining the centre of gravity of the energy clusters in the BEMC, a position resolution of 1.3 cm has been achieved, which is far better than the one to be expected from the large transverse stack size of 16 cm $\times$ 16 cm.

Table 2.4 summarizes the global parameters of the BEMC. A more detailed description of the BEMC can be found in [13].

The plug Calorimeter (PLUG)

The aim of the forward plug calorimeter is to minimize the missing part of the total transverse momentum due to hadrons emitted at small forward angles. The geometrical limitations (it must be situated between the beam pipe at 0.6° and the forward part of the liquid argon calorimeter at 3°) can only be met by the most compact calorimeter design.

The plug calorimeter is a Cu/Si calorimeter with 672 silicon detectors. It has a good angular resolution of 4 mrad, and an energy resolution of $150\%/\sqrt{E}$.

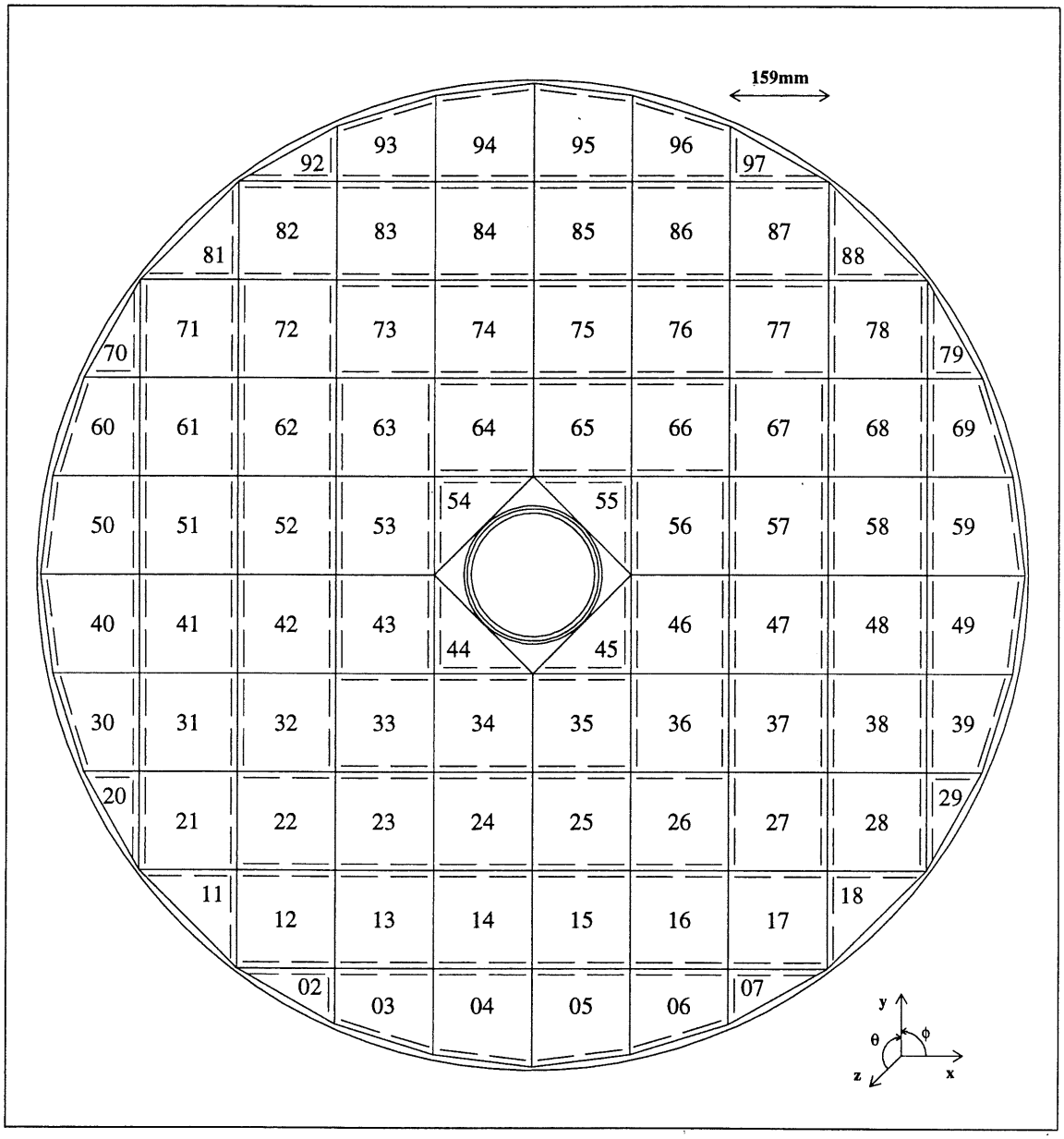

Figure 2.14: **Transverse view of the backward electromagnetic calorimeter (BEMC) and the position of the wave length shifters (WLS).**

Distance interaction point–BEMC barrel front line	144.0 cm
Distance interaction point–1st scintillator plate	146.1 cm
Average density of sampling structure	4.98 g/cm^3
Sensitive length (total)	22.5 X_0, 0.97 λ, 34.25 cm
Sensitive length (short WLS only)	6.8 X_0, 0.29 λ, 10.35 cm
Molière-radius	3.4 cm
Minimum sensitive radius (full azimuth)	15.9 cm
Maximum sensitive radius	$\approx$ 79 cm
Maximum polar angle coverage	$151.4° < \theta < 176.5°$
Full containment polar angle coverage (z = 0 cm)	$156.2 < \theta <\approx 173.6°$
Full containment polar angle coverage (z = +25 cm)	$158.9 < \theta <\approx 174.5°$
Full containment polar angle coverage (z = -25 cm)	$152.9 < \theta <\approx 172.3°$
BPC acceptance (4 planes, z = 0 cm)	$155.4° < \theta < 173.8°$
Total weight	$\approx$ 3000 kg
Electromagnetic energy resolution σ/E	$10\%/\sqrt{E}$

Table 2.4: **Global parameters of the BEMC**

2.2.5 Muon chambers and instrumented iron

The muon detectors consist actually of two different detectors: the instrumented iron, which is located behind the coil, and the forward muon spectrometer.

The instrumented iron

The iron yoke, which is needed to close the magnetic field lines, is equipped with streamer tubes. These tubes, which are actually the same as the ones of the 'tail catcher' to detect the tail of hadronic avalanges, is also used to detect muons.

The streamer tubes consist of maximally 6.5 m long plastic profiles with a central anode wire. On top of the profiles are rectangular (25 cm × 25 cm) electrodes ('pads'), used for the calorimetric measurements (tail catcher), and 'strips' perpendicular to the wire direction, which are used for the muon detection together with the wire readout. The pad signals are read out in an analogue way, while the anode wires and the strips are digitised and read out.

The detection system allows to measure muons with momenta greater than 1.5 GeV/c.

The forward muon spectrometer

The forward muon spectrometer is used to measure high energy muons at angles between 3° and 17°. The detector consists of drift chambers with radial and azimuthal wires, and of a steel toriod, in which a magnetic field is present. The magnetic field within this toriod varies with radius, from 1.75 T at radius 0.65 m to 1.5 T at radius 2.90 m.

With this detector, muons with momenta between 5 GeV/c and 200 GeV/c can be measured.

The tail catcher (TC)

Some hadrons do not deposit all their energy in the hadronic part of the liquid argon calorimeter. In order to measure the hadronic energy leaking out, eleven of the sixteen streamer tube (LST) layers of the instrumented iron (used for muon detection) are equipped with readout electrodes (pads).

The energy response of the tail catcher is linear up to at least 30 GeV, while the obtained energy resolution is $\sigma/E \simeq 100\%/\sqrt{E}$.

2.2.6 Luminosity measurement

H1 determines the luminosity by measuring the rate of the bremsstrahlung reaction $ep \longrightarrow ep\gamma$, by detecting both the final state electron and photon. For this purpose, two small crystal calorimeters are installed down the beam pipe (in the electron direction): a photon calorimeter (*photon detector* or PD) located about 100 m from the interaction point ('upstream') and an electron calorimeter (*electron tagger* or ET), at about 30 m. Figure 2.15 shows the positions of the electron tagger and photon detector with respect to the backward part of the H1 detector.

There are two major reasons which make the Bethe-Heitler (bremsstrahlung) process suitable for luminosity measurement purposes: the cross section of this reaction can be calculated theoretically with a high precision, and Bethe-Heitler events are easy to detect experimentally, since they satisfy the constraint that $E_e + E_\gamma = E_{e-beam}$ as shown by the diagonal band of figure 2.16. The measured energy spectrum in the photon detector is typical of a bremstrahlung process and agrees well with expectations. The final state proton is not observed, so that bremstrahlung from residual gas gives the same experimental signature, and must be subtracted statistically. A good estimate of this background can be obtained by using the unpaired electron bunches (which have no associated proton colliding bunch). The experimental error on the luminosity of the 1994 e^+p data is 1.8%. The several contributions to this error are summarized in table 2.5.

The electron tagger and photon detector are also a essential devices for studying photoproduction and radiative events. These subjects will be explained in greater detail in later chapters.

2.2.7 Scintillators

There are two scintillator detectors, the time of flight counters and the veto wall, both located in the backward region. They are designed to reject proton beam associated background at the first trigger level.

Time of flight counters

The time of flight device (ToF) is a scintillator hodoscope consisting of two planes of plastic scintillator, mounted perpendicular to the beam pipe, located in the electron direction at $z \approx$ -2 m upstream of the interaction region. The mean time separation between particles from proton background and those from ep collisions at this point is $\sim$ 13 ns. It is by measuring this 'time of flight' with respect to the HERA clock, that the ToF is able to contribute significantly to the background rejection.

Contribution	e^-p	e^+p
$\sigma_{Bethe-Heitler}$ corrections	0.5%	0.5%
Trigger efficiency	0.3%	0.3%
Statistics, e-gas bgr. subtraction	1.3%	0.4%
γ-energy scale (calib. & resol.)	1.1%	0.9%
Geometrical acceptance of γ-arm	0.5%	0.5%
Multiple photon effect (pile-up)	0.3%	0.4%
Counting and rounding errors	0.5%	0.5%
Total error from lumi system	2.0%	1.4%
Satellite bunch correction	1.3%	1.1%
Overall error δL	2.4%	1.8%

Table 2.5: **Contributions to the experimental error on the luminosity.** *Preliminary values for the 1994 run period from [54].*

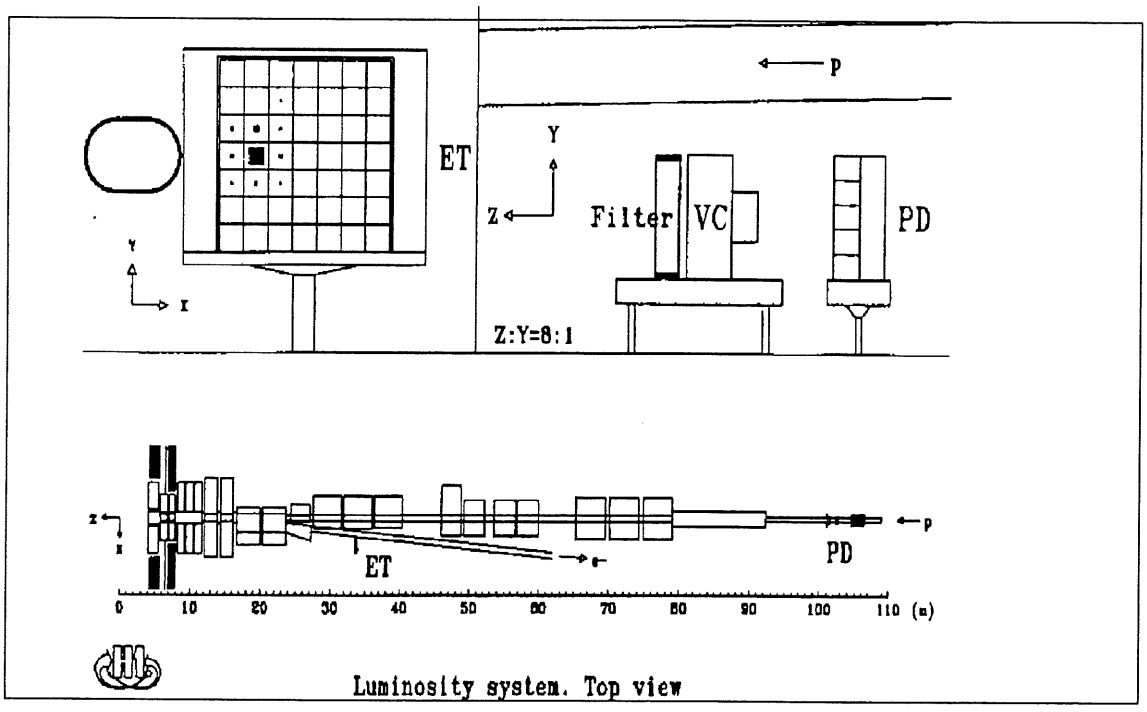

Figure 2.15: **Longitudinal view of the electron tagger and photon detector.**

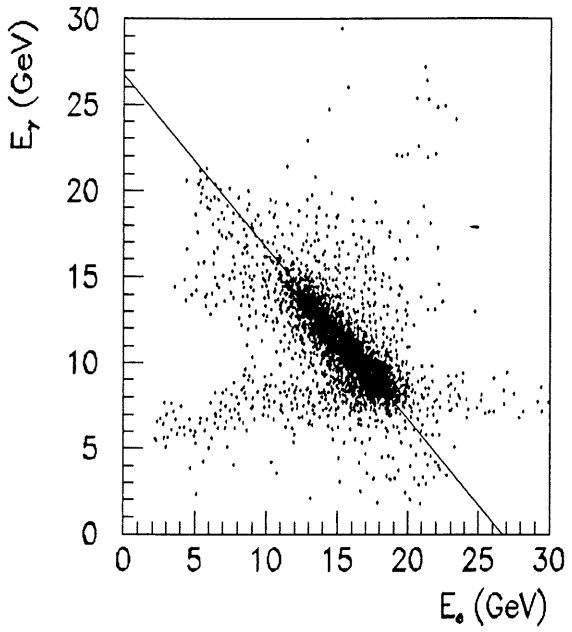

Figure 2.16: **Correlation plot of electron and photon energies from the $ep \longrightarrow ep\gamma$ reaction.**
Bethe-Heitler events satisfy the constraint $E_e + E_\gamma = E_{e-beam}$. Data from the 1993 HERA runs at 26.7 × 820 GeV collision energy.

The plane nearest to the interaction point (ToF1) lies at $z = -1.95$ m and has 16 counters, measuring 317 mm × 317 mm thus matching the size of four BEMC stacks. The other plane (ToF2) lies at $z = -2.25$ m and has eight larger counters (317 mm × 634 mm).

The ToF uses 24 photomultiplier (PM) tubes which can operate in the high magnetic field of 1.14 T. The signals from the 24 PMs are discriminated and strobed in three time windows: background, interaction and global. A logical OR of the signals from each of the two walls is made for the three time windows and any coincidence causes a corresponding trigger signal to be send to the central trigger logic (CTL). The background signal is used as a veto for most triggers, and generally leads to a 99% decrease of the overall trigger rate.

Signals from each counter in each time window, as well as the three coincidence triggers (75 in total), are also sent to the data acquisition for off-line use.

The veto wall

In addition to the ToF, two groups of scintillator planes are located at $z = -6.5$ m and $z = -8.1$ m, behind a 4 cm thick lead wall, built with the aim to absorb particles off the proton beam axis. Penetrating background particles are then identified in coincidence with the two scintillators.

The big veto wall consists of 26 large scintillator sheets, arranged in two layers, and covers a circle with a radius of approximately 2.5 m around the beam axis, which is almost the whole liquid argon and instrumented iron area. A square hole of 60 cm × 60 cm left in the centre is covered down to a circle with radius = 26 cm by the small veto wall, placed

1.5 m further upstream.

2.2.8 Trigger

The time interval between two succeeding beam crossings at HERA is 96 ns, which is equivalent to a clock period of 10.4 MHz. This means that every 96 ns interactions can occur. At the design luminosity 1.5×10^{31} $cm^{-2}s^{-1}$, the dominant physics process will be photoproduction at a rate of $\mathcal{O}(100)$ Hz. Other physics processes will only contribute by a small fraction of this rate (table 2.6). To compensate for those rather low physics cross sections, high beam currents are necessary. Unfortunately, off-momentum protons (and to a lesser extend electrons), whose number is proportional to the beam current, interact with residual gas atoms ('beam gas') or with the beam pipe ('beam wall'). This initiates a huge background in the order of 100 kHz.

This background situation, as well as the short bunch crossing time of 96 ns and the request for low deadtime of the readout system, meant a new challenge for H1. To cope with these conditions, a multilevel trigger system was designed for H1.

It is impossible to make a trigger decision within the time interval between two bunch crossings. A simple solution would be to buffer the frontend information and ignore the following bunch crossings until the decision to keep the event is taken. However, this would introduce an unacceptable deadtime and would lead to the loss of a substantial part of the luminosity provided by the HERA machine.

In H1, the first trigger level is 'pipelined', i.e. the trigger logic runs in step with the HERA clock. This means that the first triggering event will occur 2.2 μs after the first occurence, but then every bunch crossing might deliver a trigger. This means that the first trigger level is completely deadtimeless. Together with pipelining, a multi-level trigger and buffering scheme is used. For H1 four trigger levels were proposed. The higher the level, the more time-consuming and complex is the process.

Level 1 The analogue signals from the subdetectors are discriminated and fed both into a pipeline of the frontend digitising unit and into the subdetector trigger input. The trigger combines this information into so-called trigger elements, i.e. yes/no decisions encoded in bits. Examples are encoded energy thresholds for calorimeters ($E > E_{threshold}$) or encoded hit patterns for multiwire proportional chambers. The emphasis is placed on speed rather than accuracy. The longest L1 trigger decision time in H1 is 2.2 μs. If after this time the event satisfies the loaded trigger condition of level 1 (L1), the pipeline of the frontend is stopped and deadtime starts to accumulate. As long as no event satisfies the L1 trigger decision, the system is completely deadtimeless. Note that it is mandatory to include at least one trigger element with a good time resolution, so that the correct bunch crossing can be identified. Such trigger elements are called T_0 bits.

To accomodate the various trigger decision times from the various triggers, a pipeline of 32 positions was used. This allows also that the data of several bunch crossings before and after T_0 can also be read out, which is necessary for the finetuning of the readout delays.

Level 2 is a hardware trigger with deadtime, starting at L1-Keep. The L2 trigger starts the readout of the subdetectors with maximum precision. The L2 decision is limited

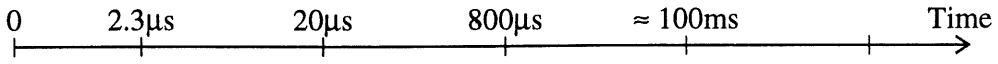

	L1	L2	L3	L4	(L5)
Dead time	0	20μs	< 800μs	-	-
Rate 1994	20-50 Hz	-	-	5-10 Hz	< 5 Hz
Data rate 1994	1.2 MB/s	-	-	≈ 1 MB/s	0.3 MB/s
Maximum rate	1-5 kHz	200 Hz	50 Hz	5 Hz	≈ 1 Hz
	Subdetector Electronics	Electronics		Filter farm ≥15 RISC	≥2 SGI
	Hardware	Hardware	Hardware	Software	Software
Action	Stop pipeline	Start reading signals	Start event building	Begin data transfer	Production of POT and DST
Function	ToF: Veto MWPC: Vertex e-Tagger: Ee LAr: Ee,Et,Etot.. BEMC: BSET Muon system: μ Drift chamber: rΦ etc.	1992-1994 not active	1992-1994 not active	Filter during reconstruction: -central tracks -energy clusters Vertex cut Energy cut	Online reconstruction Event classification Data selection

Table 2.6: **Overview of the H1 trigger.**

at 20 μs, which is sufficient time to combine trigger bits from different detector parts. The L2 level will reduce the L1 event rate from 1 kHz to about 200 Hz.

Level 3 This is a hardware trigger, planned to be operational in 1995. The L3 trigger starts in parallel with L2, to further reduce the event rate to 50 Hz. Dedicated microprocessor-based hardware will compute the L3 decision in 800 μs on the basis of more complex matching of the information of the different detector components. The L3 trigger may possibly issue a reject condition, which causes an abort of the event readout cycle. This decreases the deadtime of the readout.

Level 4 is a software filter. The aim of this level is to reduce the data volume before it is finally sent to the data storage media at the DESY computer center. The calculations are performed by the processor farm on the full event data, asynchronously with the rest of the trigger ('filter farm'). This algorithms are based on charged track, vertex and energy cluster information. The main filtering criterion, effective against beam gas and beam wall backgrounds, is based of (x,y,z)-vertex reconstruction.

The aim is to reduce the final logging rate to $\sim$ 5 Hz.

In the next chapter, more technical details of the trigger will be discussed.

2.2.9 Data acquisition

The H1 data acquisition system is designed to read out and digitise over a quarter of a million analogue channels, resulting in some 3 Mbytes of raw digitised information for a triggered event. As the time between successive *ep* bunch crossings is just 96 ns, various levels of hardware triggering, software filtering and digital compression are employed in order to reduce the final data size to acceptable storage media recording sizes.

Every subdetector is connected to a dedicated analogue and/or digital 'front-end' system, which is specifically designed to process the signals of that particular subdetector. All those 'local' DAQ systems are connected together via an optic fibre link to a 'central data acquisition' system (CDAQ). The CDAQ system coordinates the overall readout chain, transfers the data of the local DAQ systems to a central memory buffer and merges the fractional event information into full H1 events. The latter are sent to the L4 filter farm, and later to a central mainframe computer, which writes the data onto magnetic tape cartridges.

Additionally, various monitoring systems are connected along the readout chain. They include histogram and event display facilities, with which any user can monitor the proper functioning of the whole DAQ and trigger chain. Closely integrated into the DAQ system are various user interfaces, to control, set-up, calibrate and test the DAQ, trigger and slow control systems (high voltage, gas flows and pressures, temperatures, ...).

A more detailed description of the functioning of the H1 DAQ systems can be found in the next chapter.

Chapter 3

The MWPC data acquisition

In chapter 2 the H1 data acquisition (DAQ) as well as the H1 trigger were briefly described. In order to explain the MWPC DAQ software in particular, a more detailed description of the H1 DAQ and trigger will be given in sections 3.1 and 3.2 respectively.

Both the MWPC DAQ hardware layout and software underwent several stages of development from 1987 to 1993. This chapter only deals with the first stage, which was the 'first day' DAQ, as it was used during the data taking of the first H1 cosmic runs in 1991 and 1992, as well as for the *ep* runs in 1992. The software of this period was largely the result of my personal work. Section 3.5 summarises the MWPC DAQ hardware, while the software is described in sections 3.4, 3.6 and further. A glossary with an explanation of most of the abbreviations that are used in this chapter can be found at the end in section 3.11.

3.1 The H1 data acquisition

3.1.1 Overview of the structure of the data acquisition in H1

In section 2.2.9 it was already explained that the H1 data acquisition system is physically and logically split into a central data acquisition (CDAQ) system and several subdetector front-end systems. Those front-end systems form 12 branches, shown on figure 3.1 and listed in table 3.1.

Each branch is autonomous and can be operated as an independent unit for test measurements and system development. Due to the very different nature of its associated subdetector, each branch has its own configuration, with specific acquisition modules, interfaces and computer systems. However, some uniformity in the general design concepts was maintained. The majority of the roughly 200 electronic crates in H1 follow the VME-bus standard [1], and some of the VME modules, like processor, memory and interface boards, are of the same type for all the branches.

3.1.2 The central data acquisition and the event building

The different front-end systems have to communicate with the CDAQ and this communication is done in a standardized way. Every subsystem has a dedicated VMEtaxi module, which is responsible for the handling of the communications with the CDAQ and for transferring the data from the front-end buffers to the central DAQ. All the VMEtaxi communication modules are connected together and to the CDAQ via an optic fibre ring, as shown on figure 3.1.

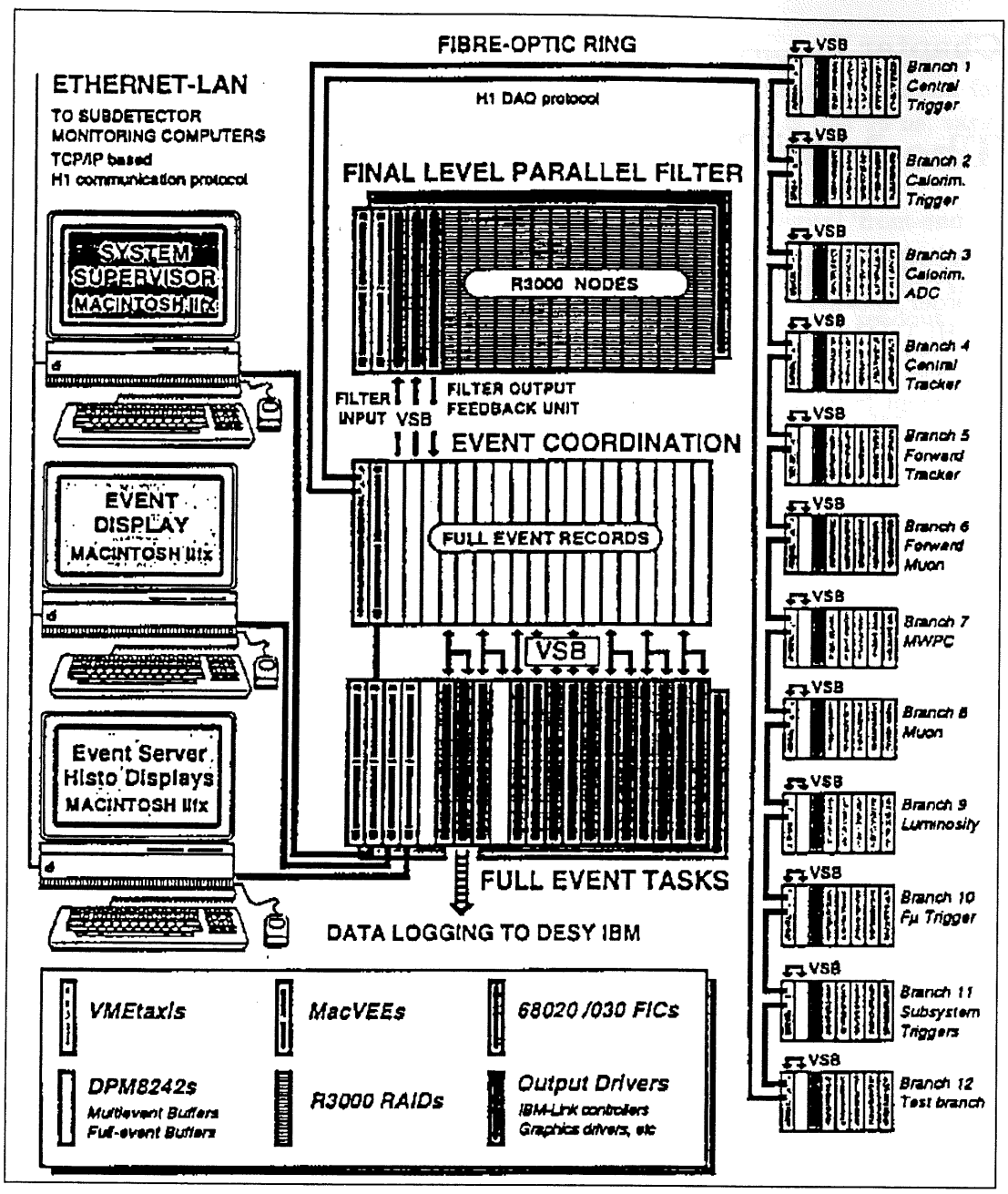

Figure 3.1: **Overview of the subdetector branches of the H1 data acquisition system.**
The data of the front-end crates is transferred via a fast VME Subsystem Bus (VSB) to an interface module (VMEtaxi) in each crate. These VMEtaxi modules are connected together via an optical fibre chain to the central DAQ system. The data of the front-end crates is then merged into full event records in the Full Event Buffer (FEB).

Branch		Description
1.	Trigger	Central trigger controller (L1,L2 logic)
2.	Calorimeter trigger	LAr trigger system
3.	Calorimeter ADC	LAr calorimeters, BEMC, plug and tail catcher readout
4.	Central tracker	CJC, CIZ and COZ readout
5.	Forward tracker	Planar and radial chambers readout
6.	Forward muon	Muon spectrometer readout
7.	MWPC	MWPC and associated triggers readout + TOF
8.	Muon	Muon streamer chamber readout
9.	Luminosity	Luminosity calorimeter readout
10.	Forward muon trigger	Muon spectrometer trigger system
11.	Subsystem triggers	Central DC trigger systems
12.	Test branch	This branch is used for test purposes

Table 3.1: **Branch partitions of the H1 data acquisition system.**

Every subsystem holds one so-called 'master crate', which is a VMEbus crate. It is in those master crates that the communication modules are placed. VMEbus crates are widely used at the front-end level, but the use of other busses is not excluded at this level.

Every subsystem collects the data of its detectors and stores it into a multi-event buffer (MEB). Those event records are transferred to the CDAQ and merged into the full-event buffer (FEB). This process is called 'full event building' and runs under the control of a CDAQ VME bus processor, the 'event coordinator' (figure 3.1).

Given the different software overheads, this system achieves a throughput of 3 Mbytes/s for the 12 subdetector branches and an average event size of 60 kbytes, so that the maximum event building rate is about 50 Hz. In 1993 the VMEtaxi ring has been upgraded to allow 200 Hz, but due to overheads at the level of the subsystems, the maximal rate is still 50 Hz.

The main task of the FEB is the data logging, but it also performs additional tasks, such as level 4 filtering, event display and data monitoring (histograms). The level 4 filter farm performs complex tasks, as already mentioned in section 2.2.8, and consists of a farm of RAID8235 boards [20], which contain 25 MHz RISC R3000 processors. The data logging task allows to send full events over an optic fibre to the DESY central IBM facility, located some 3 km away from the H1 experimental hall. Disk writing limits the maximum logging rate to 1.2 Mbytes/s, but the link itself allows rates up to 7 Mbytes/s. In case of a link failure, a backup storage device is stand-by in the CDAQ control room.

3.2 The H1 trigger

The H1 trigger levels have already been described in 2.2.8. The only relevant input signals to the MWPC DAQ system are the L2keep, L3keep and L3reject signals.

After an L2 trigger decision, an L2keep signal is sent to all the subsystems, which initiates the readout of the data. In parallel with this readout, the L3 processors prepare the third-level trigger decision. An L3keep signal is used as a flag to indicate that the

Detector	Channels
Forward proportional chambers (FPC)	1152
Central inner proportional chambers (CIP)	960
Central outer proportional chambers (COP)	576
Backward proportional chambers (BPC)	1248
Time of flight (ToF)	75
Z-vertex trigger	19
Forward ray finder trigger	60

Table 3.2: **The channels read by the MWPC DAQ system.**

event has to be passed to the next stage of the acquisition. If an event is rejected by the L3, the front-end is immediately aborted.

As soon as all the front-end data has been read, the subsystem signals a *Front-End Ready (FER)*. Only when all the subsystems have issued a FER, the central trigger controller (CTC) is enabled to continue with the next event.

The L2keep, L3keep and L3reject will generate VME interrupts which control the MWPC DAQ program. This will be explained in greater detail in 3.3.

3.3 The MWPC data acquisition and trigger

3.3.1 Tasks of the MWPC data acquisition

The MWPC DAQ system was designed to read the data of the four multiwire proportional chambers (CIP, COP, FPC and BPC) as well as the time-of-flight (ToF) scintillators. Furthermore, the two MWPC-based triggers, the z-vertex trigger and the forward ray finder trigger, also provide data to be read out by the MWPC DAQ. Table 3.2 summarizes the channels which are read out by the MWPC DAQ system. All the channels mentioned in this table represent a yes/no (1 bit) signal.

The already amplified signals of the detectors are sent over a 30 m long cable, after which they are discriminated and synchronized with the HERA clock (figure 3.2). As in all the other H1 subsystems, the MWPC data is then stored into pipelines. Most H1 subsystems only transfer the data belonging to the trigger bunch crossing (t_0) after a positive trigger decision. The MWPC DAQ on the other hand, offers the option of also transferring the data of several bunch crossings before and after the trigger bunch crossing. This allows to study the event history. This history was used to adjust the trigger timing at the initial start of the experiment before all pipeline delays were properly set up [44]. It was also proposed to use this history information to study the calorimeter pile-up [45].

The number of bunch crossings (also referred to as *time slices*) to read can be freely set by software. It was originally proposed to read out 9 time slices for the forward MWPCs and only 3 for the central and backward MWPCs. The larger number for the forward part arised from the higher particle multiplicity in that direction. This would then lead to a total data quantity of about 3 kBytes of raw digitized MWPC information per event. Reading more time slices is possible but one must seek a compromise between readout time and the amount of useful information.

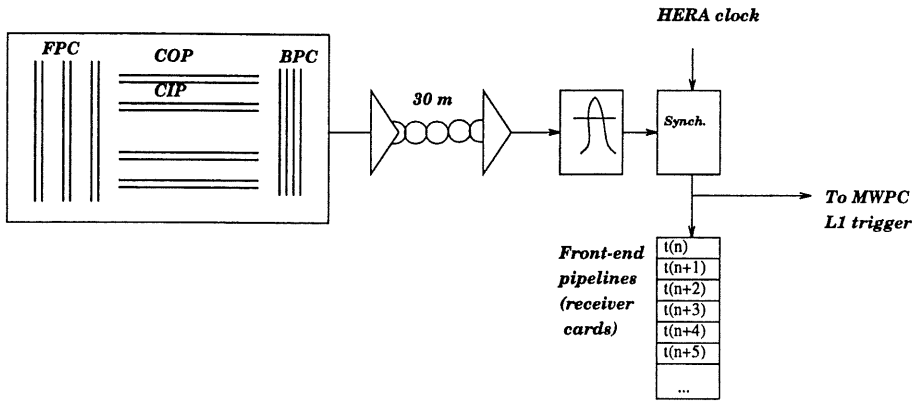

Figure 3.2: **The MWPC data flow.**
The amplified signals of the multiwire proportional chambers are sent over a 30 m long cable, after which they are shaped and synchronized with the HERA clock. The data of several bunch crossings is stored into a 32-position deep pipeline, so that the history of the signals can be read out. The shaped and synchronized data is used by the MWPC z-vertex and forward ray triggers.

3.3.2 System overview

The MWPC system is schematically represented in figure 3.3 and consists of the following parts: the front-end electronics, the master crate, the subtrigger controller and a Macintosh to control and monitor the local functioning of the DAQ. The central data acquisition does not belong to the MWPC subsystem, and is already discussed in section 3.1.

The MWPC master crate contains a dedicated Motorola 68020 microprocessor module, the FIC, which controls the whole functioning of the MWPC DAQ system. It reacts to trigger signals from the subtrigger controller (which in its turn gets them from the central trigger) and reads accordingly the data of the various multiwire proportional chambers, the time-of-flight scintillators and also the two MWPC-based trigger systems. This raw data is then zero-compressed and translated into an off-line data format (BOS banks), which are sent to the central DAQ. A local supervising Macintosh computer provides full control and monitor capabilities of this process.

In section 3.4 the software of the MWPC DAQ system will be described, while an overview of the hardware components of the front-end electronics, the master crate and the subtrigger controller follows in section 3.5. More details can be found in [44], [75] and [74]. A very detailed discussion of the MWPC DAQ software will be given in sections 3.6, 3.7, 3.8 and 3.9.

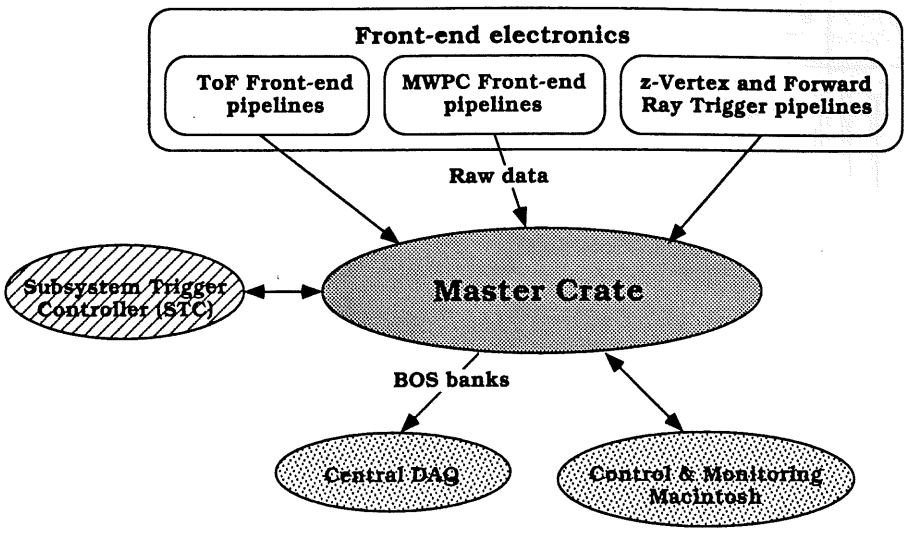

Figure 3.3: *The master crate is the heart of the MWPC data acquisition system. It reads the raw data from the various multiwire proportional chambers (both pad data as well as trigger information) and the time-of-flight system, and converts the data into off-line BOS data banks, which are sent to the central data acquisition. The master crate is locally controlled and monitored by a Macintosh computer. The readout is steered by trigger signals, which originate from the central trigger system.*

3.4 The MWPC data acquisition software

3.4.1 The MWPC DAQ programs

The MWPC DAQ software consists of three parts:

MWPC DAQ A readout program on the FIC processor, which controls the proper functioning of the hardware described above, reads out all the detector data, converts the data into an appropriate format and sends it to the central DAQ. During this process an extensive handshaking with the central trigger is done. The master crate contains *branch driver cards (BDCs)*, each of which drives a chain of front-end crates. It is via these BDCs that the raw front-end data is read out.

The MWPC DAQ program was entirely written in 68k Assembler. The development was done on Macintosh computers, on which an MPW environment [8] was installed. On the FIC itself no operating system was running, and only the VMEUA1 monitor and debugging system [23] was available.

MWPC Control A control program, which is the user interface to the readout program. The readout program runs on the FIC processor and has only a simple terminal access, while the complex environment required a more advance graphical user interface. MWPC Control is such a user-friendly control program which was implemented on a Macintosh II computer. This program interacts with the MWPC DAQ program.

MWPC Monitor To test the MWPC data and the MWPC detector performance, the MWPC subsystem is able to run 'locally', i.e. without the central DAQ and/or central trigger. Even when the MWPC data is sent to the CDAQ, a local monitor program is useful, since the CDAQ event display program does not have all the desired histogramming or display capabilities. Additionally, the functioning of the many complex tasks of the readout program needs to be monitored.

Therefore, a separate MWPC monitor program was developed to run on a Macintosh computer, with all the necessary histogramming and event display possibilities. Like the control program, this program interacted with the readout program on the FIC processor.

3.4.2 Interaction with the Central DAQ and the Central Trigger

The system supervisor is the central console of the central data acquisition (CDAQ), with which the whole DAQ can be controlled. On this supervisor, the *run start* and *run stop* commands can be given, which are then broadcast to the DAQ subsystems and to the central trigger controller (CTC).

The CDAQ also manages the event buffer space of the subsystems. On request of a subsystem, the CDAQ assigns a buffer space in which the subsystem can place its event data. When ready, the data is tranferred via a fast optical fibre to the CDAQ. As soon as the data of all the subsystems is available, the CDAQ merges this data into one event. This process is called *event building.*

The subsystems also communicate with the central trigger controller. Signals from the CTC generate interrupts, which are broadcoast to all the subsystems. The subsystem send back handshaking signals.

The communication between the CDAQ, the CTC and the MWPC DAQ branch is schematically illustrated on figure 3.4, and whill be further discussed in greater detail in section 3.6.

3.4.3 Functioning of the MWPC DAQ program

Upon a positive L2keep decision, the central trigger controller sends out an L2keep signal to all the subsystems, including the MWPC branch. The MWPC system will then promptly start to read the pipelines in the receiver cards for the presetted number of time slices. This is illustrated on figure 3.5.

The L2keep signal is followed by either an L3keep or an L3reject signal, depending on whether the L3 trigger logic decided to keep or to reject the event. In the case of L3keep (figure 3.5a) the transfer continues until all the data of the time slices has been read out of the front-end pipelines. The DAQ program indicates the end of the transfer to the CTC by issuing a Front-End Ready (FER) signal.

The MWPC DAQ has to discard the event immediately if an L3reject is received. If the data of the event is still being transferred from the front-end crates, this process has to be stopped promptly (figure 3.5b) and a FER is given shortly after.

The L3keep and L3reject signals have to be properly acknowledged so that the central trigger is aware of a possible problem with the subsystem DAQ. Only after all the subsystems have acknowledged the L3keep/L3reject signals and after all the subsystems have

Branch	Detector group	Crates	RC	Bunches	4-byte words
1	FPC	1×2	20×2	9	180
2	FPC	1×2	20×2	9	180
3	CPC	3×2	60×2	3	180
4	BPC	2×2	40×2	3	120

Table 3.3: **The front-end configuration of the MWPC system.** *These numbers are only approximate. The load of the several receiver cards is chosen in such a way, that the total event length read by each BDC is about equal if the number of read bunch crossings is taken into account.*

finished their front-end transfers of the data (*Front-End Ready or FER*), the CTC will proceed with the next event.

After the event is read, its data is further processed and after several stages sent to the central DAQ. Section 3.7 reveals the deeper details of these stages.

3.5 The MWPC DAQ hardware

3.5.1 The front-end electronics

The analogue signals of the various multwire proportional chambers are connected to *receiver cards* (RC), see figure 3.6. Every receiver card holds 16 channels, so in total there are 264 receiver cards needed for all the MWPC and ToF channels. In the receiver cards, the analogue detector signals are shaped and discriminated with respect to a pre-setable threshold, resulting in one bit information per channel. The receiver cards further contain gate-arrays with a 32-bit deep pipeline. The decision data of the z-vertex (ZVTX) and forward ray finder (FWRF) trigger systems are stored into shift registers, which are similar to the MWPC pipelines, and which are read out in the same way.

The receiver cards are located in 14 front-end (FE) crates, also called *Easybus* crates. Easybus is a simple 16-bit wide bus derived from VMEbus, but with less control and address signals and with additional analogue lines. Every Easybus crate contains one *controller card* (CC), which acts as crate controller. Several controller cards are connected in cascade into *branches*, and every branch is driven by a *branch driver card (BDC)* in the master crate. Table 3.3 shows the configuration of the front-end electronics. From this table, one can see that there are two branches consisting of two front-end crates, one branch of six and one branch of four. The reason for this asymmetric grouping was to obtain a roughly equal load for all the branches, taking into account the numbers of bunch crossings to be read for the different MWPCs as mentioned in 3.3.1. The branches are then linked to the master crate, which is described in section 3.5.2.

In the following sections the relevant components of the front-end hardware will be briefly described.

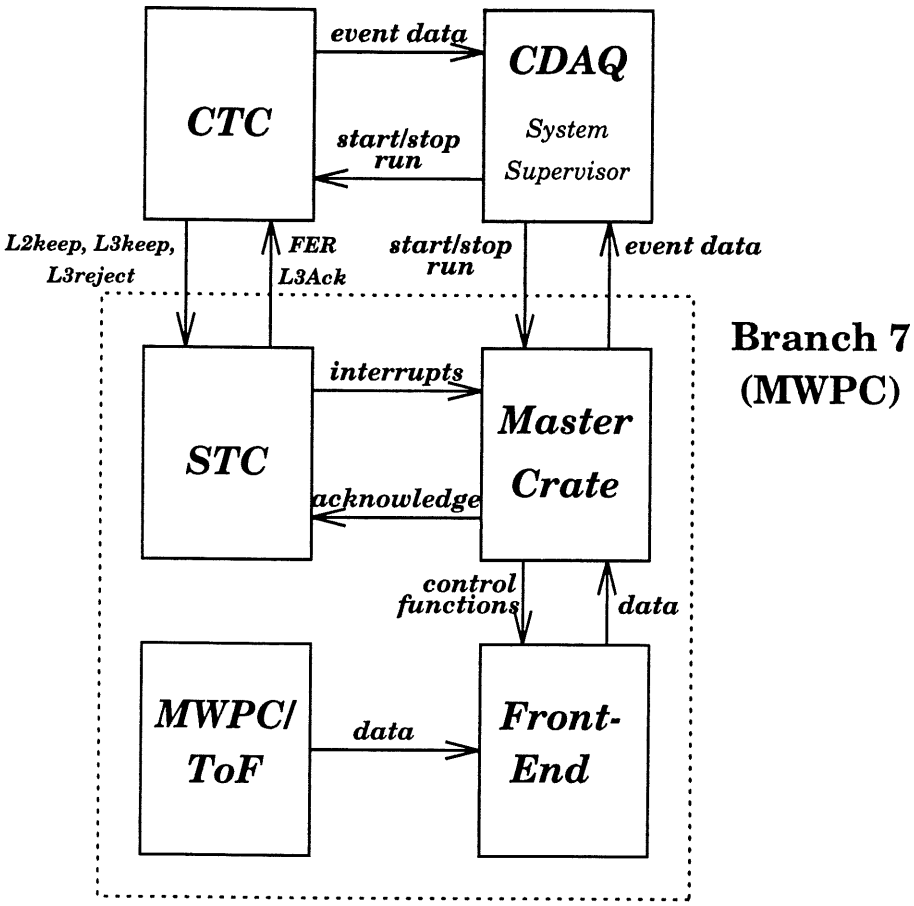

Figure 3.4: **The communication between the CDAQ, the CTC and the MWPC DAQ branch.**
The System Supervisor, which is a part of the CDAQ, broadcasts run start and run stop commands, and controls the overall run functions. The CDAQ manages the event buffers and transfers the event data from the subsystem to the central event logging. The CTC sends trigger signals via the STC to the master crate of the subsystem. The subsystem answers by sending acknowledge signals.

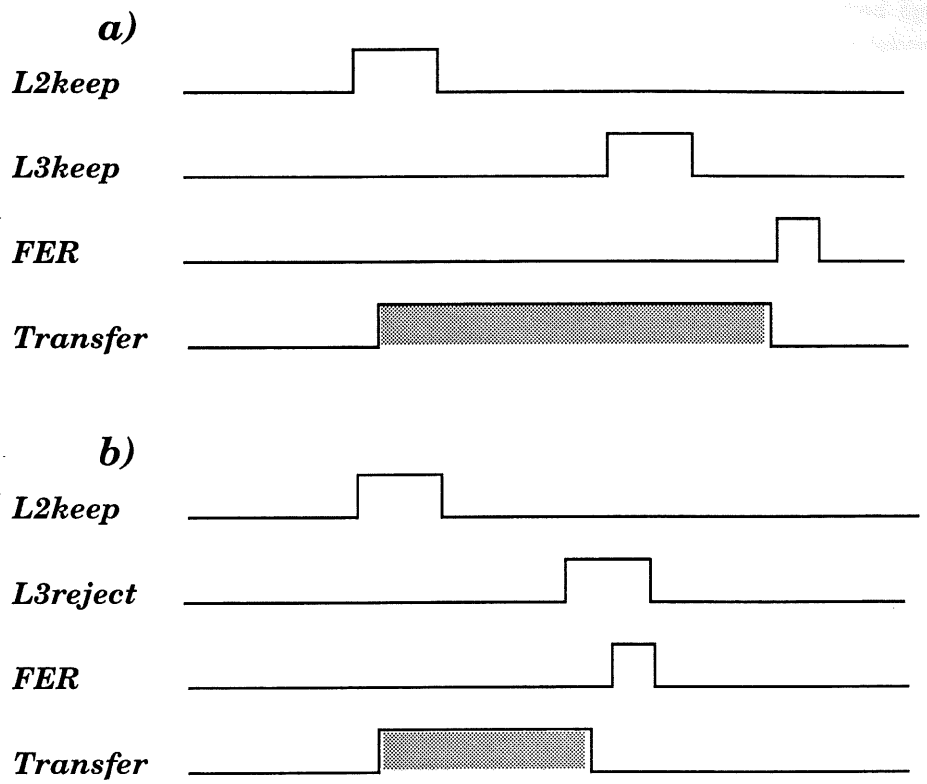

Figure 3.5: **Time diagram of the L2—L3 interrupt sequences.**
An L2keep trigger initiates the front-end transfer of the data from the pipelines to the MWPC buffers. An L3keep signal (a) just confirms that the data is to be kept, and the transfer continues until completed, after which a Front-End-Ready (FER) signal is given by the MWPC DAQ. An L3reject signal (b) interrupts the transfer promptly to minimize deadtime. For clarity the acknowledge signals of L3keep and L3reject are not drawn. Only after FER and the acknowledgement of the L3 signal, the CTC can proceed with the next trigger.

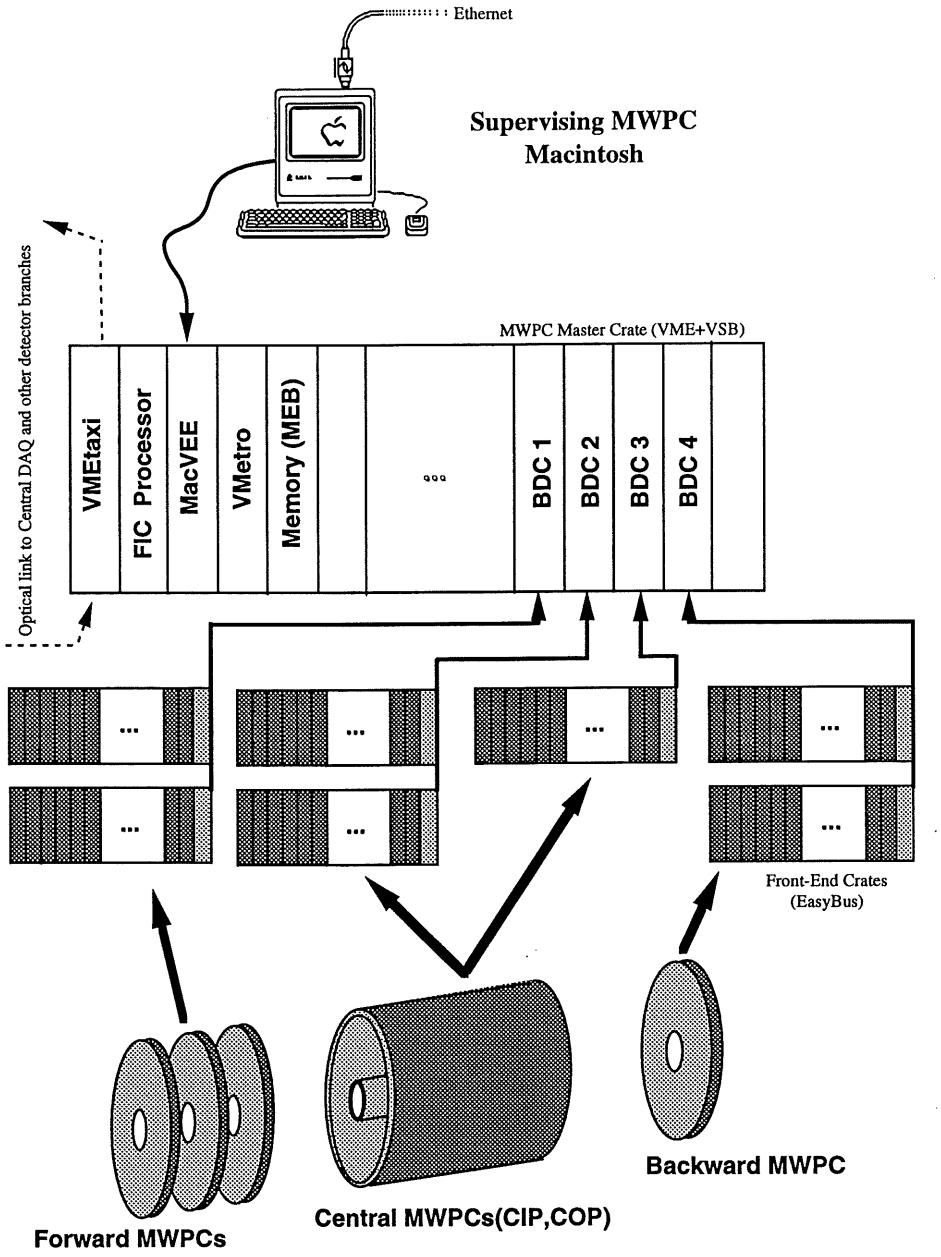

Figure 3.6: **The MWPC readout system.**
The branch driver cards in the master crate are connected to the front-end crates, in which the receiver cards reside, which in turn are connected to the various multiwire proportional chambers and the time-of-flight system (not shown). The data is retrieved via an optical link by the central data acquisition. The local MWPC configuration is controlled by a Macintosh computer.

The receiver card

The main purpose of the receiver cards is to shape the already preamplified MWPC pulses, to discriminate them w.r.t. a settable threshold, to synchronize them with the HERA clock, and to store them into a 32-bit deep front-end pipeline buffer (FEP). Sixteen detector signals can be processed simulaneously by one receiver card.

The receiver cards have additional components to control the functioning of the card. Each of the sixteen thresholds can be set individually via software, and the values are adjustable in the range between zero and one Volt. Instead of the chamber signals, every channel can be switched to a test signal loaded by software into the "test-pattern" registers. This allows to test the subsequent logic independently of the detector response and to replace defective or noisy channels by signals which are permanently on or off. There are two test-pattern registers, and it is possible to switch from one to the other repetitively at the rate of the HERA clock, to create 0–1 signal sequences. Whether the chamber signals or the test-patterns are used for read out, is determined by the values in the "switch-latch" register. Finally, it is possible to connect an oscilloscope to a front-panel LEMO connector, so that any of the sixteen unsynchronized analogue signals can be observed. The desired channel is software-setable via the "front-panel" register. A 16-fold logical OR of any combination of the sixteen digital signals is also available for building a simple MWPC trigger logic. The OR-combination of the signals can be set in the "digital or" register.

The controller card

There is one controller card per Easybus crate. The primary function of these cards is to convert the front-end bus cycles (from the branch driver card) to Easybus cycles, so that the Easybus will appear as a part of the VMEbus memory space. Furthermore, the controller cards have a signal port, to transfer some STC signals to the Easybus backplane. These signals are the control signals of various circuits on the receiver cards: the synchronization-pipeline gate array, the HCk and PEn signals, the test-patterns and the generator test-pulse. Finally, the controller cards are equipped with an analogue-to-digital converter, to measure various analogue voltages on the Easybus. This allows to measure the thresholds values of each channel, as well as the tension on several points (power supply and preamplifiers) of the receiver cards.

3.5.2 The master crate

The master crate contains the electronic modules that on one hand control the MWPC DAQ and on the other link the various parts of the system with the CDAQ and the central trigger. The backplane is a standard 32-bit wide VMEbus and the crate contains the following components (figure 3.6):

FIC processor is a 68020-based microprocessor module, with additional components such as a DMA device, a RAM, a first-in-first-out (FIFO) buffer, interrupt logic and an EPROM with a CERN-developed monitor and debugging system for the UA1 experiment [23].

VMEtaxi This module connects the MWPC system to the H1 central data acquisition system via an optical fibre link. Several control signals are sent via ordinary serial

lines. The information is transferred from a dual-ported (VME/VSB) multi-event memory board via an auxiliary VSBbus. This leaves the VMEbus free for the front-end data acquisition transfers.

Memory board The multi-event buffer (MEB) is a DPM 8242 memory board from CES. This dual ported static RAM module is interfaced to both the VME as well as the VSB bus, and contains 512 kbytes of battery backed-up SRAM with an access time of 70 ns.

VMetro This module allows to monitor all the signals and the overall activity of the VME bus. It is connected to and controlled via a VT100-compatible terminal. The VMetro can be switched in a transparent mode, so that the terminal can be used to interact directly with the FIC processor module. The VMetro turned out to be a useful tool for the debugging of the complex real-time DAQ routines.

VMIC The connection between the master crate and the subsystem trigger controller is done via a VMIVME Repeater Link from VMIC. This link consists of a software transparent two-board set that allows to extend the VME bus to additional crates. The slots in the extended crate can only function as VME bus slave modules, and all VME interrupts are transferred.

MacVEE This module connects the VME bus to a Mactintosh computer, so that the VME memory space is mapped into the Macintosh memory, in a way which is transparent to the user. All 68020-based data transfer operations in the 24-bit addressing range of the Mac are allowed and will be automatically translated into the appropriate VME operations if the address lies within the VME range.

Branch Driver Card The branch driver card (BDC) is the link between the MWPC master crate and the front-end (vertical) bus. Every BDC can be connected up to 8 Easybus crates.

The BDC has two functional modes. In the first mode, the Easybus crates are simply mapped into the 32-bit VME address space and the BDC appears to be transparent to the VME user. This mode is useful for direct loading and reading of the receiver and controller cards, which is necessary in the initialisation phase, but also for debugging.

In the second mode, the BDC provides a high-speed 32-bit block transfer facility, coupled to a dual-ported buffer (FIFO) and a zero wait-state memory. This function is necessary during the actual data-taking, when the transfer rate needs to be high. The 32-bit format allows to operate two front-end crates in parallel.

The heart of the BDC is a direct memory access controller (DMAC). The DMAC is steered via a description list, which is resident in a local SRAM. On every BDC, a 4 k $\times$ 32-bit FIFO buffer is also present. The DMAC can transfer the front-end data directly into this FIFO, while the FIC processor asynchronously reads the FIFO output via the VME bus.

3.5.3 The subsystem trigger controller

The fast card The fast card [50] is the central module of the STC. The CTC 'fast signals' (L1keep, HCk, PEn) are broadcast to the fast card. The card contains handshake logic to signal the status of the subsystem to the CTC, and an interface to the other STC modules. Additionally a set of scalers is present, which count the bunches and the HERA beam revolutions. Finally a local trigger sequencer and various simulators for machine signals allow the MWPC DAQ to operate in several test modes, without the CTC.

There are five possible operation modes, numbered from 0 to 4, which correspond to different levels of dependence on the CTC. Mode 0 is the CTC submissive mode: all the signals are received from the CTC. This is the normal data taking mode. Mode 4 is the STC autonomous mode: all the actions of the STC are completely independent of the CTC and the trigger sequence is controlled by local logic. Mode 3 is similar to mode 4, but the 10.4 MHz HERA clock signal is received from the CTC. The other modes are hardly used in pratice.

The slow card The slow card [58] is used to synchronize the data acquisition with the trigger signals broadcast by the CTC. The slow card module translates these signals into VME interrupt signals, which can influence the flow of the MWPC DAQ program. The priorities of each interrupt, as well as the interrupt number can be selected via a wire-wrap matrix. In the STC autonomous mode (mode 4), the interrupts will be generated by software commands.

The fanout cards The fanout cards [49],[51] distribute the internal STC signals to the MWPC electronics. It is possible to delay, to gate and to simulate these signals by software.

Six fanout cards are used to operate the front-end electronics: one for each of the MWPC detector groups (forward, central, backward), one for the ToF counters, one for the forward ray finder trigger and one for the z-vertex trigger. These cards all serve to distribute the HERA clock (HCk) and pipeline enable (PEn) signals. Additionally, the FPC, CIP/COP and BPC receiver cards get test-pulse and test-pattern signals, which are also generated by their corresponding fanout card.

Trigger bits card The trigger bits card [52] contains scalers, which count the number of L1keep, L2keep and L2reject pulses. The L2keep count value is added to every event which is sent to the central DAQ. This allows the event builder to make sure that the partial events from the subsystems belong to the same trigger, when they are merged. The trigger bit scalar data is also used by the on-line MWPC monitoring system.

3.6 Communication between the Central Trigger, Central DAQ and MWPC DAQ

3.6.1 Communication with the central trigger

As explained in 3.2, the central trigger and the front-end systems communicate via several signals. Only five signals are used by the MWPC system. The L2keep, L3keep and L3reject signals have already been discussed earlier. The two additional signals are *PrepRun* (at run start) and *TermRun* at run stop. All the signals from the CTC to the STC have an acknowledge signal from the STC to the CTC. Usually the acknowledgement is given promptly by the subsystem. An exception is FER (response to L2keep), which is only given after the MWPC system is ready to accept another trigger. All these five signals with their acknowledgement partners are described here in detail:

1. Signals from CTC to STC

   L2keep Is sent after a positive decision of the L2 trigger from the CTC to the subsystem. Its action is handshaked by the FER of that subsystem.

   L3keep Is sent out by the CTC after a positive decision of the L3 trigger logic and is stricly excluding L3reject. It means that this event is now allowed to be sent to the CDAQ, i.e. the signal MEB_READY can be sent now (but it can be later).

   L3reject Is sent out any time after L2keep (earliest 10 μs after L2keep—this is a requirement of the calorimeter subsystem) and before the L3 timeout (less then 800 μs—a requirement from the slowest DAQ subsystem) to the subsystems.

   PrepRun At the start of every run the CTC sends out a Prepare Run interrupt to all the subsystems, to warn that from that moment on an L2keep interrupt may follow. The MWPC DAQ system does not use this interrupt, since it is already warned by the CDAQ that a new run has started (see MEB_DAQINFO in 3.6.2). The interrupt is therefore simply acknowledged, but no further action is taken.

   TermRun At the end of every run, the CTC sends out a Terminate Run interrupt. Similarly to the PrepRunn signal, this interrupt is merely acknowledged by the MWPC DAQ without any further action.

2. Signals from STC to CTC

   FERi The Front-End Ready signal is sent by the subsystem to the CTC, when the 'hardware' is ready to accept a new L1keep. It is also to be set at the beginning of a run, when the conditions to accept the first L1keep are fullfilled. It is reset at latest at the next L2keep. FERi indicates that a L2keep request is successfully fullfilled.

   L3rejectAckn Is sent by the subsystem to the CTC, indicating that L3reject has been taken note of.

   L3keepAckn Is sent by the subsystem to the CTC, indicating that L3keep has been taken note of and that the STC is ready to accept the PipEnable again.

PrepRunAckn The PrepRun interrupt is automatically acknowledged by hardware.

TermRunAckn The TermRun interrupt is automatically acknowledged by hardware.

3.6.2 Communication with central DAQ

As explained earlier, the front-end branches are linked to the central data acquisition by means of Micro-Research VMEtaxi modules (one in every branch), which are connected in a ring via optical fibres. These modules are controlled by VMEXI_SSP (VMEtaxi System Software Package [43]), a complete functional environment geared up for large multi-crate VME/VSBbus data acquisition systems. Currently the software is configured for a single master (CDAQ) controlling a ring of slaves (front-end systems).

A general protocol "XIDAQ" [43] has been built on top of VMEXI_SSP, making much of the DMA handling and buffer managment a lot easier. This protocol can be accessed via the "XIUSER" library, ready to be linked to any 68k series development system, e.g. Macintosh MPW.

In contrast to the communication with the central trigger, where the information is passed via hardware interrupt signals, the XIDAQ protocol is based on communication via software flags, which are set by one party, and polled by the other. Those flags and variables are resident in a dual ported RAM memory in the VMEtaxi module, so that they can be accessed by the central DAQ as well as by the MWPC FIC processor.

Programs for processors working at the front-end readout stage need only a few routines of XIUSER. They have direct Assembler entry points, either at fixed offsets from the XIUSER object origin or as MPW linkable imports. We will briefly describe the function of all the XIUSER routines, which are relevant to MWPC DAQ.

MEB_INIT

This routine is called by a MEB user in order to initialize the unit in the XIDAQ system. The user has to request the maximum number of buffers and the maximum number of bytes per buffer. The only possible error condition is that the initialisation cannot take place since XIDAQ is in the middle of a run.

MEB_DAQINFO

Called when a user whishes to request the current run conditions (run stopped, prepare for run, pulsed run, warm start, normal run start, normal run). The status of the various possible conditions is returned in a bit-packed format.

MEB_REQUEST

In order to request a buffer from the XIDAQ managment system, one must call MEB_REQUEST. The XIDAQ returns a data address of a free buffer, where the user can place the next event. Together with the address, the maximum number of bytes is returned. It should be clear that under no circumstances should the user write data into the buffer beyond this limit.

The corresponding buffer number must be retained in order to indicate its readiness later via a call to MEB_READY.

MEB_READY

On reading out and filling a buffer (or a number of consecutive buffers) with valid event data, the MEB user must indicate this to the XIDAQ system via a call to this routine. The exact length of the data must be indicated together with any possible readout error information. The XIDAQ system will transfer the contents of the buffer as soon as possible and mark the buffer as free. The XIDAQ sends the collected data to the event builder, where it is checked and eventually merged with the data of the other subsystems.

The event number must also be indicated since XIDAQ cross-checks all branches and multi-events buffers for any possible conflicts. The possibility exists to send priority events, but this feature has not been used by MWPC DAQ.

MEB_MESS

Called when a user whishes to send a message through the VMEtaxi system to be eventually output on a supervising external processor. Two character strings can be send to the XIDAQ, which will eventually appear on the central H1 supervising console. A variable allows to indicate the severity of the message on a priority basis, to distinguish between general information and serious alarm warnings.

3.6.3 Communication with MWPC Control

The MWPC Control program is the local user-interface of the MWPC DAQ system. Apart from controlling the MWPC DAQ program in stand-alone mode, it allows to set up the electronics of the MWPC system.

All the information of the MWPC Control program to MWPC DAQ is passed via one file, which is a sequence of data 'blocks'. This file, named *SetupData*, is actually an array of 32-bit integer words and is logically divided into several "blocks", each containing a specific type of information. Every "block" has a variable length and starts with a four-character name (packed ASCII) and an ID number, followed by a length word. The typical structure of a "block" is shown in table 3.4. The end of the list of blocks is indicated by a zero word ($00000000) in the Name field. Table 3.5 shows the "blocks" used by MWPC DAQ and gives a brief description of their function.

The order in which the blocks appear in SetupData is irrelevant, since they can be individually identified through their name and number. The order in which they are read on the other hand is very important, since the information of one block may already be used while processing another one. An example is the 'DEBU' block, which contains debugging options. An other example is the 'CONF' block, which contains information on the configuration of the system. This block has to be read before the 'SWLA', 'PAT1', 'PAT2' or 'THRE' blocks.

The file *SetupData* is downloaded from the MWPC Macintosh to the FICs memory via a menu command in the MWPC Control program. The file is read by MWPC DAQ and all the parameters are downloaded in all the appropriate modules at every run start (warm start or run start).

Contents	Example	Hexadecimal Value
Name	'DEMO'	$44454D4F
ID	12	$0000000C
Data Length (words)	4	$00000004
Data 1	$12345678	$12345678
Data 2	$AFEE17AD	$AFEE17AD
Data 3	10	$0000000A
Data 4	-1	$FFFFFFFF

Table 3.4: **Structure of a "block" (example).**
These blocks contains the variables which are transferred from the MWPC Control program to the MWPC DAQ program. Every block is identified by a unique four-letter name and a number.

Block name	Contents
'BCRO'	Bunch crossing information. *Contains the number of bunchcrossings to be read by the forward, central, backward MWPCs and the ToF.*
'CONF'	Information on the electronics configuration. *Describes which receiver cards are active and which unit and BDC they are connected to.*
'CVTF'	Bitmap conversion table Forward *relates RC bits to MWPC channel numbers.*
'CVTC'	Bitmap conversion table Central
'CVTB'	Bitmap conversion table Backward
'DEBU'	Debugging options
'FANO'	Fanout Card(s) settings
'FAST'	Fast Card settings
'PAT1'	Test-Pattern 1 register (RC)
'PAT2'	Test-Pattern 2 register (RC)
'SWLA'	Switch-Latch register (RC)
'GENE'	General register (RC)
'MASK'	Mask register (RC)
'THRE'	Thresholds (RC)
'CTOF'	ToF assignments
'STOF'	ToF settings
'CCDE'	Controller Card delays

Table 3.5: **Overview of blocks used by MWPC DAQ.**

3.6.4 Communication with MWPC Monitor

The aim of the MWPC Monitor program is twofold:

- Monitoring of the MWPC data quality by means of histograms.
- Monitoring of the functioning of the MWPC DAQ hard- and software.

In 1991 and 1992 only a preliminary version of the monitor program existed. The histogramming was based on an own implementation for the Macintosh of the CERN HBOOK code [28], while the user interface was entirely written in SuperCard [7]. Dedicated underlying subroutines were written in MPW Pascal [10] and MPW Assembler [9].

The MWPC Monitor program samples a fraction of the events which are stored in the MWPC Multi-Event Buffer (MEB), by reading them directly via a MacVEE connection. The mechanism will be explained in 3.9.

3.6.5 Event formats

The data, as it comes from the receiver cards, is simply the sequence of the values read from the various BDC FIFOs. The status of every channel of a particular detector in a particular bunch crossing is stored in a bit in this buffer. Such a format depends on how the various pads are cabled to the receiver cards and on the way these cards are read out. This is not very suitable for off-line analysis because:

- the information is stored in a hardware-dependent way,
- the event information is not zero-compressed.

All H1 off-line data is stored in a data format called *BOS-banks* [17], and it was agreed that all the data, which is sent from the DAQ subsystems to the event builder, had to be in BOS banks too. In 1987 the H1 detector has been described by a GEANT [27] application program (H1SIM), and several BOS banks had been defined in this simulation:

Detector	BOS bank
FPC	FRME
CIP	CRME
COP	CRME
BPC	BRME
ToF	BRTE

The off-line data formats are all characterized by two features: pads which are not hit are not stored (zero-suppression) and the pads are identified by a unique pad number. From this number, the geometrical position within the detector can be easily calculated. Table 3.6 shows the definitions of the channel numbers of the various proportional chambers. To convert the 'raw events' to the correct BOS format, a look-up table is used.

3.7 Flow chart of the MWPC DAQ program

This section describes the logic of the MWPC DAQ program at the flow chart level.

Detector	Channel number	Values	Geometrical meaning
FPC	(SuperModule-1)*384 +(Chamber-1)*192 +Sector*24 +Pad	0...1151	SuperModule=1,2,3 Chamber=1,2 Sector=0...7 Pad=1...24
CIP	(InOut-1) * 480 +(Phi-1)*60 +Pad	0...959	InOut=1 means inner CIP InOut=2 means outer CIP Phi=1...8 Pad=1...60
COP	960 + (InOut-1) * 288 +(Phi-1)*18 +Pad	960...1535	 InOut=1 means inner COP InOut=2 means outer COP Phi=1...16 Pad=1...18
BPC	(Plane-1)*312 +Wire	0...1247	Plane=0,1,2,3 Wire=0...311
TOF	Channel Time window	000...007 100...115 101(2) 110(2)	000...007 (ToF 0) 100...115 (ToF 1) 101(2) = physics 110(2) = background

Table 3.6: **Relation between the MWPC channel numbers and the geometry.**
Every MWPC channel can be represented by a unique value. The 24 ToF channels are gated with three time windows, and therefore require an extra 3-bit word.

3.7.1 Run start procedure

After the VME Master Crate is reset, the MWPC DAQ program is automatically booted. After the initialisation of various parameters, variables and modules (called the *cold start*), the program enters an idle loop (see figure 3.7) in which MEB_INFO is polled to get the current run status. The latter may signal a *Warm Run Start* or a *Run Start.* The purpose of a Warm Run Start is to allow some subsystems to download many variables into their electronics. For some systems (in particular for the calorimeter branches) this procedure is time-consuming (several minutes) and because it is usually not necessary to repeat this step before every run, it is done seperately. In the MWPC DAQ system initializing the electronics takes a short time (in the order of milliseconds), so the Warm Start procedure is the same as the Run Start procedure. The details of this procedure will be revealed together with the description of the *asynchronous loop.*

If the Central DAQ signals a Run Start, all the electronics is loaded with the correct values (thresholds, test-patterns, ...) and various variables are initialized. Finally, the Front-End Ready bit of the Fast Card is set to true, which enables the CTC to send L2keep interrupts. The program then enters the *asynchronous loop.* This the program can only exit from this loop in two ways: after a Run Stop has been detected or after a fatal error. In the latter case the cold start procedure is called again before the program resumes at the initial idle loop.

3.7.2 Data flow

To understand the functioning of the MWPC DAQ program, it is necessary to explain the data flow, which is shown in figure 3.8.

The data is transferred is various stages, which can be considered as independent processes. The reason of this decoupling is to make the front-end deadtime as low as possible, while time-consuming tasks, such as the transformation of the receiver card data to an off-line data format, are done in a later stage. The latter step is skipped for events, which are rejected by the L3 trigger logic. The event data undergoes the following transfers:

1. The raw data is transferred from the received cards to the *FIFO buffers* in the branch driver cards by the DMA controllers of those BDCs. This step, which is dictated by the transfer time of the FE data into the FIFOs, mainly determines the deadtime of the MWPC DAQ system, unless the FIFOs are full. In this case, the deadtime increases to much higher values (basically dictated by the zero-suppression time). The size of the FIFOs is chosen sufficiently large to avoid this situation for typical event rates. In case of an L3reject decision, the data will not go beyond this stage and the events are flushed when they reach the end of the FIFOs.

2. Later the FIC processor merges the data of all the various BDC FIFOs into one event in the *Raw Event Buffer (REB)*, which is allocated memory space in the FIC's memory.

3. Then the data is translated into off-line BOS banks in the *BOS Event Buffer (BEB).* The data is translated from a bitmap format into lists of numbers of hit channels. Since only the information of the channels which are hit are stored, this step is also called the zero-suppression.

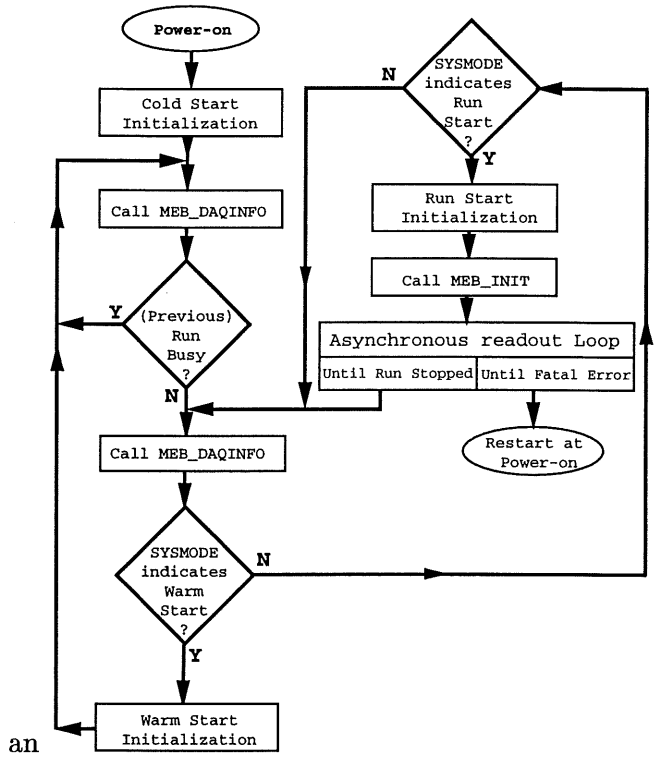

an

Figure 3.7: **Flow chart of the MWPC DAQ program.**
The program stays idle until the CDAQ signals a Warm Start or a Run Start. In the case of a Warm Start, only the Run Start procedure is executed. In the case of a Run Start, the same Run Start procedure is called, and the program enters the asynchronous loop until the CDAQ broadcasts a Run Stop or until a fatal error occurs.

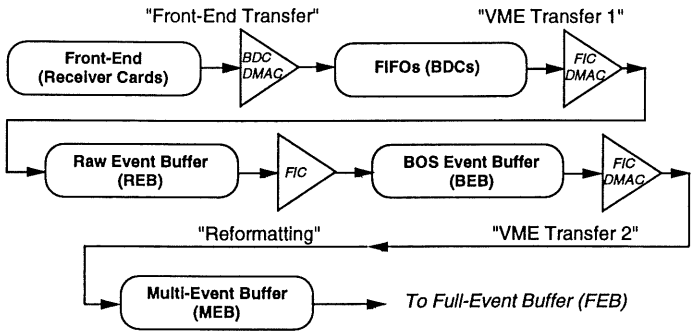

Figure 3.8: **The data transfers from raw data to BOS banks.**
For an explanation of the various transfer steps, see the text.

4. The FIC's DMA controller sends the full BOS events to the *Multi-Event Buffer (MEB)*, where it can be collected by the central data acquisition.

Figure 3.9 shows an example on how the data is treated in the steps 1 and 2. The events are read by several BDCs and every BDC may read a different number of words. Already during transfer step 1, a REB space is allocated. In parallel, the REB index is stored in a software-emulated FIFO buffer (*SoftFifo* or *FIC's FIFO*). For every event in the BDC's FIFOs a corresponding REB index is present in the SoftFifo. A REB status word of a particular event indicates the status of the transfer. As soon as the STC has signalled an L3 result (keep/reject) to the subsystem, the appropriate value is set in the REB status (CodeRebKept or CodeRebReject). In case of an L3reject interrupt, the correct number of data words in the FIFO to flush, which depends on the time on which the L3reject interrupted the front-end data transfer, is also stored in the REB.

After the front-end transfer (step 1) the data resides in the different FIFOs of the BDCs. In step 2, the program checks the L3 status of the event. In case of an L3keep event, the FIC's DMAC will transfer the partial event into the allocated REB space. In case of an L3reject event, the BDC's FIFOs are flushed by the appropriate amount of words.

3.7.3 Asynchronous loop

When the MWPC DAQ program was developed, no multi-tasking operating system was available for the FIC processor. However, as explained in the previous section, the several data transfers can be treated as different processes, which run semi-independently. Basically, there are three tasks: the front-end data taking (steered by L2keep-L3keep/L3reject sequences), the event recombination (from BDC FIFOs to REB) and the event reformating (from REB to BEB).

The asynchronous loop (figure 3.10) decouples the front-end (L2–L3) cycles from the event-reformat cycles. The BDC FIFOs status is constantly polled on the presence of an event. An L3reject event is flushed as soon as it reaches the end of the FIFOs, the data of

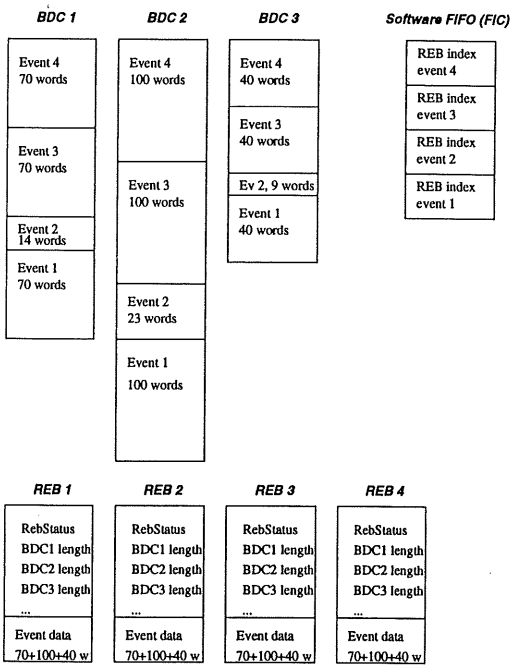

Figure 3.9: **The BDC FIFO and the Raw Event Buffers.**
This is an example of four events, the data of which is read by three BDCs. In this example a full event consists of 70, 100 and 40 words in BDC 1, BDC 2 and BDC 3 resp. Events 1, 2 and 4 are kept by L3 and event 3 is rejected, therefore it is only partially read since the DMAC transfers were interrupted by L3reject. Only the kept events are transferred to a free REB buffer space. The data of the different BDCs is merged into one sequential data block in one REB. The SoftFifo holds the REB indices of all the events, even before they are transferred to the REB. In case of an L3 rejected event, the REB only holds the length of the (partially) read events in the FIFOs, so that these events can be flushed when they reach the end of the FIFOs.

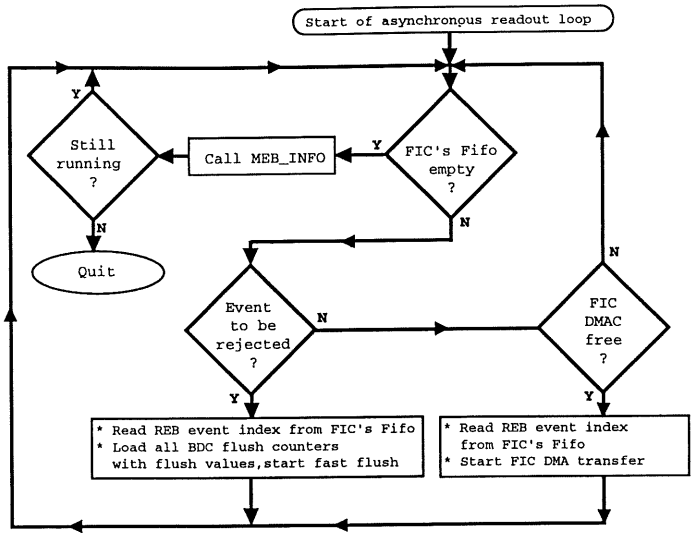

Figure 3.10: **Flow chart of the asynchronous loop.**
In this loop, the status of the FIC's FIFO buffer is continuously polled. As long as there are events, they are read from the FIFO and either flushed (in case of an L3reject event) or transferred to the Raw Event buffer (REB) by the FIC's DMAC.

an L3keep events is merged into one "raw" event block in the REB. For optimal speed, the FIC's DMAC, which has four separate channels available, is used to perform this transfer. The channels are dynamically allocated so that they are used efficiently.

Inside the asynchronous loop, no other tasks are performed. The major actions of the program are driven by interrupts, some of which originate from the CTC, some are generated by the BDCs and the FIC's DMACs.

3.8 The MWPC Control program

The MWPC Control program is the user-interface of the MWPC DAQ program. It has the following functions:

- Set-up of the hardware configuration, i.e. the number of used receiver cards and which detector parts they are wired to. Also the receiver card—controller card—branch driver card connections can be configured with this program.
- Set-up of the variable delays in the readout chain.
- Local run control
- Local trigger control
- Selective switching on/off individual branches
- Setting of RC test-patterns, test-pulses, switch-latch, front-panel and threshold values. The thresholds can also be read back and displayed on the screen.

- All the delays of the fanout cards and controller cards can be set individually.
- The number of bunch crossings to be read for all the detector groups can be set.
- All the settings can be bundled into one single run database.

The control program is entirely written in MPW Pascal [10], and behaves as a normal window-based Macintosh application.

3.9 The MWPC Monitor program

The MPWC Monitor program was in an experimental stage during the first two years of operation of H1. The program requested an event to the MWPC DAQ program by setting a flag. As soon as an event is ready in the BEB space, it is held there until the Monitor program signalled that the event has been completely transferred to the Macintosh.

The BOS banks are then decoded and several histograms are filled (hit multiplicities, cluster multiplicities, number of hits vs. time slice, ...). Since the raw event data (as it appears in the REB) can be included as a BOS-bank in the normal data stream, the zero-suppression routine can be verified by the Monitoring program.

The whole user interface was written in a dedicated interpreter language *SuperCard* [7], which allowed quick changes in the lay-out. A major drawback was the incompatibility of this platform with the normal Macintosh graphical interface. The interface with the DAQ program was also prone to problems: problems with the DAQ propagated to the Monitoring and vice versa. Finally, the event transfer rate to the Monitoring was low, and put an extra load onto the DAQ, since it used extra VME cycles.

3.10 Limitations of the first MWPC DAQ implementation and upgrade

The MWPC DAQ system as it was first conceived, operated succesfully during the cosmic runs of 1991 and 1992, as well as during the *ep* runs in 1992. However, it became soon clear that the original concepts needed to be changed, to keep up with the steadily increasing luminosity and event rate.

When the DAQ was designed, an event rate of 5 Hz was planned. In 1992 this number was raised to 50 Hz, pushing the originally designed system to its limits. The zero-suppression and BOS-bank output was not originally foreseen either, but was an off-line requirement which was imposed in the course of 1991. This task put an extra load on the DAQ system as well.

The fact that one single FIC processor had both a data-acquisition task as well as a monitor task to fullfill, further increased the load of this processor. Another disavantage of this concept was that any problem with the monitoring software, which was under continuous development, propagated itself to the data-acquisition part.

Together with the new MWPC DAQ program, a new Monitoring interface was developed. A description of this new interface is described in [44]. The MWPC Control program was slightly modified, but was continued to be used.

3.11 Abbreviations

BC *Bunch Crossing*

BDC *Branch Driver Card*

BEB *BOS Event Buffer = buffer in FIC's local memory*

CDAQ *Central Data-Acquisition*

CI *Crate Interconnect*

CTC *Central Trigger Controller*

DMA *Direct Memory Access*

DMAC *Direct Memory Access Controller*

FE *Front-End*

FEB *Full-Event Buffer = VME Memory of Central DAQ*

FIFO *First-In First Out memory*

HCk *HERA Clock*

MacVEE *Microcomputer Applied to the Control of VME Electronic Equipment*

MEB *Multi-Event Buffer = VME Memory of MWPC DAQ*

MWPC *Multi-Wire Proportional Chamber(s)*

PEn *Pipeline Enable*

RC *Receiver Card*

REB *Raw Event Buffer = buffer in FIC's local memory*

STC *Sub-Trigger Controller*

VEV *VMEbus Easybus Vertical bus*

VSB *VME Subsystem Bus*

Chapter 4

The experimental method

4.1 Calculation of the proton structure function F_2

In this chapter we give a detailed description of the F_2 measurement. As will be developped in the next section, the experimental value of the proton structure function F_2^{exp} for a fixed x_c and Q_c^2 inside a bin with size $\Delta x, \Delta Q^2$, can be defined by:

$$F_2^{exp}(x_c, Q_c^2) = \bar{\sigma}_{exp}(\Delta x, \Delta Q^2) \left(\frac{F_2(x_c, Q_c^2)}{\bar{\sigma}(\Delta x, \Delta Q^2)} \right)_{th} . \tag{4.1}$$

In this equation, $\bar{\sigma}_{exp}(\Delta x, \Delta Q^2)$ is the cross section in bin $\Delta x, \Delta Q^2$. The theoretical values of $F_2(x, Q^2)$ are obtained from a structure function parametrisation (see the end of section 4.2) and the cross section $\bar{\sigma}_{th}$ from a Monte Carlo simulation (see next chapter). The experimental cross section can be measured by counting the number of selected DIS events in the bin:

$$\bar{\sigma}_{exp}(\Delta x, \Delta Q^2) = \int_{bin} \frac{d^2\sigma_{exp}}{dx\, dQ^2}\, dx\, dQ^2 = \frac{N_D - N_{\gamma p} - N_{bg}}{Acc \cdot \mathcal{L}_D \cdot \epsilon_{eff}}, \tag{4.2}$$

where the symbols have the follow meaning:

1. $N_D, N_{\gamma p}, N_{bg}$

   N_D is the number of observed DIS candidates, i.e. events selected by a few 'basic' characteristics of deep inelastic scattering. These cuts will be described in detail in the next chapter. The event sample which is obtained this way is by no means pure and still contains a number of photoproduction ($N_{\gamma p}$) and beam-gas/beam-wall background events (N_{bg}). These types of background will be explained in following sections. Their contribution can be estimated from the data (section 4.8) and is subtracted statistically from the number of observed events. As we will see in the next chapter, the background can be well controlled by appropriate cuts, and will be at most a couple of percent in some parts of the kinematical plane.

2. $\mathcal{L}_D$

   $\mathcal{L}_D$ is the integrated luminosity of the accelerator corrected for the dead time of the detectors. This number is obtained externally with the help of the electron and photon taggers (see section 2.2.6, [54]).

3. Acc

   The reconstructed energy and angle (and therefore the reconstructed Q^2 and x) are not necessarily the true values, i.e. some events are reconstructed in another bin

than the bin they in reality belong to. These *migrations* are entirely due to the imperferctions of the detector, and will be calculated by means of a Monte Carlo simulation. The Monte Carlo acceptance is here defined as

$$Acc(\Delta x, \Delta Q^2) = \frac{N_{rec}(\Delta x, \Delta Q^2)}{N_{gen}(\Delta x, \Delta Q^2)}, \tag{4.3}$$

where N_{rec} is the number of reconstructed events in a particular bin after all the event selection cuts, and N_{gen} the number of generated events in that bin. This formula is a good approximation if the bins are not much bigger than the resolution requires such that the migration of events to and from the bin is small.

4. ϵ_{eff}

   The event selection cuts, which are chosen such that the amount of remaining background is reduced as much as possible, also reject some good DIS events. This means that the selection cuts have an efficiency ϵ_{eff}. In the case of equation (4.3) the efficiencies of the cuts are already included in the acceptance *Acc*. Only efficiencies which are not incorporated in the Monte Carlo should enter ϵ_{eff} separately.

4.2 Monte Carlo method

The cross section of a one-photon exchange DIS event can be written as:

$$\begin{aligned} \sigma_{Born} &= \frac{d^2\sigma_{Born}}{dx\, dQ^2} \\ &= \frac{4\pi\alpha^2}{Q^4 x}\left(1 - y + \frac{y^2}{2(1+R)}\right) F_2^{th}(x, Q^2) \\ &= \kappa(R)\, F_2^{th}(x, Q^2). \end{aligned} \tag{4.4}$$

The dependence of the cross section on the longitudinal structure function F_L and thus on R is factorised in $\kappa(R)$. In this analysis, R is obtained from the Altarelli-Parisi NLO QCD formula, which relates F_L to the evolution of quarks and gluon distributions. $\kappa(R)$ depends only weakly on the structure function, and variations of $\kappa(R)$ for MRSD0 and MRSD- parametrisations are less than 1%.

The radiative cross section relates to the Born cross section as:

$$\bar{\sigma}_{th}(\Delta x, \Delta Q^2) = \int_{bin} \sigma_{th}\, dx\, dQ^2 \tag{4.5}$$

$$\simeq (1 + \bar{\delta}) \int_{bin} \sigma_{Born}\; dx\, dQ^2. \tag{4.6}$$

The influence of the radiative corrections can thus be isolated in the factor $(1 + \bar{\delta}) = \bar{\sigma}_{th}/\bar{\sigma}_{Born}$.

Equation (4.1) can then be written as:

$$F_2^{exp}(x_c, Q_c^2) = \bar{\sigma}_{exp} \frac{\bar{\sigma}_{Born}}{\bar{\sigma}_{th}} \frac{F_2^{th}(x_c, Q_c^2)}{\bar{\sigma}_{Born}} \tag{4.7}$$

$$= \bar{\sigma}_{exp} \frac{1}{1+\bar{\delta}} \frac{F_2^{th}(x_c, Q_c^2)}{\bar{\sigma}_{Born}} \tag{4.8}$$

$$= \bar{\sigma}_{exp} \frac{1}{1+\bar{\delta}} \frac{\sigma_{Born}(x_c, Q_c^2)}{\bar{\sigma}_{Born}} \frac{1}{\kappa(R)}. \tag{4.9}$$

This means that for a given average radiative correction $\bar{\delta}$ and a factor R, the measurement of the radiative cross section of DIS can be transformed into a measurement of F_2. The factor $\sigma_{Born}/\bar{\sigma}_{Born}$ in equation (4.9) is called the *bin centre correction*, since it transforms the cross section averaged over the whole bin into the cross section in a chosen point (x_c, Q^2). The bin centre corrections are small if the bins belong fully to the kinematic region which is covered. In a later section we choose the bin sizes and values of x_c and Q_c^2.

The method to calculate F_2 according to equations (4.1) and (4.9) is called the *factorisation method*, since the acceptances, efficiencies, radiative corrections and bin centre corrections are all factorised out. However, by using the number of generated Monte Carlo events N_{MC} and the corresponding luminosity $\mathcal{L}_{MC}$ so that

$$\bar{\sigma}_{th} = \frac{N_{MC}}{\mathcal{L}_{MC}}, \tag{4.10}$$

it is possible to write $F_2^{exp}(x_c, Q_c^2)$ as:

$$F_2^{exp}(x_c, Q_c^2) \simeq \bar{\sigma}_{exp}(\Delta x, \Delta Q^2) \frac{F_2^{th}(x_c, Q_c^2)}{\frac{N_{MC}}{\mathcal{L}_{MC}}}. \tag{4.11}$$

Equation (4.11) can be written in the following compact way:

$$F_2^{exp} \simeq \frac{N_D}{N_{MC}} \times \frac{\mathcal{L}_{MC}}{\mathcal{L}_D} \times F_2^{th}. \tag{4.12}$$

This method is called the *Monte Carlo* method. It is only applicable to the extent that the Monte Carlo describes the data well and has a higher statistical precision than the data. By definition, the acceptance (4.3) contains all the efficiencies which are described in the Monte Carlo.

In this analysis we use for F_2^{th} the GRV parametrisation from Glück, Reya and Voght [55], since earlier measurements by H1 [38], [41] and Zeus [78] gave evidence of a steeply rising $F_2(x, Q^2)$ with small x, similar to the rise predicted by the GRV parametrisation.

4.3 Reconstruction of the kinematical variables with H1

In the first chapter we have seen than the structure function F_2 depends on two kinematic variables, for instance x and Q^2. At fixed target experiments usually the polar angle and the energy of the scattered electron were measured to determine x and Q^2. At HERA it is possible to measure the energies and angles of both the scattered electron as well as the hadronic final state, which allows several additional methods to determine the kinematic variables. The measurement accuracy that can be obtained by each of those methods varies strongly over the phase space. Several detailed studies of these methods have been presented [12], [33], [48], and we will here repeat the major formulae and advantages of some of them.

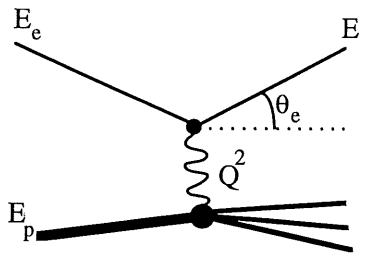

Figure 4.1: **Schematic view of a deep inelastic scattering event.**
The kinematics of a DIS event can be completely reconstructed from the reconstructed energy (E) and polar angle (θ_e) of the scattered electron.

The choice of the variables in which the kinematic bins are defined could be different from x and Q^2, and could be for example the energy (E) and the polar angle of the scattered electron (θ_e). However, to make the comparison of the measured DIS cross section and F_2 with other experiments easier, it was decided to use x and Q^2 bins throughout this analysis.

In the following formulae, the electron and proton masses are always neglected, and we use the variables (see figure 4.1):

E	:	energy of the scattered electron.
θ_e	:	polar angle of the scattered electron w.r.t. the incident proton.
E_e	:	the incident electron energy.
E_p	:	the incident proton energy.

Only two of the kinematic variables are independent:

$$Q^2 = xys, \tag{4.13}$$

but for completion the expressions for Q^2, x and y will be given here.

1. **Electron only:** The variables Q^2, x and y can be expressed in terms of the energy (E) and angle (θ_e) of the scattered electron in the laboratory frame:

$$Q_e^2 \simeq 4E_eE\cos^2\frac{\theta_e}{2} \tag{4.14}$$

$$x_e \simeq \frac{E_eE\cos^2\frac{\theta_e}{2}}{E_p(E_e - E\sin^2\frac{\theta_e}{2})} \tag{4.15}$$

$$y_e \simeq 1 - \frac{E}{E_e}\sin^2\frac{\theta_e}{2}. \tag{4.16}$$

Straightforward calculations yield the following expressions for the relative errors:

$$\frac{\delta Q_e^2}{Q_e^2} = \frac{\delta E}{E} \oplus \tan\frac{\theta_e}{2}\delta\theta_e \tag{4.17}$$

$$\frac{\delta x_e}{x_e} = \frac{1}{y}\left(\frac{\delta E}{E} \oplus 2(1 - \frac{E}{E_e})\frac{\sin^2\frac{\theta_e}{2}}{\sin\theta_e}\delta\theta_e\right) \tag{4.18}$$

$$\frac{\delta y_e}{y_e} = \frac{1-y}{y}\frac{\delta E}{E} \oplus \frac{1-y}{y}\cot\frac{\theta_e}{2}\delta\theta_e \tag{4.19}$$

The iso-angle and iso-energy lines of the scattered electron in the (x, Q^2) plane are shown on figure 4.2. An important limitation of the kinematical range is introduced by the beam pipe, which at present excludes angles to the electron beam directions below about 6 degrees for tracking and calorimetry. This angular limit introduces a cut at small $Q^2 \simeq 8.5$ GeV^2 in most of the x region, except at very small x (below 10^{-3}), where lower Q^2 values can be reached.

From equations (4.17), (4.18) and (4.19), the following qualitative conclusions can be made:

- The resolution of Q^2 depends mainly upon the energy resolution of the calorimeter, except for high angles where the angular resolution is more important.
- At low y (high x and low Q^2) the resolution of x gets bad because of the $1/y$ factor in (4.18).

2. **Hadrons only: 'Jacquet Blondel' method**

Jacquet and Blondel [3] have remarked that the four-vector q can be written as

$$q = p_H - p = \sum_h p_h - p, \tag{4.20}$$

where the summation runs over all the particles of the hadronic final state. By substituting this q of (4.20) and $p = (0, 0, p_z, E_p)$, $k = (0, 0, -k_z, E_e)$ into the standard formula of y (1.7), we get

$$y = \frac{p_z \sum p_{h,z} - E_p \sum E_h - p_z^2 + E_p^2}{p_z k_z - E_p E_e}. \tag{4.21}$$

It is convenient to define

$$\Sigma = \sum_h E_h - p_{h,z} \qquad p_T^{h\,2} = (\sum_h p_{h,x})^2 + (\sum_h p_{h,y})^2. \tag{4.22}$$

If we neglect all the particles' masses, expression (4.21) simplifies to

$$y_h = \frac{\Sigma}{2E_e}. \tag{4.23}$$

One can also define the so-called 'hadronic angle' θ_h:

$$\tan\frac{\theta_h}{2} = \frac{\Sigma}{p_T^h}. \tag{4.24}$$

Similarly, one can calculate Q^2_{JB}:

$$Q^2_{JB} = \frac{p_T^{h\,2}}{1-y_h}. \tag{4.25}$$

The advantage of this method is that it allows to reconstruct the kinematical variables, without having to make any assumption on the final hadronic state, i.e. not jet finding algorithm is needed. Another asset is that the measured variables are rather insensitive to the fact that the remnant jet disappears largely into the beampipe, because its transverse momentum is close to zero.

The combination of y_h and Q_e^2 defines the mixed method [33] which is well suited for medium and low y measurements and was used in the F_2 analysis of the H1 data of 1992. However, a major limitation of the y_h measurement is occuring at large $y \geq 0.5$, where the hadronic jet enters the BEMC (see figure 4.3), a detector which is not suitable for measuring hadrons.

3. **Electron and hadrons: 'double angle method'** The double angle method [70] uses only θ_e and θ_h:

$$y_{DA} = \frac{\tan\frac{\theta_h}{2}}{\tan\frac{\theta_e}{2} + \tan\frac{\theta_h}{2}} \qquad Q^2_{DA} = 4E_e^2 \frac{\cot\frac{\theta_e}{2}}{\tan\frac{\theta_e}{2} + \tan\frac{\theta_h}{2}} \tag{4.26}$$

This method is rather insensitive to the absolute energy calibration of the detector and has a good resolution at large Q^2 where the jet energies are high, but the resolution deteriorates at $x < 0.001$.

4. **Electron and hadrons: 'sigma method'** The variables y and Q^2 can also be constructed independently from the incident electron energy. Replacing $2E_e$ in equation (4.23) by $\Sigma + E(1-\cos\theta_e)$, allowed by conservation of the total $\Sigma_h E_h - p_{h,z}$ of the event, and $(1-y_e)$ by $(1-y_\Sigma)$ in equation (4.16), one obtains:

$$Q^2_\Sigma = \frac{E^2 \sin^2\theta_e}{1-y_\Sigma}, \tag{4.27}$$

$$x_\Sigma = \frac{E}{2E_p}\frac{1+\cos\theta_e}{y_\Sigma}, \tag{4.28}$$

$$y_\Sigma = \frac{y_h}{(1-y_e)+y_h} \equiv \frac{\Sigma}{\Sigma + E(1-\cos\theta_e)}. \tag{4.29}$$

In a following section we will show that an important part of the radiative events are events where the lepton radiates a photon before the interaction with the proton takes place. In such events, the lepton energy at the $e\gamma^*$-vertex is less than the initial energy E_e. Since E_e does not appear in the formula of y_Σ, the sigma method is not sensitive to this kind of radiation, in contrast to y_h. The electron method suffers even more from the effect of the radiation, since the energy of the scattered electron E enters directly in the numerator of the expression for Q^2 and x without any compensation in the denominator.

The resolution of y_e was already given in equation (4.19), and one can compare this to y_Σ and y_h:

$$\frac{\delta y_\Sigma}{y_\Sigma} = (1-y_\Sigma)\frac{\delta y_h}{y_h} \oplus y_\Sigma \frac{\delta y_e}{y_e}, \tag{4.30}$$

$$\frac{\delta y_h}{y_h} = \frac{\delta E_h}{E_h} \oplus \cot\frac{\theta_h}{2}\,\delta\theta_h. \tag{4.31}$$

In the small y domain, the resolution of y_e becomes worse, while y_h improves there because the hadrons enter the central and forward part of the detector. (At high y the current jet goes mostly backwards, where the hadronic measurement is not precise.) The sigma method is a compromise between the two. Since the Jacquet Blondel method does not offer any significant advantage over the electron method concerning the radiative corrections, we will only consider the electron ('E') and sigma ('Σ') methods. One can see that y_Σ is more precise than y_e for small y:

$$\frac{\delta y_\Sigma}{y_\Sigma}|_E = y_e \frac{\delta y_e}{y_e}|_E, \tag{4.32}$$

$$\frac{\delta y_\Sigma}{y_\Sigma}|_{\theta_e} = y_e \frac{\delta y_e}{y_e}|_{\theta_e}. \tag{4.33}$$

In Q^2 the resolution as a function of energy is a factor two worse:

$$\frac{\delta Q^2_\Sigma}{Q^2_\Sigma}|_E = 2\frac{\delta Q^2_e}{Q^2_e}|_E, \tag{4.34}$$

$$\lim_{\theta_e \to \pi} \frac{\delta Q^2_\Sigma}{Q^2_\Sigma}|_{\theta_e} = (1-y_e)\frac{\delta Q^2_e}{Q^2_e}|_{\theta_e}, \tag{4.35}$$

while as a function of θ_e one gains a factor of two for $y_\Sigma \leq 0.5$. The Σ method is superior to determine x at low y:

$$\frac{\delta x_\Sigma}{x_\Sigma}|_E = (2-y_e)\, y_e \frac{\delta x_e}{x_e}|_E, \tag{4.36}$$

$$\lim_{\theta_e \to \pi} \frac{\delta x_\Sigma}{x_\Sigma}|_{\theta_e} = \frac{1+y_e}{1-y_e} y_e \frac{\delta x_e}{x_e}|_{\theta_e}, \tag{4.37}$$

while at large $y \geq 0.5$ the electron method is better (see next section and [76]).

4.4 Comparison of the electron and sigma methods

In the next chapter we will use the electron and sigma methods to measure to reconstruct the kinematic variables x and Q^2 for the F_2 measurement. In this section we will study the resolution and bias of the reconstructed x and Q^2 for both methods. In our analysis we will study the low Q^2 region, in which the scattered electron enters the BEMC. We will show that the electron and sigma methods together allow to cover the complete region of low Q^2 with the best possible precision.

This study is based on a Monte Carlo event sample, generated by DJANGO [35], which we shall discuss in greater detail in the next chapter. The generated DIS events were processed through the H1 analysis chain, which includes a detailed simulation of the H1 detector based on the GEANT program [27]. This simulation includes in a realistic way the effect of all the inhomogeneities and small miscalibrations of the real detector. The event selection will also be thoroughly described in the next chapter, but here is suffices to say that the same selection criteria were applied as for the real data.

The distributions of Q^2_{method}/Q^2_{gen}, x_{method}/x_{gen} and y_{method}/y_{gen} are shown in figures 4.4, 4.5 and 4.6 respectively. For each variable, we distinguish five y intervals: very

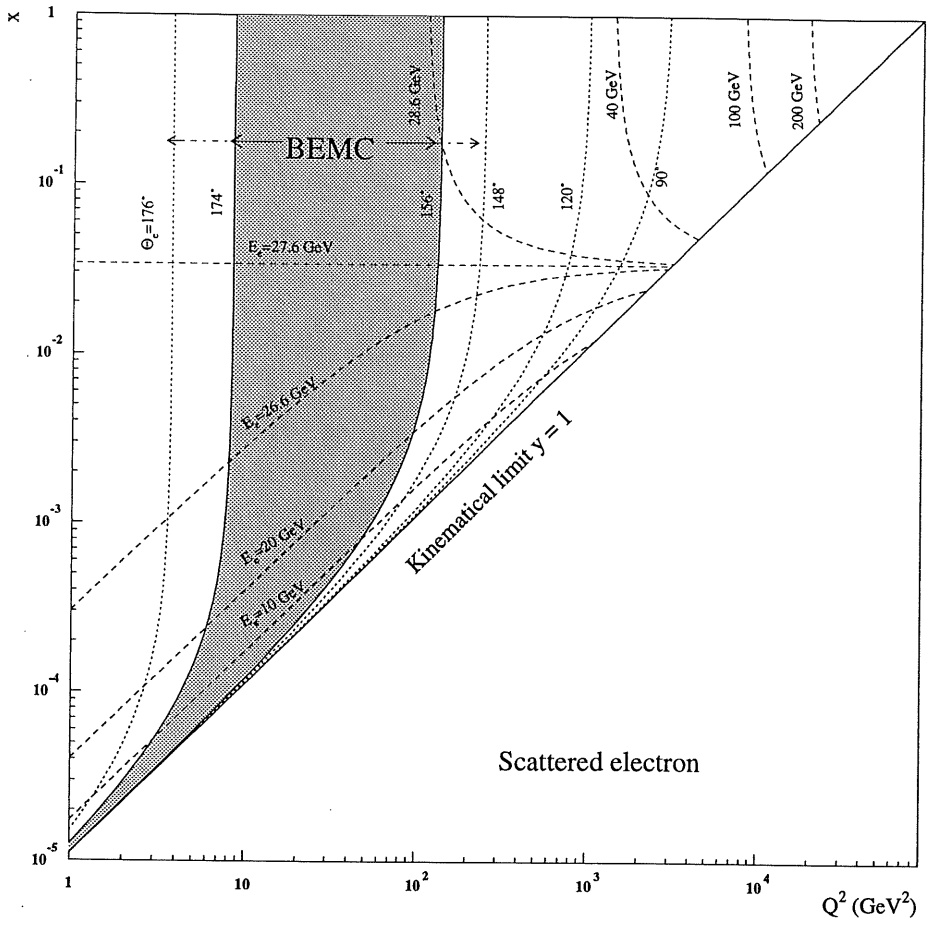

Figure 4.2: **Kinematic x, Q^2-plane for the scattered electron.**
The lines of constant polar angle (dotted) and constant energy (dashed) of the scattered electron are shown. The acceptance region of the BEMC is hatched. The larger angular acceptance range of the BEMC is when the z-vertex smearing is taken into account.

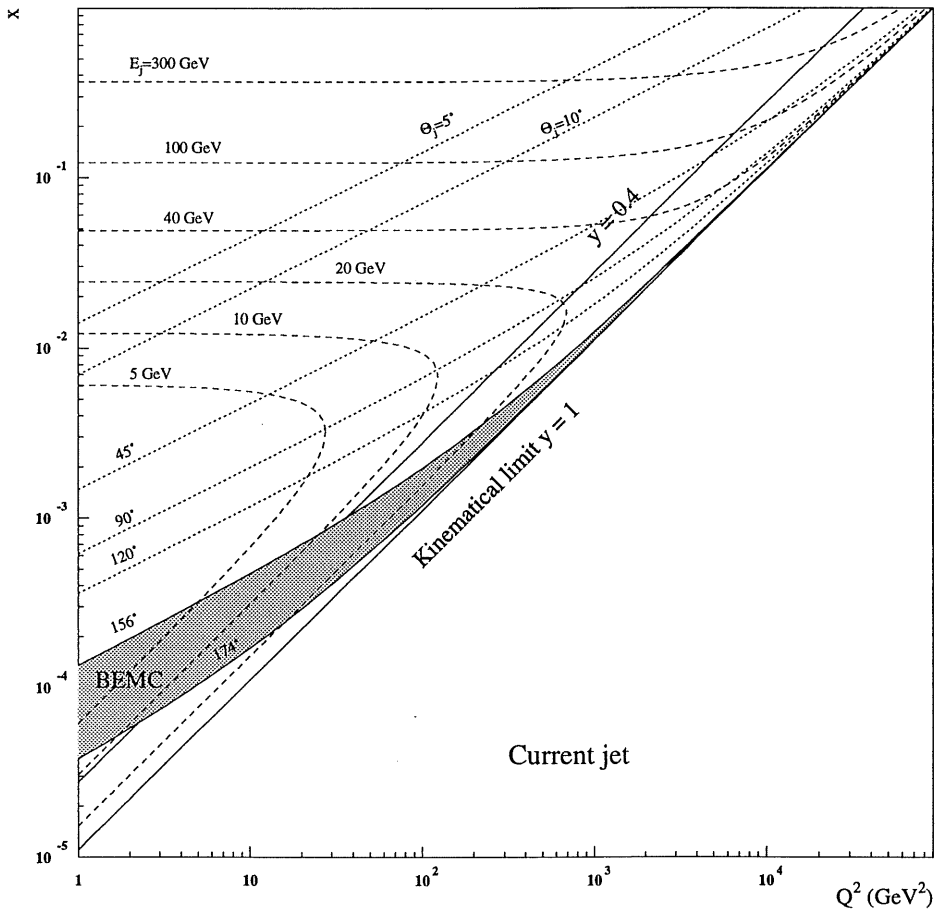

Figure 4.3: **Kinematic x, Q^2-plane for the current jet.**
The lines of constant azimuthal angle (dotted) and constant energy (dashed) of the current jet are shown. The acceptance region of the BEMC is hatched.

high (0.5–0.8), high (0.2–0.5), medium (0.1–0.2), low (0.05–0.1) and very low (0.01–0.05). For a given value of Q^2, the lowest x are at highest y and vice versa. No bias on the reconstructed variable is observed when the distribution peaks at 1. From these distributions, one may conclude that:

- Q_e^2 has always a negligable bias (smaller than 1%) and a good resolution (typically 4–6%), for all values of y. Q_Σ has equally no significant bias and a good resolution (7%) for very low to medium y, but becomes imprecise at high $y > 0.2$, with a bias up to 13% and a resolution of 19%.

- x_e has bias smaller than 2% and a resolution of 10% at very high y, but the precision deteriorates towards lower y. The bias of x_Σ is rather insensitive to y and stays below 8%, and its resolution, albeit slightly worse than x_e at very high and high y (13–16%), allows to penetrate the low y range further than the electron method.

- The distributions of y_e/y_{gen} and y_Σ/y_{gen} confirm the previous conclusion that the electron method is better for high and very high y (thus low x), but that the sigma method provides a good cross check in this region, and furthermore allows to probe down to much lower values of y.

Similar distributions for the double angle and Jacquet Blondel method are presented in [2], showing that the sigma method is always superior to the Jacquet Blondel method, and that the double angle method has a very poor resolution at very high y, while it does not offer any significant improvement at low y compared to the sigma method.

Therefore, we will only use the electron and sigma methods in the next chapter to make a complete measurement in the low Q^2 kinematic range. The double angle ('DA') method will only be used to estimate the resolution of the BEMC, and we will not use the Jacquet Blondel method at all.

4.5 Binning

In this analysis the selected DIS events will be counted in x, Q^2 bins. The choice of the size of the x,Q^2 bins depends on the statistics and on the migrations. The smaller the bins are, the less events they contain, but also the bigger the probability is that events migrate from one bin to another because of the detector resolution (smearing). The bins used in this analysis were chosen such that the statistical errors were typically less then 1% for most of the bins (see next chapter). The following bins are defined:

Q^2 ($\mathbf{GeV^2}$): for low Q^2 values (where the scattered electron enters the BEMC) 8 Q^2 bins per decade[1], for higher Q^2 (electron in the LAr calorimeter) 4 Q^2 bins per decade.

x: 4 x bins per decade for $x > 10^{-3}$, and 6 x bins per decade for $x < 10^{-3}$.

This leads to the following bin boundaries:

[1] Since Q^2 and x are usually plotted in a logarithmic frame (base 10), the bins are chosen to be logarithmically equidistant.

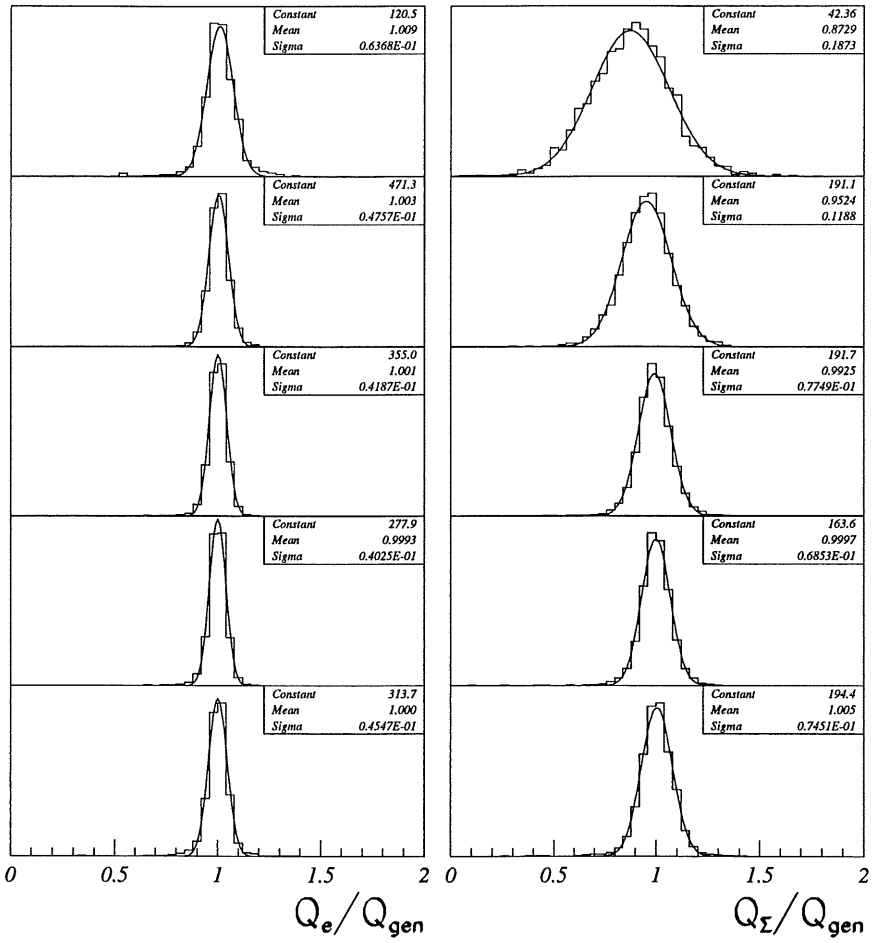

Figure 4.4: **Resolution and bias of Q for the electron and sigma methods.** *Comparison of Q_e/Q_{gen} (electron method) and Q_Σ/Q_{gen} (sigma method). From top to bottom, each row represents a y interval: very high (0.5–0.8), high (0.2–0.5), medium (0.1–0.2), low (0.05–0.1), very low (0.01–0.05).*

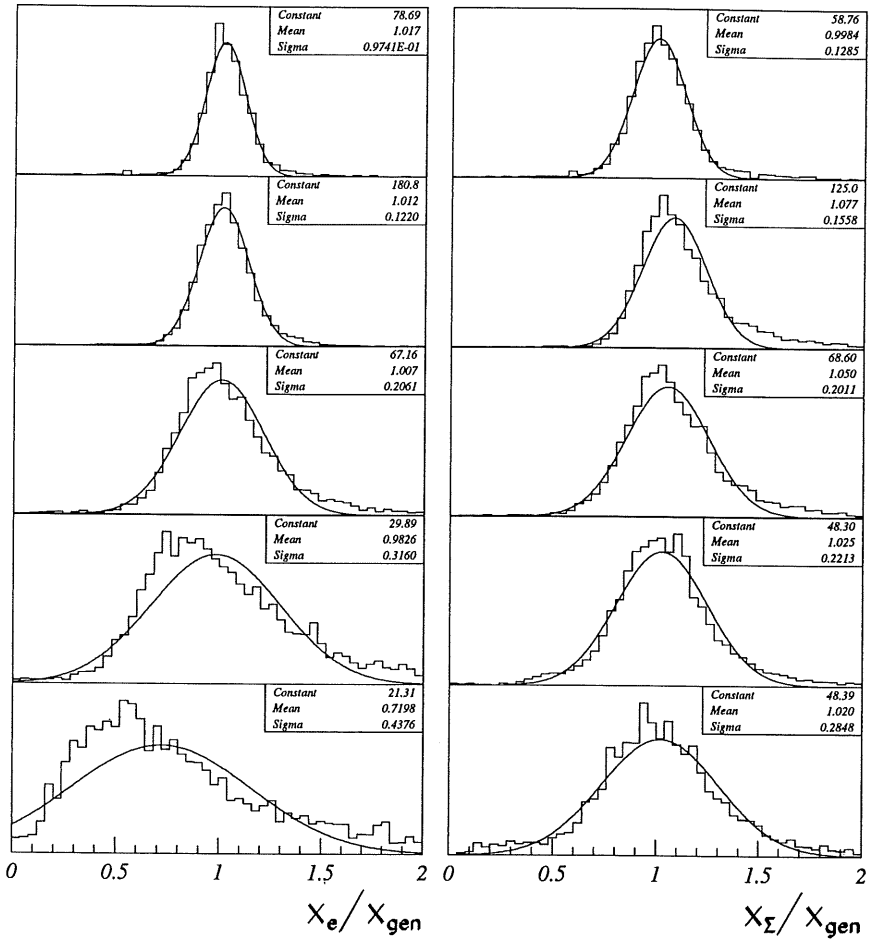

Figure 4.5: **Resolution and bias of x for the electron and sigma methods.** *Comparison of x_e/x_{gen} (electron method) and x_Σ/x_{gen} (sigma method). From top to bottom, each row represents a y interval: very high (0.5–0.8), high (0.2–0.5), medium (0.1–0.2), low (0.05–0.1), very low (0.01–0.05).*

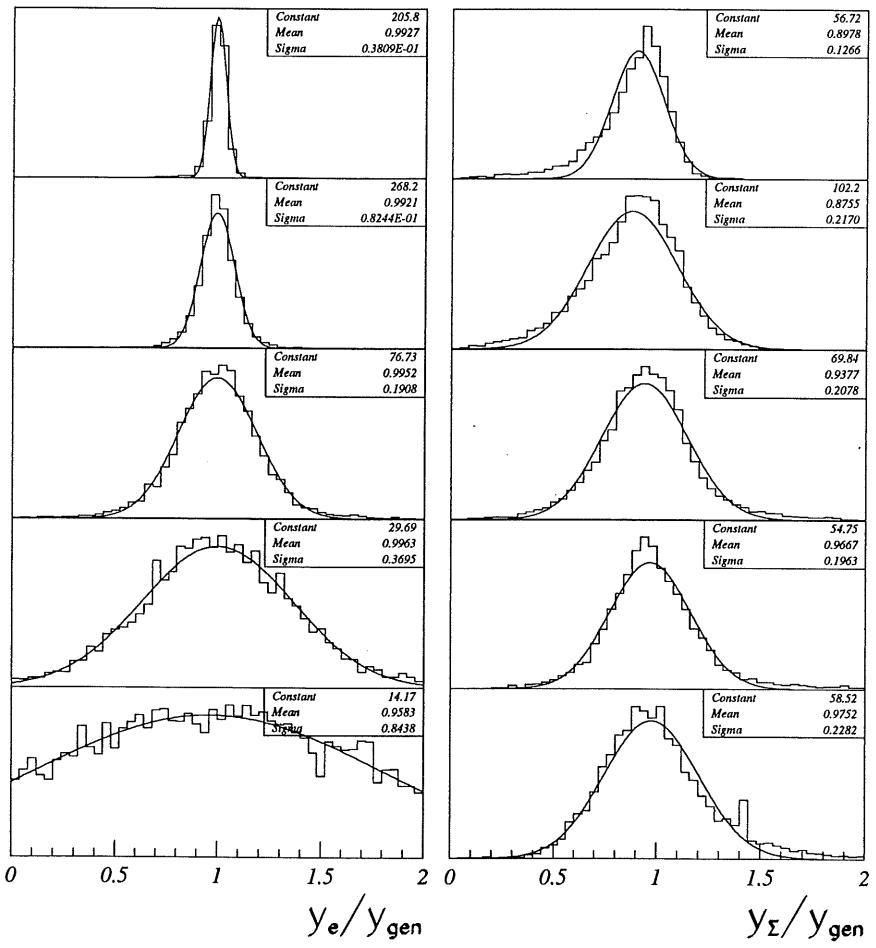

Figure 4.6: **Resolution and bias of y for the electron and sigma methods.** *Comparison of y_e/y_{gen} (electron method) and y_Σ/y_{gen} (sigma method). From top to bottom, each row represents a y interval: very high (0.5–0.8), high (0.2–0.5), medium (0.1–0.2), low (0.05–0.1), very low (0.01–0.05).*

Q^2:								
	2.371	2.738	3.162	3.651	4.217	5.623	7.499	10.00
	13.34	17.78	23.71	31.62	42.17	56.23	74.99	100.0
	133.4	177.8	237.1	316.2	421.7	562.3	749.9	1000.
	1334.	3162.	10000.					

x:					
			.0000251	.0000398	.0000631
.000100	.000158	.000251	.000398	.000631	
.00100	.00158	.00251	.00398	.00631	
.0100	.0158	.0251	.0398	.0631	
.100	.158	.251	.398	.631	

This study is limited to the angular range where the scattered electron goes into the BEMC by using only bins such that $4.217 \leq Q^2 \leq 74.99$. Complementary studies of the 1994 H1 data have been presented [22], which expand the covered kinematical range from $1.5 \leq Q^2 \leq 10000$. These analysis involved different systematical studies.

Figure 4.7 shows the standard binning of the analysis, together with the iso-angular and iso-y lines.

The differential cross sections and the F_2 will be measured for a discrete set of Q^2, x values. These *"bin centre"* values Q_c^2, x_c were chosen to be:

Q_c^2:								
	2.5	3	3.5	4	5	6.5	8.5	12
	15	20	25	35	50	65	80	120
	150	200	250	350	500	650	800	1200
	1200	2000	5000					

x_c:					
			.000032	.00005	.00008
.00013	.0002	.00032	.0005	.0008	
.0013	.002	.0032	.005	.008	
.0130	.02	.032	.05	.08	
.130	.2	.32	.5		

This choice of Q_c^2, x_c allows an easy comparison with other experiments (in particular Zeus), as well as with earlier H1 measurements. The bin centre values are roughly in the centre of the bins, so that the bin centre corrections never exceed 15% (section 5.15).

4.6 Radiative corrections

4.6.1 Classification of radiative events

Radiative events are higher order QED and electroweak corrections of the basic DIS process. Figures 4.8 and 4.9 show the possible radiative events up to the first order ($\mathcal{O}(\alpha^3)$), the former showing the contribution with real photon emission, the latter with virtual boson exchange. Since we want to measure the Born cross section, which is the cross section of the lowest order DIS process and which contains the information on the structure of the proton, radiative corrections must be applied to the measured cross section before it can be compared to theory. One can distinguish four kinds of radiative corrections:

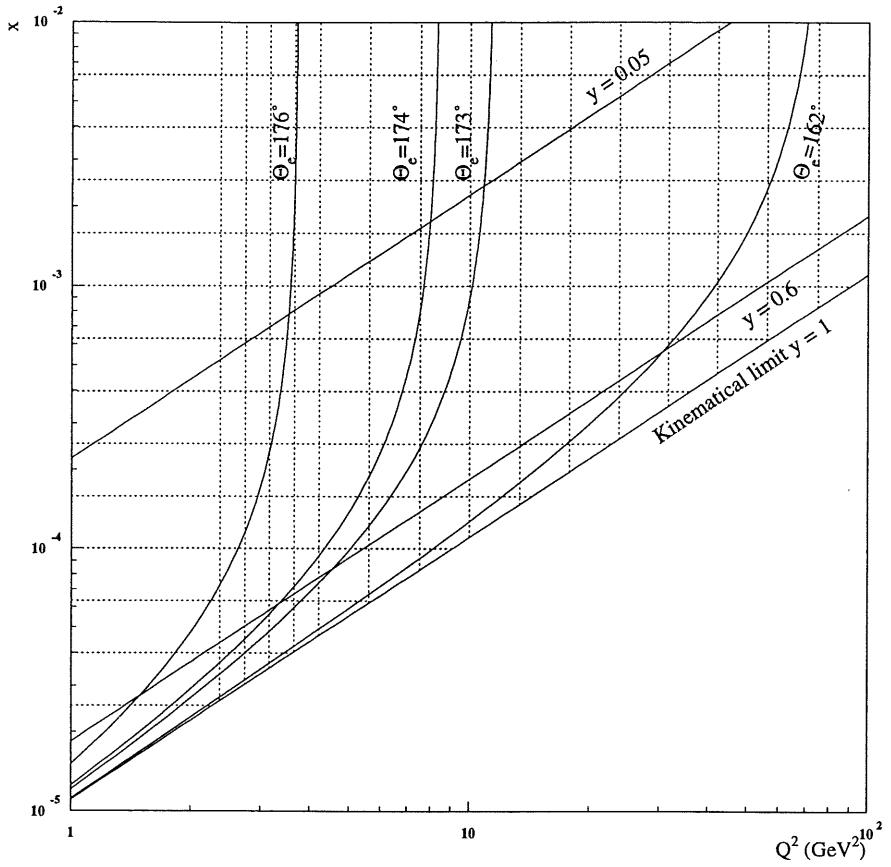

Figure 4.7: **Kinematic x, Q^2-plane with the bins and selected events.**
The kinematic x, Q^2-bins are indicated on this picture. Because of an angular cut, some bins are only partially used.

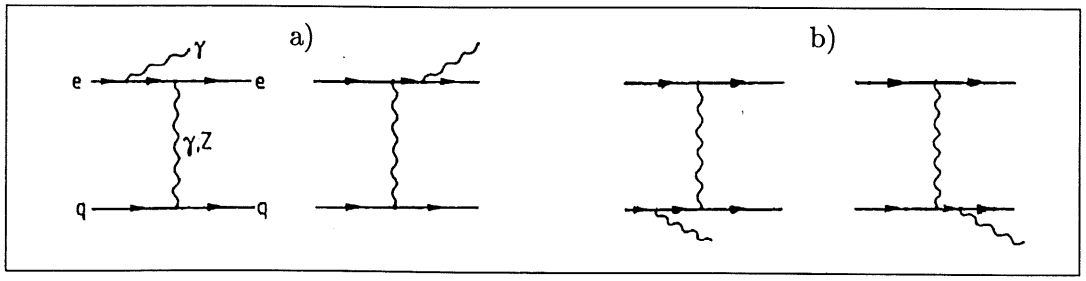

Figure 4.8: **Single photon bremstrahlung diagrams.**
Both the electron (a) as well as the quark (b) can emit a photon in the initial and final state.

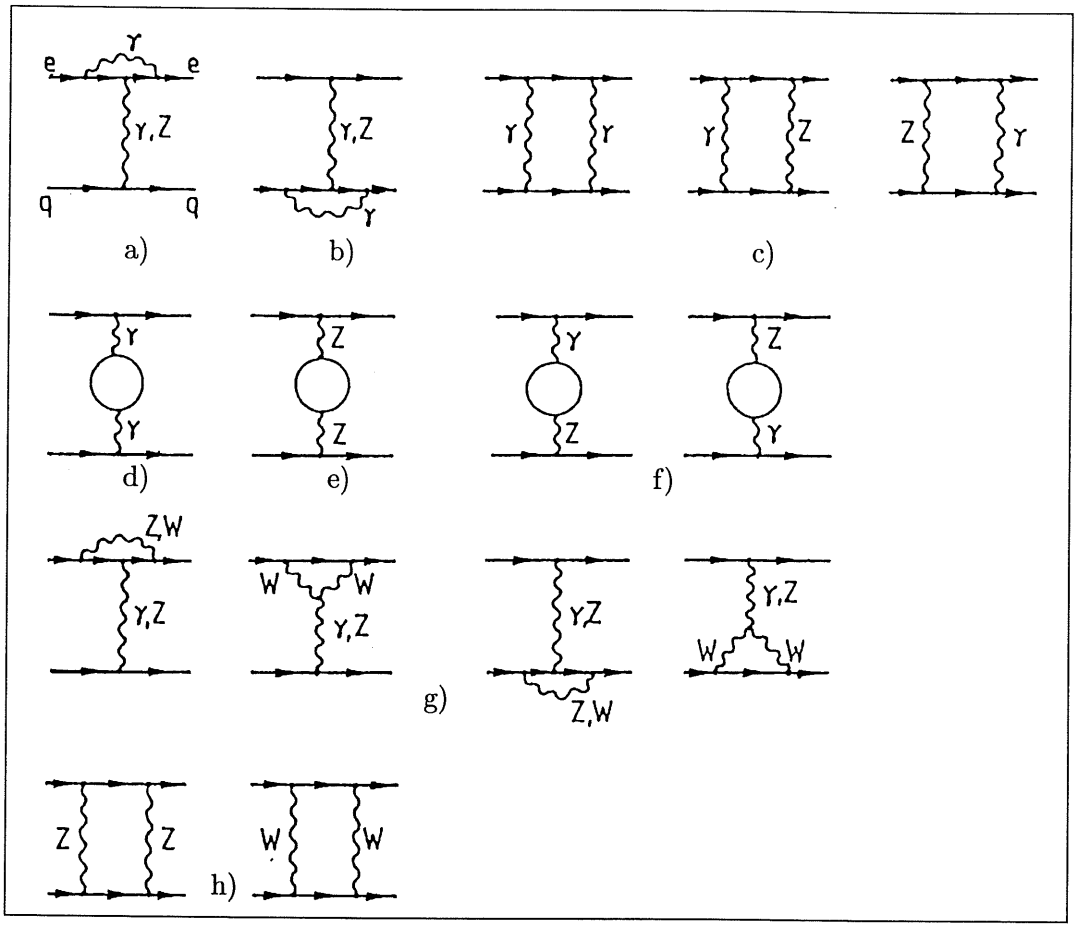

Figure 4.9: **Virtual radiative corrections of the first order.**
One can distinguish purely leptonic corrections (a), purely quarkonic corrections (b), lepton-quark interference corrections (c) and weak corrections (d—h). In (c) and (h) the crossed diagrams are not shown.

Purely leptonic corrections: In those diagrams a photon is coupled to an electron line. This processes include Bremstrahlung and a virtual correction at the electron vertex.

Purely quarkonic corrections: These processes are analogue to the purely leptonic corrections. The corrections are proportional to the square of the charge and increase with the inverse of the mass of the quarks, and are therefore less important than the leptonic corrections.

Interferences of leptonic and quarkonic corrections: These diagrams are box diagrams with γ and/or Z^0 exchange. These corrections are proportional to the charge of the quarks.

Purely weak corrections: All the other diagrams (figures 4.9d—h) belong to this group. They are processes in which no additional photon is produced.

Since this analysis is limited to low values of $Q^2 \ll M_W^2$, the weak corrections are negligable.

At HERA, the cross section for radiative events $ep \longrightarrow e+\gamma+X$ is large, and especially at low x, can be of the same order of magnitude as the non-radiative cross section. This originates from the fact that the emission probability of real or virtual photons colinear with the entering or scattered electron is proportional to $\alpha \log(Q^2/m_e^2)$. The 'electron' method is very sensitive to these corrections.

The quarkonic corrections are less important [31] and depend little on Q^2. If the 'electron' method is used only a vertex correction in the order of a few percent is necessary, and the hard photon radiation off the quarks is negligable. The remaining purely electromagnetic corrections (c,d in figure 4.9) do not depend on the reconstruction method and can be calculated exactly. We will now discuss the effect of the radiative corrections on the measurement of the cross section in greater detail.

Events with real photon emission can be divided into two classes: Initial state radiation (ISR) and final state radiation (FSR). In case of initial state radiation, the directions of the emitted photons are spread around the direction of the incoming photon. The available electron-quark center of mass energy is less for ISR events than for non-radiative events, and therefore all calculated kinematic variables are wrong, since they were calculated under the assumption of fixed beam energies. In the case of ISR events, the effective available energy E_{eff} is smaller than the electron beam energy E_e:

$$E_{eff} = E_e - E_{miss} = zE_e. \tag{4.38}$$

The missing energy E_{miss}, which is carried by the emitted photon, can be obtained by combining y_e and y_h:

$$E_{miss} = E_e(y_e - y_h). \tag{4.39}$$

The true kinematic variables Q^2_{true}, x_{true}, y_{true} can then be calculated by using E_{miss}:

$$Q^2_{true} \simeq 4(E_e - E_{miss})E\cos^2\frac{\theta_e}{2} \tag{4.40}$$

$$x_{true} \simeq \frac{(E_e - E_{miss})E\cos^2\frac{\theta_e}{2}}{E_p(E_e - E_{miss} - E\sin^2\frac{\theta_e}{2})} \tag{4.41}$$

$$y_{true} \simeq 1 - \frac{E}{(E_e - E_{miss})}\sin^2\frac{\theta_e}{2}. \tag{4.42}$$

For non-radiative events $E_{miss} = 0$, so that equations (4.40) to (4.42) can replace (4.14)–(4.16).

The relation between the measured and the Born cross sections can be written as follows:

$$\frac{d^2\sigma}{dx_e\, dy_e} = (1 + \delta_{RC}(x_e, y_e)) \frac{d^2\sigma_{Born}}{dx\, dy}, \tag{4.43}$$

where δ_{RC} is the radiative correction. Note that $d^2\sigma/dx_e\, dy_e$ can easily be transformed into $d^2\sigma/dx_e\, dQ_e^2$, but it is customary to express radiative corrections as a function of x_e and y_e.

The measured differential cross-section $d^2\sigma/dx_e\, dy_e$ in a particular x_e, y_e point depends upon the shape of the structure function in the whole domain $x > x_e$ and $y < y_e$:

$$\frac{d^2\sigma}{dx_e\, dy_e} = \int_{x_e}^{1}\int_{0}^{y_e} dx\, dy\, K(x_e, y_e; x, y) \frac{d^2\sigma_{Born}}{dx\, dy}. \tag{4.44}$$

The analytical form of the kernel $K(x_e, y_e; x, y)$ can be found in [18]. This means that the size of the radiative correction depends, in the case of HERA, upon the a priori unknown shape of the structure function in the unmeasured kinematical region. This is illustrated on figure 4.10, where the radiative correction is shown for various parametrisations of the F_2 structure function, which were tuned to pre-HERA data.

The sensitivity of the radiative correction to the shape of the input structure function arises from hard photon emission processes. Figure 4.11 shows the integration region contributions to the cross section in the point $x_e = 0.001$, $Q_e^2 = 95$ GeV^2. The solid line corresponds to the integration region in the case where the photon is collinear with the incoming electron, the dotted line corresponds to the case where the photon is collinear with the outgoing electron. The solid line (ISR) is described by:

$$Q^2 = z_i\, Q_e^2, \tag{4.45}$$

$$x = \frac{x_e y_e z_i}{y_e + z_i - 1}, \tag{4.46}$$

$$y_e = \frac{Q_e^2}{x_e s} \tag{4.47}$$

$$z_i = \frac{E_0 - E_\gamma}{E_0} \tag{4.48}$$

$$\frac{1 - y_e}{1 - x_e y_e} \leq z_i \leq 1 \tag{4.49}$$

while the dotted line (FSR) is described by:

$$Q^2 = z_f\, Q_e^2, \tag{4.50}$$

$$x = \frac{x_e y_e z_f}{1 - z_f + z_f y_e}, \tag{4.51}$$

$$z_f = \frac{E_e + E_\gamma}{E_e} \tag{4.52}$$

$$\frac{1}{1 + x_e y_e - y_e} \leq z_f \leq 1. \tag{4.53}$$

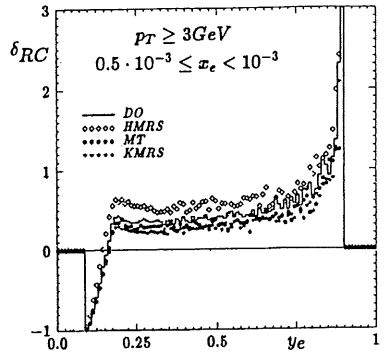

Figure 4.10: **Radiative corrections for various parametrisations of structure functions**
This plot shows that the size of the radiative corrections depend strongly upon the input structure function. The parametrisations which are shown have all been tuned to pre-HERA data.

The dominant contribution to the measured cross section at (x_e,y_e) comes from narrow paths around both curves. The widths of these paths are $\approx \sqrt{m_e/E_0}$ and $\approx \sqrt{m_e/E_e}$ respectively, and reflect the peaking behaviour of the photon angular distribution. A third radiative contribution to the measured cross section originates from the fact that the Born cross section is very large in the $Q^2 \to 0$ region, which can outweight the small kernel value $K(x_e, y_e; x, y)$ there. This contribution is called the *Compton contribution*, since it can be viewed as resulting from the emission of a quasi real photon from a quark, followed by a subsequent Compton scattering $e\gamma \to e\gamma$. Finally, a fourth contribution comes from elastic electron-proton scattering near $x = 1$, where the cross section is large at small Q^2, but falls rapidly with increasing Q^2.

The above observations allow to understand the qualitative behaviour of the radiative corrections as a function of x_e and y_e. At large y_e and small x_e, the lower kinematical bound of z_i approaches zero, and the solid line on figure 4.11 is pushed towards the low Q^2 region, where the cross section is considerably larger than at Q_e^2. Additionally, this line crosses the elastic region $x \approx 1$ at small Q^2, where the elastic cross section is still large. At low y_e and low x_e the z_i domain shrinks and only soft photons of energies up to $\approx y_e E_0$ are kinematically allowed, so that the radiative corrections remain small.

When the 'electron' method is used to calculate the kinematic variables, a cut in y is necessary to make sure that the initial state radiation does not become too large. A cut of $y \leq 0.6$ avoids corrections beyond 100%. The corrections for the 'sigma' method are much smaller, and are never larger than 7% (see tables in Appendix A).

In case of final state radiation, the photon is emitted very close to the scattered electron direction. These almost collinear photons cannot be resolved, since the deposited energies of the scattered electron and the emitted photon are usually merged into one cluster, due to the coarse angular granularity of the calorimeters. Therefore FSR contributions to radiative corrections do not have to be calculated, since they do not disturb the measurent.

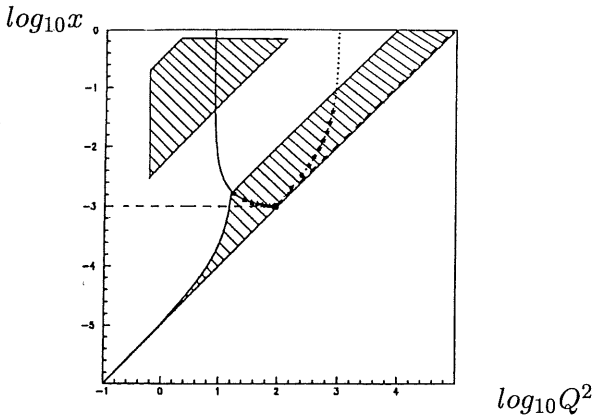

Figure 4.11: **Topology of the x, Q^2 domains that contribute to the radiative differential cross section at $x_e = 0.001$, $Q_e^2 = 95$ GeV.**
The solid line corresponds to the integration region in the case where the photon is collinear with the incoming electron, the dotted line corresponds to the case where the photon is collinear with the outgoing electron. The upper hatched region indicates the area of fixed target DIS experiments, the lower hatched area is a schematical indication of the area where H1 can measure the proton structure function.

4.6.2 Calculation of radiative corrections

Several programs exist to calculate radiative corrections, but only two have been used in this analysis.

HERACLES The HERACLES program [4] is an event generator, which takes into account all the leptonic and quarkonic terms, as well as the interference terms up to $\mathcal{O}(\alpha)$. All the individual QED-corrections, such as ISR, FSR, QED-compton and quarkonic corrections, can be switched on and off individually. The parton distributions are all obtained from the PDFLIB [63] library. HERACLES generates the events at the parton level, and all fragmentation and hadronisation has to be done outside the program. Therefore, HERACLES is combined together with LEPTO [34] and JETSET [72] into one program DJANGO [35].

The advantage of the latter Monte Carlo program is that the complete detector geometry can be implemented, allowing realistic studies of all the cuts.

TERAD The analytical program TERAD [6] uses analytical methods to calculate the differential cross-section of neutral current and charged current *ep* interactions. TERAD allows to calculate the radiative corrections for the 'electron', 'sigma' and 'Jacquet Blondel' methods.

The disadvantage of TERAD is that—due to its analytical nature—only simple geometrical cuts can be implemented, such as a cut on the angle of the scattered electron.

Since DJANGO and TERAD are complementary methods, we will use TERAD as a cross-check to calculate the radiative corrections.

4.7 Photoproduction background

An important limitation in the exploration of the low x domain in deep inelastic scattering results from background due to *photoproduction* processes. Quasi real photoproduction processes can be accessed with low Q^2 ep collisions, and because of the $1/Q^4$-dependence of the cross-section, ($\sigma_{tot}(\gamma p) \simeq$ 100–200 μb vs. $\sigma_{DIS}(ep) \simeq$ 20 nb) high statistics of photoproduction events are expected with respect to deep inelastic scattering events. The average centre of mass energy squared of these γp reactions, $W_{\gamma p}$, is about 200 GeV^2, exceeding the maximum enegy reached in fixed target experiments by an order of magnitude. Secondaries from these γp processes can mimic an electron in the backward part of the H1 detector. A typical example is a γ and $\pi^{\pm}$ combination, which may leave a significant energy deposition in the BEMC (caused by the γ), spatially overlapped with a hit in the BPC (caused by the $\pi^{\pm}$). The real scattered electron disappears down the beampipe, as $Q^2 \sim 0$ and $\theta_e \sim 180°$.

4.7.1 Photoproduction Monte Carlo study

There are three classes of photoproduction: direct, VDM and anomalous:

- In direct photoproduction interactions, the photon couples directly to quarks, in a direct pointlike way. This gives rise to hard scattering processes, leading to two high p_T jets in γp events, and which are expected to become important at high energy. Figures 4.12a and 4.12b show two *direct* photon interactions. The cross section of these processes can be calculated perturbatively.

- The photon can also interact hadronic-like with the proton. The hadronic component is commonly described in terms of the vector dominance model (VDM). In this picture, the photon couples to a vector meson V, (V=ρ, ω, ϕ), which interacts with the proton in a non-perturbative way. Figure 4.13a shows such a VDM interaction.

- Direct photoproduction interactions and the VDM model alone cannot explain the total cross-section of photoproduction, and additional processes have to be included. Figure 4.13b shows the anomalous component of the photon. The photon fluctuates into a quark-antiquark pair and possibly subsequentially into a gluon. This process can be calculated perturbatively within the framework of QCD.

Sometimes the VDM and anomalous components are combined into one photon structure function and the events are called *resolved.* Another classification is to call direct and anomalous *hard* processes, and VDM *soft.* The total photoproduction cross section can thus be written as:

$$\sigma_{tot}^{\gamma p} = \sigma_{dir}^{\gamma p} + \sigma_{VDM}^{\gamma p} + \sigma_{anom}^{\gamma p}. \tag{4.54}$$

4.7.2 Experimental signature of photoproduction in H1

Photoproduction appears as a large cross section enhancement at low BEMC cluster energies. The scattered electron, which disappears into the beampipe, can sometimes be identified by the electron tagger. The eletron tagger is sensitive to scattered electrons

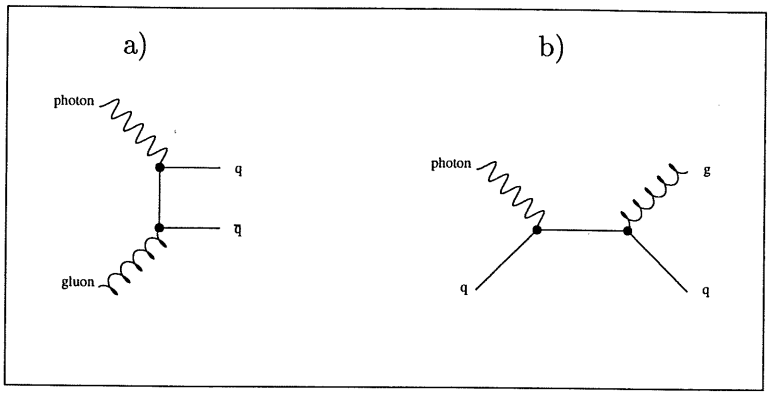

Figure 4.12: **Two direct photoproduction processes.**
(a) Photon-gluon fusion and (b) QCD compton scattering. The photon interacts with a $q\bar{q}$ pair in a pointlike way.

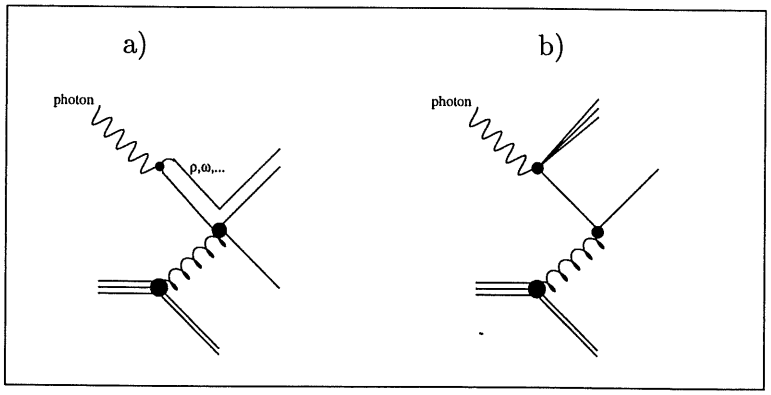

Figure 4.13: **Two resolved photoproduction processes.**
The photon scatters via its quark or gluon content, resulting in resolved processes. (a) VDM interaction and (b) Anomalous component of the photon.

with an energy above 4 GeV and a scattering angle of 0–5 mrad. However, the acceptance of the tagger is not uniform and depends on y. Only a few percent of the photoproduction events are identified as such because the electron is tagged, so identification of photoproduction events on an event-by-event basis is not possible. Figure 4.15 shows the photoproduction peak at lower BEMC energies in a sample of selected DIS candidates. Also shown are 'tagged' events, i.e. at least 4 GeV was depostited in the electron tagger.

The photoproduction events can be classified as follows:

π^0: π^0s convert within the interaction region into two photons. These may later convert into an electron and positron in the dead material (cables, electronics and endflanges which is located between the CJC and the BPC).

γ: The energy of pure photons is well measured in the BEMC, but they pass undetected through the BPC. However, a part of the photons may convert into an electron-positron pair in the dead material.

$\pi^{\pm}$: The BEMC is an electromagnetic calorimeter with a hadronic interaction length of $\lambda = 0.97$. Figure 4.14 shows that most hadrons traverse the BEMC as minimum ionising particles (mip), but some deposit higher energies so that they can fake an electron nevertheless.

$\gamma\pi^{\pm}$ **overlap:** In this case a photon causes a visible energy deposit in the BEMC, while the charged pion is detected by the BPC. If the photon and the pion are closely together, this may contribute to the background.

Previous Monte Carlo studies have shown that 79% of the 'fake' electrons in the BEMC are either 2γ (π^0), γ or $\gamma\pi^{\pm}$, and that 21% is of a purely hadronic nature [29].

4.7.3 Estimation of the photoproduction background

To estimate this background, more than 1.5 million photoproduction events were simulated, corresponding to the luminosity of the data. The 'soft' vector meson contribution was simulated using the RAYVDM program [57], the 'hard' contribtution using the PYTHIA program [14]. In the latter the direct, the resolved and the heavy quark production processes were included. The relative contributions of these processes were adjusted to agree with the photoproduction data [40] and are listed in table 4.1.

Details of this Monte Carlo simulation and the comparison with the data will be presented in the next chapter (section 5.5.2). Only in 6 bins, out of a total of 79 bins, the photoproduction background was estimated to represent more than 3% of the number of selected events. The contamination never exceeds more than 8% in any bin.

4.8 Non-*ep* background

At low Q^2 the main sources of non-*ep* background are due to proton beam interactions with residual gas ('beam-gas') and beam line elements upstream of the H1 detector ('beam-wall'). The rate of these interactions is three orders of magnitude larger than the rate of DIS events, but an efficient reduction of this background is provided by requiring the reconstructed vertex to be centered on the beam axis, and by demanding it to be within

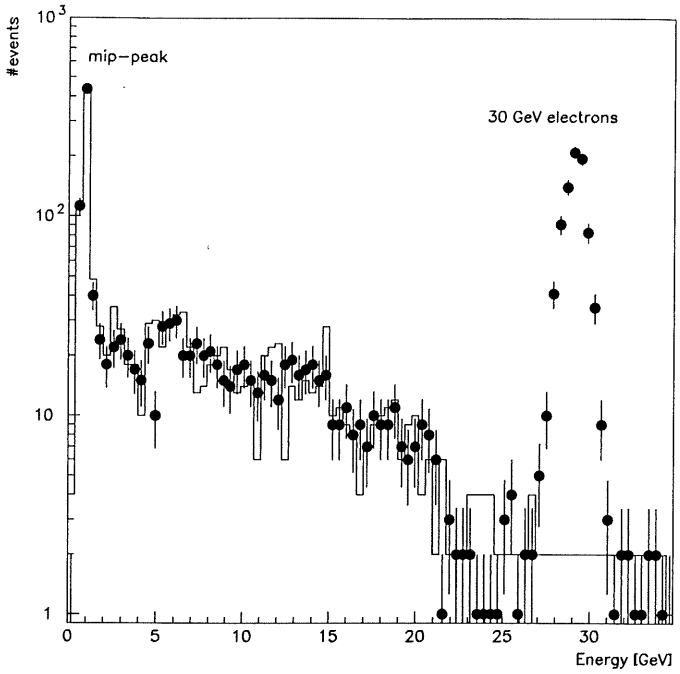

Figure 4.14: **Energy deposition of 30 GeV pions in a BEMC module.** *Data from the 1990 CERN test beam measurements with 30 GeV pions shot perpendicularly into the BEMC. The solid line is the comparison with the Monte Carlo simulation. The Monte Carlo is normalized to the number of events in the mip-peak. The peak at 30 GeV originates from a remaining fraction of 30 GeV electrons in the beam.*

Generator type	N_{ev} **generated**	N_{ev} **passed turbo sim**	**lumi MC** [$\mathbf{nb^{-1}}$]	**relative weight**
RAYVDM	629888	3800	89.98	1
Resolved	968988	6904	218.40	0.412
Direct	104438	2066	417.75	0.216
Heavy	79999	81	851.06	0.106

Table 4.1: **Summary of turbo simulated and reconstructed MC events.** *The relative contributions of these processes were adjusted to agree with the photoproduction data [40].*
To save CPU time, not all the generated events were simulated, but only those where the scattered electron enters the geometrical acceptance of the BEMC ("turbo simulation", see chapter 5).

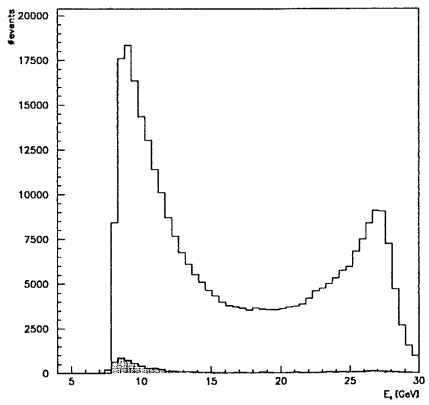

Figure 4.15: **Energy distribution of selected DIS candidates together with tagged events.**
The solid histogram represents selected DIS candidates based on a simple energy deposition criterion in the BEMC. The peak at lower energies is caused by photoproduction events, where the scattered electron goes down the beampipe, and photons and/or hadrons deposit energy in the BEMC faking an electron. This is illustrated by the fact that a small fraction of the scattered electrons are detected by the electron tagger (hatched histogram). The small contribution of the tagged events around 27.6 GeV is caused by random overlaps of Bethe-Heitler and γp events.

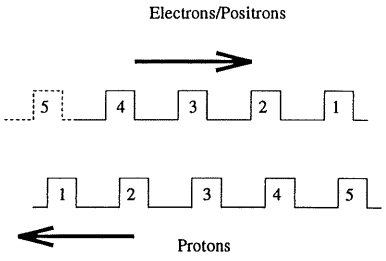

Figure 4.16: **Example of a pilot bunch.**
Bunches 1 to 4 have a colliding partner, while bunch 5 of the proton beam has no colliding partner, and is therefore a pilot bunch. In reality, there are electron/positron as well as proton pilot bunches. These pilot bunches allow to estimate the amount of non-ep background in the event sample.

a certain distance from the nominal interaction point. Together with a minimum energy requirement in the calorimeters, these cuts reduce this background to the percent level.

The residual background can be estimated by means of unpaired non-colliding particle bunches ('pilot bunches', see figure 4.16). Since pilot bunches have no matching bunch to collide with, they can only interact with residual beam gas or beam line elements. Since it is assumed that pilot bunch background interactions occur with approximately equal probability as the colliding bunches, the number of 'pilot' events in the final sample can be used to estimate the fraction of beam wall and beam gas background that is present in the final data sample.

The amount of beam gas and beam wall events that are present in the data sample can be estimated by using the following formula:

$$n_{bg} = N_{p-pilot} \times \frac{n_{colliding}}{n_{p-pilot}} + N_{e-pilot} \times \frac{n_{colliding}}{n_{e-pilot}}. \tag{4.55}$$

with $N_{p-pilot}$, $N_{e-pilot}$ the number of proton respectively electron pilot bunch events in the final event sample. The numbers $n_{p-pilot}$, $n_{e-pilot}$ and $n_{colliding}$ are the number of proton-pilot, electron-pilot and colliding bunches in the HERA beam. This is a valid approximation, on condition that the interaction probability of a pilot bunch with a beam gas particle or with the beam wall is equal to the interaction probability of a colling bunch with the beam gas and wall. On figure 4.17 the time evolution of the bunch currents is shown. Since the time evolution is similar, equation (4.55) should hold.

In 1994 HERA operated with maximum 170 electron (or positron) bunches and 168 proton bunches, of which 153 bunches were colliding, seventeen electron pilot and fifteen proton pilot bunches. In some runs these numbers vary by one or two bunches. As will be shown in chapter 5, the residual background in the DIS event sample was estimated to be smaller than 1%.

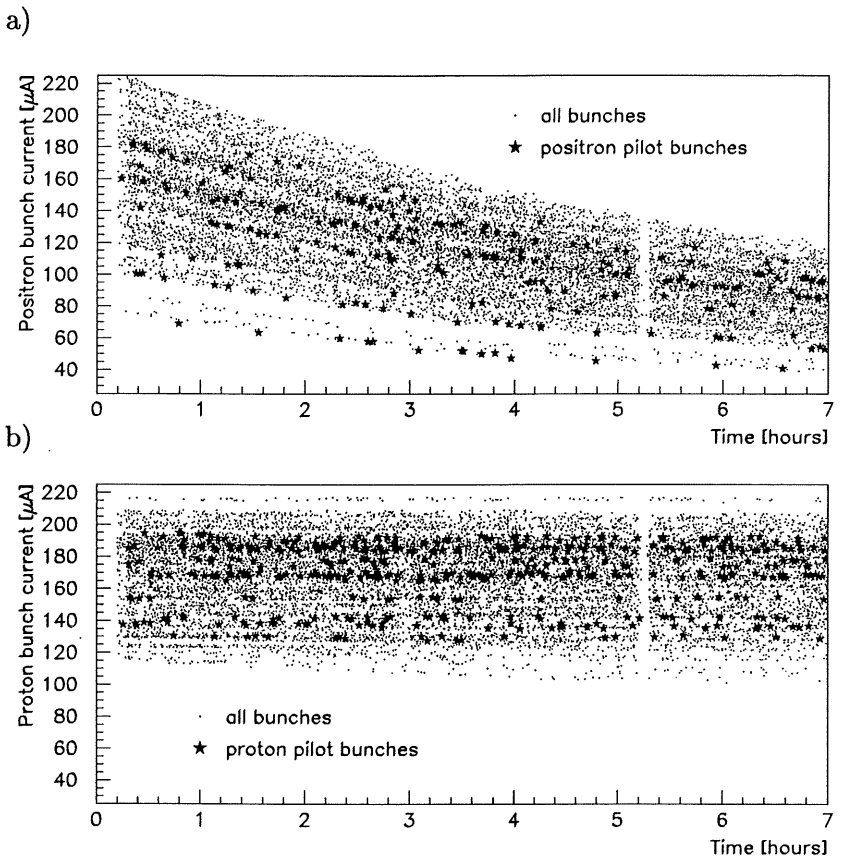

Figure 4.17: **Time evolution of the bunch current colliding and non-colliding ('pilot') bunches.**
The bunch currents of pilot bunches show a similar time evolution as colliding bunches, both for positron (a) as for proton (b) bunches. This allows pilot bunches to be used for estimating the non-physical background to DIS. One can also observe the much shorter lifetime of the positron bunches.

Chapter 5

Measurement of the proton structure function F_2

5.1 Introduction

In this chapter we present a detailed description of the measurement of the proton structure function $F_2(x, Q^2)$, based on the H1 e^+p data[1] of 1994. In this analysis we only use the data where the scattered positron enters the backward electromagnetic calorimeter (BEMC), which corresponds to the kinematic region of low Q^2 ($5\ \text{GeV}^2 < Q^2 < 100\ \text{GeV}^2$) and low x ($10^{-5} < x < 10^{-2}$). As pointed out in the first chapter, this low x region is of particular interest for QCD studies.

In our analysis we use the *Monte Carlo* (equation (4.12)) method to obtain the structure function $F_2(x, Q^2)$. We use both the electron (E) and sigma (Σ) methods to calculate the kinematical variables, since their systematics are different (see chapter 4) and they can be considered complementary. The radiative corrections of the E method reach values up to 30% at low y, while they are always smaller than 7% for the Σ method. For the final F_2 data points we will use the method with the smallest total error.

An advantage of the 1994 data over the 1993 data is that in a part of the 1994 data the inner BEMC triangles (figure 2.14) were included in the BEMC trigger (see next section), while in 1993 they were not. The boundary of the inner triangles lies around $\theta_e \leq 173°$, which is equivalent to $Q^2 \geq 10\ \text{GeV}^2$. By using the data with the inner BEMC triangles included in the BEMC trigger, events could be measured with lower angles ($\theta_e \leq 174°$) of the scattered electron, therefore allowing to probe down to lower Q^2 values ($Q^2 \geq 5\ \text{GeV}^2$).

5.2 Trigger for low Q^2 DIS

When looking for an efficient trigger for neutral current DIS events, it is clear that the main trigger must be an electron trigger, based on the calorimeter information. The most powerful electron selector is the deposition of substantial, well localised energy in the calorimeter. Such triggers are usually robust, relatively simple and independent of model assumptions, and have a high efficiency.

Since this study covers the low Q^2 DIS domain ($Q^2 < 100\ \text{GeV}^2$) where the scattered electron enters the BEMC, a special trigger was used: the BEMC Single Electron Trigger (BSET). The basic idea of the BSET trigger [46] is to look for well localised high energy depositions in the BEMC stacks. Groups of stacks with signals above preset thresholds

[1] Although we will only use the positron-proton data, we will often still refer to the scattered *electron*, for historical reasons.

are called clusters. From the electromagnetic cluster size and the cell size one can always expect at least one stack with a least 25% of the total energy.

To determine whether adjacent stacks belong to a cluster, a hardware cluster recognition algorithm has been developed. The logic is based on two thresholds: a low threshold LT and a high threshold HT. The HT works as a cluster initiator or seed, and a cluster is only built if there is at least one stack above the HT. Neighbouring stacks above the LT contribute to the trigger energy sum. The LT is set to 3–4 σ above the noise level. From Monte Carlo studies [53] it could be deduced that the HT should be set to 30–40% of the electron energy that one wants to trigger on. This means that with a HT = 3 GeV, one will trigger on $E > 10$ GeV with an efficiency close to 100%.

The BSET trigger has been used with three preset thresholds for the cluster energy sum: 4, 7 and 15 GeV. Each of these values defines a trigger element (TE), labelled **CL1**, **CL2** and **CL3** respectively. The CL2 trigger element is the most suitable for the analysis of low Q^2 DIS events, since dedicated studies [53] have shown that it is 100% efficient for electrons with $E > 10$ GeV. For 8–10 GeV electrons the efficiency is still > 90%. The CL1 trigger suffers from much higher background rates, while the efficiency of CL3 is too low, and the high y region, where interesting new physics is expected, is not covered by this trigger. Figure 5.1 shows the efficiencies of the CL1, CL2 and CL3 triggers as a function of the energy [53]. The CL2 trigger will be a basic DIS event selection criterion in this analysis.

The trigger efficiency can be strongly affected by the energy leakage out of the detector. Leakage problems arise close to the beam pipe at angles above 173°, the boundary between the inner triangular stacks and the quadratic stacks, where the electrons hit the BEMC near the edge and where a part of the energy is lost due to the transversal size of the shower. Due to the triangular shape of the innermost BEMC stacks, the energy losses are also dependent on the azimuthal angle ϕ.

At angles smaller than 156° there is a containment problem, because the BEMC depth seen by the traversing particle is not sufficient for full containment. Since the BEMC geometry is not projective, side energy losses are also important at those angles.

Other areas where some fraction of the energy is lost, even in the good angular region, are the spaces between the BEMC stacks, called *cracks*. These cracks will require larger energy corrections, up to 20%, than other parts of the BEMC, where the corrections are only a few percent (see section 5.8).

5.3 Run selection

Before we describe the DIS event selection in detail in the next section, we need to define which data samples will be used. To measure the relevant kinematical quantities of DIS events, we will use various subdetectors of H1, such as the BEMC, the BPC, the trackers, etc. We will therefore accept only runs in which the subdetectors relevant to our analysis were simultaneously operational. In addition to this we use more criteria to select runs, a complete description of which is given here:

Leptons: Only runs with **positron-proton** beams were used. The electron-proton data only represent 20% of the 1994 data, and was taken in the beginning of the run period, when the beam and detector conditions were less stable.

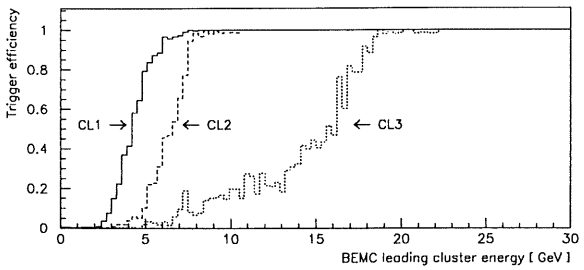

Figure 5.1: **Efficiency of the CL1, CL2 and CL3 BEMC triggers.**

Run phase: there are four run taking phases, which differ in the trigger prescaling factors that were set. Phases 1 to 2 are characterised by high trigger rates, during or shortly after the period of injection when the beam is not completely stable yet. Phases 3 and 4 are for stable beam conditions, phase 3 having higher trigger reduction rates than phase 4. In this analysis only runs belonging to **phases 3 and 4** are used.

High voltage: The high-voltage state of all the subdetectors is continuously monitored. To guarantee stable conditions, only runs were taken in which $\geq$**80%** of the time the following detectors were simultaneously under tension: the BEMC, the BPC, the MWPCs, the LAr, the ToF, the CJC. All these detector parts were used in the event selection. This selection rejects only 0.4% of the data sample.

Run period: In this analysis only data with a z-vertex around the nominal interaction point (see table 5.1) is used, and runs with a displaced ('shifted') interaction point at $z = 68$ cm are not included.

Due to hardware problems in the central tracker, only runs after run 87568 are selected.

Events per luminosity: The number of accepted events (see section 5.4) per luminosity ('yield') was checked to be constant and is shown in figure 5.2. Runs with a yield more than five standard deviations away from the average are rejected.

Trigger conditions The main trigger for low Q^2 DIS events is based on the BEMC calorimeter and is called BSET (BEMC Single Electron Trigger) (see section 5.2). Runs in which this trigger is downscaled are excluded from this analysis.

Two periods of different data-taking conditions must be distinguished in the 1994 HERA positron data:

1. The *closed triangle data*, in which the inner triangular stacks of the BEMC were excluded from the BEMC energy trigger. This is the experimental situation of the data of 1993, and since this limits the angular acceptance range to approximately $\theta_e \leq 173°$, only Q^2 to values above approximately 10 GeV^2 can be measured.

The integrated luminosity of this sample is 1267.8 nb^{-1}, which corresponds roughly to 1.75×10^6 events.

2. The *opened triangle data*, in which the inner triangular stacks of the BEMC were included into the BEMC energy trigger. This data allows to reach lower angles (approximately $\theta_e \leq 174°$ of the scattered electron, and therefore lower values of Q^2 ($Q^2 > 5$ GeV^2). The integrated luminosity of this sample is 265.7 nb^{-1} (approximately 360000 events), about five times less than the closed triangle sample. The calibration of the inner triangles will be given special attention in section 5.8.

In this analysis both data samples will be used to measure F_2. The BEMC triangular stacks are close to the BEMC pipe, and have never before been included in a measurement. Therefore, the opened triangle data allows for the first time to measure down to lower values of Q^2, but offers less statistics than the closed triangle data. Because of this, we can consider the closed triangle data as a consistency check for the opened triangle data, in the part of the kinematical domain where they overlap.

As explained in 2.2.6 the luminosity of the selected runs was determined from the cross-section of the Bethe-Heitler reaction $ep \longrightarrow ep\gamma$ [54]. The luminosity of the selected runs was found to be equal to:

	L [nb^{-1}]	δL [nb^{-1}]
Opened triangles	265.7	4.8
Closed triangles	1267.8	22.8

The sources of the errors of the luminosity measurement were already given in section 2.2.6.

5.4 Event selection

Figure 5.3 shows a typical DIS event in the H1 detector. To measure the kinematical quantities of the events, we will use the BEMC for the energy of the scattered electron, and the combination of the reconstructed z-vertex and BPC impact point (tracking detectors) for the angle. Alternatively we will also use the LAr calorimeter to calculate the quantities necessary for the Σ method. The tracker information will also be used to calculate the hadron jet angle θ_h, which we will use to measure the energy resolution of the BEMC and to check its calibration.

The event selection can be divided into the following categories: 1. kinematical cuts, 2. electron identification and background rejection, 3. event vertex requirement. Some cuts will depend on the method with which the kinematical variables are reconstructed. A summary of all the cuts is given in table 5.2, and we will describe them in detail in the sections below.

5.4.1 Kinematic cuts

Figure 5.4 shows the energy distribution of the scattered electron in the BEMC, before any cuts were applied. The peak at lower energies is due to quasi real photoproduction processes, which, as already explained in 4.7, are an important background to DIS at those

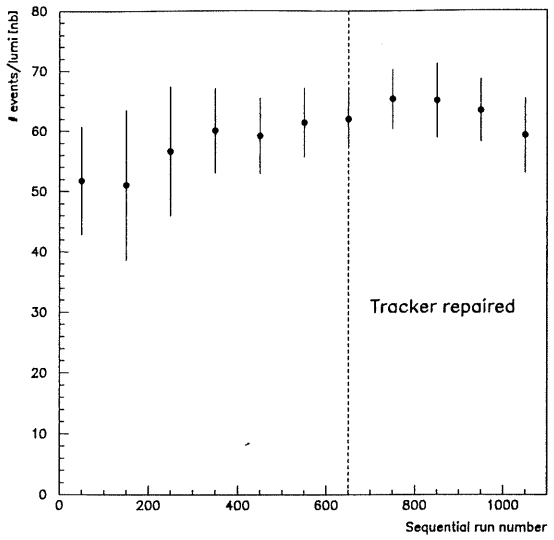

Figure 5.2: **The event per luminosity ratio of the selected runs.**
The yield value is averaged over 100 consecutive selected runs, and the error bar shows one standard deviation of the yield for this average. This figure also includes the runs before the trackers were repaired, although data of these runs was discarded in this analysis.

energies. To keep this background down to tolerable levels, we will introduce an energy cut of $E \geq 11$ GeV. This cut will also ensure that the BSET CL2 trigger efficiency is nearly 100% (figure 5.1). Further cuts to reduce the photoproduction background will be described in a next section and the remaining photoproduction will be estimated and subtracted statistically (see 5.5.2).

Another important kinematic cut is the cut on the maximum electron scattering angle, which ensures that the scattered electron stays within the fiducial volume of the BEMC. In this analysis we demand that the maximum electron scattering angle is 173° for the closed triangle data and 174° for the opened triangle data.

Finally, we will introduce a cut on y_e. In section 4.4 we already pointed out that what the limitations are of the electron and the sigma methods. The electron method allows measurements up to high y, only limited by the increasing radiative corrections and to a lesser extend the photoproduction background. For the E method we therefore require $y_e \leq 0.6$, above which the radiative corrections would exceed 100% in some bins. The sigma method is less good at very high y, and we require $y_\Sigma \leq 0.5$, since above thia value the hadronic particles start entering the BEMC, which does not allow to measure the energy of hadronic showers.

On the low y side the electron method is also limited, since the precision of the x measurement degrades as $1/y_e$ (see equation (4.18)). We therefore demand that $y_e \geq 0.05$, below which the resolution of $\delta x_e/x_e < 2$, would exceed 30%. For the Σ method one can go down to $y_e \geq 0.02$, still guaranteeing that the resolution of x_Σ stays below 30%.

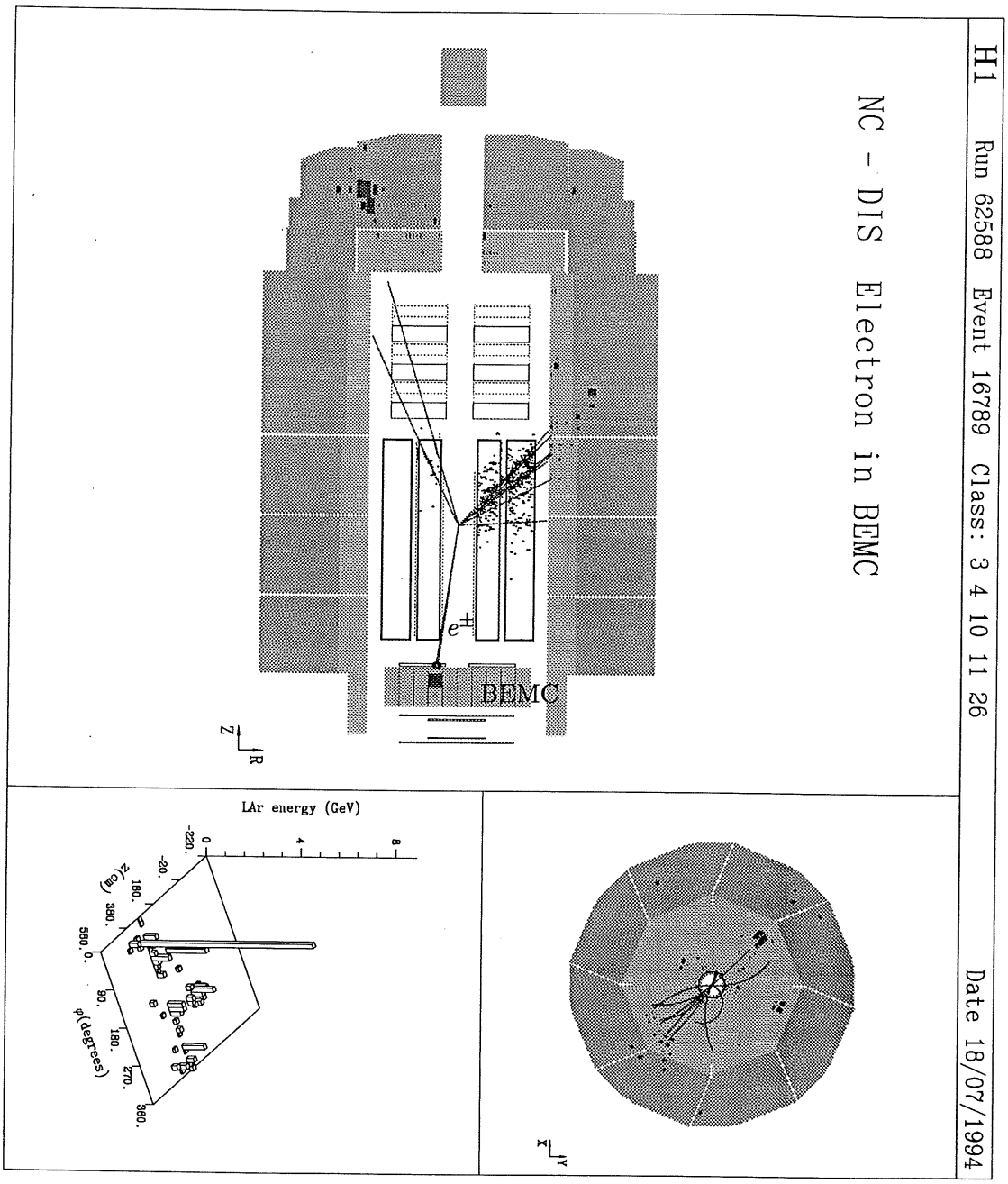

Figure 5.3: **A typical NC DIS event at $Q^2 = 20$ GeV in the H1 detector.** *The energy deposition of the scattered electron is visible in the BEMC. The angle is precisily measured from the reconstructed BPC hits and the z-vertex position.*

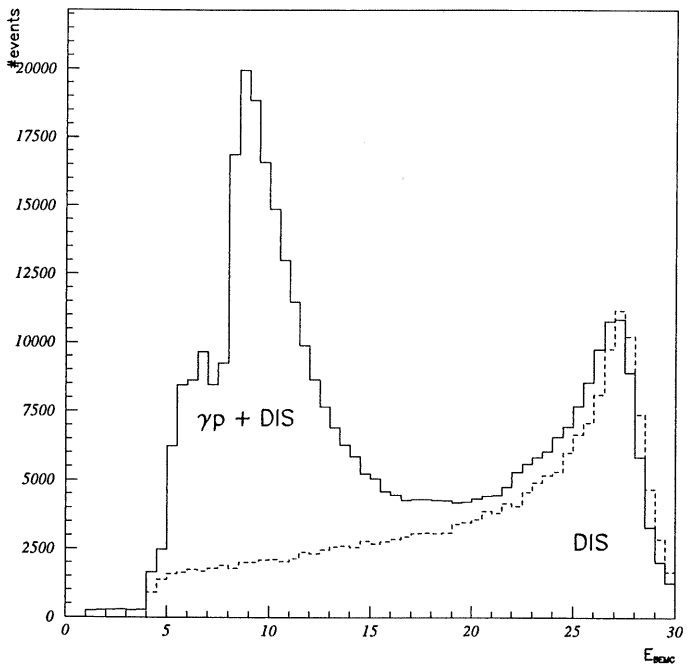

Figure 5.4: **Distribution of the energy of the scattered electron before cuts.** *The peak in the data at low energies consists mainly of photoproduction background events. The full histogram represents the H1 events, the dashed line is the Monte Carlo (normalised to the kinematic peak).*

Run end	z_0 [cm]	σz_0 [cm]
76344	0.000	11.000
78380	-0.900	10.800
82005	0.200	10.600
82960	0.200	10.600
83819	4.200	10.600
84040	7.400	10.400
84600	3.000	10.900
85300	1.800	12.100
86000	-3.500	10.300
86750	3.300	10.400
89468	5.700	10.400
89928	3.800	10.600
90003	65.900	10.000
90026	70.200	10.000
90419	5.200	10.100

Table 5.1: **H1 database lookup table of the nominal z-vertex for H1 run ranges.**
The nominal z-vertex position depends slightly on the run. The run range of the shifted z-vertex position $\simeq$ 70 cm can be clearly identified. Due to hardware problems in the central tracker, only runs after run 87568 are selected for this analysis.

5.4.2 Electron identification and background rejection

We will identify the scattered electron as the most energetic cluster in the BEMC. This is a good criterion for our analysis, since in figure 5.5 one can see that in the Monte Carlo and for $E \geq 11$ GeV, the probability that the scattered electron is not the highest energy cluster is smaller than 0.1%.

As we already pointed out in chapter 4, the photoproduction background events to DIS are characterised by neutral and charged hadronic particles entering the BEMC (see also [56]). The showers that they produce may mimic the signature of a scattered DIS electron. There are two ways by which a considerable fraction of such fake events can be rejected: the first relies on the fact that these showers are not always accompanied by a matching BPC hit, since charged partcles should always be detected by the BPC. The second method is based on the fact that hadronic showers in the BEMC have typically a larger opening angle than electron showers. Unfortunately, photoproduction events with a π^0 in the hadronic shower will not be rejected by either method, since π^0 particles will decay into e^+e^- before they even hit the BPC and BEMC. Also photoproduction events with a $\gamma + \pi^{\pm}$ will not be rejected with the above methods. According to the photoproduction Monte Carlo study of the previous chapter, about 50% of the photoproduction events are of the type $\gamma + \pi^{\pm}$ or π^0. Nevertheless, we will define two criteria based on the principles we just described.

BPC impact points are reconstructed at $z = -141.5$ cm (BPC plane), while showers in the BEMC reach their maximum approximately 15 cm further at $z \approx$ -156 cm. By using

Basic cuts	
1.	11 GeV $\leq E \leq$ 30 GeV
2.	$\lvert z_{vertex} - z_0 \rvert \leq 30$ cm
3.	DCLBP ≤ 3.5 cm
4.	ECRA ≤ 5 cm
5.	$\sigma z_{vertex} \leq 6$ cm
6.	BSET CL2 triggered
Method-dependent cuts	
'E' MC method, closed Δ	
7.	$\theta_e \leq 173°$
8.	$0.05 \leq y_e \leq 0.6$
'E' MC method, opened Δ	
7.	$\theta_e \leq 174°$
8.	$0.05 \leq y_e \leq 0.6$
'Σ' MC method, closed Δ	
7.	$\theta_e \leq 173°$
8.	$0.02 \leq y_\Sigma \leq 0.5$
'Σ' MC method, opened Δ	
7.	$\theta_e \leq 174°$
8.	$0.02 \leq y_\Sigma \leq 0.5$

Table 5.2: **Summary of the DIS event selection for the E and Σ methods and event samples.**
The z_0 of the interaction point is run dependent, and varies between -5 cm and +6 cm. For every run, the correct value of z_0 was obtained from table 5.1.

the reconstructed z-vertex position (see next section), the (x, y)-position of the cluster is projected onto the BPC plane, and the distance between this point and the closest reconstructed BPC point is called DCLBP (*Distance CLuster-BPc*). This distance can be used to veto a fraction of the photoproduction background, as shown in figure 5.6a, which shows the distribution of DCLBP for Monte Carlo DIS (DJANGO) and Monte Carlo photoproduction (PYTHIA+RAYVDM, see chapter 4) events. One observes clearly that the DCLBP distribution for DIS events falls rapidly after a couple of cm, while the distribution for photoproduction events is much flatter. From this plot one may conclude that a cut on DCLBP rejects a part of the photoproduction, without loosing a significant part of the DIS data. In our analysis we will require that DCLBP ≤ 3.5 cm. According to Monte Carlo, this implies a loss of 9.0% of good DIS events. (A cut at 5 cm would mean a loss of 7.7% of good events.)

Figure 5.7a shows the DCLBP distribution DJANGO events together with the H1 data events before any cuts. This confirms that DCLBP is a useful criterion to reject photoproduction events. In section 5.11 we shall see that even after all the event selection cuts the DCLBP distributions of data and Monte Carlo still disagree, which will be discussed later. However, this disagreement does not invalidate the DCLBP's usefulness as a selection criterion.

An additional benefit of a reconstructed BPC point near the cluster is an improved θ_e measurement. As we will see later in 5.9.1 the intrisic resolution from the BPC impact point measurement is 1.5 mm, while because of the large size (16×16 cm) of the BEMC stacks compared to the typical Molière radius of an electromagnetic cluster in the BEMC, the precision of the centre of gravity of the measured cluster is only $\simeq$1.3 cm. Together with the reconstructed z-vertex position (next section), the BPC impact point will be used to determine the angle θ_e of the scattered electron.

The second electron selection requirement is based on the energy-weighted lateral cluster radius 'ECRA' (*Energy Cluster RAdius*), defined as:

$$ECRA = \frac{1}{E_{cluster}} \sum_{i=1}^{n} E_i \times |r_i - r_{cog}|, \tag{5.1}$$

where $E_{cluster}$ is the total energy of the cluster, n is the number of stacks in the cluster (because of the cluster algorithm this is usually 9), $r_i = (x_i, y_i)$ is the centre of stack i, and $r_{cog} = (x_{cog}, y_{cog})$ the centre of gravity of the cluster, given by:

$$x_{cog} = \frac{1}{E_{cluster}} \sum_{i=1}^{n} E_i \, x_i, \tag{5.2}$$

$$y_{cog} = \frac{1}{E_{cluster}} \sum_{i=1}^{n} E_i \, y_i. \tag{5.3}$$

Electromagnetic particles in the BEMC are observed as clusters with a typical radius of at most 5 cm, while clusters initiated by hadrons have larger radii, as shown in figure 5.6b. Similarly to the DCLBP cut, we can use ECRA to reject a part of the photoproduction background, without loosing a significant part of the DIS data. In this analysis, we demand that ECRA$\leq$ 5 cm, which, according to Monte Carlo, means a loss of 3.0% of good DIS events. Figure 5.7b shows the comparison of DJANGO events and H1 data before any cuts, and this confirms the validity of the selection criterion.

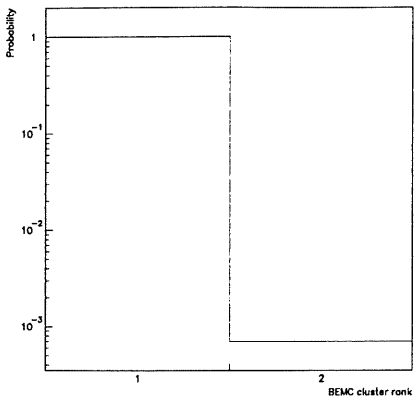

Figure 5.5: **Probability that the first and second most energetic BEMC clusters correspond to the scattered electron in the event generator.**
"1" stands for the most energetic cluster, "2" for the second most energetic cluster in the BEMC. The probability that the second most energetic BEMC cluster corresponds to the scattered electron is negligable. [from Monte Carlo, for events with $E \geq 11$ GeV]

The DCLBP and ECRA selection cuts only reject a fraction of the photoproduction background. The remaining background will be estimated in section 5.5.2, and will later be statistically subtracted from the number of selected events.

5.4.3 Event vertex

Together with the reconstructed BPC impact point near the BEMC cluster, the reconstructed interaction vertex is needed to calculate the angle of the scattered electron. A good measurement of this angle is necessary for a precise determination of the kinematics with the electron method. The vertex is defined by fitting the reconstructed tracks to a common vertex.

Additionally, the requirement of a reconstructed interaction vertex within a certain boundary around the interaction point is necessary to reject remaining background events (beam gas and beam wall interactions outside the interaction region, beam halo and cosmic particles). Most of these events are rejected by the time of flight detector (ToF), which has an efficiency between 99% and 100%. Since the number of the background events is two orders of magnitude larger than the number of DIS events, a non-negigable quantity of background events is present in the selected sample. As we pointed out the section 4.8, pilot bunch events are tagged background events and can be used to estimate the total number of background events. In the next section (5.5.1) we will use the pilot bunch events to measure the remaining number of background events after all the event selections. Figure 5.8 shows the z-vertex distributions of all the events and of the pilot bunch events only. Since the ratio of colliding bunches and pilot bunches is approximately ten (see next section), the total number of background events is a factor of ten larger than the number of the pilot bunch events. The background events show a much broader z-vertex distribution, indicating that a z-vertex cut is a strong rejection criterion for background. Requiring a

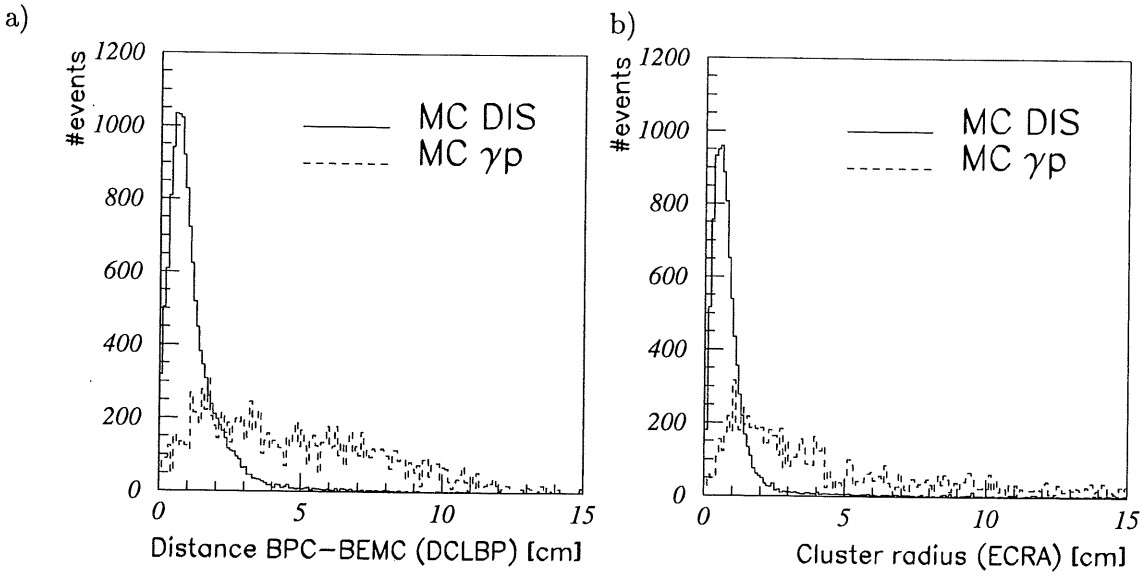

Figure 5.6: **Photoproduction rejection cuts.**
(a) Distribution of the distance of the most energetic BEMC cluster and the closest BPC point (DCLBP) for DJANGO DIS events and MC photoproduction events according to section 4.7, and (b) distribution of the BEMC cluster radius (ECRA) for the same event sets. According to Monte Carlo, both DCLBP and ECRA are larger for photoproduction events than for DIS events.

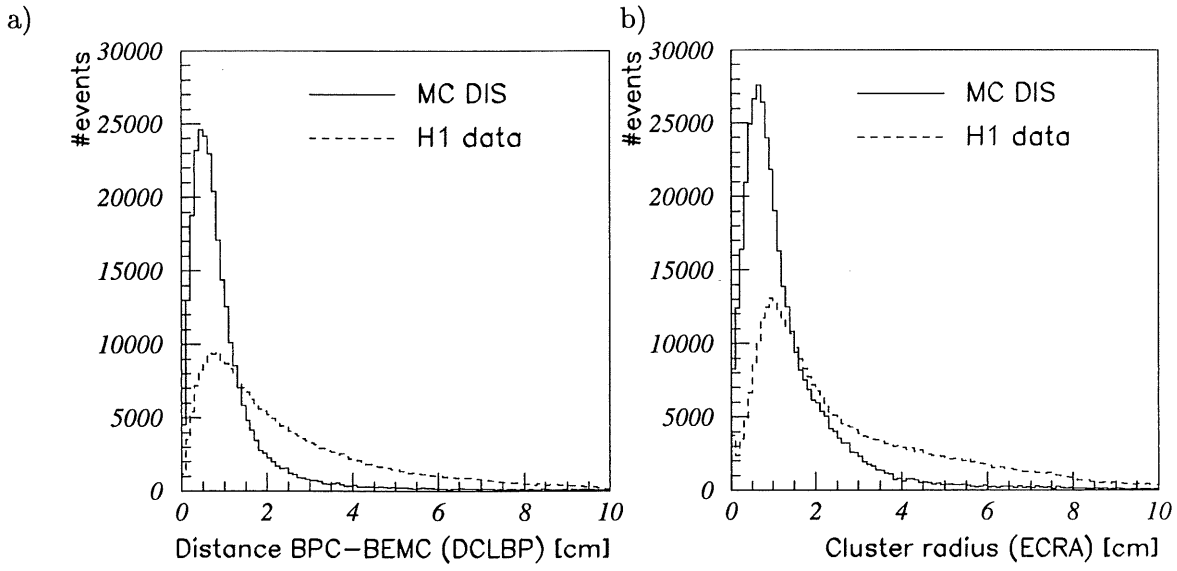

Figure 5.7: **DCLBP and ECRA distributions in H1 data and DJANGO.** *(a) Distribution of the distance of the most energetic BEMC cluster and the closest BPC point (DCLBP) for H1 data and DJANGO events before any cuts, and (b) distribution of the BEMC cluster radius (ECRA) for the same event sets.*

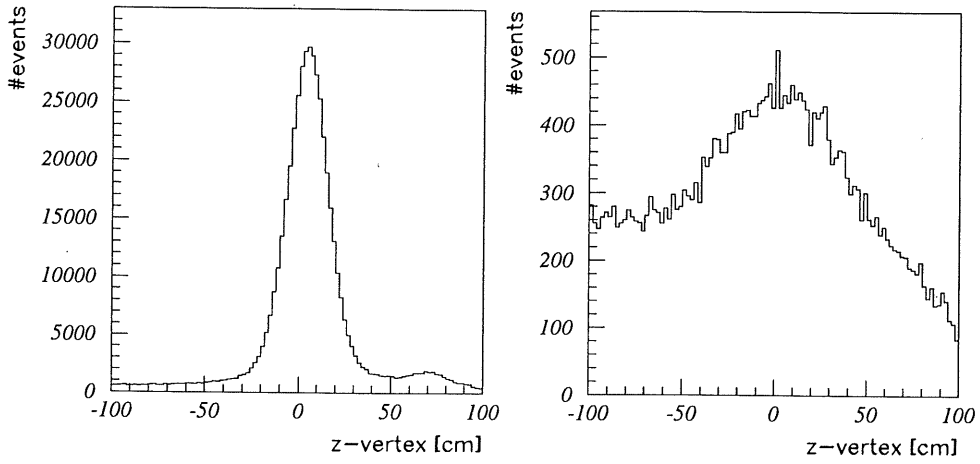

Figure 5.8: **Distribution of the z-vertex for the low Q^2 data before event selection.**
The plot on the left shows all the events, the plot on the right shows pilot events. These pilot events are a fraction of the beam-gas or beam-wall events (see section 5.5.1).

z-vertex of $\pm$ 30 cm around the nominal vertex position reduces the total number of events by 34%

This vertex requirement is also necessary to exclude events caused by bunches of protons which are out of time by approximately 20, 40 and 60 ns, corresponding to the 52 MHz RF field of HERA. These bunches are called *satellite* bunches and they show up in the z-vertex distribution around $z \approx 70$ cm (figure 5.8 and also 5.34). By requiring that that the z-position of the reconstructed interaction vertex lies $\pm$30 cm around the nominal beam interaction point, this background is reduced below the 0.1% level. The nominal interaction point is slightly run dependent and is listed in table 5.1.

It was found that events with a reconstructed vertex which was only composed of forward tracks, contained a higher amount of beam-gas and beam-wall background, up to 5% in some kinematic bins. When only events with a vertex from at least one central track are selected, the background is never larger than 1–2% (see section 5.5.1). Forward tracks are on the other hand useful for the low y region, since with decreasing y the hadronic particles are emitted at smaller polar angles. In figure 5.9 one can see the fraction of forward vertices (i.e. vertices reconstructed with forward tracks only) as a function of y_e, before and after the beam-gas and beam-wall background was statistically subtracted. For events with $y_e > 0.2$ the fraction of forward vertices is about 2% in both the data as well as in the Monte Carlo. For events with $y_e > 0.2$ the background induces extra forward vertices and it was decided to reject events with a vertex consisting of only forward tracks for this y range.

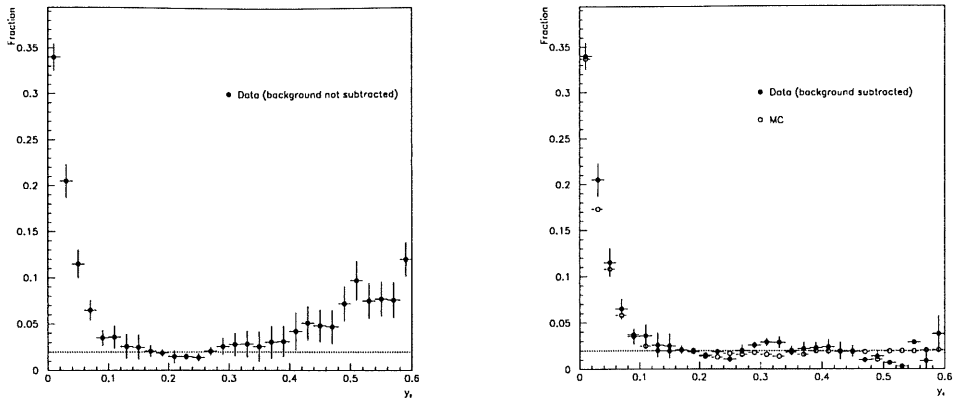

Figure 5.9: **Fraction of forward vertices as a function of y_e.**
The plot on the left shows the fraction of events with forward vertices (i.e. reconstructed from forward tracks only) before the beam-gas and beam-wall background is subtracted. The plot on the right shows the fraction after the background is statistically subtracted by means of the pilot bunches. For $y_e < 0.2$ the background does not lead to a higher fraction of forward vertices.

The distribution of the error on the reconstructed z-vertex is shown in figure 5.10, and the Monte Carlo agrees well with the data. More than 99% of the events have a z-vertex with an error less than 1 cm. To reject events with an badly reconstructed z-vertex, a cut of $\sigma z < 6$ cm, corresponding to one standard deviation of the z-vertex distribution, was introduced, which limits the uncertainly on θ to 5–10 mrad, depending on R_{BPC}.

The distribution of the reconstructed z-vertex after all the cuts (including the vertex cut) is shown in figure 5.11 together with the Monte Carlo, and shows good agreement.

5.5 Background estimation

After the event selection cuts of the previous sections, there are still background events in the final data sample. As explained in chapter 4, one can distinguish non-*ep* background and photoproduction background. In this section we will estimate the fraction of the remaining background for both types, and this fraction will be statistically substracted from the final number of selected events.

5.5.1 Non-*ep* background

In section 4.8 the beam-gas and beam-wall background was already introduced, together with the pilot bunches, which are a valuable tool to estimate this background. Since the DIS events are only selected from colliding bunches, equation (4.55) can be used to estimate the background in the final sample. However, in the data of 1994 it was found that also bunches with no positrons or protons could contribute to the event sample. These *empty* bunches are defined as $I_e < 2$ μA and $I_p < 4$ μA. The precise nature of

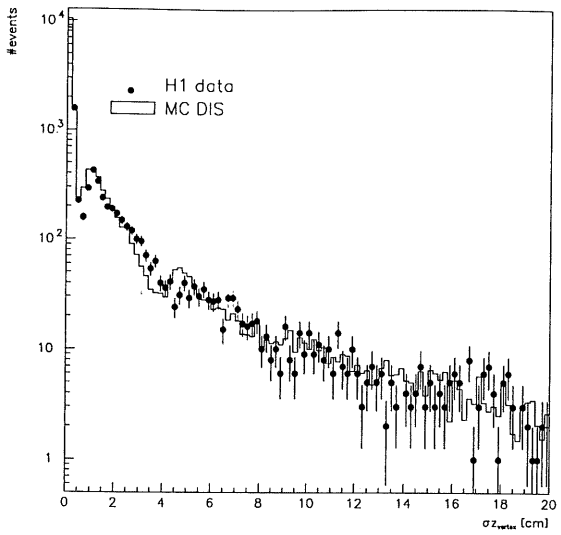

Figure 5.10: **Error of the z-vertex position.**
The error of the z-vertex position is well described by the Monte Carlo. One of the criteria for good DIS events is $\sigma z \leq 6$ cm.
The peak at $\sigma z < 0.5$ cm corresponds to tracks with at least one CIZ or COZ hit, which significantly improves the precision of the θ measurement of the track. Events with $\sigma z > 1$ cm correspond to tracks with no CIZ or COZ hits.

	empty bunch	**p-pilot**	**e-pilot**
number of bunches ratio	4.4	9.1	10.5
ratio of bunch currents	-	11.2	11.3

Table 5.3: **Ratios of the number and current of pilot and empty bunches.**

these bunches is unclear, but they are believed to consist of residual particles of which the current could not be measured because they are outside the time window in which the current measurement takes place. Empty bunches are uniformly distributed over the maximum available bunches. The number of pilot and empty bunches in the final data sample can be used to estimate the remaining background by using equation (5.4), a modified version of equation (4.55):

$$n_{bg} = N_{p-pilot} \times \frac{n_{colliding}}{n_{p-pilot}} + N_{e-pilot} \times \frac{n_{colliding}}{n_{e-pilot}} + N_{empty} \times \frac{n_{empty}}{n_{colliding}}. \qquad (5.4)$$

In this formula $N_{p-pilot}$, $N_{e-pilot}$ and N_{empty} represent the number of observed p-pilot, e-pilot and empty events respectively, and $n_{p-pilot}$, $n_{e-pilot}$, n_{empty} the number of these bunches in the beam. The estimated background is then statistically subtracted in each bin. The ratios of the bunches are listed in table 5.3. These values are comparable to the ratios of the currents (except for the empty bunches, where the measured current is close to zero).

To avoid double counting of the contribution of empty bunches to the pilot bunches in

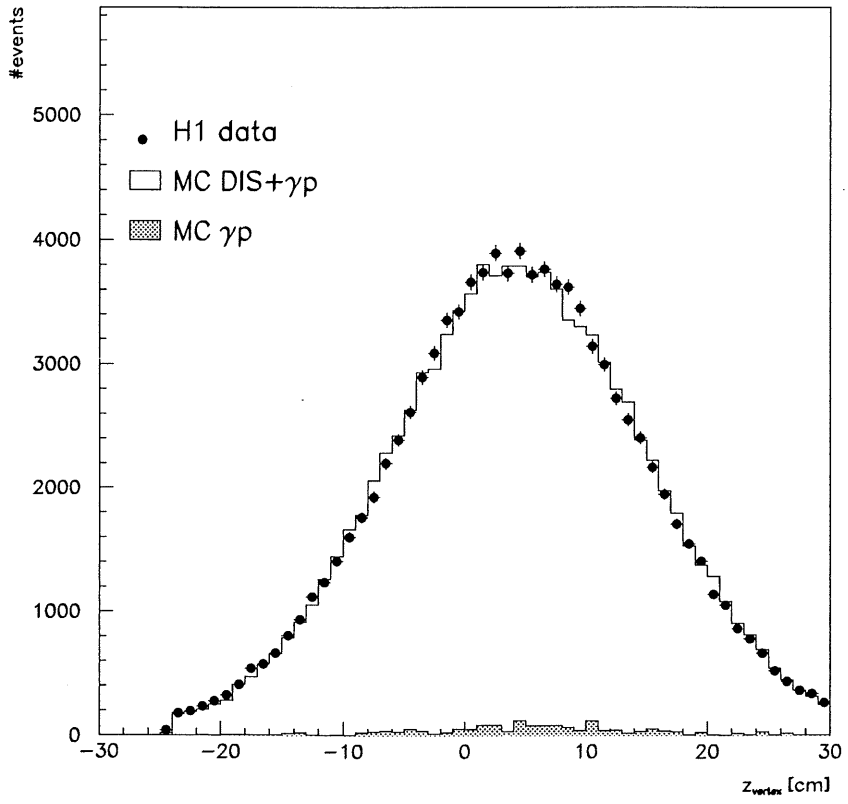

Figure 5.11: **Distribution of the z-vertex for the low Q^2 data.**
The H1 data is represented by closed circles, the Monte Carlo simulation by the open histogram. The Monte Carlo calculation is normalised to the luminosity. The hatched histogram is the estimation of the background due to photoproduction processes, see later section 5.5. (Opened triangle data)

equation (5.4), we can use the following formula:

$$\begin{aligned} n_{bg} &= \psi\left(N_{p-pilot} - N_{empty}\frac{n_{p-pilot}}{n_{empty}}\right) \times \frac{n_{colliding}}{n_{p-pilot}} \\ &+ \psi\left(N_{e-pilot} - N_{empty}\frac{n_{e-pilot}}{n_{empty}}\right) \times \frac{n_{colliding}}{n_{e-pilot}} \\ &+ N_{empty}\frac{n_{colliding}}{n_{empty}}, \end{aligned} \tag{5.5}$$

with

$$\psi(x) = \begin{cases} 0, & \text{if } x \leq 0 \\ x, & \text{if } x > 0 \end{cases} \tag{5.6}$$

Both equations (4.55) and (5.4) result in estimations of the background, which differ less than 0.5%. This difference is negligable for our measurement of F_2. After all the event selection cuts, the remaining background is estimated to be less than 1% in 95% of the bins, and less than 2% in the remaining bins. This estimated background (column $frac(bg)$) for the E and Σ methods of reconstructing the kinematical variables is included in tables A.3, A.4, A.7, A.8, A.11, A.12, A.16, A.17 and A.18, and is statistically subtracted from every bin.

5.5.2 Photoproduction background

In section 5.4.2 we introduced a minimum energy cut ($E > 11$ GeV), a cut on the lateral cluster radius (ECRA$<$ 5 cm) and the cut on the distance BPC-BEMC cluster (DCLBP $<$ 3.5 cm), to reduce the photoproduction background in the event sample and the remaining photoproduction is estimated by means of a Monte Carlo study. More than 1.5 million photoproduction events were simulated, corresponding to the luminosity of the data (see section 4.7). This number had to be so large to obtain a statistically representative sample, because despite the high cross section of photoproduction processes, less than 0.1% fake an electron candidate in the BEMC. Only a few hundred events survive all the DIS selection cuts and mimic a DIS event.

This large number of generated events implies a heavy load on the available CPU-time, because a complete H1SIM-simulation of an event is very time-consuming. To speed up the simulation phase, a *turbo simulation* method [76] was developped. In this method, the backward part of the detector (BEMC and BPC) was simulated first, and only events with a potential 'fake' electron candidate were kept for further simulation. The number of generated and simulated events can be seen in table 4.1. A factor of 140 was saved in CPU-time by using the turbo simulation.

Figure 5.12 shows the energy and the angle of the fake electron detected in the BEMC for photoproduction events, compared to the simulation. Since only a small fraction (typically 10%) of the photoproduction events in the sample are identified by means of the electron tagger, this detection efficiency was taken into account to produce this plot. The discrepancies visible on this plot (up to 30%) have a negligible influence on the calculation of the final number of DIS events, i.e. smaller than 2.5%.

Tables A.3, A.4, A.7, A.8, A.11, A.12, A.16, A.17 and A.18, list the photoproduction estimation (column $frac(\gamma p)$) for the E and Σ methods. Only in 6 bins, out of a total of

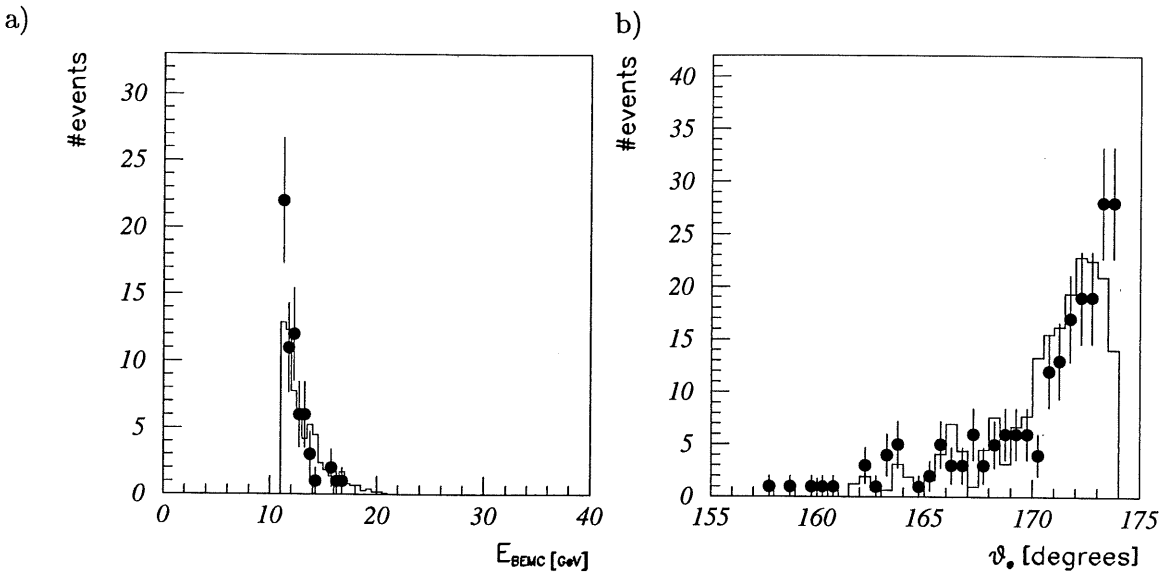

Figure 5.12: **Energy and angle of the identified ('fake') scattered electron for tagged events.**
a) Energy in BEMC of the fake electron, b) angle of the fake electron. The dots represent the H1 events of which the real scattered electron was detected by the electron tagger, corrected for the efficiency of this tagger. The open histogram is the prediction from the photoproduction Monte Carlo (section 4.7).

79 bins, the photoproduction background was estimated to represent more than 3% of the number of selected events. The contamination is the highest in the high y, low Q^2 bins, but never exceeds more than 8% in any bin. On several plots of kinematical distributions in this document we will indicate the estimated photoproduction background as a hatched area (for example figure 5.11).

5.6 Number of DIS events

The number of selected DIS events (N_{DATA}) for every method in this analysis and in all the kinematic bins are listed in tables A.3, A.4, A.7, A.8, A.11, A.12, A.16, A.17 and A.18. These values are already statistically corrected for the estimated beam-gas and γp backgrounds. The amounts of subtracted beam-gas and photoproduction background are also separately included in the tables (columns $frac(bg)$ and $frac(\gamma p)$). The distribution of selected events in the x, Q^2 plane are shown in figure 5.13. One can distinguish the opened and closed triangle events. The former extend the measurement to lower values of Q^2 (5 GeV instead of 10 GeV for the closed triangle data).

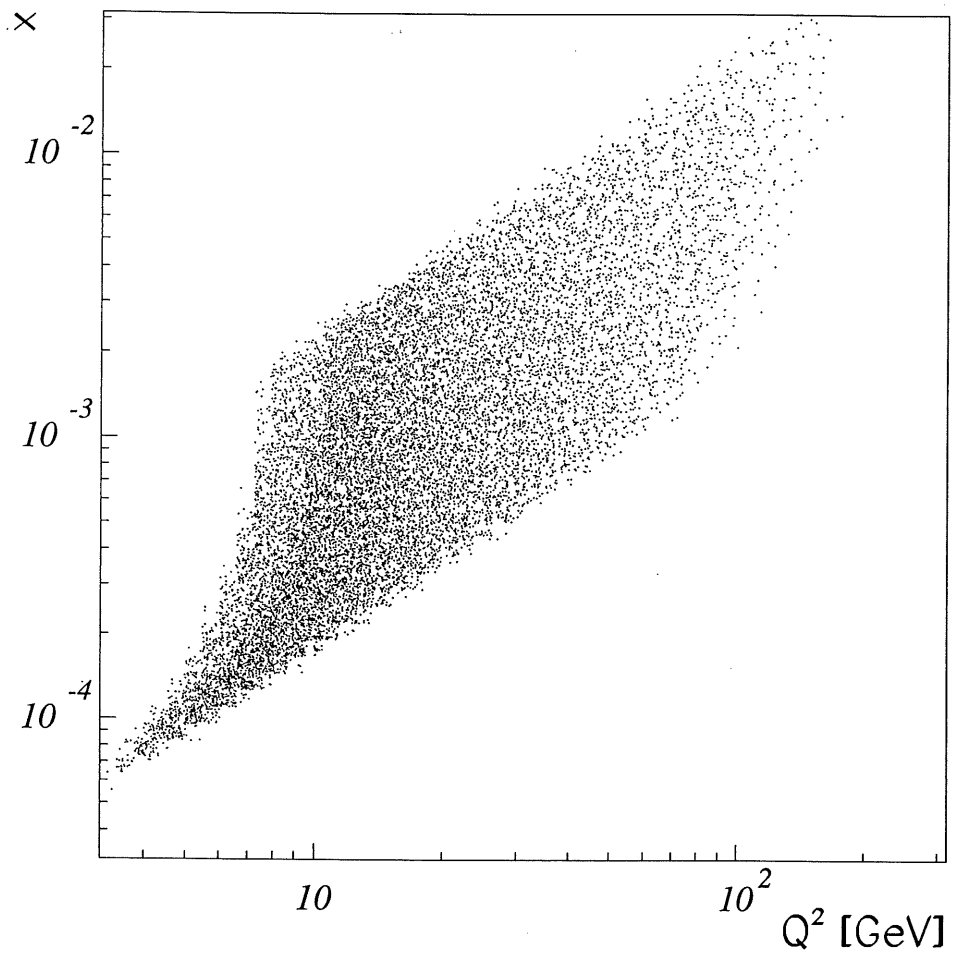

Figure 5.13: **Distribution of the selected events in the kinematic x, Q^2 plane.** *Both the opened and closed triangle data samples are superimposed. In most of the kinematic plan both samples overlap, except in a narrow band at low Q^2, where the opened triangle events extend the measurement towards smaller values of Q^2 and x (this is the area where the distribution of the scatterpoints is a little less dense).*

5.7 Monte Carlo simulation

Almost half a million of DIS events, corresponding to an integrated luminosity of approximately 9.2 pb^{-1} have been generated with the DJANGO [35] program, using the GRV [55] parton distribution parametrisation. The events were weighted according to Q^2 for values down to $Q^2 < 100$ GeV^2 ($w = 100/Q^2$) and unweighted above that. The number of generated events is sufficiently large to get statistical errors below the percent level with the chosen binning. The DJANGO program is based on HERACLES [4] for the electromagnetic interactions and on LEPTO [34] for the hadronic final state. The detector response was simulated in detail with the GEANT program [27]. After the simulation step, the Monte Carlo data was reconstructed and passed through the same analysis chain as the real data. DJANGO is known not to give a proper description of events with a hadronic invariant mass below $W < 4$ GeV, and therefore events with W below this value were rejected.

The Monte Carlo which was used does not include all the features of the real data:

1. The mean z-vertex position of the data is run dependent and varied between -4 cm and +7 cm, while the z-vertex of the Monte Carlo was at -5.8 cm. Therefore the Monte Carlo data was reweighted with weight:

$$w_{zv} = \frac{z_{vertex}^{data}(x, Q^2)}{z_{vertex}^{MC}(x, Q^2)}, \tag{5.7}$$

   where z_{vertex}^{data} was obtained as a function of the run number from a lookup table 5.1 in the H1 database. The values in table 5.1 were compared to the reconstructed z-vertex position with the trackers, and the agreement was found to be better than 0.5 cm. These small deviations have a negligable influence on the θ_e measurement. The reweighted z_{vertex}^{MC} and the z_{vertex}^{data} are shown in figure 5.11.

2. Already in 1993 H1 observed that the F_2 obtained from the GRV structure function parametrisation, which was used in the Monte Carlo, increases more quickly at low x than the F_2 of the data [41]. This influences the z-vertex efficiency at higher electron energies. To compensate for this, the Monte Carlo data is also reweighted with the MRSH parametrisation obtained by an analysis of the H1 data of 1993 [41]. The weight is then

$$w_{param} = \frac{F_2^{MRSH}(x, Q^2)}{F_2^{GRV}(x, Q^2)}. \tag{5.8}$$

Both in equations (5.7) and (5.8) the variables x and Q^2 have been calculated from the hadronic vertex, to be independent from possible radiative corrections.

5.8 Energy calibration and resolution

5.8.1 Introduction

Since in this analysis we will only use the data where the scattered electron enters the BEMC, the calibration and resolution of this detector deserves special attention. In particular when using the electron (E) method, the influence of the energy measurement on the Q_e^2 error is proportional to E over the whole kinematic domain (section 4.3).

In this analysis we will also use the Σ method to calculate the kinematical quantities. In section 4.3 we already pointed out that the Σ method is complementary to the electron method and is more suitable for measurements at low y. We will estimate the resolution of y_Σ later in section 5.10.

5.8.2 The resolution of the BEMC

The resolution of the BEMC can be parametrised as follows:

$$\frac{\sigma}{E} = \frac{\sigma_{noise}}{E} \oplus \frac{\sigma_{sampling}}{\sqrt{E}} \oplus \sigma_{constant}. \tag{5.9}$$

The DESY and CERN test beam measurements resulted in $\sigma_{noise} = 97$ MeV and $\sigma_{constant} = 11.0\%$ [47]. However, the BEMC preamplifiers which are used in these measurements were different from those which were used in the data taking. The electronic noise of the latter was $\approx$130 MeV, and this leads to even higher values when one takes into account that a shower may develop in more than one BEMC module. The standard clustering algorithm combines up to 9 cells into one cluster. This leads to $\sigma_{noise} \approx 390$ MeV for the H1 data [47].

5.8.3 Calibration of the BEMC

The calibration of the BEMC has been done on several levels and with different methods. In 1990 all the BEMC modules have been calibrated with a 5 GeV electron beam in DESY. Apart from an absolute calibration, this also provided a relative calibration of the optical chains of the modules with respect to each other. In 1991, a few of the modules have been studied in an electron test beam at CERN, reaching energies from 10 GeV up to 60 GeV. The response of the modules has also been measured with a hadron and a muon beam. Because of the short absorption length of the BEMC (typically 1 λ), hadrons will most of the time behave as minimum ionizing particles and their energy is not contained in the BEMC, while electrons will deposit most of their energy in a module. The results of all those measurements have been extensively described in [47], [60] and [62].

The calibration of the BEMC can be improved and/or checked with *ep* data in two different ways: the *kinematic peak* and the *double angle* method. In this analysis, the kinematic peak method was used to calibrate the BEMC on a stack-to-stack basis (5.8.4), and the double angle method was used to verify these corrections but also to estimate the energy resolution (see section 5.8.5). The double angle method could not be used for calibration on a stack to stack basis, because the statistics was unsufficient to do so.

5.8.4 Calibration of the BEMC with the kinematic peak

The raw BEMC data (i.e. diode readings) are converted into an energy measurement by means of a lookup table. This lookup table was obtained by test beam measurements [47],[62]. This was done using a small set of stacks, in a different setup than the final BEMC. To get a more realistic reconstruction of the energy in the BEMC, an additional correction is necessary. In previous analyses this correction was obtained from a detailed Monte Carlo study [68] in 1992. This table contains an energy correction factor in (x, y), which a precision of 1 cm in each direction. For the 1994 data, this table was

replaced by another one, based on a study [19] of a special set of H1 events. In this study the *kinematic peak* was used to calibrate the BEMC.

The kinematic peak is the prominent peak around the electron beam energy in the energy spectrum of the scattered electrons at low Q^2 (see figure 5.15). This peak finds its origin in the fact that for low values of Q^2, the energy of the scattered electron does not change much over several orders of magnitude in x and the cross section of the events in this domain is large. The right flank of this peak is independent of the proton structure function, and only depends on the detector response. Therefore, the comparison of shape and position of this flank in the data and Monte Carlo can be used to estimate the BEMC resolution and correct the energy if needed.

For the 1994 data, the determination of the BEMC energy scale was based on energies between 22 and 28 GeV, taking into account stack to stack variations of the response and correcting for dead material in front of the BEMC as well as for energy losses between the stacks. The energy correction as a function of the x,y position is shown in figure 5.14 (from [19]). One notices clearly that the corrections are large in the crack regions, and are typically between 5% and 20%.

Figure 5.15 displays the distribution of the reconstructed energy E of the scattered electron for the closed triangle data sample after all the corrections, together with the Monte Carlo. This figure shows an excellent agreement between data and Monte Carlo. The energy distribution of the opened triangle sample is not shown, but is similar.

5.8.5 Estimation of the BEMC resolution and energy shift with the double angle method

In this section we will cross check the BEMC calibration with the double angle method and also estimate the BEMC resolution. Of particular interest are the *cracks*, since the corrections there are very large (figure 5.14).

The double angle method (see section 4.3) can be used to get an absolute energy calibration and an estimate of the resolution of the BEMC. The energy of the scattered electron can be calculated from:

$$E_{DA}(\theta_e, \theta_h) = \frac{E_e(1 - y_{DA})}{\sin^2 \frac{\theta_e}{2}}, \tag{5.10}$$

where y_{DA} is obtained from equation (4.26) and the hadronic angle θ_h from equation (4.24). y_{DA} depends only on θ_e and θ_h, so the latter is the relevant parameter. In figure 5.16 one can see the typical distribution of the hadronic angle θ_h for data and Monte Carlo, which are in excellent agreement.

In figure 5.17, E_{DA} is plotted as an analytical function of θ_h for three values of θ_e spanning the whole angular range of the BEMC. One can observe that at low values of θ_h, E_{DA} does only weakly depend on the hadronic energy scale and on θ_e and that in that region E_{DA} is approximately equal to the electron beam energy.

Within the interval $\theta_h \in [15°, 50°]$ the spread of E_{DA} is about four times smaller as the typical BEMC resolution, (see figure 5.18) therefore enabling to use E_{DA} as a handle to estimate the BEMC energy resolution and the absolute scale calibrarion. The reason that the double angle method was not used initially to calibrate the BEMC, is that there was not sufficient statistics at larger values of θ_e to allow a precise calibration.

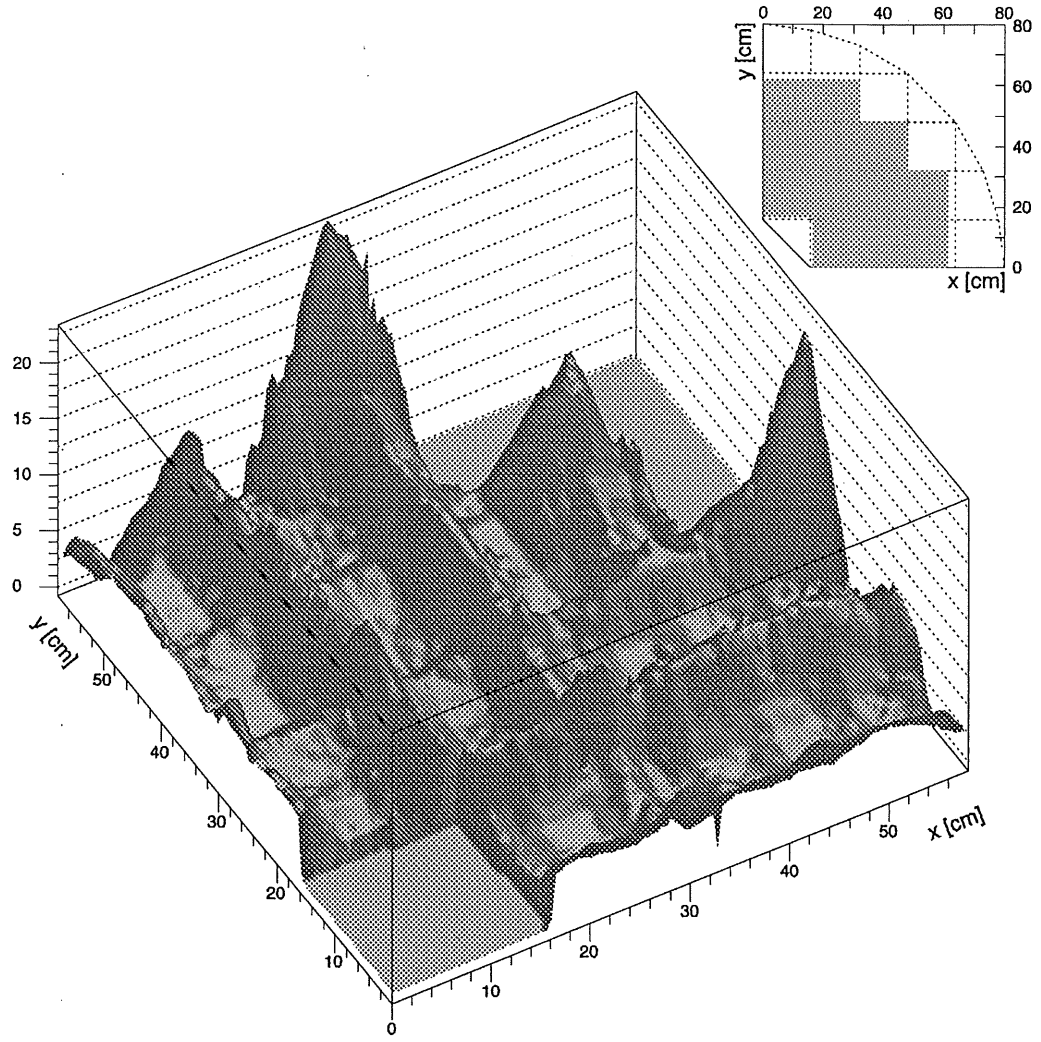

Figure 5.14: **The energy correction of the BEMC cluster energy as a function of the impact point position.**
From [19].

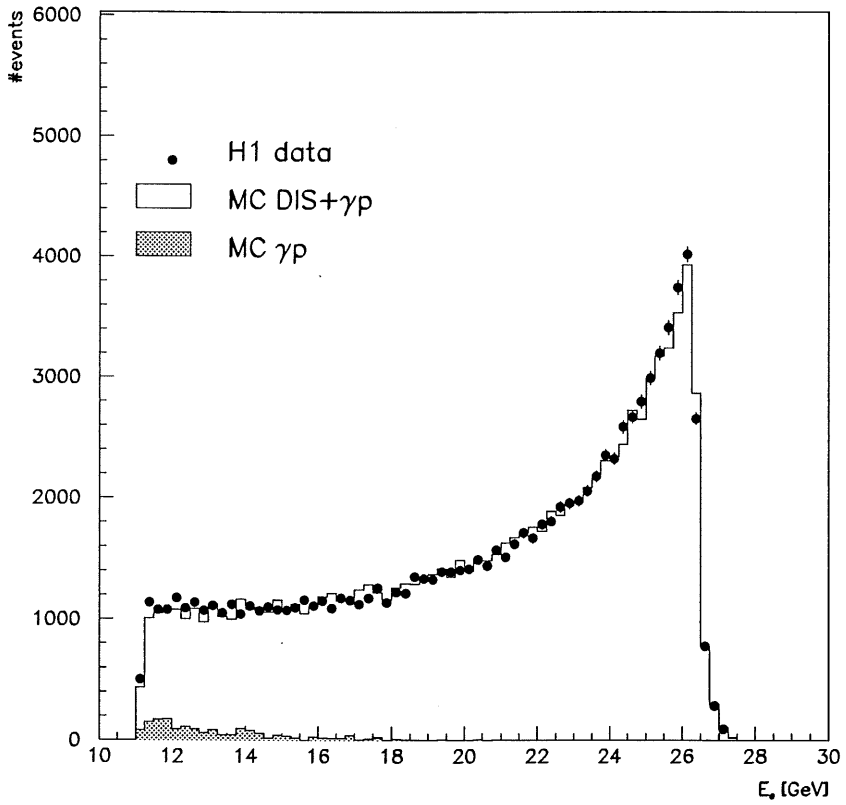

Figure 5.15: **Distribution of the energy of the scattered electron (E) for the 'closed triangle' low Q^2 data.**
The H1 data is represented by closed circles, the Monte Carlo simulation by the open histogram. The Monte Carlo calculation is normalised to the luminosity. The hatched histogram is the estimation of the background due to photoproduction processes.

Since we are mainly interested in the resolution in and outside the cracks, we introduce the quantity max_{xy}, which is defined as:

$$max_{xy} = max(|X_{BPC}|, |Y_{BPC}|), \tag{5.11}$$

where X_{BPC} and Y_{BPC} are the projections onto the BEMC plane of the coordinates of closest BPC hit near the BEMC cluster. This corresponds to the quadratic topology of the BEMC, and $max_{xy} = n \times 16$ cm coincides with the nth crack.

The selected events with θ_h in the interval $[15°, 50°]$ are then used to verify the energy calibration of the BEMC as a function of max_{xy}. In figures 5.19a and b one sees the relative difference of the BEMC energy and the double angle energy as a function of max_{xy}. The average of the difference and the error on this average is shown in figures 5.19c and d. The presence of the cracks at 16 cm and 32 cm is noticeable for the Monte Carlo events. In the H1 data only the crack at 16 cm is visible. Apart from the crack regions, the Monte Carlo describes the data qualitatively well. Depending on the position in the BEMC, the reconstructed BEMC energy is typically overestimated by 1–2% compared to the double angle energy.

5.9 Angular resolution

5.9.1 Reconstruction of the impact point with the BPC

As already explained in section 2.2.3, the BPC consists of four planes with 312 wires each. The wires of the successive planes are rotated by 45° with respect to each other.

The BPC hit reconstruction works as follows: a hit wire defines a strip of width d along the wire, where d is the distance between two wires within one plane. A set of such strips can be defined for the perpendicular planes 0 (with wires along x) and 2 (wires along y). The intersection of those strips defines a set of squares, which are the first approximation of the possible impact points. The same procedure is repeated for planes 1 and 3. Finally, the reconstructed BPC points are the intersection of the 'squares' of planes 0–2 and planes 1–3. In the 1994 reconstruction algorithm a modification on this scheme was applied, and points are also reconstructed if only three wires intersect with each other. An example of this reconstruction with the BPC can be seen in figure 2.10.

The intrinsic coordinate resolution of the BPC is 1.5 mm, which means at best 1 mrad angular error on the polar angle θ.

5.9.2 Detector alignment

A different way to reconstruct the polar angle θ of the scattered electron, is to use the CIP detector (see also [59] and [36]). The CIP is composed of two cathode planes, which are divided into pads of 3.65 cm length, and which cover an azimuthal angle of 45°. The radii of the anode planes are respectively 15.7 cm and 16.6 cm. Although the CIP was originally designed as a fast trigger detector, it allows to determine the polar angle of the scattered electron (figure 5.22). The geometrical acceptance of the CIP does not cover the whole BPC-range and is limited to $R|_{z=z_{BPC}} > 23$ cm for the nominal z-vertex position. The angular precision that can be obtained with one CIP layer is typically 6 mrad, but

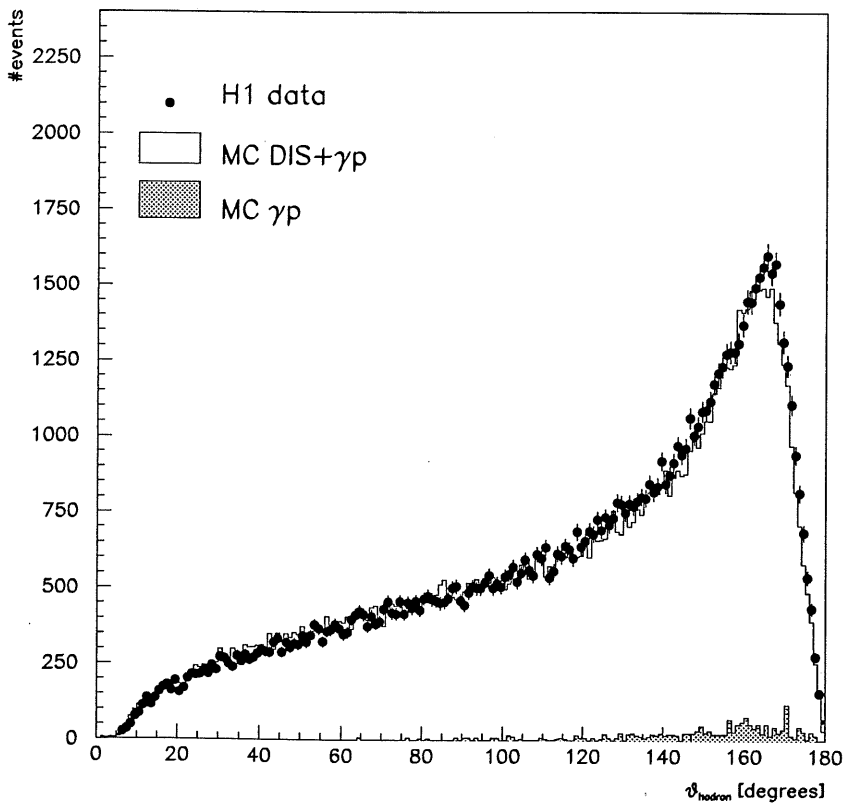

Figure 5.16: **Distribution of the hadronic angle θ_h.**
The H1 data is represented by closed circles, the Monte Carlo simulation by the open histogram. The Monte Carlo calculation is normalised to the luminosity. The hatched histogram is the estimation of the background due to photoproduction processes. (Opened triangle data)

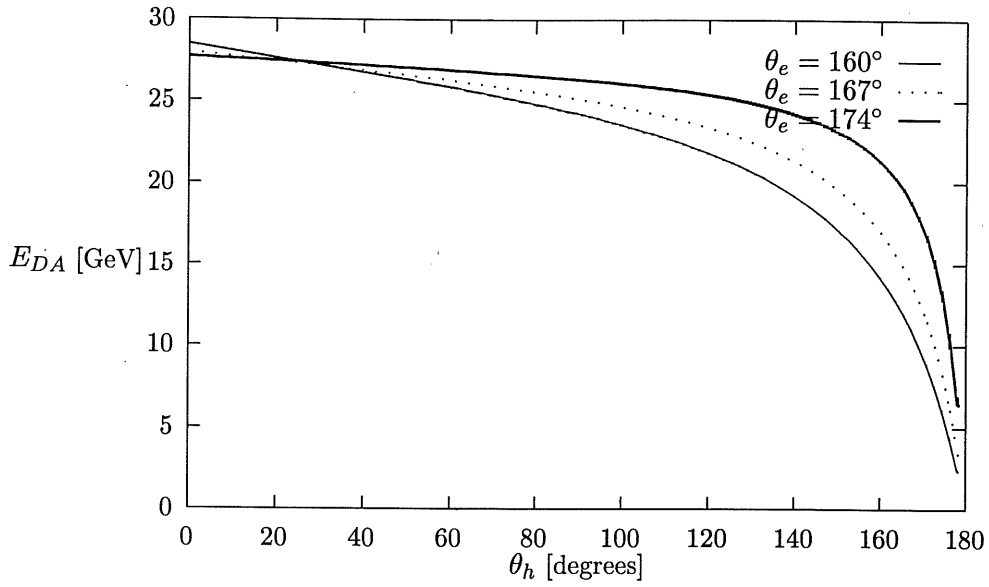

Figure 5.17: **The double angle energy as a function of the hadronic angle.** *The curves have been calculated analytically from equation (5.10) and show $E_{DA}(\theta_h)$ for three different values of θ_e, spanning the full BEMC geometrical acceptance.*

this precision can be improved to 3.5 mrad by requiring a coincidence of two CIP layers (figure 5.22). The CIP angle, θ_{CIP} is then defined as

$$\theta_{CIP} = \frac{\theta_3 + \theta_2}{2}. \tag{5.12}$$

However, equation (5.12) introduces a bias on the mean angle since the θ_e distribution is very steeply rising towards high angles (see figure 5.20). Therefore a correction was introduced in the calculation of θ_{CIP} to avoid this bias.

It was observed that $\theta_{CIP} - \theta_{BPC}$ varied as a function of the azimuthal angle ϕ_{BPC}, which is defined as

$$\phi_{BPC} = \arctan \frac{y_{BPC}}{x_{BPC}}. \tag{5.13}$$

This ϕ-dependance of $\theta_{CIP} - \theta_{BPC}$ is shown in figure 5.23 and reveals a sinusoidal structure. Each solid dot on the plot represents the mean of a gaussian fit for the histogram band in a ϕ-interval. The continuous sine curve was then fitted to these dots, with p_1, p_2 and p_3 as free parameters:

$$\theta_{CIP} - \theta_{BPC} = p_1 \sin\left(\frac{\pi}{180}(\phi_{BPC} - p_2)\right) + p_3. \tag{5.14}$$

The sine structure can be explained by a possible relative shift of the BPC detector in the x,y-plane over a distance over Δx,Δy. The variable p_1 gives the magnitude of the shift in the x,y-plane, p_2 gives the direction of the shift, and p_3 corresponds to the global mismatch

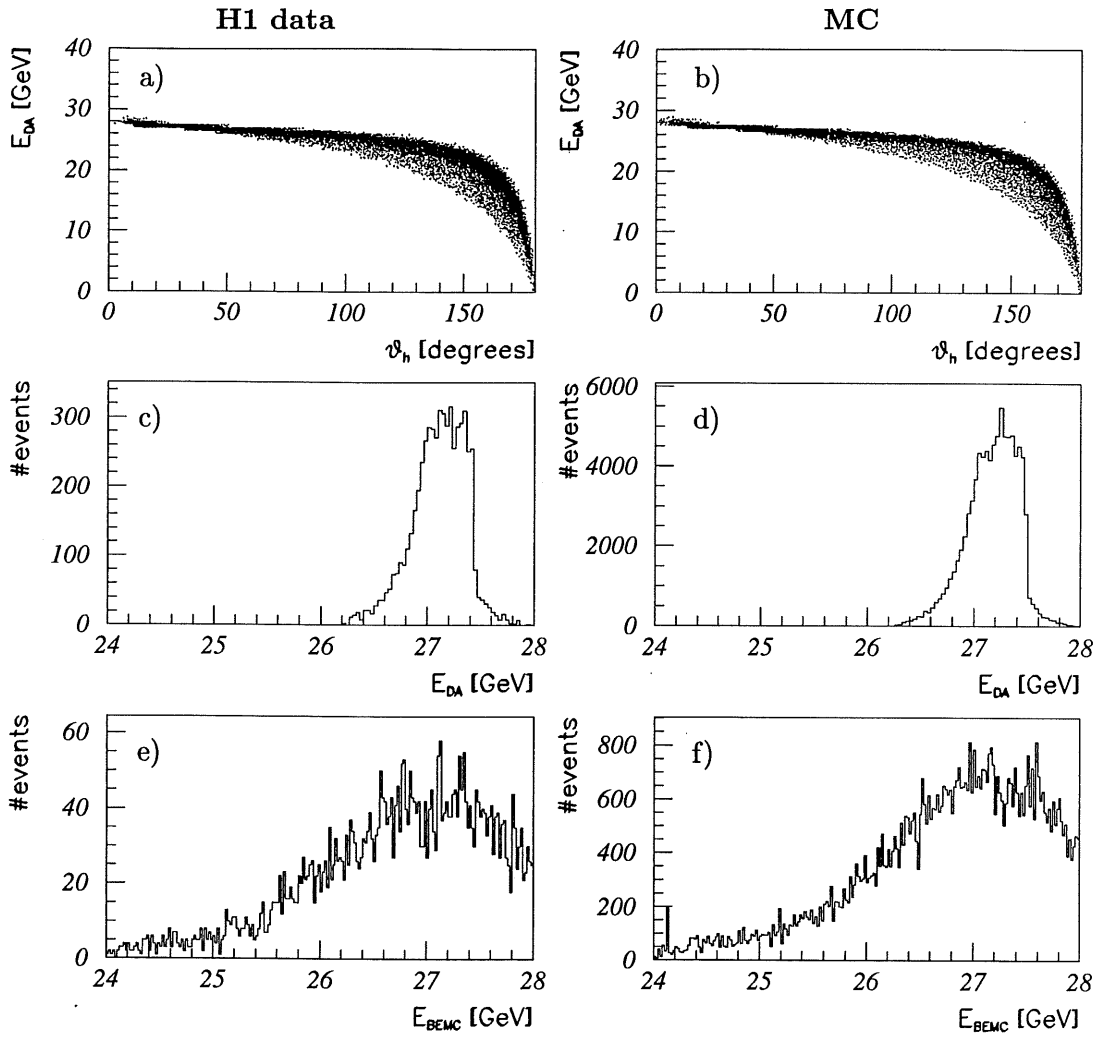

Figure 5.18: **For low values of the hadronic angle, the double angle energy is near the electron beam energy and depends only weakly on the hadronic angle.**
The events are selected from the opened triangle sample, and for plots c)—f) there is the additional requirement $15° < \theta_h < 50°$.

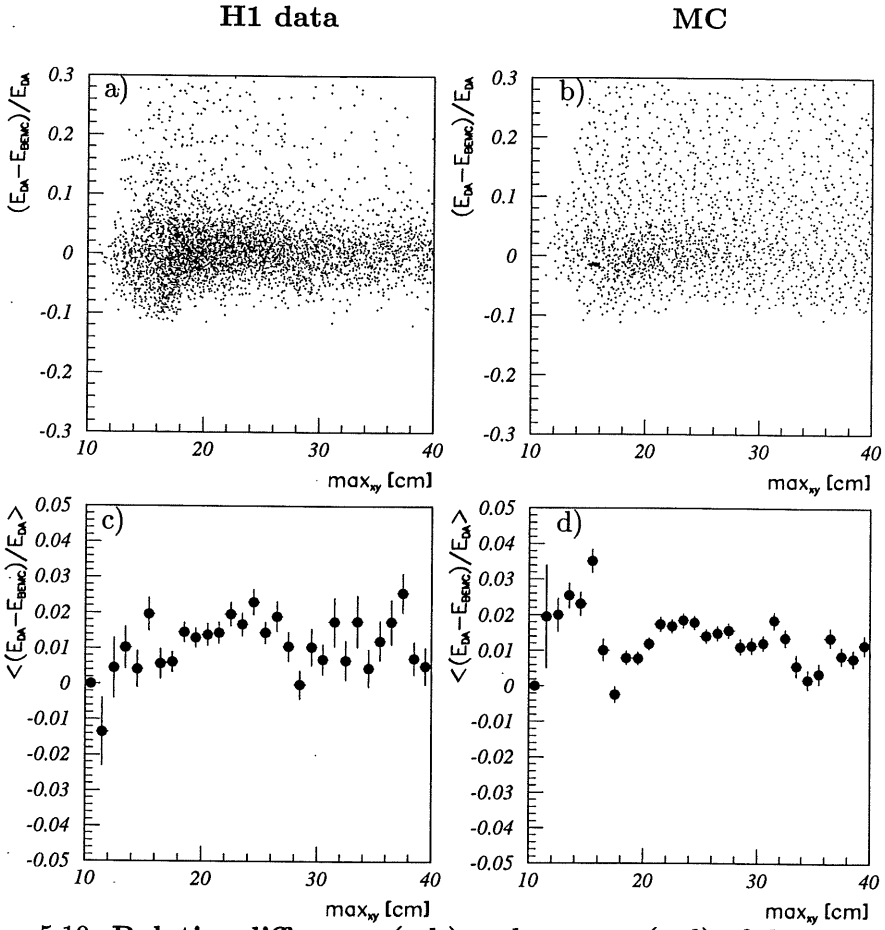

Figure 5.19: **Relative difference (a,b) and average (c,d) of the BEMC energy and double angle energy as a function of max_{xy}.**
Based on opened triangle sample, with $15° < \theta_h < 50°$.

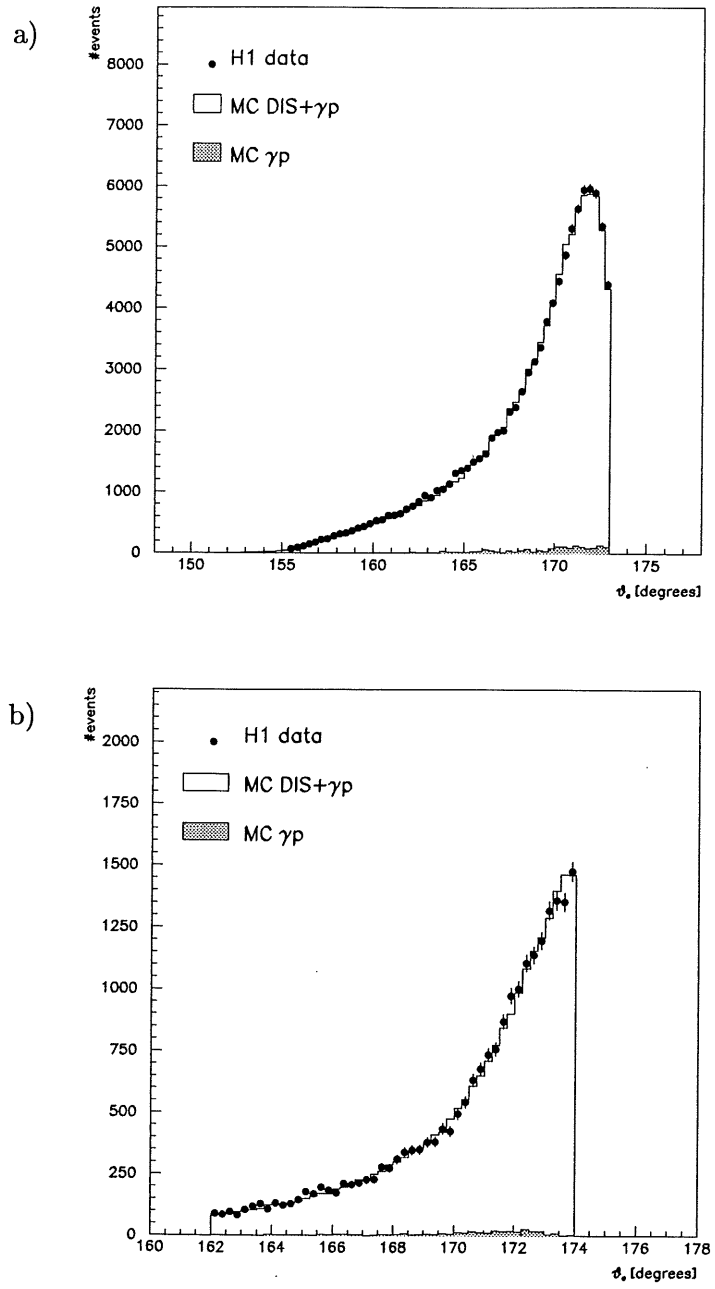

Figure 5.20: **Distribution of the angle of the scattered electron (θ_e) for the low Q^2 data.**
The H1 data is represented by closed circles, the Monte Carlo simulation by the open histogram. The Monte Carlo calculation is normalised to the luminosity. The hatched histogram is the estimation of the background due to photoproduction processes.
a) 'closed triangle' data, b) 'opened triangle' data.

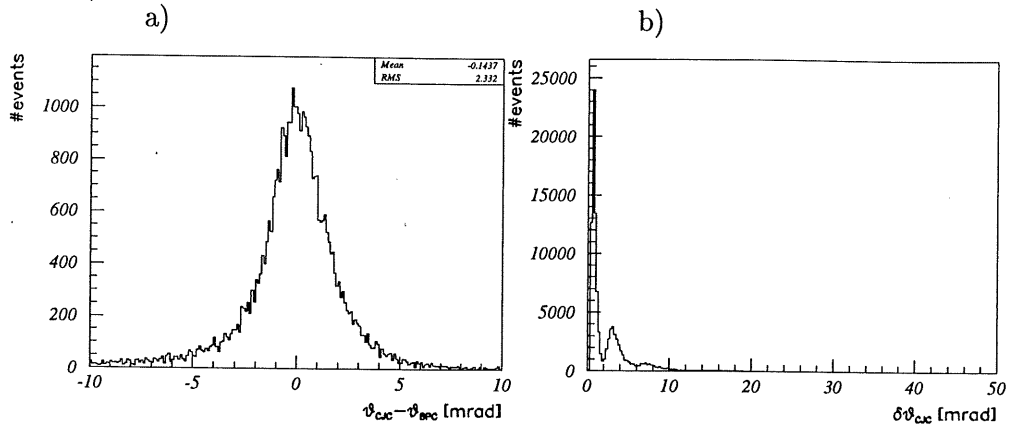

Figure 5.21: **Resolution and shift of θ_e estimated with the CJC.** *Plot a) shows the difference of the polar angle determined with precise tracks ($\delta\theta \leq 2$ mrad) and θ determined with the BPC. Plot b) shows the distribution of the error on θ for all the tracks in the events. The precise tracks contain one or more points from the CIZ or COZ chambers, which allow a better θ-measurment than the CJC alone.*

of the θ measurement. Redefining $p_1 - p_2$ in terms of a BPC shift in the x,y-plane, leads to a shift of $\Delta x = 0.14$ cm and $\Delta y = 0.24$ cm. The global θ mismatch is less than 0.5 mrad.

To calculate the polar angle of the scattered electron (θ_e) in this analysis, the BPC shift over Δx,Δy was corrected for.

Figures 5.20a and 5.20b show the angle θ of the scattered electron for the closed and opened triangle data, respectively. The small contribution due to photoproduction is also displayed. The Monte Carlo distributions are normalised to the luminosity measurement and agree well with the data.

5.9.3 Resolution of the electron angle θ_e

To estimate the resolution of the electron angle θ_e which is measured with the BPC, an independent measurement of this angle is needed. Unfortunately the BPC is the only available tracker in a large part of the backward area of the H1 detector. Because of the large stack size (16 × 16 cm) the precision of the reconstructed centre of gravity of BEMC clusters is only 1.3 cm, which is unacceptable for the determination of the angle of the scattered electron. The central trackers (CJC and CIZ) allow a more precise measurement of the angle, but only in the angular range 155°–165° they overlap with the geometrical acceptance of the BPC.

To verify the calibration of the BPC with the central tracks, we must select tracks with a high angular precision, which is typically less than 2 mrad (figure 5.21b) for CJC tracks with a CIZ or a COZ-hit. CJC tracks without CIZ or COZ hits are less precise and correspond to the second peak of figure 5.21b ($\theta > 2$ mrad). By requiring a match between the BPC point and a track with $\delta\theta_{CJC} \leq 2$ mrad, the resolution of θ_{BPC} is 2.3 mrad (see figure 5.21a), while a possible θ-shift is of the order of 0.15 mrad.

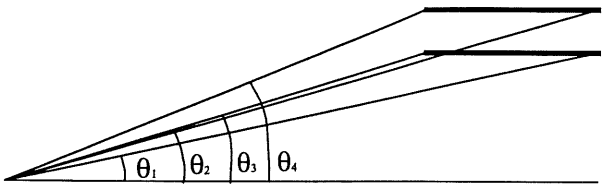

Figure 5.22: **Reconstruction of θ_e with the CIP.**
The precision of the polar angle determination with the CIP and the reconstructed z-vertex can be increased by requiring the coincidence of hit pads in both the inner and outer CIP layers. The theoretical precision with one CIP pad is given by $\theta_4 - \theta_2$ or $\theta_3 - \theta_1$, which is typically 6 mrad. By requiring a coincidence of two layers, the theoretical precision is limited by $\theta_3 - \theta_2$, which is of the order of 3.5 mrad. (Note that the drawing is not to scale.)

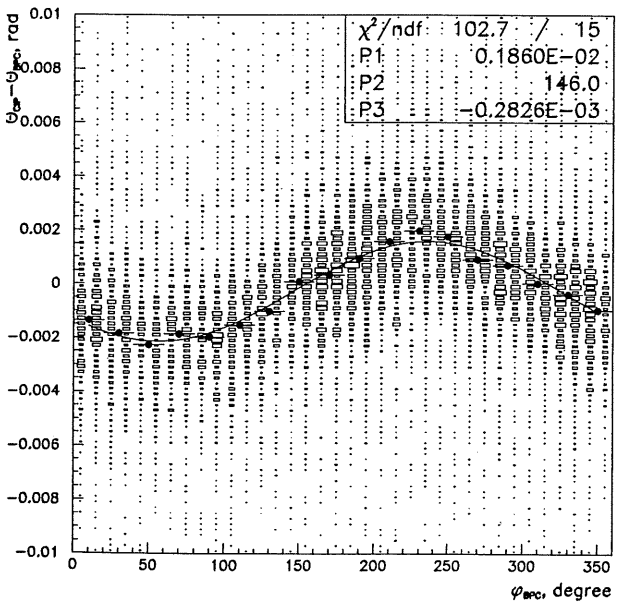

Figure 5.23: **Detector alignment.**
$\theta_{CIP} - \theta_{BPC}$ as a function of ϕ_{BPC}. The values $P1$, $P2$ and $P3$ correspond to a simple sinusoidal fit (see text and [36]).

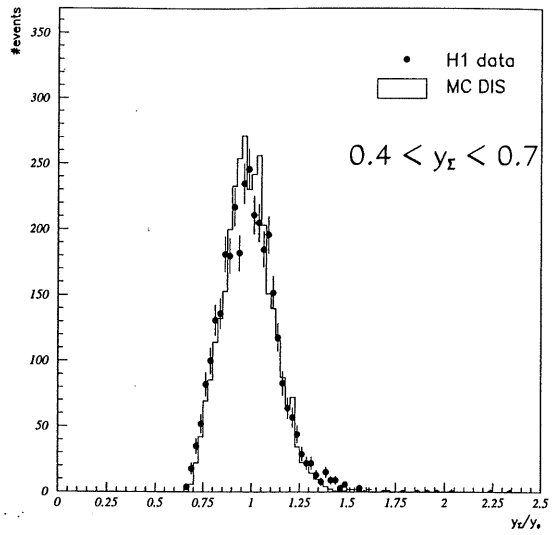

Figure 5.24: **Distribution of y_Σ/y_e.**
Experimental and Monte Carlo distibutions of y_Σ/y_e for the high y_Σ range, between 0.4 and 0.7.

5.10 The resolution of y_Σ

Since the resolution of y_Σ dominates the resolution of Q^2_Σ and x_Σ (see equations (4.27) and (4.28)), it is important to estimate $\delta y_\Sigma/y_\Sigma$ experimentally.

In the high y region, where the resolution of y_e is good (4%), this can be done by means of the ratio y_Σ/y_e. Figure 5.24 shows that this distribution is centered around 1, and that the mean value and the resolution (15%) are well produced by the Monte Carlo. The resolution of this distribution is a convolution of the resolutions of y_e and y_Σ. Since we know the experimental resolution of y_e from the energy resolution, we can estimate the resolution of y_Σ, which is approximately 14%. This is compatible with the Monte Carlo result of figure 4.6.

In the low y region the energy noise is important since an energy deposition of 300 MeV in the backward part of the detector contributes about 0.01 to y. However, the noise handling was sufficient to allow reconstructing y_Σ values below 0.01, as suggested in figure 5.25. At low y the y_e resolution is bad, so this could not be used to estimate the resolution of y_Σ in this region. A detailed Monte Carlo study [41] showed a good agreement and a resolution of 27% in the low y region ($0.005 < y_\Sigma < 0.015$).

5.11 Distance closest BPC point and BEMC cluster

Figures 5.26a and 5.26b show the distribution of the distance between the clostest BPC point to the most energetic cluster in the BEMC (DCLBP), for the closed and opened data samples respectively. The Monte Carlo does not describe the data well, and generally

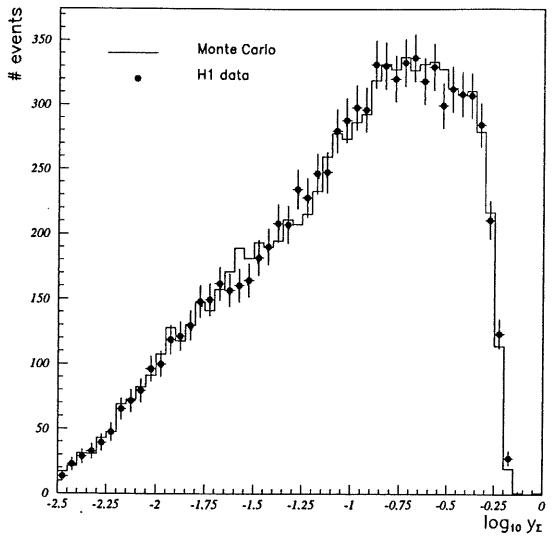

Figure 5.25: **Distribution of** $\log_{10} y_\Sigma$**.**
Experimental (closed circles) and Monte Carlo (open histogram) distibutions of $\log_{10} y_\Sigma$*. The Monte Carlo is normalised to the luminosity.*

predicts a smaller value for DCLBP than in the data. This is related to the fact that the Monte Carlo predicts a smaller BPC hit multiplicity than the observed in the data, as illustrated in figure 5.27.

We have made the same distribution as in figure 5.26 but for all the Q^2, x bins. Within the fiducial region of our analysis, the overall disagreement between the Monte Carlo and data is less than 2%, independent of the position in the x, Q^2 plane.

5.12 The lateral BEMC cluster radius

Figures 5.28a and 5.28b show the distribution of the lateral cluster radius (ECRA) of the most energetic cluster in the BEMC for the closed and opened data samples respectively. The Monte Carlo does not describe the data well and generally predicts a smaller value for ECRA than in the data, except for ECRA$>$ 3 cm, where the agreement is good.

Despite the disagreement at lower values of ECRA, x, Q^2 bin-dependent plots of the ECRA distribution reveal no kinematically dependent bias. According to Monte Carlo, a cut on ECRA$<$ 5 cm implies a loss of 3% of good DIS events. Since the data and Monte Carlo agree well for values of ECRA above 3 cm, and since there are no kinematically dependent effects, no additional efficiency correction for the cut on ECRA was introduced.

a)

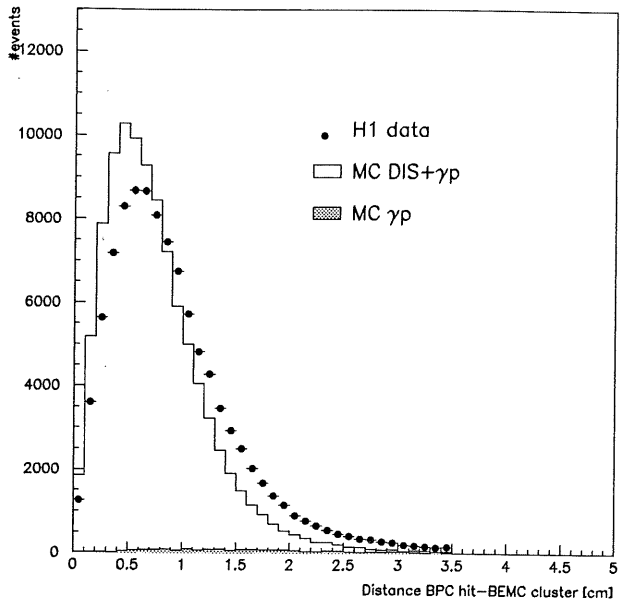

b)

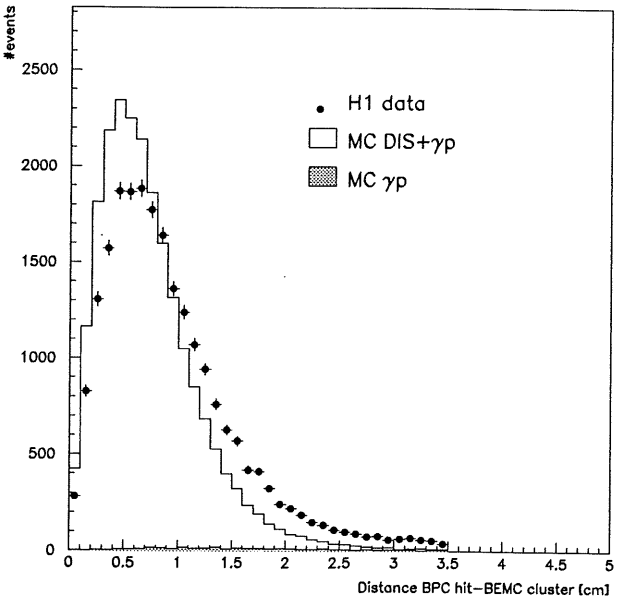

Figure 5.26: **Distribution of the distance closest BPC-BEMC cluster of the scattered electron (DCLBP) for the low Q^2 data.**
The H1 data is represented by closed circles, the Monte Carlo simulation by the open histogram. The Monte Carlo calculation is normalised to the luminosity. The hatched histogram is the estimation of the background due to photoproduction processes.
a) closed triangle data, b) opened triangle data.

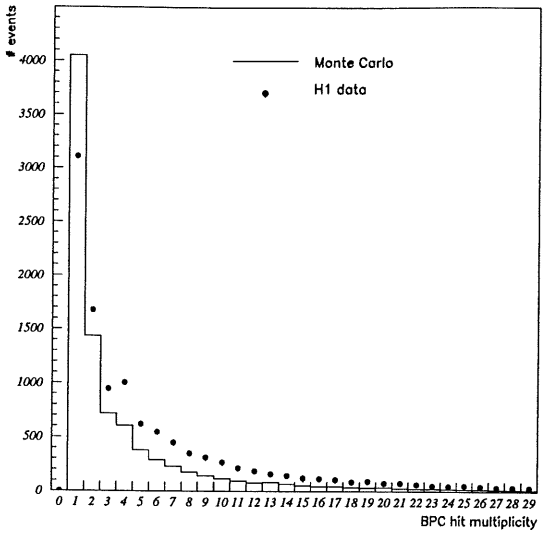

Figure 5.27: **Multiplicity of BPC hits in the Monte Carlo and H1 data, after all event selection cuts.**
The Monte Carlo underestimates the BPC hit multiplicity.

5.13 The vertex efficiency

The vertex efficiency is defined as

$$\epsilon_{vtx} = \frac{N_{events\ with\ vertex}}{N_{total\ events}}, \tag{5.15}$$

where an event is said to have a vertex if:

1. a central vertex has been reconstructed, or a forward vertex if $y_e < 0.2$ (see 5.4.3).
2. the position of the vertex lies within a 3σ region of the nominal vertex position,
3. the error on the z-vertex (σz_{vertex}) is less than 6 cm.

In our analysis we will use the Monte Carlo method to calculate F_2 (see equation (4.12)). With this method, it is not necessary to calculate any efficiency explicitely to obtain F_2. However, it is mandatory that the Monte Carlo describes the efficiencies of the data well, otherwise an additional factorised efficiency must be introduced. In this section we will verify whether the vertex efficiency of the data sample that we use, is correctly described by the Monte Carlo.

The vertex requirement is an important selection criterion of our event sample, since it removes beam-gas, beam-wall and satellite bunch events, but also because the z-coordinate of the vertex position is used to calculate the angle of the scattered electron. The presence of background and satellite events in the data and not in the Monte Carlo results in different vertex efficiences in the data and Monte Carlo, because there are more events in

a)

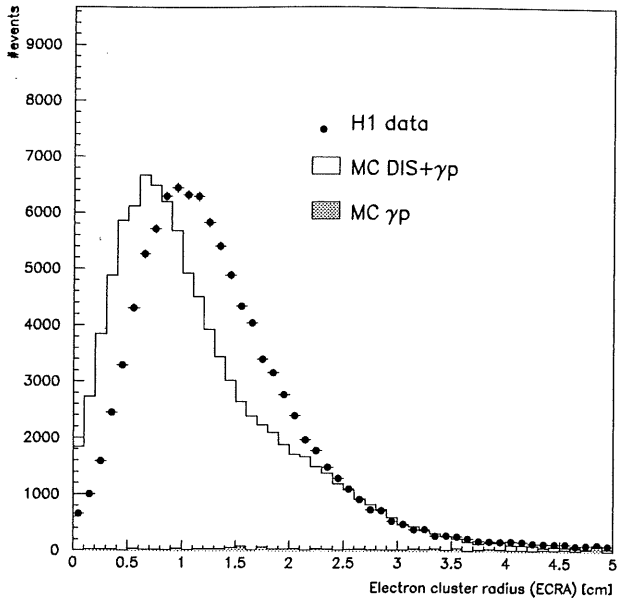

b)

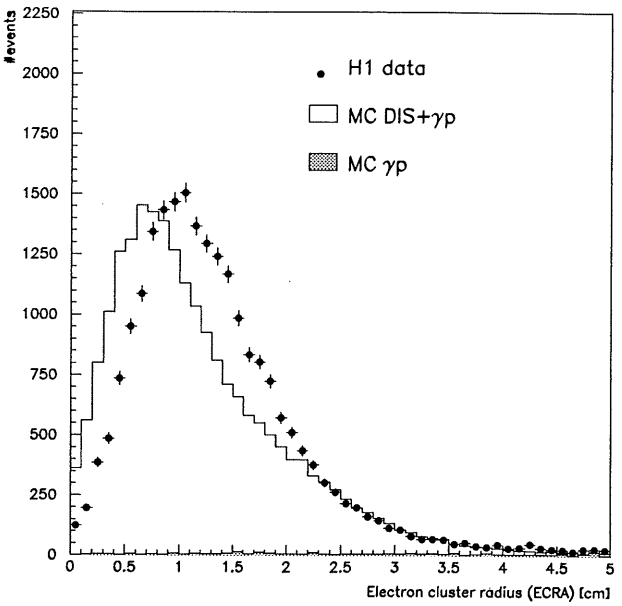

Figure 5.28: **Distribution of the cluster radius of the scattered electron (ECRA) for the low Q^2 data.**
The H1 data is represented by closed circles, the Monte Carlo simulation by the open histogram. The Monte Carlo calculation is normalised to the luminosity. The hatched histogram is the estimation of the background due to photoproduction processes.
a) closed triangle data, b) opened triangle data.

the denominator of equation (5.15) for the data than for the Monte Carlo. To remove the background and satellite events and still be able to calculate the vertex efficiency, we will use the CIP detector. Unfortunately, due to geometrical constraints, this detector does not allow to reach the lowest values of Q^2. This means that for some kinematical bins we will have to use stronger cuts to reduce the background, as well as a separate estimation of the influence of the satellite bunches.

Apart from the background and satellite bunches, there are two effects in the Monte Carlo which also cause a discrepancy between the vertex efficiency in the data and the Monte Carlo: (i) the choice of the parametrisation in the Monte Carlo has a measurable influence on the vertex efficiency; (ii) the Monte Carlo does not describe the full W^2 range of the data, which, due to migrations, also has a visible effect on the vertex efficiency. In the following sections we will study all these effect in detail, starting with the influence of the structure function parametrisation.

5.13.1 Influence of the structure function parametrisation

In section 5.7 we mentioned that the Monte Carlo events are reweighted according to equation (5.8), to account for the influence of the structure function on the vertex efficiency. Events with hard initial state radiation migrate from a lower to a higher W region. The proportion of radiative to non-radiative events depends on the structure function behaviour, and this dependence is more important in the high y region, where there are more radiative events. This effect leads to a lower vertex efficiency for the MRSH parametrisation compared to the GRV parametrisation, as shown in figure 5.29. The effect is maximum 1% at lower energies (high y) and negligable at higher energies. Since the Monte Carlo events which we use are reweighted according to equation (5.8), we mean the vertex efficiency from the MRSH parametrisation when we refer to the vertex efficiency of the Monte Carlo.

We will not include the error on the vertex efficiency due to the influence of the structure function parametrisation together with the other systematical vertex efficiency errors, but rather quote it as a separate systematical error. We calculated F_2 also with the $MRSD^-$ parametrisation instead of $MRSH$, and found that the differences were smaller than 2%.

5.13.2 Comparison of the vertex efficiency in the Monte Carlo and data

Figure 5.32 shows the vertex efficiency as a function of the energy E of the scattered electron for data and for Monte Carlo. The strong discrepancies, especially at lower energies, is mainly due to the presence of beam-gas and beam-wall events in the data. Tables 5.5 and 5.7 show the same efficiencies in the x, Q^2 bins. As we have seen in section 5.4.3 the vertex requirement rejects 34% of the events, which are practically all background or satellite bunch events. The satellite bunches (see section 5.4.3) also affect the vertex efficiency of the data, since they contribute to the denominator in equation (5.15) but not to the numerator. Therefore one needs a method which is insentitive to the background and the satellite events. This can be done by using the CIP detector.

In section 5.9.3 we already mentioned that the CIP can be used to reconstruct the track of a charged particle. Inversely, the CIP can also be used to reconstruct the position of the z-vertex. Figure 5.30 illustrates how a BPC point and two CIP pads define such a CIP

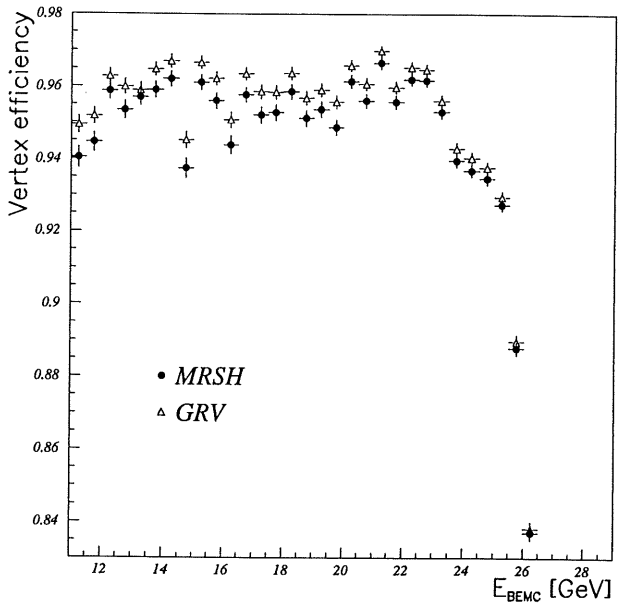

Figure 5.29: **The influence of the structure function parametrisation on the vertex efficiency.**
This figure shows the vertex efficiency for two different parametrisations GRV and MRSH in in the DJANGO Monte Carlo.

$x \setminus Q^2\ GeV^2$	$4.217 - 5.623$	$5.623 - 7.499$	$7.499 - 10.0$	$10.0 - 13.34$	$13.34 - 17.78$
$1.00 \times 10^{-4} - 1.58 \times 10^{-4}$			*CIP*		
$1.58 \times 10^{-4} - 2.51 \times 10^{-4}$				*CIP*	*CIP*
$2.51 \times 10^{-4} - 3.98 \times 10^{-4}$				*CIP*	*CIP*
$3.98 \times 10^{-4} - 6.31 \times 10^{-4}$					*CIP*
$6.31 \times 10^{-4} - 1.00 \times 10^{-3}$					*CIP*
$1.00 \times 10^{-3} - 1.58 \times 10^{-3}$					
$1.58 \times 10^{-3} - 2.51 \times 10^{-3}$					
$2.51 \times 10^{-3} - 3.98 \times 10^{-3}$					
$3.98 \times 10^{-3} - 6.31 \times 10^{-3}$					
$x \setminus Q^2\ GeV^2$	$17.78 - 23.71$	$23.71 - 31.62$	$31.62 - 42.17$	$42.17 - 56.23$	$56.23 - 74.99$
$1.00 \times 10^{-4} - 1.58 \times 10^{-4}$					
$1.58 \times 10^{-4} - 2.51 \times 10^{-4}$					
$2.51 \times 10^{-4} - 3.98 \times 10^{-4}$	*CIP*	*CIP*			
$3.98 \times 10^{-4} - 6.31 \times 10^{-4}$	*CIP*	*CIP*	*CIP*		
$6.31 \times 10^{-4} - 1.00 \times 10^{-3}$	*CIP*	*CIP*	*CIP*	*CIP*	
$1.00 \times 10^{-3} - 1.58 \times 10^{-3}$	*CIP*	*CIP*	*CIP*	*CIP*	*CIP*
$1.58 \times 10^{-3} - 2.51 \times 10^{-3}$	*CIP*	*CIP*	*CIP*	*CIP*	*CIP*
$2.51 \times 10^{-3} - 3.98 \times 10^{-3}$	*CIP*	*CIP*	*CIP*	*CIP*	*CIP*
$3.98 \times 10^{-3} - 6.31 \times 10^{-3}$	*CIP*	*CIP*	*CIP*	*CIP*	*CIP*

Table 5.4: **Overview of the bins for which the CIP can be used.**
The bins marked "CIP" correspond to $\theta_e < 171°$.

vertex candidate. Figure 5.31 shows the distribution of the vertex position reconstructed with the tracks and with the CIP, illustrating that the CIP allows a good reconstruction of the z-vertex indeed (see also [59]).

The vertex reconstruction efficiency can thus be defined as:

$$\epsilon_{vtx,CIP} = \frac{N_{events\ with\ vertex\ and\ CIP\ vertex}}{N_{events\ with\ CIP\ vertex}}, \tag{5.16}$$

for the events that passed the standard set of cuts except the vertex cut. An event has a CIP z-vertex if

$$|z_{vertex,CIP} - z_0| \leq 30\,\text{cm}, \tag{5.17}$$

similar to the normal vertex cut. The advantage of definition (5.16) is this method is much less[2] sensitive to background events and not to satellite bunch events at all.

Unfortunately the CIP method has its limitations: due to the limited geometrical acceptance of the CIP, the distance of the used BPC hit to the beam axis has to be larger than 23 cm for the method to work, corresponding to $\theta_e < 171°$. For larger angles, an alternative way to reduce the background considerably, is to use strong cuts. The bins for which the CIP can be used are marked *CIP* in table 5.4.

[2]Background events with a z-vertex within a 30 cm range of the nominal interaction point will still be accepted.

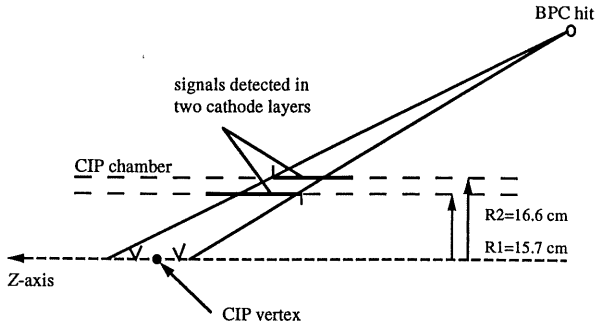

Figure 5.30: **The reconstructed z-vertex with the CIP.**
Schematic drawing how the CIP and the BPC impact point can be used to reconstruct the z-vertex position. (from [59])

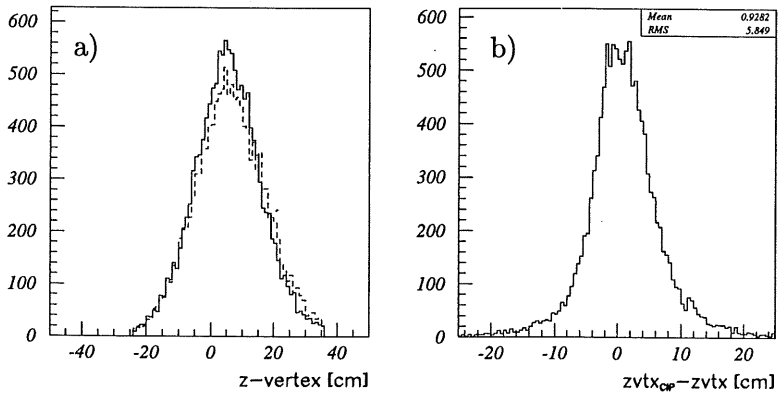

Figure 5.31: **The reconstructed z-vertex with tracks and with the CIP.**
a) Distribution of the z-vertex with tracks (full line) and with the CIP (dashed line). b) Difference of the z-vertex from the CIP and z-vertex from the tracks. (Opened triangle data.)

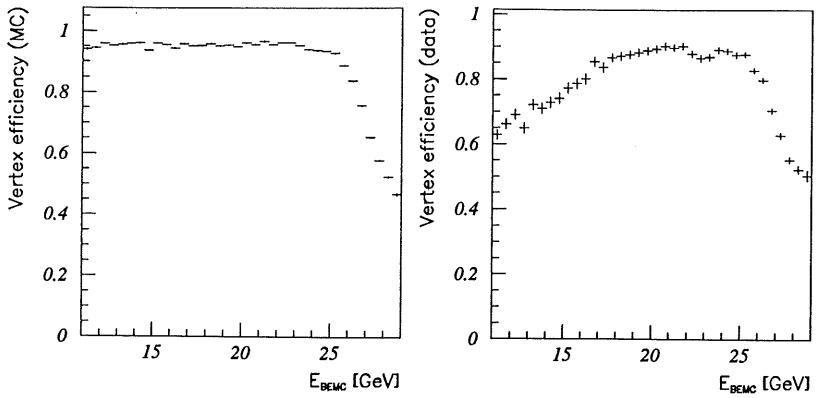

Figure 5.32: **The vertex efficiency in Monte Carlo and data.**
The efficieny obtained from equation (5.15) reveals discrepancies between Monte Carlo and data, mainly due to the presence of beam-gas and beam-wall events, and to a lesser extent to satellite bunch events.

Comparison of the vertex efficiency in the MC and data with the CIP

Table 5.6 shows the vertex efficiency of the data calculated with the CIP method according to equation (5.16). A comparison with table 5.7 indicates differences up to 3% with the vertex efficiency of the Monte Carlo.

Comparison of the vertex efficiency in the MC and data without the CIP

In the bins where the CIP cannot be used to calculate the vertex efficieny, we applied 'strong' cuts, which are not correlated ('orthogonal') with the vertex requirement. From a pilot bunch study we found that the cuts DCLBP < 1.5 cm and ECRA< 2.0 cm reduce the background by 87%. These cuts are not correlated to the vertex cut and therefore do not bias the vertex efficiency.

The vertex efficiency of the data and the Monte Carlo after applying the strong cuts is shown in tables 5.8 and 5.9 respectively. A comparison of the Monte Carlo vertex efficiency after the normal and strong event selection cuts (tables 5.7 and 5.9) shows differences which are at most 1%, confirming that the cuts do not significantly bias the event sample. This is also illustrated in figure 5.33, showing the effect of the strong cuts as a function of the energy. The strong cuts move the overall vertex efficiency from 74.9% up to 78.5%. In the kinematic bins where the CIP cannot be used, the effect of the strong cuts on the vertex efficiency of the data varies between zero and 5%.

The strong cuts do not reject satellite bunch events, which also affect the vertex efficiency of the data. In the next section we will estimate the influence of the satellite bunch events.

$x \setminus Q^2\ GeV^2$	$4.217 - 5.623$	$5.623 - 7.499$	$7.499 - 10.0$	$10.0 - 13.34$	$13.34 - 17.78$
$1.00 \times 10^{-4} - 1.58 \times 10^{-4}$					
$1.58 \times 10^{-4} - 2.51 \times 10^{-4}$			0.58		
$2.51 \times 10^{-4} - 3.98 \times 10^{-4}$			0.69	0.69	0.71
$3.98 \times 10^{-4} - 6.31 \times 10^{-4}$			0.79	0.80	0.84
$6.31 \times 10^{-4} - 1.00 \times 10^{-3}$			0.82	0.86	0.86
$1.00 \times 10^{-3} - 1.58 \times 10^{-3}$			0.84	0.89	0.89
$1.58 \times 10^{-3} - 2.51 \times 10^{-3}$				0.92	0.93
$2.51 \times 10^{-3} - 3.98 \times 10^{-3}$					0.89
$3.98 \times 10^{-3} - 6.31 \times 10^{-3}$					
$x \setminus Q^2\ GeV^2$	$17.78 - 23.71$	$23.71 - 31.62$	$31.62 - 42.17$	$42.17 - 56.23$	$56.23 - 74.99$
$1.00 \times 10^{-4} - 1.58 \times 10^{-4}$					
$1.58 \times 10^{-4} - 2.51 \times 10^{-4}$					
$2.51 \times 10^{-4} - 3.98 \times 10^{-4}$					
$3.98 \times 10^{-4} - 6.31 \times 10^{-4}$	0.84	0.81			
$6.31 \times 10^{-4} - 1.00 \times 10^{-3}$	0.89	0.89	0.93		
$1.00 \times 10^{-3} - 1.58 \times 10^{-3}$	0.90	0.91	0.93		
$1.58 \times 10^{-3} - 2.51 \times 10^{-3}$	0.92	0.93	0.93	0.94	
$2.51 \times 10^{-3} - 3.98 \times 10^{-3}$	0.88	0.89	0.81	0.82	
$3.98 \times 10^{-3} - 6.31 \times 10^{-3}$		0.75	0.87	0.62	

Table 5.5: **Vertex efficiency from the data.**
The efficiency is calculated by using equation (5.15).

$x \setminus Q^2\ GeV^2$	$4.217 - 5.623$	$5.623 - 7.499$	$7.499 - 10.0$	$10.0 - 13.34$	$13.34 - 17.78$
$1.00 \times 10^{-4} - 1.58 \times 10^{-4}$					
$1.58 \times 10^{-4} - 2.51 \times 10^{-4}$					
$2.51 \times 10^{-4} - 3.98 \times 10^{-4}$				0.76	0.74
$3.98 \times 10^{-4} - 6.31 \times 10^{-4}$					0.88
$6.31 \times 10^{-4} - 1.00 \times 10^{-3}$					0.92
$1.00 \times 10^{-3} - 1.58 \times 10^{-3}$					
$1.58 \times 10^{-3} - 2.51 \times 10^{-3}$					
$2.51 \times 10^{-3} - 3.98 \times 10^{-3}$					
$3.98 \times 10^{-3} - 6.31 \times 10^{-3}$					
$x \setminus Q^2\ GeV^2$	$17.78 - 23.71$	$23.71 - 31.62$	$31.62 - 42.17$	$42.17 - 56.23$	$56.23 - 74.99$
$1.00 \times 10^{-4} - 1.58 \times 10^{-4}$					
$1.58 \times 10^{-4} - 2.51 \times 10^{-4}$					
$2.51 \times 10^{-4} - 3.98 \times 10^{-4}$					
$3.98 \times 10^{-4} - 6.31 \times 10^{-4}$	0.88	0.87			
$6.31 \times 10^{-4} - 1.00 \times 10^{-3}$	0.93	0.92	0.97		
$1.00 \times 10^{-3} - 1.58 \times 10^{-3}$	0.93	0.94	0.98		
$1.58 \times 10^{-3} - 2.51 \times 10^{-3}$	0.99	0.98	0.98	1.00	
$2.51 \times 10^{-3} - 3.98 \times 10^{-3}$	0.96	0.98	0.98	1.00	
$3.98 \times 10^{-3} - 6.31 \times 10^{-3}$		1.00	1.00	1.00	

Table 5.6: **Vertex efficiency from the data with the CIP method.**
The efficiency is calculated by using equation (5.16). Only bins which are completely within the CIP geometrical acceptance are shown.

$x \setminus Q^2\ GeV^2$	$4.217 - 5.623$	$5.623 - 7.499$	$7.499 - 10.0$	$10.0 - 13.34$	$13.34 - 17.78$
$1.00 \times 10^{-4} - 1.58 \times 10^{-4}$					
$1.58 \times 10^{-4} - 2.51 \times 10^{-4}$			0.63		
$2.51 \times 10^{-4} - 3.98 \times 10^{-4}$			0.73	0.76	0.74
$3.98 \times 10^{-4} - 6.31 \times 10^{-4}$			0.84	0.87	0.88
$6.31 \times 10^{-4} - 1.00 \times 10^{-3}$			0.89	0.91	0.94
$1.00 \times 10^{-3} - 1.58 \times 10^{-3}$			0.94	0.94	0.95
$1.58 \times 10^{-3} - 2.51 \times 10^{-3}$				0.95	0.96
$2.51 \times 10^{-3} - 3.98 \times 10^{-3}$					0.95
$3.98 \times 10^{-3} - 6.31 \times 10^{-3}$					
$x \setminus Q^2\ GeV^2$	$17.78 - 23.71$	$23.71 - 31.62$	$31.62 - 42.17$	$42.17 - 56.23$	$56.23 - 74.99$
$1.00 \times 10^{-4} - 1.58 \times 10^{-4}$					
$1.58 \times 10^{-4} - 2.51 \times 10^{-4}$					
$2.51 \times 10^{-4} - 3.98 \times 10^{-4}$					
$3.98 \times 10^{-4} - 6.31 \times 10^{-4}$	0.88	0.88			
$6.31 \times 10^{-4} - 1.00 \times 10^{-3}$	0.94	0.94	0.95		
$1.00 \times 10^{-3} - 1.58 \times 10^{-3}$	0.96	0.96	0.97		
$1.58 \times 10^{-3} - 2.51 \times 10^{-3}$	0.96	0.97	0.99	1.00	
$2.51 \times 10^{-3} - 3.98 \times 10^{-3}$	0.96	0.99	0.99	0.99	
$3.98 \times 10^{-3} - 6.31 \times 10^{-3}$		0.99	1.00	1.00	

Table 5.7: **Vertex efficiency from the Monte Carlo.**
The efficiency is calculated by using equation (5.15).

$x \setminus Q^2\ GeV^2$	$4.217 - 5.623$	$5.623 - 7.499$	$7.499 - 10.0$	$10.0 - 13.34$	$13.34 - 17.78$
$1.00 \times 10^{-4} - 1.58 \times 10^{-4}$					
$1.58 \times 10^{-4} - 2.51 \times 10^{-4}$			0.57		
$2.51 \times 10^{-4} - 3.98 \times 10^{-4}$			0.69		
$3.98 \times 10^{-4} - 6.31 \times 10^{-4}$			0.79	0.81	
$6.31 \times 10^{-4} - 1.00 \times 10^{-3}$			0.81	0.88	
$1.00 \times 10^{-3} - 1.58 \times 10^{-3}$			0.86	0.92	0.90
$1.58 \times 10^{-3} - 2.51 \times 10^{-3}$				0.94	0.95
$2.51 \times 10^{-3} - 3.98 \times 10^{-3}$					0.94
$3.98 \times 10^{-3} - 6.31 \times 10^{-3}$					
$x \setminus Q^2\ GeV^2$	$17.78 - 23.71$	$23.71 - 31.62$	$31.62 - 42.17$	$42.17 - 56.23$	$56.23 - 74.99$
$1.00 \times 10^{-4} - 1.58 \times 10^{-4}$					
$1.58 \times 10^{-4} - 2.51 \times 10^{-4}$					
$2.51 \times 10^{-4} - 3.98 \times 10^{-4}$					
$3.98 \times 10^{-4} - 6.31 \times 10^{-4}$					
$6.31 \times 10^{-4} - 1.00 \times 10^{-3}$					
$1.00 \times 10^{-3} - 1.58 \times 10^{-3}$					
$1.58 \times 10^{-3} - 2.51 \times 10^{-3}$					
$2.51 \times 10^{-3} - 3.98 \times 10^{-3}$					
$3.98 \times 10^{-3} - 6.31 \times 10^{-3}$					

Table 5.8: **Vertex efficiency from the data with strong cuts.**
The efficiency is calculated by using equation (5.15). Only bins which are outside the CIP geometrical acceptance are shown.

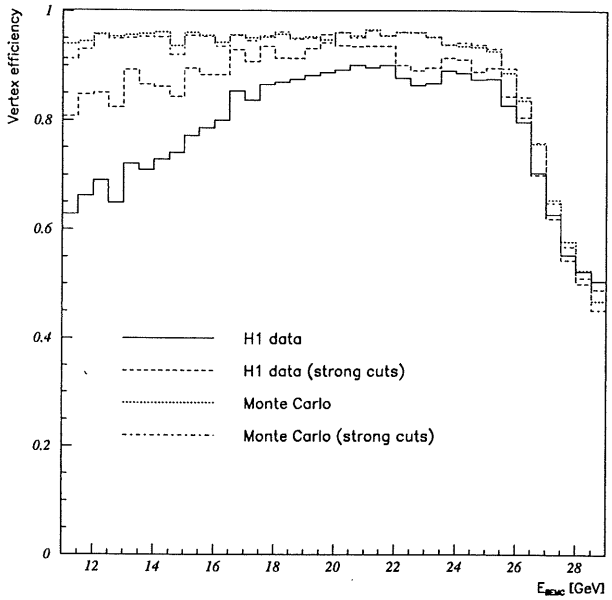

Figure 5.33: **The influence of the background on the vertex efficiency.** *The strong cuts are DCLBP* < 1.5 *cm and ECRA* < 2.0 *cm. These cuts do not affect the vertex efficiency in the Monte Carlo, but the effect on the data is significant, especially at lower values of the energy of the scattered electron. On average, the strong cuts move the vertex efficiency of the data from 74.9% up to 78.5%.*

$x \setminus Q^2\ GeV^2$	4.217 – 5.623	5.623 – 7.499	7.499 – 10.0	10.0 – 13.34	13.34 – 17.78
$1.00 \times 10^{-4} - 1.58 \times 10^{-4}$					
$1.58 \times 10^{-4} - 2.51 \times 10^{-4}$			0.62		
$2.51 \times 10^{-4} - 3.98 \times 10^{-4}$			0.73		
$3.98 \times 10^{-4} - 6.31 \times 10^{-4}$			0.85	0.88	
$6.31 \times 10^{-4} - 1.00 \times 10^{-3}$			0.90	0.92	
$1.00 \times 10^{-3} - 1.58 \times 10^{-3}$			0.94	0.95	0.95
$1.58 \times 10^{-3} - 2.51 \times 10^{-3}$				0.95	0.95
$2.51 \times 10^{-3} - 3.98 \times 10^{-3}$					0.94
$3.98 \times 10^{-3} - 6.31 \times 10^{-3}$					
$x \setminus Q^2\ GeV^2$	17.78 – 23.71	23.71 – 31.62	31.62 – 42.17	42.17 – 56.23	56.23 – 74.99
$1.00 \times 10^{-4} - 1.58 \times 10^{-4}$					
$1.58 \times 10^{-4} - 2.51 \times 10^{-4}$					
$2.51 \times 10^{-4} - 3.98 \times 10^{-4}$					
$3.98 \times 10^{-4} - 6.31 \times 10^{-4}$					
$6.31 \times 10^{-4} - 1.00 \times 10^{-3}$					
$1.00 \times 10^{-3} - 1.58 \times 10^{-3}$					
$1.58 \times 10^{-3} - 2.51 \times 10^{-3}$					
$2.51 \times 10^{-3} - 3.98 \times 10^{-3}$					
$3.98 \times 10^{-3} - 6.31 \times 10^{-3}$					

Table 5.9: **Vertex efficiency from the Monte Carlo with strong cuts.** *The efficiency is calculated by using equation (5.15). Only bins which are outside the CIP geometrical acceptance are shown.*

5.13.3 The satellite bunch correction

Figure 5.34 shows the z-vertex distribution of all the events of the closed triangle period. The highest peak corresponds to the nominal vertex position around $z \simeq 5$ cm. The smaller peak around $z \simeq 70$ cm originates from the so-called *satellite bunches*. Satellite bunches are protons which are out of time by approximately 20, 40 and 60 ns, corresponding to the 52 MHz RF field of HERA. These satellite bunches escape the ToF veto and therefore also contribute to the luminosity. This contribution, $\mathcal{L}$, was determined in a dedicated study [71].

The number of events in a small fiducial volume around a (R_{BPC}, E)-point is equal to:

$$N(R, E; R + dR, E + dE) = dR\,dE \left(\mathcal{L}_{nom} \frac{d^2\sigma_{nom}}{dR\,dE} + \mathcal{L}_{sat} \frac{d^2\sigma_{sat}}{dR\,dE} \right), \tag{5.18}$$

with $R_{BPC} = \sqrt{x_{BPC}^2 + y_{BPC}^2}$. The probability that an event originates from the main and not the satellite bunch can then be written as ([36]):

$$p_{main} = \frac{\mathcal{L}_{nom} \frac{d^2\sigma_{nom}}{dR\,dE}}{\mathcal{L}_{nom} \frac{d^2\sigma_{nom}}{dR\,dE} + \mathcal{L}_{sat} \frac{d^2\sigma_{sat}}{dR\,dE}} \tag{5.19}$$

The differential cross sections in equation (5.19) are calculated using the PDF library [63] and the GRV parametrisation. The probability p_{main} can thus be calculated on an event

$x \setminus Q^2\ GeV^2$	$4.217 - 5.623$	$5.623 - 7.499$	$7.499 - 10.0$	$10.0 - 13.34$	$13.34 - 17.78$
$1.00 \times 10^{-4} - 1.58 \times 10^{-4}$					
$1.58 \times 10^{-4} - 2.51 \times 10^{-4}$			0.57		
$2.51 \times 10^{-4} - 3.98 \times 10^{-4}$			0.68		
$3.98 \times 10^{-4} - 6.31 \times 10^{-4}$			0.78	0.79	
$6.31 \times 10^{-4} - 1.00 \times 10^{-3}$			0.80	0.84	
$1.00 \times 10^{-3} - 1.58 \times 10^{-3}$			0.83	0.89	0.88
$1.58 \times 10^{-3} - 2.51 \times 10^{-3}$				0.90	0.92
$2.51 \times 10^{-3} - 3.98 \times 10^{-3}$					0.88
$3.98 \times 10^{-3} - 6.31 \times 10^{-3}$					
$x \setminus Q^2\ GeV^2$	$17.78 - 23.71$	$23.71 - 31.62$	$31.62 - 42.17$	$42.17 - 56.23$	$56.23 - 74.99$
$1.00 \times 10^{-4} - 1.58 \times 10^{-4}$					
$1.58 \times 10^{-4} - 2.51 \times 10^{-4}$					
$2.51 \times 10^{-4} - 3.98 \times 10^{-4}$					
$3.98 \times 10^{-4} - 6.31 \times 10^{-4}$					
$6.31 \times 10^{-4} - 1.00 \times 10^{-3}$					
$1.00 \times 10^{-3} - 1.58 \times 10^{-3}$					
$1.58 \times 10^{-3} - 2.51 \times 10^{-3}$					
$2.51 \times 10^{-3} - 3.98 \times 10^{-3}$					
$3.98 \times 10^{-3} - 6.31 \times 10^{-3}$					

Table 5.10: **Vertex efficiency from the data with the satellite bunch correction.**
The efficiency is calculated by using equation (5.15). Only bins which are outside the CIP geometrical acceptance are shown.

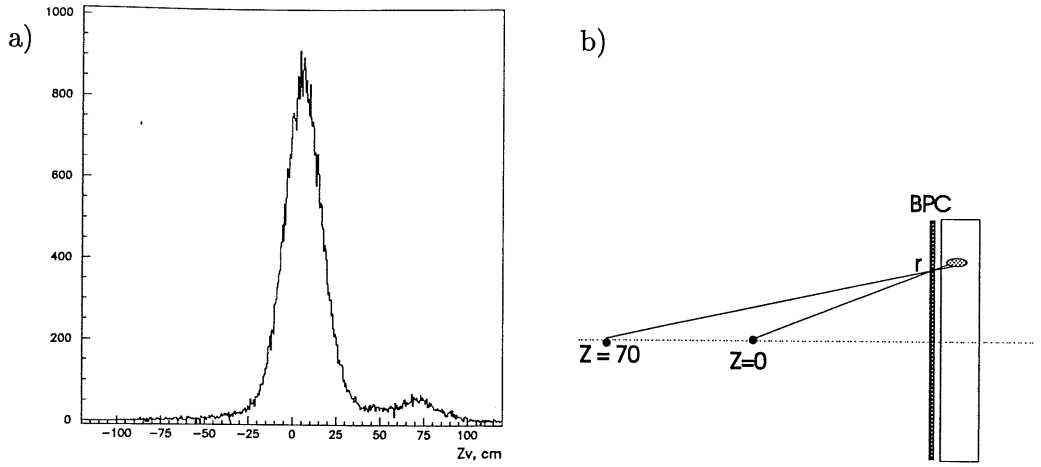

Figure 5.34: **The z-vertex distribution with the satellite bunch.**
a) The highest peak corresponds to nominal bunch events, the lowest peak are satellite bunch events. This illustrates that the satellite bunch events also contribute to the luminosity.
b) The satellite bunch is located at $z \approx 70$ cm, which means that for a particular impact point in the BPC, the scattering angle θ_e and thus also Q^2, is lower for satellite bunch events than for nominal bunch events. (Closed triangle data; plot from [36])

by event basis, and was used as a weight in the summation over any fiducial volume to correct the effect of the satellite bunches. This is shown in figure 5.36 and table 5.10, where the vertex efficiency obtained from the data is compared to the vertex efficiency corrected for the satellite bunches. The effect is maximum 2%, independently of the energy[3].

5.13.4 W-cut dependence

As we already mentioned, the DJANGO Monte Carlo program has a lower limit for the hadronic invariant mass W in its definition of the kinematical region for the event generation. This limit is $W > 4$ GeV and is due to difficulties to generate events with HERACLES [4] in the presence of resonances. As a result of this limit, the migration from the very low W-region is not present in the Monte Carlo. Although in this analysis we only measure events with $W > 20$ GeV (this follows automatically from the vertex requirement), migrations from lower to higher values of W mean that an imperfect description of the Monte Carlo at low values of W may still affect the vertex efficiency of the data sample which was used.

The effect of a W-cut is illustrated in figure 5.37, which shows the vertex reconstruction efficiency in the Monte Carlo as a function of the W-cut. The curve corresponds to a straight line fit in the region 4 GeV $< W_{cut} <$ 10 GeV. From this one can see that one must apply an additional correction of 1.5% on the Monte Carlo vertex efficiency. However, this correction is x, Q^2-dependent, since a vertex could be reconstructed if the scattered

[3]The fact that this correction is independent of the energy also means that it is independent of the value of Bjorken y.

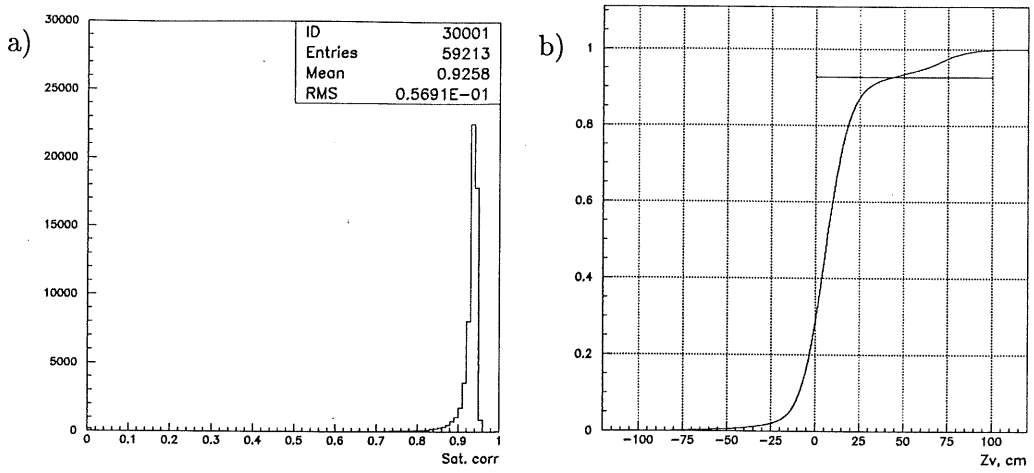

Figure 5.35: **Distribution of the satellite correction.**
a) Distribution of p_{main} calculated according to equation (5.19), for the opened triangle data.
b) Integrated distribution of the z-vertex of the opened triangle data. The 'kink' around $y = 0.926$ corresponds to the satellite bunch, which contributes to the luminosity. (plot from [36])

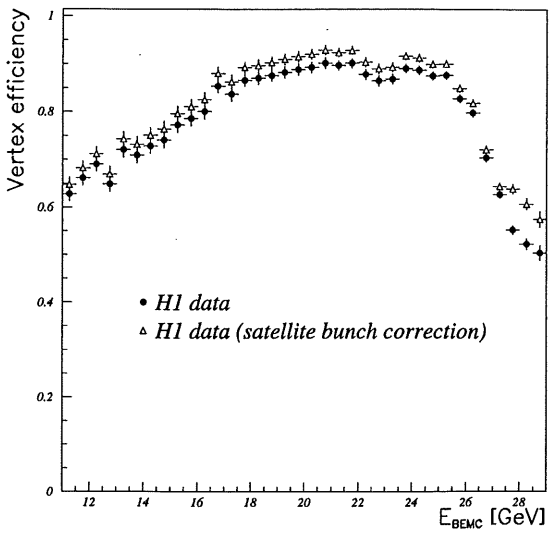

Figure 5.36: **Influence of the satellite correction on the vertex efficiency.**

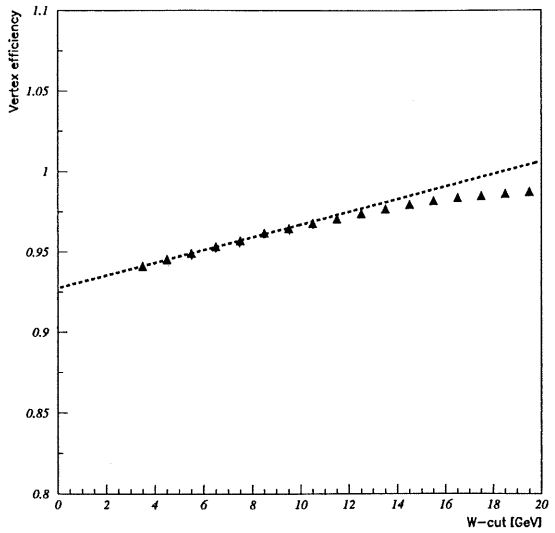

Figure 5.37: **Vertex efficiency as a function of the W-cut in the Monte Carlo.** *The Monte Carlo data only describes the data for $W > 4$ GeV. The straight line is a linear fit of the data points in the region $W = 4$–10 GeV.*

electron enters the jet chambers. Figure 5.38 shows the extra efficiency due to the W cut in all the Q^2 bins. In the high Q^2 region this extra correction is negligable. Table 5.11 shows the same corrections obtained from the same extrapolation, but in all the x, Q^2 bins.

5.13.5 Summary

In the previous sections we studied the discrepancies between the vertex efficiency of the data and the Monte Carlo and several contributions to the systematical error due to the discrepancies are added:

- The error due to the W cut correction procedure is x,Q^2-dependent, and reaches values up to 5% in certain bins.
- In the bins where the CIP can be used, an additional error up to 3% at larger values of x is added.
- In the low Q^2, high x bins where the CIP cannot be used due to geometrical limitations, the additional error varies between zero and 3.5%. This is the result of the study with the strong electron identification cuts, and the satellite bunch correction, which accounts for about 1.5%, independently of the energy.

5.14 Acceptances and migrations

In equation (4.3) we defined the acceptance Acc as the ratio of the reconstructed events to the number of generated events. Since we will use the Monte Carlo method to calculate

$x \setminus Q^2\ GeV^2$	4.217 – 5.623	5.623 – 7.499	7.499 – 10.0	10.0 – 13.34	13.34 – 17.78
$1.00 \times 10^{-4} - 1.58 \times 10^{-4}$			0.942	0.949	0.958
$1.58 \times 10^{-4} - 2.51 \times 10^{-4}$			0.953	0.966	0.977
$2.51 \times 10^{-4} - 3.98 \times 10^{-4}$			0.970	0.982	0.985
$3.98 \times 10^{-4} - 6.31 \times 10^{-4}$		0.969	0.985	0.987	0.986
$6.31 \times 10^{-4} - 1.00 \times 10^{-3}$		0.981	0.985	0.993	0.983
$1.00 \times 10^{-3} - 1.58 \times 10^{-3}$		0.980	0.989	0.984	0.983
$1.58 \times 10^{-3} - 2.51 \times 10^{-3}$		0.976	0.980	0.985	0.982
$2.51 \times 10^{-3} - 3.98 \times 10^{-3}$		0.967	0.983	0.984	0.988
$3.98 \times 10^{-3} - 6.31 \times 10^{-3}$		0.909		0.940	
$6.31 \times 10^{-3} - 1.00 \times 10^{-2}$					
$1.00 \times 10^{-2} - 1.58 \times 10^{-2}$					
$1.58 \times 10^{-2} - 2.51 \times 10^{-2}$					
$2.51 \times 10^{-2} - 3.98 \times 10^{-2}$					
$3.98 \times 10^{-2} - 6.31 \times 10^{-2}$					
$6.31 \times 10^{-2} - 1.00 \times 10^{-1}$					
$1.00 \times 10^{-1} - 1.58 \times 10^{-1}$					

$x \setminus Q^2\ GeV^2$	17.78 – 23.71	23.71 – 31.62	31.62 – 42.17	42.17 – 56.23	56.23 – 74.99
$1.00 \times 10^{-4} - 1.58 \times 10^{-4}$	0.964	0.975	0.990	0.997	
$1.58 \times 10^{-4} - 2.51 \times 10^{-4}$	0.986	0.987	0.993	0.997	
$2.51 \times 10^{-4} - 3.98 \times 10^{-4}$	0.993	0.991	0.998		
$3.98 \times 10^{-4} - 6.31 \times 10^{-4}$	0.991	0.992	0.996		
$6.31 \times 10^{-4} - 1.00 \times 10^{-3}$	0.993	0.996	0.998		
$1.00 \times 10^{-3} - 1.58 \times 10^{-3}$	0.991	0.997			
$1.58 \times 10^{-3} - 2.51 \times 10^{-3}$	0.987	0.997			
$2.51 \times 10^{-3} - 3.98 \times 10^{-3}$					
$3.98 \times 10^{-3} - 6.31 \times 10^{-3}$					
$6.31 \times 10^{-3} - 1.00 \times 10^{-2}$					
$1.00 \times 10^{-2} - 1.58 \times 10^{-2}$					
$1.58 \times 10^{-2} - 2.51 \times 10^{-2}$					
$2.51 \times 10^{-2} - 3.98 \times 10^{-2}$					
$3.98 \times 10^{-2} - 6.31 \times 10^{-2}$					
$6.31 \times 10^{-2} - 1.00 \times 10^{-1}$					
$1.00 \times 10^{-1} - 1.58 \times 10^{-1}$					

Table 5.11: **Extra vertex efficiency due to the W cut as a function of Q^2, x.** *The extra vertex efficiency is calculated by extrapolating the efficiency at $W = 4$ GeV to $W = 0$, as show in figure 5.37, but for every Q^2, x bin separately. In bins without a number, there is no extra efficiency correction necessary.*

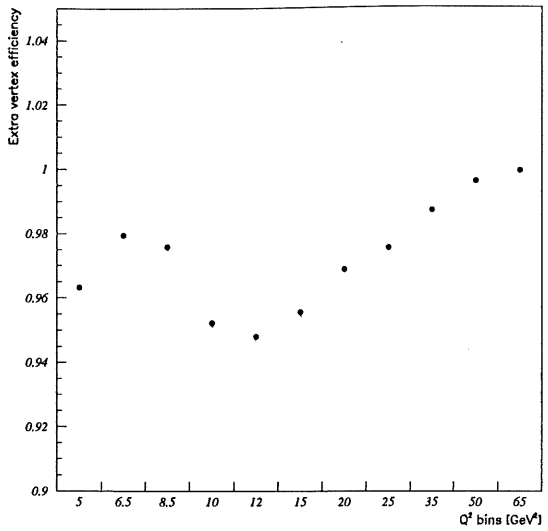

Figure 5.38: **Extra vertex efficiency as a function of Q^2 from the W-extrapolation.**
The extra vertex efficiency is calculated by extrapolating the efficiency at $W = 4$ GeV to $W = 0$, as shown in figure 5.37, but for every Q^2 bin separately.

F_2 in our analysis (see equation (4.12)) it is not necessary to calculate the acceptance explicitely to obtain F_2. However, we will use the acceptance as a quality criterion to select bins for which we will present F_2. Additionally, we can define two related quantities:

$$Acc_{migration} = \frac{|N_{in}(\Delta x, \Delta Q^2) - N_{out}(\Delta x, \Delta Q^2)|}{N_{rec}(\Delta x, \Delta Q^2)}, \tag{5.20}$$

and

$$Acc_{stability} = \frac{N_{stay}(\Delta x, \Delta Q^2)}{N_{gen}(\Delta x, \Delta Q^2)}. \tag{5.21}$$

The migration matrix $Acc_{migration}$ (or smeared acceptance) is defined as the difference of the events migrating into the bin (N_{in}) and those migrating out of the bin (N_{out}), divided by the total number of reconstructed events. The stability matrix $Acc_{stability}$ is the fraction of the generated events which stay in the bins.

In our analysis we only present F_2 in bins for which the acceptance lies between:

$$50\% \leq Acc \leq 150\%. \tag{5.22}$$

However, the acceptance can be very high, even when there are very few events which are generated in a particular bin, compared to the number of reconstructed events in the same bin. Therefore, we also require:

$$Acc_{migration} \leq 50\% \tag{5.23}$$

$$50\% \geq Acc_{stability} . \tag{5.24}$$

The y cuts which we introduced in section 5.4.1 already have the same effect as the cuts on Acc, $Acc_{migration}$ and $Acc_{stability}$, and none of the bins which are within our kinematical cuts violate the acceptance criterion. The acceptances for all the bins are included in the tables B.1 and B.2. The acceptances are calculated with the MRSH parametrisation. The mean acceptance is 0.90.

5.15 The bin centre corrections

The *bin centre correction* factor $\sigma_{Born}/\bar{\sigma}_{Born}$ in equation (4.9) was calculated by using a numerical integration program together with the PDF library package [63]. The obtained numerical precision was better than 0.1%. By doing the same calculation for the structure function parametrisation with and without F_L, a systematic difference of less than 1% was observed.

5.16 Structure function measurement

5.16.1 The Structure function $F_2(x, Q^2)$

The structure function $F_2(x, Q^2)$ was derived after radiative corrections from the one-photon exchange cross section

$$\frac{d^2\sigma}{dx\, dQ^2} = \frac{2\pi\alpha^2}{Q^4 x}\left(2 - 2y + \frac{y^2}{1+R}\right) F_2(x, Q^2). \tag{5.25}$$

The ratio $R = F_2/2xF_1 - 1$ has not yet been measured at HERA, and was calculated with the DJANGO program, using the GRV structure function parametrisation. The values are given in tables A.1, A.2, A.5, A.6, A.9, A.10, A.13, A.14 and A.15. Since the term with R in equation (5.25) has a weight y^2, the effect of an error on R is very small on F_2. For example at $y = 0.6$ a 20% error on R corresponds only to a 2% uncertainty on F_2 for values of R between 0.6 and 1. We will add no extra error to F_2 due to the uncertainty of R, since the values for R are quoted.

We will use both the opened triangle data and the closed triangle data to measure F_2. The opened triangle data allows a measurement of F_2 at lower Q^2, typically between 5 GeV^2 and 10 GeV^2, and consequently at lower x, compared to the closed triangle data.

We use both the electron and sigma methods to calculate the kinematical quantities x and Q^2. The electron method has the best resolutions on x and Q^2 at large y and is independent of the hadron reconstruction, apart from the vertex requirement. The sigma method has small radiative corrections and extends from very low to large y values. The combination of both methods means that a larger kinematic range could be covered for the measurement of $F_2(x, Q^2)$.

Figure 5.39 represents the data at lower x in the full Q^2 range, obtained with the E method, and figure 5.40 shows the result of the Σ method. The systematic errors will be summarised below. The full line on figures 5.39 and 5.40 is the fit result of a phenomenological parametrisation of previous H1 (1993), NMC and BCDMS data [41]. This parametrisation is written as:

$$F_2(x, Q^2) = \left\{ax^b + cx^d\left(1 + e\sqrt{x}\right)\left(\log Q^2 + f\log^2 Q^2\right)\right\}(1-x)^g, \tag{5.26}$$

and this parametrisation reflects the following observations: (i) it is constructed to describe the F_2 data from H1, but also NMC and BCDMS, over four orders of magnitude in Q^2 and x; (ii) F_2 is known to vanish like $(1-x)^g$ for large x, with g near 3 in agreement with the quark counting rules and previous experiments; (iii) the integral of F_2 over x is nearly independent of Q^2 due to momentum conservation, which means that the rise of F_2 with Q^2 at low x must be compensated by a decrease of F_2 with Q^2 at higher x (figure 5.41); (iv) the Q^2 dependence of F_2 is expected to logarithmic. Since the data is attempted to be decribed over four orders of magnitude, a quadratic term in $\log Q^2$ is added; (v) an extra term, independent of Q^2 is also introduced.

The fit parameters of the analysis of the 1993 data are:

a	b	c	d	e	f	g
3.07	0.75	0.14	-0.19	-2.93	-0.05	3.65

The H1 results of our F_2 measurement are in good agreement with this parametrisation.

The opened triangle sample clearly extends the measurement to lower values of Q^2, where F_2 was never measured before. On the other hand, the sigma method extends the electron measurements to higher values of x, into an area measured by fixed target experiments. We observe a smooth transition between the fixed target data and our data. The results of the electron and sigma methods, and the opened and closed triangle samples, agree well within the errors where they overlap.

The corresponding values of measured structure function are given in tables A.1, A.2, A.5, A.6, A.9, A.10, A.13, A.14 and A.15 together with their statistical and systematic errors.

Tables D.1, D.2 and D.3 list an overview of the F_2 measurement of our analysis, and contain the F_2 data points with the smallest total error, taken from the electron and sigma methods, and the opened and closed triangle samples. Figure 5.41 shows the final F_2 points of tables D.1, D.2 and D.3 as a function of Q^2 for several values of x, together with NMC (open squares) and BCDMS (open triangles) data, as well as the GRV parametrisation and the fit result of the phenomenological parametrisation [41].

5.16.2 Systematic errors

The systematic errors on F_2 orignate from several sources, and part of them affect differently the F_2 measurement based on different methods. One can distinguish global errors and bin-dependent errors.

Global errors

1. An error on the luminosity of 1.8% (see section 2.2.6).

2. An error on the ToF selection efficiency of 1% [15].

3. An error on the L4 selection efficiency of 1% [15].

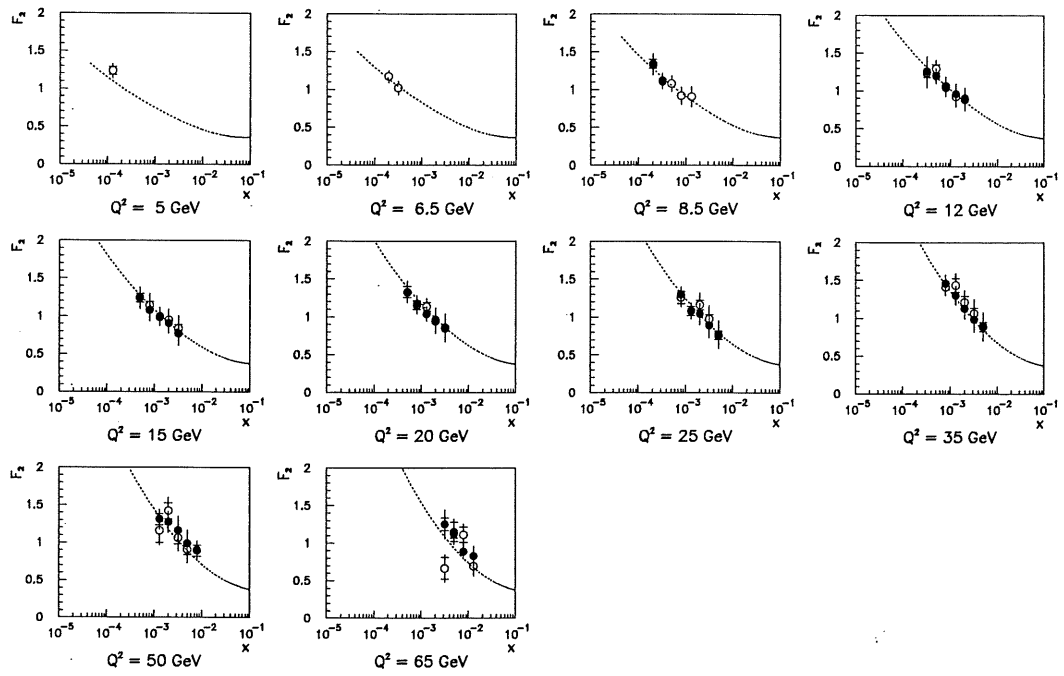

Figure 5.39: **Measurement of $F_2(x, Q^2)$ with the 'electron' (E) Monte Carlo method.**
The closed circles represent the closed triangle data, the open circles the opened triangle data. The full line is the fit result of a phenomenological parametrisation of previous H1 (1993), NMC and BCDMS data [41].

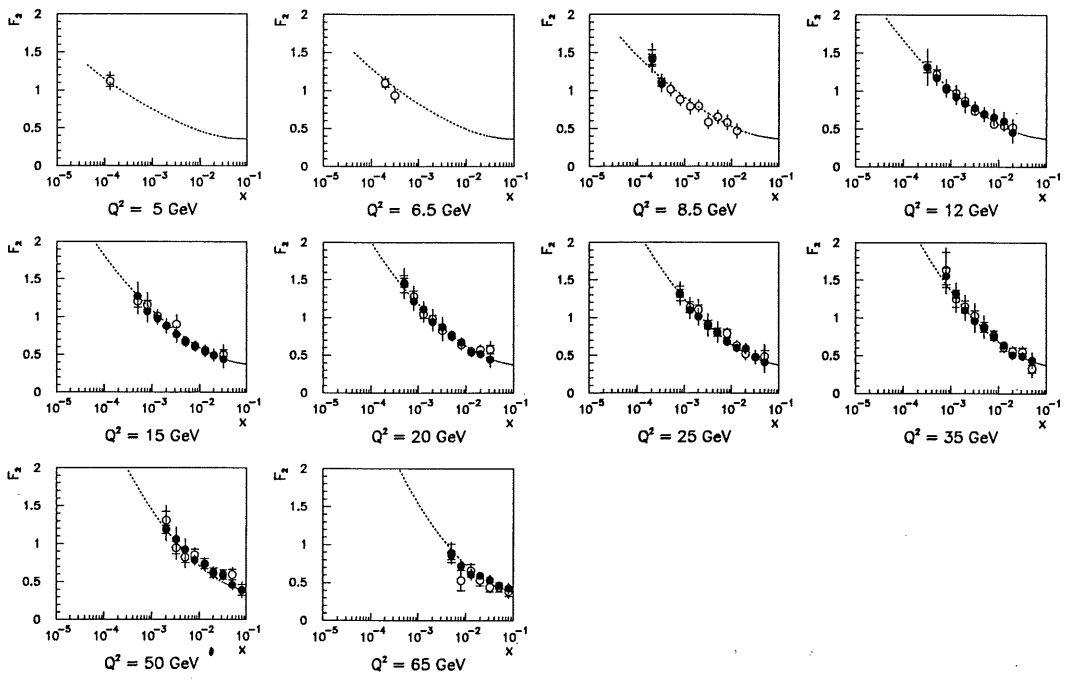

Figure 5.40: **Measurement of $F_2(x, Q^2)$ with the 'sigma' (Σ) Monte Carlo method.**
The closed circles represent the closed triangle data, the open circles the opened triangle data. The full line is the fit result of a phenomenological parametrisation of previous H1 (1993), NMC and BCDMS data [41].

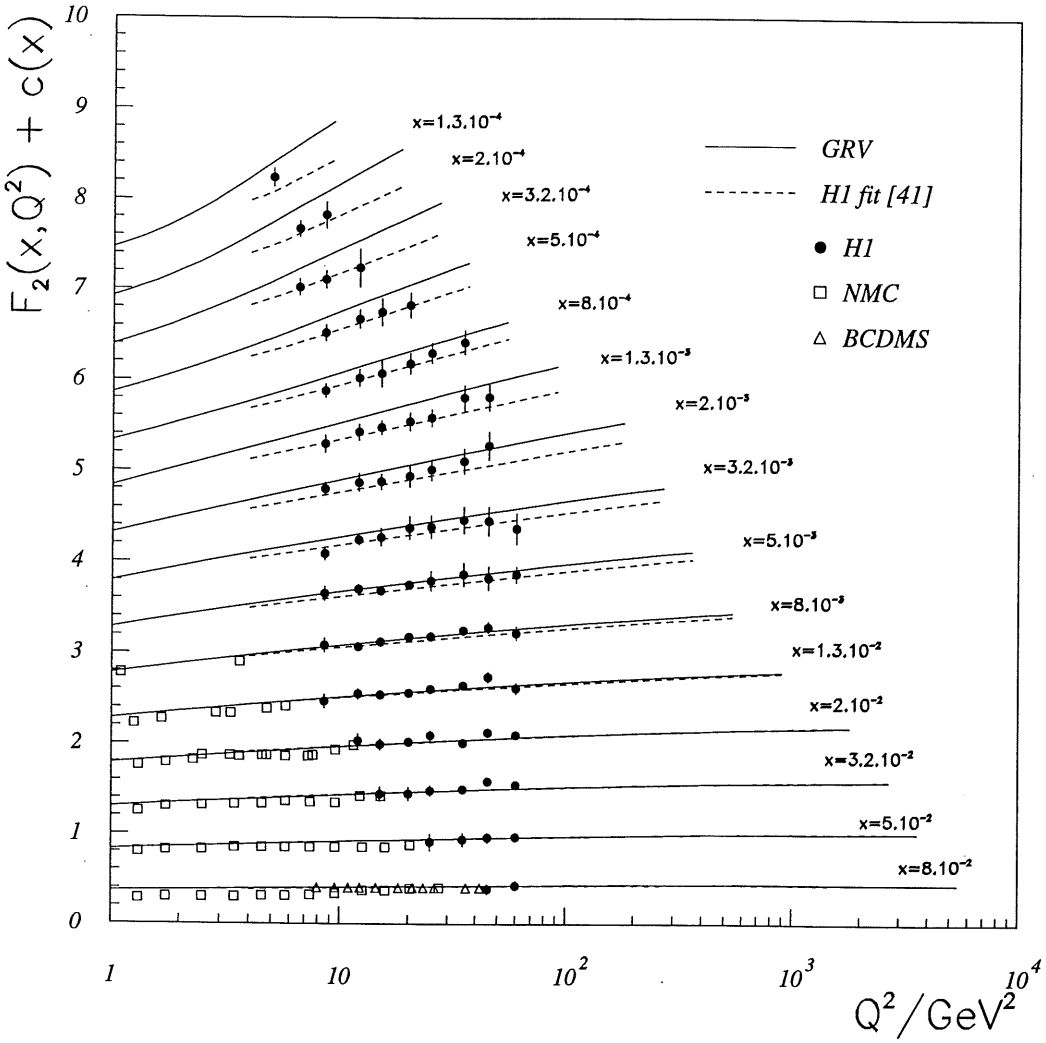

Figure 5.41: **Scaling violation of $F_2(x, Q^2)$.**
The H1 data (closed circles) is shown together with the fixed target experiments NMC and BCDMS. The full line is the F_2 prediction by the GRV parametrisation and the dashed line the fit result of a phenomenological parametrisation of previous (1993) H1, NMC and BCDMS data [41]. The F_2 values are plotted with the total errors in a linear scale adding a term $c(x) = 0.5(i_x - 1)$ to F_2, where i_x is the bin number starting at $i_x = 1$ for $x_c = 8 \times 10^{-2}$.

Bin-dependent errors

1. A potential miscalibration of the electronic energy scale in the BEMC was estimated to be 2% (section 5.8.3).

2. A shift of up to 2.3 mrad for the electron polar angle (section 5.9).

3. An error of up to 3% in the radiative correction due to uncertainties from second order corrections and the absence of the soft photon exponentiation in the HERACLES Monte Carlo. The accuracy was cross checked by comparing the Monte Carlo with TERAD, and a direct estimate has been made comparing the cross section from the E method by using DJANGO and TERAD.

   This relative ratio of the radiative corrections obtained from DJANGO and TERAD is quoted in table C.1.

4. The structure function dependence of the acceptance and bin size corrections which was controlled better than 2%. This result was obtained by calculating F_2 with a reweighted Monte Carlo, according to the MRSD$^-$ parametrisation, instead of MRSH (see equation (5.8)).

5. The discrepancy between the tagged photoproduction events and the Monte Carlo prediction is smaller than 30%. Taking into account the fraction of the photoproduction events in the DIS sample, the uncertainty due to this background was assumed to be smaller than 2.5%. This only affects the highest y bins at lower Q^2.

6. It was verified that the Monte Carlo describes the all the inefficiencies of the data, except the distribution of the distance between the closest BPC point to the BEMC cluster. The agreement between the individual simulated and experimental efficiencies was better than 2%, so an overall error of 2% was added.

7. An additional error was added to take into account the vertex reconstruction efficiency variation. This error is x,Q^2-dependent, and reaches values up to 8.5% in some bins (see section 5.13.5).

These systematic uncertainties affect the E and Σ methods differently, as can be seen in figures 5.39 and 5.40.

Statistical errors in the Monte Carlo acceptance and efficiency calculations were computed and added quadratically to the systematic error. The statistical errors are typically less than 4% for the closed triangle sample (although they reach 8% in some bins) and twice as large for the opened triangle sample.

5.16.3 Discussion

Our analysis extends the measurement of F_2 by fixed target experiments by two orders of magnitude, down to $x = 1.3 \times 10^{-4}$, while the highest x value where we measured is 0.08. The agreement between the opened and closed triangle data is very good, while the former allowed to reach the lowest bins in x and Q^2. The electron and sigma methods methods display consistency and, as expected, the sigma method is better to measure F_2 at low y,

while the electron method is superior at higher values of y. Compared with the HERA data of 1993, an extension of the kinematic range is achieved towards low x and low Q^2.

Figures 5.39 and 5.40 show that the structure function F_2 rises steeply with x decreasing to $x = 1.3 \times 10^{-4}$, which confirms earlier observations by Zeus and H1 based on 1993 data. This rise exludes an F_2 based on Regge models, predicting a rather flat F_2 as a function of x (e.g. $MRSD^0$). The NLO DGLAP evolution equations describe the data well over the whole kinematical range, so that there is no indication that more terms or different dynamical mechanisms such as BFKL, are necessary. However, the data does not exclude this either. Recent NLO fit results by H1 [22] confirm that the strong rise of F_2 at small values of x can indeed be described by the conventional DGLAP evolution equations.

As can be seen on all these figures, the dependence of F_2 on Q^2 is weak for $x \leq 0.1$. The violation of scaling appears to be stronger for smaller values of x, a trend already observed in fixed target experiments.

Our data sample is a subset of the full H1 data. By using events with the scattered electron detected by the liquid argon (LAr) calorimeter, the structure function F_2 could be measured up to $Q^2 = 5000$ GeV^2. By using selected radiative events and data from the satellite bunch interactions, Q^2 values down to 1.5 GeV^2 could be reached. The results of the ongoing H1 analysis based on the extended data are compatible with our own results [22].

Chapter 6

The gluon density of the proton at low x

6.1 Introduction

Gluons carry about half of the proton momentum, and yet it is not trivial to measure the gluon momentum density inside the proton, because in the lowest order of perturbative QCD photons do not couple to gluons. In leading order (LO) logarithmic scaling violation of F_2 occurs, caused by gluon bremstrahlung and $q\bar{q}$-pair creation from gluons. In the previous chapter we observed that the rise of F_2 as a function of $\log Q^2$ (scaling violation) is x-dependent, and this scaling violation increases with decreasing x. For $x < 0.12$ the scaling violation is positive, which means that with increasing Q^2, the $q\bar{q}$ production causes the structure function to rise at low x. At low $x < 10^{-2}$ the creation of sea quarks from gluons dominates the contribution from gluon bremstrahlung.

In this chapter, the gluon momentum distribution in the proton will be approximatively determined by using the method of Prytz, which we introduced in section 1.8. This LO method assumes that at low x only the gluons play a role and uses the slope in Q^2 of the structure function $F_2(x, Q^2)$ to calculate $xg(x)$:

$$\frac{dF_2(x,Q^2)}{d\log Q^2} = \frac{10}{27}\frac{\alpha_s(Q^2)}{\pi}\, g^*(2x, Q^2), \tag{6.1}$$

where $g^*(x, Q^2) = xg(x, Q^2)$. The gluon density at $2x$ can thus be estimated by determining $dF_2(x, Q^2)/d\log Q^2$. As we pointed out, the error of this approximation can be up to 20%, and the method is limited to $x < 10^{-1}$.

The method of Prytz is useful as a first order estimation of the gluon density in the proton as a function of x. In this chapter we will present the result of the estimation of $xg(x, Q^2)$ for $Q^2 = 20$ GeV^2, and compare the result with a LO QCD fit of the H1 data.

6.2 Calculation of $dF_2/d\log Q^2$

We assume the following parametrisation for $F_2(x, Q^2)$ as a function of x for a fixed value of Q^2:

$$F_2(x, Q^2) = a_1(x) + a_2(x)\ \log(Q^2/GeV^2). \tag{6.2}$$

The values of $dF_2/d\log Q^2 = a_2(x)$ are obtained from a linear fit through the F_2 points of tables D.1, D.2 and D.3, taking into account the statistical error on every point.

To estimate the systematical errors of $dF_2/d\log Q^2$, the following procedure was used: every data value of $F_2(x, Q^2)$ was raised and lowered by the systematical error $\delta F_2(syst)$ of the point. For N data points per value of x, this results in 2^N combinations. For

x	$\frac{dF_2}{d\log Q^2}$	δ_{stat}	δ_{syst}	δ_{tot}	N_{points}
0.000200	0.556	0.238	0.444	0.504	2
0.000320	0.428	0.090	0.226	0.243	3
0.000500	0.356	0.069	0.150	0.165	4
0.000800	0.364	0.044	0.110	0.118	6
0.001300	0.311	0.029	0.093	0.097	7
0.002000	0.259	0.028	0.083	0.088	7
0.003200	0.275	0.023	0.068	0.072	8
0.005000	0.153	0.023	0.061	0.065	8
0.008000	0.114	0.020	0.054	0.057	8
0.013000	0.114	0.019	0.055	0.058	8
0.020000	0.054	0.022	0.062	0.065	7

Table 6.1: $dF_2/d\log Q^2$ **as a function of** x
Based on a linear fit of the F_2 data of this analysis.

each combination, the linear fit was made, and the maximum difference of the slope with respect to the original value of $dF_2/d\log Q^2$ was used as the systematical error.

The result of the fits are listed in table 6.1 together with the statistical and systematical errors. and the obtained values of $dF_2/d\log Q^2$ are plotted in figure 6.1. The full line in the figure corresponds to the result of $dF_2/d\log Q^2$ calculated with the GRV parametrisation in LO for $Q^2 = 20$ GeV^2. For values $x < 10^{-2}$ one observes a strong scaling violation.

6.3 Calculation of the gluon density $xg(x, Q^2)$

A first order approximation of the gluon density $xg(x, Q^2)$ can be calculated by using equation (6.1) from the fit results of $dF_2/d\log Q^2$. In this linear approximation, $dF_2/d\log Q^2$ is only a function of x, from which $\alpha_s(Q^2)\ g^*(x, Q^2) = a_2(x)$ follows. By fixing $\alpha_s(Q^2)$, the Q^2-dependence of the gluon density is determined.

We calculated the gluon density at $Q^2 = 20$ GeV^2, because the result of a LO QCD fit [22] of H1 was also presented at this value. The value of α_s follows from

$$\alpha_s = \frac{4\pi}{\beta_0 \log \frac{Q^2}{\Lambda^2}}, \tag{6.3}$$

where $\beta_0 = 11 - 2n_f/3 = 11 - 8/3$, since we set the number of active quark flavours n_f to 4. Further we use $\Lambda = 185$ MeV, which is the result of a recent LO QCD analysis of H1. A variation of ± 80 MeV for Λ results in a 15% change of α_s, and thus of $xg(x)$.

The gluon density $xg(x, Q^2)$ at $Q^2 = 20$ GeV^2 is plotted in figure 6.2, and shows a significant rise at low x, already observed by a previous measurement [41]. As a comparison, the result of a recent LO QCD fit [22] of H1 using the DGLAP evolution is superimposed on the plot, and is in good agreement with our result. Also shown in figure 6.2 are the recent results of the NMC collaboration [11]. Figure 6.2 shows the significant increase

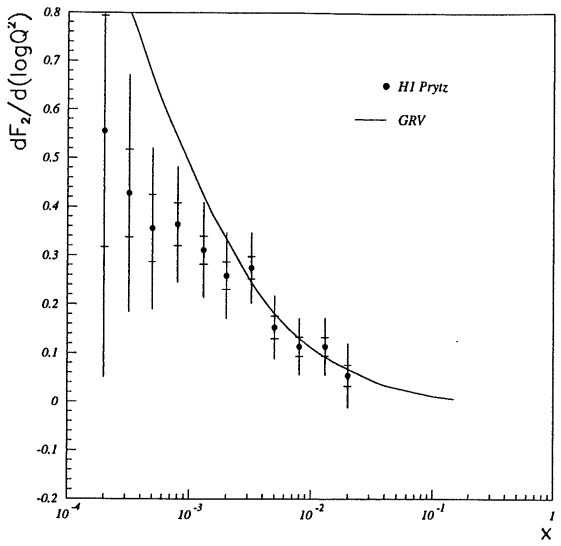

Figure 6.1: $dF_2/d\log Q^2$ **as a function of** x**.**
Based on a linear fit of the F_2 data of this analysis. The inner error bars represent the statistical errors, the total error bars correspond to the statistical and systematical errors added in quadrature. The full line is calculated from the GRV parametrisation in LO at $Q^2 = 20\ GeV^2$.

of the kinematical range ($2 \cdot 10^{-4} < x < 2 \cdot 10^{-2}$) in which the gluon density could be determined by H1, compared to NMC (and in fact all the fixed target experiments).

The rise of $xg(x)$ at small values of x has caused much debate as to whether it results from conventional DGLAP QCD evolution of the parton densities, or whether a new regime is entered where the dynamics is described by the BFKL evolution equation. The latter resums all leading $\log(1/x)$ terms in the perturbative expansion, and is therefore expected to be particularly suited for the study of the small x region. However, our result agrees sufficiently well with the H1 DGLAP QCD fit result [22] (figure 6.2) to conclude that the DGLAP evolution equations describe the rise of $xg(x)$ well in the new low x kinematic domain.

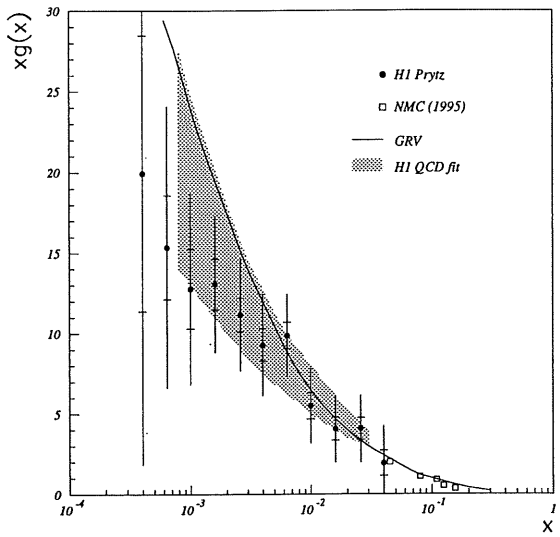

Figure 6.2: **The gluon density $xg(x)$ at $Q^2 = 20$ GeV^2.**
The data points are the values obtained by the method of Prytz. The inner error bars correspond to the statistical errors, the total error bars correspond to the statistical and systematical errors added in quadrature. The full line is calculated from the GRV parametrisation in LO at $Q^2 = 20$ GeV^2.

Chapter 7

Summary

In this thesis we described the measurement of the proton structure function F_2 and an approximate determination of the gluon momentum density $xg(x)$, based on deep inelastic e^+p scattering events observed by the H1 detector in 1994.

We introduced the theoretical framework for the description of deep inelastic lepton-nucleon scattering, which are based on a model of quark-parton scattering and QCD. We then showed how the Q^2 evolution of the structure function can be calculated, and looked in particular at the low x region, experimentally unexplored before HERA and where new physics is expected. We summarised different parametrisations of the structure function, and presented an approximate method which allows to estimate the gluon momentum density of the proton from the scaling violation of the structure function.

We described the H1 detector in detail, focussing on the detector components which are relevant to our analysis. One chapter was dedicated to the data acquisition of the multiwire proportional chambers, to which a substantial personal contribution was made. The data acquisition is based on an interrupt-driven real-time microprocessor system, that has to meet the most stringent requirements of speed and data flow capacity. Roughly 4000 channels are to be read out at a typical rate of 50 Hz, after which the data needs to be zero-surpressed and sent to the central data acquisition. This was achieved by using an optimal combination of performant hardware and machine level software. The data acquisition software was complemented by user-friendly control and monitoring software with a graphical user-interface (GUI). The software which we designed and implemented was responsible for the 'first day' MWPC data taking of the H1 cosmic runs in 1991 and 1992, and the *ep* runs in 1993.

Before HERA and H1, F_2 was only measured by fixed target experiments for $x \geq 0.008$. It is expected from QCD that only at x values below 10^{-2} the gluons start to play a dominant role in deep inelastic scattering and in the composition of the proton. Extrapolating the fixed target F_2 measurements to lower x according to different theoretical models leads to very divergent results due to a lack of experimental constraints, and before HERA existed it was impossible to predict the low x behaviour of the proton structure function.

With the advent of the HERA collider, it is possible to extend the measurement of the structure function to low x with two orders of magnitude. The measurement over a several orders of magnitude in Q^2 at different values of x allow to test the validity of the DGLAP evolution equations. An unsolved question is whether an additional dynamical mechanism such as BFKL, with an evolution of F_2 proportional to $x^{-\frac{1}{2}}$, is necessary to describe the evolution.

Our analysis is based on a sample of e^+p deep inelastic scattering events with an integrated luminosity of 2.5 pb−1, about then times the statistics of the H1 data of 1993.

With the H1 detector it is possible to measure both the leptonic and the hadronic final state, which makes it possible to use different methods for the reconstruction of the kinematical variables. In our analysis we used two complementary methods, one based on the scattered electron energy and angle, the other based on a combination of electron and hadron information. Both methods partially overlapped kinematically, allowing to cross check the systematic errors. We found good agreement between the results obtained from both methods. At high values of the scaling variable y (typically $y \geq 0.15$), the method based on the scattered electron has a superior resolution, while for lower y the method which uses electron and hadron information is less sensitive to radiative corrections and calibration errors. Together both methods allow to cover the whole kinematical range accessible by H1. Our analysis is limited to events in which the scattered electron enters the Backward ElectroMagnetic Calorimeter (BEMC), since it corresponds to the physically most interesting domain of low Q^2 and low x. A smooth transition is observed from the fixed target high x data to the HERA low x data.

Apart from a ten times higher statistics compared to the data available in 1993, the 1994 data included measurements by the innermost part of the Backward Electromagnetic Calorimeter (BEMC), allowing to measure scattered electrons down to 174° instead of 173°. In our analys we made use of this data, expanding the Q^2 range of our measurement from 10 GeV^2 down to 5 GeV^2 and thus to smaller x from 2×10^{-4} to 1.3×10^{-4}.

A detailed analysis of the systematical errors in the range 5 GeV^2 $< Q^2 <$ 65 GeV^2 and $1.3 \times 10^{-4} < x < 8 \times 10^{-2}$ for the two reconstruction methods and the two data samples was made, and resulted in typical systematical errors up to 10% and statical errors below 4%.

The rise of the structure function with decreasing x at fixed Q^2 was already observed by H1 and Zeus based on the analysis of the 1993 data, and is confirmed by our analysis. This rise excludes an F_2 based on Regge models, predicting a rather flat F_2 as a function of x (e.g. $MRSD^0$). The NLO DGLAP evolution equations seem to describe the data well over the full kinematical range, including the NMC and BCDMS data. This means that the BFKL mechanism is not necessary, although the data does not exclude it either.

The rate of growth of F_2 at low x increases with increasing Q^2 which has been one of the very first predictions of perturbative QCD. This rise of F_2 does not vanish at rather low Q^2. To study the transition towards $Q^2 \longrightarrow 0$ it is interesting to study the F_2 evolution further at even lower values of Q^2. This will be possible with the 1995 data (and later), since the backward electromagnetic calorimeter (BEMC) has been replaced by a lead-fibre optic calorimeter (SPACAL), allowing measurements down to $Q^2 \approx 1$ GeV^2.

Our data sample is a subset of the full H1 data. By using events with the scattered electron detected by the liquid argon (LAr) calorimeter, the structure function F_2 could be measured up to $Q^2 = 5000$ GeV^2. By using selected radiative events and data from the satellite bunch interactions, Q^2 values down to 1.5 GeV^2 could be reached. The results of the ongoing H1 analysis based on the extended data are compatible with our own results [22]. A GRV fit at $Q_0^2 = 0.3$ describes the data well over four orders of magnitude in Q^2 and x.

We calculated the gluon momentum density $xg(x)$ of the proton for $Q = 20$ GeV^2 by using an approximate method by Prytz, based on the scaling violation of the structure function. This method assumes that the gluons dominate entirely the rise of F_2 at low x. We found good agreement with a recent QCD fit analysis by H1. The gluon density $xg(x)$

rises for decreasing values of x and this rise can be well described by the DGLAP evolution equations in the new kinematic domain.

The present measurements are dominated by their systematical errors. To increase the kinematical range of the measurement and to decrease the systematic errors, several new detector components were introduced into H1 in 1995: SPACAL (which, as we mentioned, replaces the BEMC), has an electromagnetic and a hadronic part, leading to an improved tagging of photoproduction events and a more precise reconstruction of the kinematical quantities with the sigma method. The BPC was replaced by a drift chamber and a new silicium-detector telescope in the backward part of H1 allows to measure tracks down to 176°, corresponding to $Q^2 = 1.5$ GeV^2, $x = 10^{-6}$.

Appendix A

Tables with the measured F_2 data and related quantities

Meaning of the quantities in the tables:

F_2	Experimental value of F_2
$\delta F_2(stat)$	Statistical error on F_2
$\delta F_2(syst)$	Systematic error on F_2
$\delta F_2(tot)$	Total error on F_2
R_{QCD}	Value of R calculated from the GRV parametrisation
y	Bjorken y in the bin centre
Rad. Corr	Radiative corrections calculated with TERAD
F_2 GRV	F_2 calculated based on the GRV parametrisation
N_{DATA}	Number of selected events, with all backgrounds subtracted
frac(bg)	Fraction of beam-gas and beam-wall background (%)
frac(γp)	Fraction of photoproduction background (%)
N_{MC}	Number of selected Monte Carlo events (weighted)
N_D/L_D	Events per lumi ('yield') in data [nb^{-1}]
N_D/L_D	Events per lumi ('yield') in Monte Carlo [nb^{-1}]
N_{gen}	Number of generated events (unweighted)

The Q^2 and x values in the tables are the values in the centre of each bin (Q_c^2, x_c). The bin boundaries of the corresponding bins are given in section 4.5.

$Q^2 = 8.5$ GeV^2								
x	F_2	$\delta F_2(stat)$	$\delta F_2(syst)$	$\delta F_2(tot)$	R_{QCD}	y	Rad. Corr.	F_2 GRV
0.000200	1.320	0.036	0.162	0.166	0.299	0.471	1.317	1.752
0.000320	1.106	0.032	0.096	0.102	0.297	0.297	1.254	1.516

$Q^2 = 12$ GeV^2								
x	F_2	$\delta F_2(stat)$	$\delta F_2(syst)$	$\delta F_2(tot)$	R_{QCD}	y	Rad. Corr.	F_2 GRV
0.000320	1.265	0.032	0.236	0.238	0.275	0.419	1.296	1.715
0.000500	1.199	0.031	0.121	0.125	0.273	0.265	1.237	1.483
0.000800	1.044	0.029	0.121	0.125	0.270	0.167	1.183	1.270
0.001300	0.958	0.028	0.118	0.122	0.265	0.105	1.131	1.080
0.002000	0.906	0.028	0.123	0.126	0.259	0.067	1.086	0.935

$Q^2 = 15$ GeV^2								
x	F_2	$\delta F_2(stat)$	$\delta F_2(syst)$	$\delta F_2(tot)$	R_{QCD}	y	Rad. Corr.	F_2 GRV
0.000500	1.248	0.033	0.162	0.165	0.260	0.331	1.262	1.589
0.000800	1.084	0.029	0.162	0.164	0.257	0.209	1.204	1.356
0.001300	1.004	0.027	0.108	0.112	0.253	0.132	1.150	1.148
0.002000	0.911	0.025	0.125	0.127	0.247	0.083	1.104	0.990
0.003200	0.775	0.025	0.124	0.127	0.239	0.052	1.055	0.843

$Q^2 = 20$ GeV^2								
x	F_2	$\delta F_2(stat)$	$\delta F_2(syst)$	$\delta F_2(tot)$	R_{QCD}	y	Rad. Corr.	F_2 GRV
0.000500	1.325	0.037	0.154	0.159	0.245	0.441	1.302	1.723
0.000800	1.181	0.033	0.115	0.119	0.242	0.278	1.234	1.464
0.001300	1.040	0.029	0.098	0.103	0.238	0.176	1.176	1.234
0.002000	0.969	0.027	0.145	0.147	0.232	0.111	1.128	1.059
0.003200	0.850	0.024	0.148	0.150	0.224	0.070	1.077	0.897

$Q^2 = 25$ GeV^2								
x	F_2	$\delta F_2(stat)$	$\delta F_2(syst)$	$\delta F_2(tot)$	R_{QCD}	y	Rad. Corr.	F_2 GRV
0.000800	1.298	0.038	0.120	0.125	0.232	0.348	1.261	1.555
0.001300	1.083	0.032	0.094	0.099	0.227	0.220	1.198	1.306
0.002000	1.044	0.031	0.151	0.154	0.222	0.139	1.148	1.117
0.003200	0.891	0.027	0.151	0.154	0.214	0.087	1.096	0.942
0.005000	0.779	0.026	0.129	0.132	0.204	0.055	1.047	0.804

$Q^2 = 35$ GeV^2								
x	F_2	$\delta F_2(stat)$	$\delta F_2(syst)$	$\delta F_2(tot)$	R_{QCD}	y	Rad. Corr.	F_2 GRV
0.001300	1.305	0.041	0.162	0.167	0.213	0.308	1.236	1.412
0.002000	1.133	0.036	0.151	0.155	0.208	0.194	1.181	1.202
0.003200	0.991	0.032	0.172	0.175	0.200	0.122	1.125	1.008
0.005000	0.907	0.030	0.159	0.161	0.191	0.077	1.075	0.854

Table A.1: **F_2 for the E Monte Carlo method, closed triangle data [part 1].** *For an explanation of the quantities, see text.*

$Q^2 = 50$ GeV^2								
x	F_2	$\delta F_2(stat)$	$\delta F_2(syst)$	$\delta F_2(tot)$	R_{QCD}	y	Rad. Corr.	F_2 GRV
0.001300	1.310	0.071	0.134	0.151	0.200	0.439	1.286	1.522
0.002000	1.275	0.045	0.184	0.189	0.195	0.277	1.220	1.289
0.003200	1.168	0.040	0.189	0.193	0.188	0.175	1.160	1.074
0.005000	0.992	0.035	0.161	0.165	0.179	0.110	1.107	0.905
0.008000	0.903	0.033	0.096	0.101	0.167	0.070	1.053	0.761

$Q^2 = 65$ GeV^2								
x	F_2	$\delta F_2(stat)$	$\delta F_2(syst)$	$\delta F_2(tot)$	R_{QCD}	y	Rad. Corr.	F_2 GRV
0.003200	1.253	0.084	0.137	0.161	0.179	0.227	1.188	1.122
0.005000	1.122	0.054	0.118	0.129	0.170	0.143	1.133	0.942
0.008000	0.888	0.040	0.086	0.095	0.159	0.090	1.077	0.788

Table A.2: **F_2 for the E Monte Carlo method, closed triangle data [part 2].** *For an explanation of the quantities, see text.*

$Q^2 = 8.5$ GeV^2							
x	N_{DATA}	frac(bg) [%]	frac(γp) [%]	N_{MC}	N_D/L_D	N_{MC}/L_{MC}	N_{gen}
0.000200	4403	1.7	6.2	22579	5.44	2.46	18835
0.000320	2519	0.3	0.9	13992	3.11	1.53	14185

$Q^2 = 12$ GeV^2							
x	N_{DATA}	frac(bg) [%]	frac(γp) [%]	N_{MC}	N_D/L_D	N_{MC}/L_{MC}	N_{gen}
0.000320	4567	0.2	2.1	25219	5.64	2.75	15843
0.000500	3906	0.0	0.1	20616	4.82	2.25	15080
0.000800	3085	0.5	0.0	16878	3.81	1.84	13600
0.001300	2322	0.4	0.0	12472	2.87	1.36	10530
0.002000	1787	0.0	0.0	9102	2.21	0.99	8539

$Q^2 = 15$ GeV^2							
x	N_{DATA}	frac(bg) [%]	frac(γp) [%]	N_{MC}	N_D/L_D	N_{MC}/L_{MC}	N_{gen}
0.000500	3909	0.2	0.8	21304	4.83	2.32	12026
0.000800	3684	0.5	0.2	20869	4.55	2.28	11276
0.001300	3451	0.0	0.0	18987	4.26	2.07	10160
0.002000	3077	0.3	0.0	16739	3.80	1.83	8865
0.003200	1729	0.0	0.0	9867	2.13	1.08	4570

$Q^2 = 20$ GeV^2							
x	N_{DATA}	frac(bg) [%]	frac(γp) [%]	N_{MC}	N_D/L_D	N_{MC}/L_{MC}	N_{gen}
0.000500	2874	0.0	3.7	16039	3.55	1.75	8842
0.000800	3128	0.3	0.3	17671	3.86	1.93	8999
0.001300	2881	0.7	0.0	16629	3.56	1.81	7947
0.002000	2857	0.7	0.0	15858	3.53	1.73	7190
0.003200	2483	0.0	0.0	13986	3.07	1.53	6110

$Q^2 = 25$ GeV^2							
x	N_{DATA}	frac(bg) [%]	frac(γp) [%]	N_{MC}	N_D/L_D	N_{MC}/L_{MC}	N_{gen}
0.000800	2426	0.4	1.3	13222	3.00	1.44	6803
0.001300	2344	0.0	0.2	13770	2.89	1.50	6416
0.002000	2244	0.2	0.0	12234	2.77	1.33	5616
0.003200	2055	0.0	0.0	11691	2.54	1.27	4717
0.005000	1504	0.0	0.0	8668	1.86	0.95	3801

$Q^2 = 35$ GeV^2							
x	N_{DATA}	frac(bg) [%]	frac(γp) [%]	N_{MC}	N_D/L_D	N_{MC}/L_{MC}	N_{gen}
0.001300	1811	0.0	0.0	9535	2.24	1.04	4891
0.002000	1756	0.2	0.0	9535	2.17	1.04	4501
0.003200	1684	0.0	0.0	9294	2.08	1.01	3801
0.005000	1535	0.0	0.0	8183	1.90	0.89	3273

Table A.3: **Number of events for the E Monte Carlo method, closed triangle data [part 1].**
For an explanation of the quantities, see text.

$Q^2 = 50$ GeV^2							
x	N_{DATA}	frac(bg) [%]	frac(γp) [%]	N_{MC}	N_D/L_D	N_{MC}/L_{MC}	N_{gen}
0.001300	400	0.0	0.0	2256	0.49	0.25	1168
0.002000	1203	0.0	0.3	6235	1.49	0.68	2828
0.003200	1395	1.0	0.0	7012	1.72	0.76	3081
0.005000	1230	0.0	0.0	6427	1.52	0.70	2528
0.008000	1081	0.0	0.0	5436	1.33	0.59	2167

$Q^2 = 65$ GeV^2							
x	N_{DATA}	frac(bg) [%]	frac(γp) [%]	N_{MC}	N_D/L_D	N_{MC}/L_{MC}	N_{gen}
0.003200	264	1.6	0.0	1298	0.33	0.14	614
0.005000	536	0.0	0.0	2590	0.66	0.28	1060
0.008000	633	0.0	0.0	3382	0.78	0.37	1233

Table A.4: **Number of events for the E Monte Carlo method, closed triangle data [part 2].**
For an explanation of the quantities, see text.

$Q^2 = 5$ GeV^2								
x	F_2	$\delta F_2(stat)$	$\delta F_2(syst)$	$\delta F_2(tot)$	$R_{\rm QCD}$	y	Rad. Corr.	F_2 GRV
0.000130	1.236	0.053	0.098	0.111	0.342	0.439	1.305	1.560

$Q^2 = 6.5$ GeV^2								
x	F_2	$\delta F_2(stat)$	$\delta F_2(syst)$	$\delta F_2(tot)$	$R_{\rm QCD}$	y	Rad. Corr.	F_2 GRV
0.000200	1.169	0.047	0.080	0.093	0.319	0.361	1.282	1.564
0.000320	1.019	0.047	0.079	0.092	0.318	0.227	1.227	1.360

$Q^2 = 8.5$ GeV^2								
x	F_2	$\delta F_2(stat)$	$\delta F_2(syst)$	$\delta F_2(tot)$	$R_{\rm QCD}$	y	Rad. Corr.	F_2 GRV
0.000200	1.340	0.059	0.165	0.175	0.299	0.471	1.317	1.752
0.000320	1.115	0.045	0.097	0.107	0.297	0.297	1.254	1.516
0.000500	1.076	0.042	0.101	0.109	0.295	0.187	1.203	1.318
0.000800	0.920	0.037	0.100	0.107	0.292	0.118	1.153	1.136
0.001300	0.906	0.037	0.119	0.125	0.288	0.075	1.103	0.972

$Q^2 = 12$ GeV^2								
x	F_2	$\delta F_2(stat)$	$\delta F_2(syst)$	$\delta F_2(tot)$	$R_{\rm QCD}$	y	Rad. Corr.	F_2 GRV
0.000320	1.235	0.055	0.230	0.237	0.275	0.419	1.296	1.715
0.000500	1.292	0.053	0.131	0.141	0.273	0.265	1.237	1.483
0.000800	1.060	0.044	0.123	0.131	0.270	0.167	1.183	1.270
0.001300	0.924	0.044	0.114	0.122	0.265	0.105	1.131	1.080
0.002000	0.885	0.040	0.120	0.126	0.259	0.067	1.086	0.935

$Q^2 = 15$ GeV^2								
x	F_2	$\delta F_2(stat)$	$\delta F_2(syst)$	$\delta F_2(tot)$	$R_{\rm QCD}$	y	Rad. Corr.	F_2 GRV
0.000500	1.241	0.057	0.161	0.171	0.260	0.331	1.262	1.589
0.000800	1.142	0.051	0.170	0.178	0.257	0.209	1.204	1.356
0.001300	0.992	0.046	0.107	0.116	0.253	0.132	1.150	1.148
0.002000	0.950	0.044	0.130	0.137	0.247	0.083	1.104	0.990
0.003200	0.837	0.051	0.134	0.144	0.239	0.052	1.055	0.843

$Q^2 = 20$ GeV^2								
x	F_2	$\delta F_2(stat)$	$\delta F_2(syst)$	$\delta F_2(tot)$	$R_{\rm QCD}$	y	Rad. Corr.	F_2 GRV
0.000500	1.332	0.074	0.155	0.172	0.245	0.441	1.302	1.723
0.000800	1.157	0.059	0.112	0.127	0.242	0.278	1.234	1.464
0.001300	1.136	0.057	0.107	0.122	0.238	0.176	1.176	1.234
0.002000	0.944	0.050	0.141	0.150	0.232	0.111	1.128	1.059
0.003200	0.863	0.047	0.150	0.158	0.224	0.070	1.077	0.897

$Q^2 = 25$ GeV^2								
x	F_2	$\delta F_2(stat)$	$\delta F_2(syst)$	$\delta F_2(tot)$	$R_{\rm QCD}$	y	Rad. Corr.	F_2 GRV
0.000800	1.260	0.082	0.116	0.142	0.232	0.348	1.261	1.555
0.001300	1.083	0.062	0.094	0.113	0.227	0.220	1.198	1.306
0.002000	1.160	0.065	0.168	0.180	0.222	0.139	1.148	1.117
0.003200	0.976	0.057	0.166	0.175	0.214	0.087	1.096	0.942
0.005000	0.762	0.054	0.126	0.137	0.204	0.055	1.047	0.804

Table A.5: **F_2 for the E Monte Carlo method, opened triangle data [part 1].**
For an explanation of the quantities, see text.

$Q^2 = 35$ GeV^2								
x	F_2	$\delta F_2(stat)$	$\delta F_2(syst)$	$\delta F_2(tot)$	R_{QCD}	y	Rad. Corr.	F_2 GRV
0.001300	1.441	0.089	0.179	0.200	0.213	0.308	1.236	1.412
0.002000	1.218	0.077	0.162	0.179	0.208	0.194	1.181	1.202
0.003200	1.069	0.069	0.185	0.198	0.200	0.122	1.125	1.008
0.005000	0.894	0.062	0.156	0.168	0.191	0.077	1.075	0.854

$Q^2 = 50$ GeV^2								
x	F_2	$\delta F_2(stat)$	$\delta F_2(syst)$	$\delta F_2(tot)$	R_{QCD}	y	Rad. Corr.	F_2 GRV
0.001300	1.161	0.163	0.119	0.201	0.200	0.439	1.286	1.522
0.002000	1.423	0.105	0.205	0.230	0.195	0.277	1.220	1.289
0.003200	1.063	0.080	0.172	0.190	0.188	0.175	1.160	1.074
0.005000	0.906	0.072	0.148	0.164	0.179	0.110	1.107	0.905
0.008000	0.891	0.073	0.095	0.119	0.167	0.070	1.053	0.761

$Q^2 = 65$ GeV^2								
x	F_2	$\delta F_2(stat)$	$\delta F_2(syst)$	$\delta F_2(tot)$	R_{QCD}	y	Rad. Corr.	F_2 GRV
0.003200	0.667	0.146	0.073	0.163	0.179	0.227	1.188	1.122
0.005000	1.153	0.130	0.121	0.177	0.170	0.143	1.133	0.942
0.008000	1.114	0.105	0.108	0.150	0.159	0.090	1.077	0.788

Table A.6: F_2 **for the E Monte Carlo method, opened triangle data [part 2].**
For an explanation of the quantities, see text.

$Q^2 = 5$ GeV^2							
x	N_{DATA}	frac(bg) [%]	frac(γp) [%]	N_{MC}	N_D/L_D	N_{MC}/L_{MC}	N_{gen}
0.000130	773	0.0	4.2	24312	3.03	2.65	15969

$Q^2 = 6.5$ GeV^2							
x	N_{DATA}	frac(bg) [%]	frac(γp) [%]	N_{MC}	N_D/L_D	N_{MC}/L_{MC}	N_{gen}
0.000200	1070	2.5	1.1	37106	4.20	4.05	22944
0.000320	600	0.0	0.0	21634	2.35	2.36	12736

$Q^2 = 8.5$ GeV^2							
x	N_{DATA}	frac(bg) [%]	frac(γp) [%]	N_{MC}	N_D/L_D	N_{MC}/L_{MC}	N_{gen}
0.000200	889	2.0	5.8	30252	3.49	3.30	18863
0.000320	990	2.2	0.6	36739	3.88	4.01	20477
0.000500	1038	1.0	0.0	36166	4.07	3.94	20032
0.000800	909	1.0	0.0	33476	3.57	3.65	17633
0.001300	791	0.0	0.0	26638	3.10	2.90	13325

$Q^2 = 12$ GeV^2							
x	N_{DATA}	frac(bg) [%]	frac(γp) [%]	N_{MC}	N_D/L_D	N_{MC}/L_{MC}	N_{gen}
0.000320	739	1.2	1.9	28174	2.90	3.07	15843
0.000500	859	1.0	0.1	28338	3.37	3.09	15080
0.000800	783	0.0	0.0	28418	3.07	3.10	13701
0.001300	705	2.6	0.0	26474	2.77	2.89	11861
0.002000	629	0.0	0.0	22102	2.47	2.41	10821

$Q^2 = 15$ GeV^2							
x	N_{DATA}	frac(bg) [%]	frac(γp) [%]	N_{MC}	N_D/L_D	N_{MC}/L_{MC}	N_{gen}
0.000500	591	0.0	0.8	21824	2.32	2.38	12026
0.000800	635	0.0	0.2	23022	2.49	2.51	11276
0.001300	594	0.0	0.0	22300	2.33	2.43	10160
0.002000	585	0.0	0.0	20546	2.29	2.24	8865
0.003200	331	1.3	0.0	11793	1.30	1.29	4570

$Q^2 = 20$ GeV^2							
x	N_{DATA}	frac(bg) [%]	frac(γp) [%]	N_{MC}	N_D/L_D	N_{MC}/L_{MC}	N_{gen}
0.000500	428	1.0	3.6	16022	1.68	1.75	8842
0.000800	456	0.0	0.3	17741	1.79	1.93	8999
0.001300	472	0.0	0.0	16805	1.85	1.83	7947
0.002000	424	0.0	0.0	16271	1.66	1.77	7190
0.003200	388	0.0	0.0	14515	1.52	1.58	6110

$Q^2 = 25$ GeV^2							
x	N_{DATA}	frac(bg) [%]	frac(γp) [%]	N_{MC}	N_D/L_D	N_{MC}/L_{MC}	N_{gen}
0.000800	353	2.8	1.3	13342	1.38	1.45	6803
0.001300	346	0.0	0.2	13696	1.36	1.49	6416
0.002000	372	0.0	0.0	12292	1.46	1.34	5616
0.003200	336	0.0	0.0	11758	1.32	1.28	4717
0.005000	219	0.0	0.0	8695	0.86	0.95	3801

Table A.7: **Number of events for the E Monte Carlo method, opened triangle data [part 1].**
For an explanation of the quantities, see text.

$Q^2 = 35$ GeV^2							
x	N_{DATA}	frac(bg) [%]	frac(γp) [%]	N_{MC}	N_D/L_D	N_{MC}/L_{MC}	N_{gen}
0.001300	296	0.0	0.0	9510	1.16	1.04	4891
0.002000	281	0.0	0.0	9552	1.10	1.04	4501
0.003200	270	0.0	0.0	9299	1.06	1.01	3801
0.005000	224	0.0	0.0	8164	0.88	0.89	3273

$Q^2 = 50$ GeV^2							
x	N_{DATA}	frac(bg) [%]	frac(γp) [%]	N_{MC}	N_D/L_D	N_{MC}/L_{MC}	N_{gen}
0.001300	52	0.0	0.0	2230	0.20	0.24	1168
0.002000	198	0.0	0.3	6205	0.78	0.68	2828
0.003200	189	0.0	0.0	7031	0.74	0.77	3081
0.005000	169	0.0	0.0	6511	0.66	0.71	2528
0.008000	161	0.0	0.0	5529	0.63	0.60	2167

$Q^2 = 65$ GeV^2							
x	N_{DATA}	frac(bg) [%]	frac(γp) [%]	N_{MC}	N_D/L_D	N_{MC}/L_{MC}	N_{gen}
0.003200	21	0.0	0.0	1305	0.08	0.14	614
0.005000	82	0.0	0.0	2599	0.32	0.28	1060
0.008000	119	0.0	0.0	3414	0.47	0.37	1233

Table A.8: **Number of events for the E Monte Carlo method, opened triangle data [part 2].**
For an explanation of the quantities, see text.

$Q^2 = 8.5$ GeV^2								
x	F_2	$\delta F_2(stat)$	$\delta F_2(syst)$	$\delta F_2(tot)$	R_{QCD}	y	Rad. Corr.	F_2 GRV
0.000200	1.408	0.065	0.224	0.233	0.299	0.471	1.317	1.752
0.000320	1.082	0.041	0.099	0.107	0.297	0.297	1.254	1.516

$Q^2 = 12$ GeV^2								
x	F_2	$\delta F_2(stat)$	$\delta F_2(syst)$	$\delta F_2(tot)$	R_{QCD}	y	Rad. Corr.	F_2 GRV
0.000320	1.313	0.047	0.299	0.303	0.275	0.419	1.296	1.715
0.000500	1.173	0.039	0.121	0.127	0.273	0.265	1.237	1.483
0.000800	1.022	0.034	0.106	0.111	0.270	0.167	1.183	1.270
0.001300	0.922	0.033	0.084	0.090	0.265	0.105	1.131	1.080
0.002000	0.841	0.034	0.078	0.085	0.259	0.067	1.086	0.935
0.003200	0.777	0.035	0.034	0.049	0.251	0.042	1.038	0.800
0.005000	0.694	0.035	0.034	0.048	0.239	0.026	0.991	0.693
0.008000	0.656	0.037	0.028	0.046	0.223	0.017	0.942	0.602
0.013000	0.604	0.041	0.035	0.054	0.203	0.011	0.890	0.529
0.020000	0.457	0.037	0.043	0.057	0.178	0.007	0.842	0.483

$Q^2 = 15$ GeV^2								
x	F_2	$\delta F_2(stat)$	$\delta F_2(syst)$	$\delta F_2(tot)$	R_{QCD}	y	Rad. Corr.	F_2 GRV
0.000500	1.271	0.043	0.194	0.199	0.260	0.331	1.262	1.589
0.000800	1.069	0.035	0.164	0.167	0.257	0.209	1.204	1.356
0.001300	0.976	0.031	0.071	0.078	0.253	0.132	1.150	1.148
0.002000	0.878	0.029	0.075	0.080	0.247	0.083	1.104	0.990
0.003200	0.767	0.028	0.090	0.094	0.239	0.052	1.055	0.843
0.005000	0.684	0.027	0.035	0.044	0.227	0.033	1.008	0.727
0.008000	0.621	0.025	0.033	0.041	0.212	0.021	0.958	0.627
0.013000	0.535	0.024	0.033	0.040	0.193	0.013	0.906	0.548
0.020000	0.492	0.026	0.036	0.044	0.169	0.008	0.858	0.497
0.032000	0.440	0.036	0.049	0.061	0.141	0.005	0.802	0.458

$Q^2 = 20$ GeV^2								
x	F_2	$\delta F_2(stat)$	$\delta F_2(syst)$	$\delta F_2(tot)$	R_{QCD}	y	Rad. Corr.	F_2 GRV
0.000500	1.464	0.061	0.227	0.235	0.245	0.441	1.302	1.723
0.000800	1.220	0.041	0.148	0.154	0.242	0.278	1.234	1.464
0.001300	1.113	0.036	0.098	0.105	0.238	0.176	1.176	1.234
0.002000	0.942	0.031	0.112	0.116	0.232	0.111	1.128	1.059
0.003200	0.874	0.030	0.110	0.114	0.224	0.070	1.077	0.897
0.005000	0.751	0.028	0.027	0.039	0.214	0.044	1.029	0.769
0.008000	0.676	0.026	0.034	0.043	0.200	0.028	0.979	0.659
0.013000	0.559	0.023	0.026	0.035	0.181	0.018	0.926	0.571
0.020000	0.520	0.024	0.027	0.036	0.159	0.011	0.878	0.514
0.032000	0.446	0.027	0.043	0.050	0.133	0.007	0.822	0.470

Table A.9: **F_2 for the Σ Monte Carlo method, closed triangle data [part 1].** *For an explanation of the quantities, see text.*

$Q^2 = 25$ GeV^2								
x	F_2	$\delta F_2(stat)$	$\delta F_2(syst)$	$\delta F_2(tot)$	R_{QCD}	y	Rad. Corr.	F_2 GRV
0.000800	1.321	0.053	0.158	0.167	0.232	0.348	1.261	1.555
0.001300	1.100	0.038	0.118	0.124	0.227	0.220	1.198	1.306
0.002000	1.010	0.034	0.116	0.121	0.222	0.139	1.148	1.117
0.003200	0.885	0.031	0.116	0.120	0.214	0.087	1.096	0.942
0.005000	0.795	0.030	0.096	0.101	0.204	0.055	1.047	0.804
0.008000	0.679	0.027	0.033	0.043	0.191	0.035	0.996	0.685
0.013000	0.600	0.025	0.029	0.039	0.173	0.022	0.943	0.590
0.020000	0.591	0.027	0.038	0.046	0.151	0.014	0.894	0.527
0.032000	0.480	0.026	0.035	0.043	0.127	0.009	0.837	0.479
0.050000	0.408	0.032	0.054	0.063	0.101	0.006	0.778	0.448

$Q^2 = 35$ GeV^2								
x	F_2	$\delta F_2(stat)$	$\delta F_2(syst)$	$\delta F_2(tot)$	R_{QCD}	y	Rad. Corr.	F_2 GRV
0.000800	1.554	0.108	0.279	0.300	0.217	0.487	1.314	1.690
0.001300	1.318	0.055	0.181	0.189	0.213	0.308	1.236	1.412
0.002000	1.104	0.040	0.144	0.150	0.208	0.194	1.181	1.202
0.003200	0.959	0.036	0.144	0.149	0.200	0.122	1.125	1.008
0.005000	0.865	0.034	0.115	0.120	0.191	0.077	1.075	0.854
0.008000	0.748	0.031	0.033	0.046	0.178	0.049	1.023	0.723
0.013000	0.641	0.028	0.029	0.041	0.162	0.031	0.968	0.617
0.020000	0.507	0.024	0.023	0.034	0.142	0.019	0.919	0.547
0.032000	0.493	0.027	0.027	0.038	0.118	0.012	0.861	0.492
0.050000	0.439	0.031	0.044	0.054	0.095	0.008	0.801	0.456

$Q^2 = 50$ GeV^2								
x	F_2	$\delta F_2(stat)$	$\delta F_2(syst)$	$\delta F_2(tot)$	R_{QCD}	y	Rad. Corr.	F_2 GRV
0.002000	1.191	0.056	0.187	0.195	0.195	0.277	1.220	1.289
0.003200	1.061	0.043	0.148	0.154	0.188	0.175	1.160	1.074
0.005000	0.926	0.039	0.112	0.119	0.179	0.110	1.107	0.905
0.008000	0.780	0.035	0.046	0.058	0.167	0.070	1.053	0.761
0.013000	0.737	0.034	0.036	0.050	0.151	0.044	0.997	0.644
0.020000	0.622	0.030	0.031	0.044	0.132	0.028	0.946	0.567
0.032000	0.581	0.030	0.024	0.039	0.111	0.017	0.888	0.505
0.050000	0.458	0.029	0.028	0.040	0.088	0.011	0.827	0.464
0.080000	0.387	0.033	0.029	0.044	0.067	0.007	0.754	0.431

$Q^2 = 65$ GeV^2								
x	F_2	$\delta F_2(stat)$	$\delta F_2(syst)$	$\delta F_2(tot)$	R_{QCD}	y	Rad. Corr.	F_2 GRV
0.005000	0.865	0.054	0.066	0.085	0.170	0.143	1.133	0.942
0.008000	0.722	0.042	0.046	0.063	0.159	0.090	1.077	0.788
0.013000	0.612	0.036	0.038	0.052	0.144	0.057	1.020	0.663
0.020000	0.594	0.034	0.023	0.041	0.126	0.036	0.968	0.580
0.032000	0.542	0.032	0.027	0.042	0.105	0.023	0.909	0.514
0.050000	0.466	0.033	0.020	0.038	0.084	0.014	0.848	0.470
0.080000	0.428	0.033	0.025	0.041	0.064	0.009	0.773	0.433

Table A.10: **F_2 for the Σ Monte Carlo method, closed triangle data [part 2].** *For an explanation of the quantities, see text.*

$Q^2 = 8.5$ GeV^2						
x	N_{DATA}	frac(bg) [%]	frac(γp) [%]	N_{MC}	N_D/L_D	N_{MC}/L_{MC}
0.000200	1696	1.0	5.0	8155	2.09	0.89
0.000320	2461	0.2	4.0	13965	3.04	1.52

$Q^2 = 12$ GeV^2						
x	N_{DATA}	frac(bg) [%]	frac(γp) [%]	N_{MC}	N_D/L_D	N_{MC}/L_{MC}
0.000320	2821	0.8	3.6	15020	3.48	1.64
0.000500	3267	0.0	1.6	17625	4.03	1.92
0.000800	3261	0.3	0.5	18237	4.03	1.99
0.001300	2649	0.0	0.2	14785	3.27	1.61
0.002000	1959	0.0	0.2	10750	2.42	1.17
0.003200	1534	0.0	0.0	8142	1.89	0.89
0.005000	1196	0.4	0.0	6335	1.48	0.69
0.008000	947	1.1	0.0	4723	1.17	0.52
0.013000	661	1.5	0.0	3187	0.82	0.35
0.020000	380	0.0	0.0	2166	0.47	0.24

$Q^2 = 15$ GeV^2						
x	N_{DATA}	frac(bg) [%]	frac(γp) [%]	N_{MC}	N_D/L_D	N_{MC}/L_{MC}
0.000500	2806	0.0	3.5	15012	3.46	1.64
0.000800	3223	0.3	0.8	18503	3.98	2.02
0.001300	3559	0.3	0.0	20159	4.39	2.20
0.002000	3005	0.0	0.0	16951	3.71	1.85
0.003200	2405	0.0	0.3	13859	2.97	1.51
0.005000	2060	1.0	0.0	11848	2.54	1.29
0.008000	1857	0.0	0.0	10419	2.29	1.14
0.013000	1402	0.0	0.0	8090	1.73	0.88
0.020000	946	0.0	0.0	5282	1.17	0.58
0.032000	378	2.3	0.0	2125	0.47	0.23

$Q^2 = 20$ GeV^2						
x	N_{DATA}	frac(bg) [%]	frac(γp) [%]	N_{MC}	N_D/L_D	N_{MC}/L_{MC}
0.000500	1464	0.0	3.5	7398	1.81	0.81
0.000800	2487	0.0	1.0	13603	3.07	1.48
0.001300	3000	0.7	0.0	16180	3.70	1.76
0.002000	2845	0.0	0.0	16233	3.51	1.77
0.003200	2442	0.0	0.2	13396	3.02	1.46
0.005000	2029	0.0	0.0	11483	2.50	1.25
0.008000	1766	0.0	0.0	9802	2.18	1.07
0.013000	1425	0.0	0.0	8439	1.76	0.92
0.020000	1186	0.0	0.0	6660	1.46	0.73
0.032000	615	0.7	0.0	3576	0.76	0.39

Table A.11: **Number of events for the Σ Monte Carlo method, closed triangle data [part 1].**
For an explanation of the quantities, see text.

$Q^2 = 25$ GeV^2						
x	N_{DATA}	frac(bg) [%]	frac(γp) [%]	N_{MC}	N_D/L_D	N_{MC}/L_{MC}
0.000800	1468	0.7	0.5	7858	1.81	0.86
0.001300	2051	0.0	0.2	11861	2.53	1.29
0.002000	2268	0.0	0.0	12779	2.80	1.39
0.003200	2001	0.0	0.0	11452	2.47	1.25
0.005000	1686	0.0	0.0	9520	2.08	1.04
0.008000	1503	0.0	0.0	8758	1.86	0.95
0.013000	1295	0.0	0.0	7502	1.60	0.82
0.020000	1091	0.0	0.0	5625	1.35	0.61
0.032000	717	0.0	0.0	4007	0.89	0.44
0.050000	282	0.0	0.0	1655	0.35	0.18

$Q^2 = 35$ GeV^2						
x	N_{DATA}	frac(bg) [%]	frac(γp) [%]	N_{MC}	N_D/L_D	N_{MC}/L_{MC}
0.000800	351	0.0	0.0	1726	0.43	0.19
0.001300	1173	0.0	0.0	6114	1.45	0.67
0.002000	1653	0.0	0.3	9208	2.04	1.00
0.003200	1573	0.0	0.0	8963	1.94	0.98
0.005000	1385	0.0	0.0	7742	1.71	0.84
0.008000	1186	0.0	0.0	6734	1.46	0.73
0.013000	1006	0.0	0.0	5829	1.24	0.64
0.020000	797	0.0	0.0	5084	0.98	0.55
0.032000	606	0.0	0.0	3460	0.75	0.38
0.050000	369	2.4	0.0	2089	0.46	0.23

$Q^2 = 50$ GeV^2						
x	N_{DATA}	frac(bg) [%]	frac(γp) [%]	N_{MC}	N_D/L_D	N_{MC}/L_{MC}
0.002000	793	0.0	0.0	4400	0.98	0.48
0.003200	1145	0.0	0.0	6332	1.41	0.69
0.005000	1083	0.4	0.0	6065	1.34	0.66
0.008000	870	0.0	0.0	5062	1.07	0.55
0.013000	857	0.0	0.0	4600	1.06	0.50
0.020000	735	0.0	0.0	4044	0.91	0.44
0.032000	636	0.0	0.0	3229	0.79	0.35
0.050000	394	0.0	0.0	2202	0.49	0.24
0.080000	210	2.0	0.0	1223	0.26	0.13

$Q^2 = 65$ GeV^2						
x	N_{DATA}	frac(bg) [%]	frac(γp) [%]	N_{MC}	N_D/L_D	N_{MC}/L_{MC}
0.005000	371	0.0	0.0	2326	0.46	0.25
0.008000	435	0.0	0.0	2859	0.54	0.31
0.013000	414	0.0	0.0	2789	0.51	0.30
0.020000	452	0.0	0.0	2702	0.56	0.29
0.032000	438	0.0	0.0	2463	0.54	0.27
0.050000	362	2.7	0.0	2037	0.45	0.22
0.080000	242	0.0	0.0	1285	0.30	0.14

Table A.12: **Number of events for the Σ Monte Carlo method, closed triangle data [part 2].**
For an explanation of the quantities, see text.

$Q^2 = 5$ GeV^2								
x	F_2	$\delta F_2(stat)$	$\delta F_2(syst)$	$\delta F_2(tot)$	R_{QCD}	y	Rad. Corr.	F_2 GRV
0.000130	1.118	0.074	0.106	0.129	0.342	0.439	1.305	1.560

$Q^2 = 6.5$ GeV^2								
x	F_2	$\delta F_2(stat)$	$\delta F_2(syst)$	$\delta F_2(tot)$	R_{QCD}	y	Rad. Corr.	F_2 GRV
0.000200	1.102	0.055	0.072	0.091	0.319	0.361	1.282	1.564
0.000320	0.937	0.050	0.078	0.092	0.318	0.227	1.227	1.360

$Q^2 = 8.5$ GeV^2								
x	F_2	$\delta F_2(stat)$	$\delta F_2(syst)$	$\delta F_2(tot)$	R_{QCD}	y	Rad. Corr.	F_2 GRV
0.000200	1.426	0.106	0.227	0.250	0.299	0.471	1.317	1.752
0.000320	1.109	0.051	0.102	0.114	0.297	0.297	1.254	1.516
0.000500	1.017	0.048	0.074	0.088	0.295	0.187	1.203	1.318
0.000800	0.879	0.039	0.062	0.073	0.292	0.118	1.153	1.136
0.001300	0.792	0.037	0.078	0.086	0.288	0.075	1.103	0.972
0.002000	0.797	0.042	0.052	0.067	0.282	0.047	1.060	0.847
0.003200	0.585	0.034	0.045	0.056	0.273	0.030	1.012	0.731
0.005000	0.651	0.041	0.052	0.066	0.260	0.019	0.966	0.639
0.008000	0.580	0.039	0.050	0.064	0.243	0.012	0.917	0.560
0.013000	0.467	0.045	0.040	0.060	0.220	0.007	0.866	0.498

$Q^2 = 12$ GeV^2								
x	F_2	$\delta F_2(stat)$	$\delta F_2(syst)$	$\delta F_2(tot)$	R_{QCD}	y	Rad. Corr.	F_2 GRV
0.000320	1.313	0.073	0.299	0.308	0.275	0.419	1.296	1.715
0.000500	1.221	0.058	0.126	0.139	0.273	0.265	1.237	1.483
0.000800	1.044	0.048	0.108	0.119	0.270	0.167	1.183	1.270
0.001300	0.972	0.045	0.089	0.099	0.265	0.105	1.131	1.080
0.002000	0.869	0.041	0.081	0.090	0.259	0.067	1.086	0.935
0.003200	0.737	0.038	0.032	0.050	0.251	0.042	1.038	0.800
0.005000	0.699	0.037	0.034	0.050	0.239	0.026	0.991	0.693
0.008000	0.567	0.033	0.024	0.041	0.223	0.017	0.942	0.602
0.013000	0.546	0.036	0.031	0.048	0.203	0.011	0.890	0.529
0.020000	0.528	0.042	0.050	0.065	0.178	0.007	0.842	0.483

Table A.13: **F_2 for the Σ Monte Carlo method, opened triangle data [part 1].** *For an explanation of the quantities, see text.*

$Q^2 = 15$ GeV^2								
x	F_2	$\delta F_2(stat)$	$\delta F_2(syst)$	$\delta F_2(tot)$	R_{QCD}	y	Rad. Corr.	F_2 GRV
0.000500	1.205	0.077	0.184	0.200	0.260	0.331	1.262	1.589
0.000800	1.156	0.058	0.177	0.186	0.257	0.209	1.204	1.356
0.001300	1.014	0.048	0.074	0.088	0.253	0.132	1.150	1.148
0.002000	0.878	0.044	0.075	0.087	0.247	0.083	1.104	0.990
0.003200	0.901	0.047	0.105	0.115	0.239	0.052	1.055	0.843
0.005000	0.665	0.039	0.034	0.052	0.227	0.033	1.008	0.727
0.008000	0.606	0.037	0.032	0.049	0.212	0.021	0.958	0.627
0.013000	0.556	0.038	0.034	0.051	0.193	0.013	0.906	0.548
0.020000	0.491	0.040	0.036	0.054	0.169	0.008	0.858	0.497
0.032000	0.500	0.061	0.056	0.083	0.141	0.005	0.802	0.458

$Q^2 = 20$ GeV^2								
x	F_2	$\delta F_2(stat)$	$\delta F_2(syst)$	$\delta F_2(tot)$	R_{QCD}	y	Rad. Corr.	F_2 GRV
0.000500	1.446	0.112	0.224	0.251	0.245	0.441	1.302	1.723
0.000800	1.280	0.074	0.156	0.172	0.242	0.278	1.234	1.464
0.001300	1.049	0.059	0.093	0.110	0.238	0.176	1.176	1.234
0.002000	0.983	0.053	0.116	0.128	0.232	0.111	1.128	1.059
0.003200	0.828	0.049	0.105	0.116	0.224	0.070	1.077	0.897
0.005000	0.768	0.048	0.028	0.056	0.214	0.044	1.029	0.769
0.008000	0.642	0.045	0.033	0.055	0.200	0.028	0.979	0.659
0.013000	0.546	0.041	0.026	0.048	0.181	0.018	0.926	0.571
0.020000	0.575	0.045	0.030	0.054	0.159	0.011	0.878	0.514
0.032000	0.578	0.057	0.055	0.080	0.133	0.007	0.822	0.470

$Q^2 = 25$ GeV^2								
x	F_2	$\delta F_2(stat)$	$\delta F_2(syst)$	$\delta F_2(tot)$	R_{QCD}	y	Rad. Corr.	F_2 GRV
0.000800	1.315	0.097	0.157	0.185	0.232	0.348	1.261	1.555
0.001300	1.135	0.071	0.122	0.141	0.227	0.220	1.198	1.306
0.002000	1.103	0.064	0.126	0.142	0.222	0.139	1.148	1.117
0.003200	0.905	0.057	0.118	0.132	0.214	0.087	1.096	0.942
0.005000	0.806	0.056	0.097	0.112	0.204	0.055	1.047	0.804
0.008000	0.789	0.055	0.039	0.067	0.191	0.035	0.996	0.685
0.013000	0.630	0.049	0.031	0.058	0.173	0.022	0.943	0.590
0.020000	0.519	0.046	0.033	0.057	0.151	0.014	0.894	0.527
0.032000	0.477	0.050	0.035	0.061	0.127	0.009	0.837	0.479
0.050000	0.488	0.074	0.065	0.098	0.101	0.006	0.778	0.448

Table A.14: **F_2 for the Σ Monte Carlo method, opened triangle data [part 2].** *For an explanation of the quantities, see text.*

$Q^2 = 35$ GeV^2								
x	F_2	$\delta F_2(stat)$	$\delta F_2(syst)$	$\delta F_2(tot)$	R_{QCD}	y	Rad. Corr.	F_2 GRV
0.000800	1.638	0.233	0.294	0.375	0.217	0.487	1.314	1.690
0.001300	1.250	0.104	0.171	0.200	0.213	0.308	1.236	1.412
0.002000	1.149	0.078	0.150	0.169	0.208	0.194	1.181	1.202
0.003200	1.025	0.071	0.154	0.170	0.200	0.122	1.125	1.008
0.005000	0.880	0.066	0.117	0.134	0.191	0.077	1.075	0.854
0.008000	0.770	0.062	0.034	0.070	0.178	0.049	1.023	0.723
0.013000	0.614	0.055	0.028	0.061	0.162	0.031	0.968	0.617
0.020000	0.559	0.052	0.026	0.058	0.142	0.019	0.919	0.547
0.032000	0.548	0.059	0.030	0.066	0.118	0.012	0.861	0.492
0.050000	0.326	0.053	0.033	0.062	0.095	0.008	0.801	0.456

$Q^2 = 50$ GeV^2								
x	F_2	$\delta F_2(stat)$	$\delta F_2(syst)$	$\delta F_2(tot)$	R_{QCD}	y	Rad. Corr.	F_2 GRV
0.002000	1.307	0.122	0.205	0.239	0.195	0.277	1.220	1.289
0.003200	0.947	0.081	0.132	0.155	0.188	0.175	1.160	1.074
0.005000	0.823	0.072	0.100	0.124	0.179	0.110	1.107	0.905
0.008000	0.854	0.076	0.050	0.091	0.167	0.070	1.053	0.761
0.013000	0.734	0.069	0.036	0.078	0.151	0.044	0.997	0.644
0.020000	0.617	0.062	0.031	0.070	0.132	0.028	0.946	0.567
0.032000	0.592	0.063	0.025	0.068	0.111	0.017	0.888	0.505
0.050000	0.592	0.071	0.036	0.080	0.088	0.011	0.827	0.464
0.080000	0.392	0.072	0.029	0.077	0.067	0.007	0.754	0.431

$Q^2 = 65$ GeV^2								
x	F_2	$\delta F_2(stat)$	$\delta F_2(syst)$	$\delta F_2(tot)$	R_{QCD}	y	Rad. Corr.	F_2 GRV
0.005000	0.889	0.122	0.068	0.139	0.170	0.143	1.133	0.942
0.008000	0.531	0.131	0.034	0.135	0.159	0.090	1.077	0.788
0.013000	0.658	0.084	0.040	0.093	0.144	0.057	1.020	0.663
0.020000	0.533	0.071	0.021	0.074	0.126	0.036	0.968	0.580
0.032000	0.443	0.062	0.022	0.066	0.105	0.023	0.909	0.514
0.050000	0.443	0.063	0.019	0.066	0.084	0.014	0.848	0.470
0.080000	0.387	0.069	0.022	0.073	0.064	0.009	0.773	0.433

Table A.15: **F_2 for the Σ Monte Carlo method, opened triangle data [part 3].** *For an explanation of the quantities, see text.*

$Q^2 = 5$ GeV^2						
x	N_{DATA}	frac(bg) [%]	frac(γp) [%]	N_{MC}	N_D/L_D	N_{MC}/L_{MC}
0.000130	393	0.0	7.9	13659	1.54	1.49

$Q^2 = 6.5$ GeV^2						
x	N_{DATA}	frac(bg) [%]	frac(γp) [%]	N_{MC}	N_D/L_D	N_{MC}/L_{MC}
0.000200	673	0.0	4.8	24748	2.64	2.70
0.000320	553	0.0	2.5	21705	2.17	2.37

$Q^2 = 8.5$ GeV^2						
x	N_{DATA}	frac(bg) [%]	frac(γp) [%]	N_{MC}	N_D/L_D	N_{MC}/L_{MC}
0.000200	373	4.7	3.3	11940	1.46	1.30
0.000320	759	0.0	2.4	28354	2.98	3.09
0.000500	834	2.2	0.2	30763	3.27	3.35
0.000800	864	1.0	0.1	33306	3.39	3.63
0.001300	736	0.0	0.2	28381	2.89	3.09
0.002000	612	1.4	0.0	21089	2.40	2.30
0.003200	417	0.0	0.2	17524	1.64	1.91
0.005000	397	1.1	0.0	13429	1.56	1.46
0.008000	319	0.0	0.0	10813	1.25	1.18
0.013000	199	4.3	0.0	7575	0.78	0.83

$Q^2 = 12$ GeV^2						
x	N_{DATA}	frac(bg) [%]	frac(γp) [%]	N_{MC}	N_D/L_D	N_{MC}/L_{MC}
0.000320	477	0.0	3.2	17109	1.87	1.87
0.000500	668	0.0	1.2	23321	2.62	2.54
0.000800	790	1.1	0.3	29136	3.10	3.18
0.001300	812	1.2	0.1	28953	3.19	3.16
0.002000	698	0.0	0.1	24986	2.74	2.72
0.003200	564	0.0	0.0	21252	2.21	2.32
0.005000	525	0.0	0.0	18588	2.06	2.03
0.008000	416	0.0	0.0	16167	1.63	1.76
0.013000	319	0.0	0.0	11461	1.25	1.25
0.020000	216	0.0	0.0	7187	0.85	0.78

Table A.16: **Number of events for the Σ Monte Carlo method, opened triangle data [part 1].**
For an explanation of the quantities, see text.

$Q^2 = 15$ GeV^2						
x	N_{DATA}	frac(bg) [%]	frac(γp) [%]	N_{MC}	N_D/L_D	N_{MC}/L_{MC}
0.000500	407	2.4	3.5	15499	1.60	1.69
0.000800	565	0.0	0.6	20235	2.22	2.21
0.001300	634	0.0	0.0	23284	2.49	2.54
0.002000	545	0.0	0.0	20710	2.14	2.26
0.003200	524	0.0	0.2	17349	2.06	1.89
0.005000	392	0.0	0.0	15601	1.54	1.70
0.008000	350	0.0	0.0	13550	1.37	1.48
0.013000	289	0.0	0.0	10808	1.13	1.18
0.020000	195	0.0	0.0	7348	0.76	0.80
0.032000	84	0.0	0.0	2795	0.33	0.30

$Q^2 = 20$ GeV^2						
x	N_{DATA}	frac(bg) [%]	frac(γp) [%]	N_{MC}	N_D/L_D	N_{MC}/L_{MC}
0.000500	214	0.0	3.5	7380	0.84	0.80
0.000800	390	0.0	0.9	13710	1.53	1.50
0.001300	427	1.0	0.0	16486	1.68	1.80
0.002000	456	0.0	0.0	16805	1.79	1.83
0.003200	361	0.0	0.2	14088	1.42	1.54
0.005000	325	0.0	0.0	12109	1.27	1.32
0.008000	257	0.0	0.0	10123	1.01	1.10
0.013000	221	0.0	0.0	9024	0.87	0.98
0.020000	204	0.0	0.0	6982	0.80	0.76
0.032000	125	0.0	0.0	3779	0.49	0.41

$Q^2 = 25$ GeV^2						
x	N_{DATA}	frac(bg) [%]	frac(γp) [%]	N_{MC}	N_D/L_D	N_{MC}/L_{MC}
0.000800	218	0.0	0.5	7927	0.86	0.86
0.001300	312	0.0	0.2	11787	1.23	1.29
0.002000	369	0.0	0.0	12825	1.45	1.40
0.003200	306	0.0	0.0	11544	1.20	1.26
0.005000	256	0.0	0.0	9601	1.00	1.05
0.008000	255	0.0	0.0	8612	1.00	0.94
0.013000	202	0.0	0.0	7507	0.79	0.82
0.020000	146	0.0	0.0	5772	0.57	0.63
0.032000	105	0.0	0.0	3980	0.41	0.43
0.050000	50	0.0	0.0	1653	0.20	0.18

Table A.17: **Number of events for the Σ Monte Carlo method, opened triangle data [part 2].**
For an explanation of the quantities, see text.

$Q^2 = 35$ GeV^2						
x	N_{DATA}	frac(bg) [%]	frac(γp) [%]	N_{MC}	N_D/L_D	N_{MC}/L_{MC}
0.000800	55	0.0	0.0	1729	0.22	0.19
0.001300	164	0.0	0.0	6075	0.64	0.66
0.002000	256	0.0	0.2	9237	1.01	1.01
0.003200	250	0.0	0.0	8982	0.98	0.98
0.005000	208	0.0	0.0	7700	0.82	0.84
0.008000	182	0.0	0.0	6764	0.71	0.74
0.013000	143	0.0	0.0	5826	0.56	0.64
0.020000	131	0.0	0.0	5102	0.51	0.56
0.032000	99	0.0	0.0	3427	0.39	0.37
0.050000	41	0.0	0.0	2097	0.16	0.23

$Q^2 = 50$ GeV^2						
x	N_{DATA}	frac(bg) [%]	frac(γp) [%]	N_{MC}	N_D/L_D	N_{MC}/L_{MC}
0.002000	129	0.0	0.0	4393	0.51	0.48
0.003200	152	0.0	0.0	6349	0.60	0.69
0.005000	144	0.0	0.0	6108	0.56	0.67
0.008000	144	0.0	0.0	5160	0.56	0.56
0.013000	128	0.0	0.0	4642	0.50	0.51
0.020000	109	0.0	0.0	4072	0.43	0.44
0.032000	97	0.0	0.0	3257	0.38	0.36
0.050000	77	0.0	0.0	2245	0.30	0.24
0.080000	32	0.0	0.0	1236	0.13	0.13

$Q^2 = 65$ GeV^2						
x	N_{DATA}	frac(bg) [%]	frac(γp) [%]	N_{MC}	N_D/L_D	N_{MC}/L_{MC}
0.005000	57	0.0	0.0	2342	0.22	0.26
0.008000	47	15.8	0.0	2891	0.19	0.32
0.013000	66	0.0	0.0	2786	0.26	0.30
0.020000	60	0.0	0.0	2692	0.24	0.29
0.032000	54	0.0	0.0	2499	0.21	0.27
0.050000	52	0.0	0.0	2070	0.20	0.23
0.080000	33	0.0	0.0	1305	0.13	0.14

Table A.18: **Number of events for the Σ Monte Carlo method, opened triangle data [part 3].**
For an explanation of the quantities, see text.

Appendix B

Table with miscellaneous bin-dependent quantities

Meaning of the quantities in the tables:

Acc	Acceptance
δAcc	Total error on the acceptance
$F_2^{th} / \int\int \sigma \, dx \, dQ^2$	Kinematical factor in equation (4.9)
E_e	Energy of the scattered electron in the bin centre
θ_e	Polar angle in the bin centre

$Q^2 = 5$ GeV^2					
x	Acc	δAcc	$F_2^{th}/\int\int \sigma\, dx\, dQ^2$	E_e	θ_e
0.000130	0.82	0.02	0.450	15.5	173.8

$Q^2 = 6.5$ GeV^2					
x	Acc	δAcc	$F_2^{th}/\int\int \sigma\, dx\, dQ^2$	E_e	θ_e
0.000200	0.85	0.02	0.308	17.7	173.4
0.000320	0.85	0.02	0.494	21.4	174.0

$Q^2 = 8.5$ GeV^2					
x	Acc	δAcc	$F_2^{th}/\int\int \sigma\, dx\, dQ^2$	E_e	θ_e
0.000200	0.85	0.01	0.450	14.7	171.7
0.000320	0.89	0.01	0.345	19.5	172.8
0.000500	0.88	0.01	0.308	22.5	173.3
0.000800	0.87	0.02	0.291	24.4	173.6
0.001300	0.82	0.02	0.318	25.6	173.7

$Q^2 = 12$ GeV^2					
x	Acc	δAcc	$F_2^{th}/\int\int \sigma\, dx\, dQ^2$	E_e	θ_e
0.000320	0.88	0.01	0.522	16.1	170.6
0.000500	0.88	0.01	0.447	20.4	171.6
0.000800	0.90	0.02	0.404	23.1	172.1
0.001300	0.87	0.02	0.380	24.8	172.4
0.002000	0.83	0.02	0.390	25.9	172.6

$Q^2 = 15$ GeV^2					
x	Acc	δAcc	$F_2^{th}/\int\int \sigma\, dx\, dQ^2$	E_e	θ_e
0.000500	0.87	0.01	0.642	18.6	170.2
0.000800	0.90	0.01	0.561	22.0	171.0
0.001300	0.90	0.02	0.516	24.1	171.4
0.002000	0.87	0.02	0.491	25.4	171.6
0.003200	0.90	0.02	0.724	26.3	171.8

$Q^2 = 20$ GeV^2					
x	Acc	δAcc	$F_2^{th}/\int\int \sigma\, dx\, dQ^2$	E_e	θ_e
0.000500	0.84	0.01	0.988	15.6	167.6
0.000800	0.87	0.01	0.805	20.1	169.1
0.001300	0.90	0.01	0.720	22.9	169.8
0.002000	0.90	0.02	0.672	24.7	170.2
0.003200	0.87	0.02	0.646	25.9	170.4

$Q^2 = 25$ GeV^2					
x	Acc	δAcc	$F_2^{th}/\int\int \sigma\, dx\, dQ^2$	E_e	θ_e
0.000800	0.89	0.01	1.167	18.2	167.2
0.001300	0.92	0.01	1.007	21.8	168.3
0.002000	0.86	0.02	0.920	24.0	168.9
0.003200	0.90	0.02	0.871	25.4	169.2
0.005000	0.82	0.02	0.974	26.3	169.4

Table B.1: **Miscellaneous bin-dependent quantities [part 1].** *For an explanation of the quantities, see text.*

$Q^2 = 35$ GeV^2					
x	Acc	δAcc	$F_2^{th} / \int\int \sigma\, dx\, dQ^2$	E_e	θ_e
0.001300	0.89	0.01	1.481	19.4	165.3
0.002000	0.88	0.02	1.308	22.6	166.4
0.003200	0.93	0.02	1.214	24.5	166.9
0.005000	0.87	0.02	1.165	25.8	167.3

$Q^2 = 50$ GeV^2					
x	Acc	δAcc	$F_2^{th} / \int\int \sigma\, dx\, dQ^2$	E_e	θ_e
0.002000	0.88	0.02	2.237	20.4	162.9
0.003200	0.90	0.02	1.712	23.2	163.9
0.005000	0.93	0.02	1.616	25.0	164.5
0.008000	0.94	0.02	1.581	26.1	164.9

$Q^2 = 65$ GeV^2					
x	Acc	δAcc	$F_2^{th} / \int\int \sigma\, dx\, dQ^2$	E_e	θ_e
0.005000	0.90	0.02	3.997	24.2	162.1
0.008000	0.98	0.02	2.849	25.7	162.6

Table B.2: **Miscellaneous bin-dependent quantities [part 2].**
For an explanation of the quantities, see text.

Appendix C

Table with the comparison of the radiative corrections

$x \setminus Q^2$ [GeV^2]	4.217 – 5.623	5.623 – 7.499	7.499 – 10.0	10.0 – 13.34	13.34 – 17.78
$1.00 \times 10^{-4} - 1.58 \times 10^{-4}$	0.007	0.011	0.067	0.235	1.000
$1.58 \times 10^{-4} - 2.51 \times 10^{-4}$	0.013	−0.004	−0.003	0.011	0.203
$2.51 \times 10^{-4} - 3.98 \times 10^{-4}$	−0.007	−0.003	0.000	−0.009	0.000
$3.98 \times 10^{-4} - 6.31 \times 10^{-4}$	−0.005	−0.017	−0.003	−0.018	−0.009
$6.31 \times 10^{-4} - 1.00 \times 10^{-3}$	−0.001	−0.009	−0.012	−0.007	−0.016
$1.00 \times 10^{-3} - 1.58 \times 10^{-3}$	−0.010	−0.005	−0.018	−0.009	−0.017
$1.58 \times 10^{-3} - 2.51 \times 10^{-3}$	0.005	0.009	−0.012	−0.024	−0.010
$2.51 \times 10^{-3} - 3.98 \times 10^{-3}$	0.005	−0.004	0.004	0.010	−0.026
$3.98 \times 10^{-3} - 6.31 \times 10^{-3}$	−0.005	−0.003	−0.010	−0.003	−0.001
$6.31 \times 10^{-3} - 1.00 \times 10^{-2}$	0.010	−0.012	−0.005	−0.026	−0.007
$1.00 \times 10^{-2} - 1.58 \times 10^{-2}$	−0.006	−0.010	−0.034	−0.015	−0.021
$1.58 \times 10^{-2} - 2.51 \times 10^{-2}$	0.016	0.022	−0.021	0.004	−0.001
$2.51 \times 10^{-2} - 3.98 \times 10^{-2}$	0.024	0.004	0.001	0.006	0.002
$3.98 \times 10^{-2} - 6.31 \times 10^{-2}$	0.030	0.014	0.023	0.007	−0.010
$6.31 \times 10^{-2} - 1.00 \times 10^{-1}$	0.013	0.023	−0.022	0.003	−0.015
$x \setminus Q^2$ [GeV^2]	17.78 – 23.71	23.71 – 31.62	31.62 – 42.17	42.17 – 56.23	56.23 – 74.99
$1.00 \times 10^{-4} - 1.58 \times 10^{-4}$					
$1.58 \times 10^{-4} - 2.51 \times 10^{-4}$	1.000				
$2.51 \times 10^{-4} - 3.98 \times 10^{-4}$	0.061	1.000	1.000		
$3.98 \times 10^{-4} - 6.31 \times 10^{-4}$	−0.007	−0.010	1.000	1.000	
$6.31 \times 10^{-4} - 1.00 \times 10^{-3}$	−0.006	−0.017	−0.007	1.000	1.000
$1.00 \times 10^{-3} - 1.58 \times 10^{-3}$	−0.014	−0.022	−0.011	−0.019	1.000
$1.58 \times 10^{-3} - 2.51 \times 10^{-3}$	−0.019	−0.021	−0.033	−0.016	−0.025
$2.51 \times 10^{-3} - 3.98 \times 10^{-3}$	−0.016	−0.003	−0.020	−0.013	−0.019
$3.98 \times 10^{-3} - 6.31 \times 10^{-3}$	−0.010	−0.002	−0.007	−0.009	−0.023
$6.31 \times 10^{-3} - 1.00 \times 10^{-2}$	−0.013	0.001	0.004	−0.019	−0.020
$1.00 \times 10^{-2} - 1.58 \times 10^{-2}$	−0.003	−0.021	−0.001	−0.008	−0.025
$1.58 \times 10^{-2} - 2.51 \times 10^{-2}$	0.002	0.007	−0.023	0.006	−0.002
$2.51 \times 10^{-2} - 3.98 \times 10^{-2}$	−0.008	−0.027	−0.022	−0.016	−0.008
$3.98 \times 10^{-2} - 6.31 \times 10^{-2}$	0.000	−0.016	0.002	−0.010	−0.015
$6.31 \times 10^{-2} - 1.00 \times 10^{-1}$	−0.006	−0.010	−0.030	−0.009	−0.040

Table C.1: **Radiative corrections calculated with TERAD and DJANGO.**
The values in the table represent $(\delta_{TERAD} - \delta_{DJANGO})/\delta_{TERAD}$.

Appendix D

Table with the final F_2 data

$Q^2 = 5$ GeV^2				
x	F_2	$\delta F_2(stat)$	$\delta F_2(syst)$	$\delta F_2(tot)$
0.000130	1.236	0.053	0.098	0.111

$Q^2 = 6.5$ GeV^2				
x	F_2	$\delta F_2(stat)$	$\delta F_2(syst)$	$\delta F_2(tot)$
0.000200	1.169	0.047	0.080	0.093
0.000320	1.019	0.047	0.079	0.092

$Q^2 = 8.5$ GeV^2				
x	F_2	$\delta F_2(stat)$	$\delta F_2(syst)$	$\delta F_2(tot)$
0.000200	1.320	0.036	0.162	0.166
0.000320	1.106	0.032	0.096	0.102
0.000500	1.017	0.048	0.074	0.088
0.000800	0.879	0.039	0.062	0.073
0.001300	0.792	0.037	0.078	0.086
0.002000	0.797	0.042	0.052	0.067
0.003200	0.585	0.034	0.045	0.056
0.005000	0.651	0.041	0.052	0.066
0.008000	0.580	0.039	0.050	0.064
0.013000	0.467	0.045	0.040	0.060

$Q^2 = 12$ GeV^2				
x	F_2	$\delta F_2(stat)$	$\delta F_2(syst)$	$\delta F_2(tot)$
0.000320	1.235	0.055	0.230	0.237
0.000500	1.173	0.039	0.121	0.127
0.000800	1.022	0.034	0.106	0.111
0.001300	0.922	0.033	0.084	0.090
0.002000	0.869	0.041	0.084	0.090
0.003200	0.737	0.038	0.032	0.050
0.005000	0.699	0.037	0.034	0.050
0.008000	0.567	0.033	0.024	0.041
0.013000	0.546	0.036	0.031	0.048
0.020000	0.528	0.042	0.050	0.065

Table D.1: **Final F_2 data points [part 1].**
Based on the F_2 data points of the opened and closed samples, calculated with the E and Σ methods. The points with the smallest total error have been selected for this table.

$Q^2 = 15$ GeV^2				
x	F_2	$\delta F_2(stat)$	$\delta F_2(syst)$	$\delta F_2(tot)$
0.000500	1.248	0.033	0.162	0.165
0.000800	1.069	0.035	0.164	0.167
0.001300	0.976	0.031	0.071	0.078
0.002000	0.878	0.029	0.075	0.080
0.003200	0.767	0.028	0.090	0.094
0.005000	0.684	0.027	0.035	0.044
0.008000	0.621	0.025	0.033	0.041
0.013000	0.535	0.024	0.033	0.040
0.020000	0.492	0.026	0.036	0.044
0.032000	0.440	0.036	0.049	0.061

$Q^2 = 20$ GeV^2				
x	F_2	$\delta F_2(stat)$	$\delta F_2(syst)$	$\delta F_2(tot)$
0.000500	1.325	0.037	0.154	0.159
0.000800	1.181	0.033	0.115	0.119
0.001300	1.040	0.029	0.098	0.103
0.002000	0.942	0.031	0.112	0.116
0.003200	0.874	0.030	0.110	0.114
0.005000	0.751	0.028	0.027	0.039
0.008000	0.676	0.026	0.034	0.043
0.013000	0.559	0.023	0.026	0.035
0.020000	0.520	0.024	0.027	0.036
0.032000	0.446	0.027	0.043	0.050

$Q^2 = 25$ GeV^2				
x	F_2	$\delta F_2(stat)$	$\delta F_2(syst)$	$\delta F_2(tot)$
0.000800	1.298	0.038	0.120	0.125
0.001300	1.083	0.032	0.094	0.099
0.002000	1.010	0.034	0.116	0.121
0.003200	0.885	0.031	0.116	0.120
0.005000	0.795	0.030	0.096	0.101
0.008000	0.679	0.027	0.033	0.043
0.013000	0.600	0.025	0.029	0.039
0.020000	0.591	0.027	0.038	0.046
0.032000	0.480	0.026	0.035	0.043
0.050000	0.408	0.032	0.054	0.063

Table D.2: **Final F_2 data points [part 2].**
Based on the F_2 data points of the opened and closed samples, calculated with the E and Σ methods. The points with the smallest total error have been selected for this table.

$Q^2 = 35$ GeV^2				
x	F_2	$\delta F_2(stat)$	$\delta F_2(syst)$	$\delta F_2(tot)$
0.000800	1.554	0.108	0.279	0.300
0.001300	1.305	0.041	0.162	0.167
0.002000	1.104	0.040	0.144	0.150
0.003200	0.959	0.036	0.144	0.149
0.005000	0.865	0.034	0.115	0.120
0.008000	0.748	0.031	0.033	0.046
0.013000	0.641	0.028	0.029	0.041
0.020000	0.507	0.024	0.023	0.034
0.032000	0.493	0.027	0.027	0.038
0.050000	0.439	0.031	0.044	0.054

$Q^2 = 50$ GeV^2				
x	F_2	$\delta F_2(stat)$	$\delta F_2(syst)$	$\delta F_2(tot)$
0.001300	1.310	0.071	0.134	0.151
0.002000	1.275	0.045	0.184	0.189
0.003200	0.947	0.081	0.132	0.155
0.005000	0.823	0.072	0.100	0.124
0.008000	0.780	0.035	0.046	0.058
0.013000	0.737	0.034	0.036	0.050
0.020000	0.622	0.030	0.031	0.044
0.032000	0.581	0.030	0.024	0.039
0.050000	0.458	0.029	0.028	0.040
0.080000	0.387	0.033	0.029	0.044

$Q^2 = 65$ GeV^2				
x	F_2	$\delta F_2(stat)$	$\delta F_2(syst)$	$\delta F_2(tot)$
0.003200	1.253	0.084	0.137	0.161
0.005000	0.865	0.054	0.066	0.085
0.008000	0.722	0.042	0.046	0.063
0.013000	0.612	0.036	0.038	0.052
0.020000	0.594	0.034	0.023	0.041
0.032000	0.542	0.032	0.027	0.042
0.050000	0.466	0.033	0.020	0.038
0.080000	0.428	0.033	0.025	0.041

Table D.3: **Final F_2 data points [part 3].**
Based on the F_2 data points of the opened and closed samples, calculated with the E and Σ methods. The points with the smallest total error have been selected for this table.

Bibliography

[1] *VMEbus Specification Manual, revision C.1.*, 1985.

[2] U. Bassler, G. Bernardi. On the Kinematic Reconstruction of Deep Inelastic Scattering at HERA: the Σ Method. Technical Report DESY 94-143, Université Paris VI et VII, 1994.

[3] F. Jacquet A. Blondel. In U. Amaldi, editor, *Proceedings of the study of an ep facility for Europe*, number DESY 79–48 391, 1979.

[4] A. Kwiatkowski, H. Spiesberger and H.-J. Möhring. *Computer Phys. Comm.*, 69:155, 1992.

[5] R.G. Roberts A.D. Martin, W.J. Stirling. *preprint RAL*, (92-053), 1990.

[6] A. Akhundov et al. Technical Report 94–115, DESY, 1994. DESY.

[7] Apple Computers Inc. SuperCard Handbook. Technical report, 1989.

[8] Apple Developers Group. MPW Reference Manual 5. Technical report, ADG, 1987.

[9] Apple Developers Group. MPW Assembler Rerference Manual. Technical report, ADG, 1989.

[10] Apple Developers Group. MPW Pascal Rerference Manual. Technical report, ADG, 1990.

[11] M. Arneodo et al. Measurement of the proton and the deuteron structure functions, F_2^p and F_2^d. *Phys. Lett.*, B(364):107, 1995.

[12] U. Bassler. *Premières mesures sur l'état final hadronique de la diffusion profondément inélastique à HERA*. PhD thesis, Université Pierre et Marie Curie, May 1993.

[13] BEMC Group. The H1 Backward Electromagnetic Calorimeter (BEMC). H1 note, DESY, August 1992. H1–08/92–233.

[14] H.U. Bengston and T. Sjöstrand. *Computer Phys. Comm.*, 46:43, 1987.

[15] G. Bernadi. Private communiction.

[16] J.D. Bjorken. The prediction of scaling in dis lepton-nucleon interactions. *Phys. Rev.*, 179:1547, 1969.

[17] V. Blobel. The BOS system—Dynamic memory management. Technical report, II. Institut für Experimentalphysik, Universität Hamburg, 1987.

[18] M. Böhm and H.Spiesberger. *Nucl. Phys*, B(294):1081, 1987.

[19] Christoph Brune. *Ph.D. Thesis in litt.* PhD thesis, Universität Heidelberg, 1995.

[20] Alan J. Campbell. A RISC Multiprocessor Event Trigger for the Data Acquisition System of the H1 Experiment at HERA. *RAL-91-060*, 1991.

[21] H1 Collaboration. The H1 Detector. *NIM, to be published*, 1994.

[22] H1 Collaboration. A Measurement and QCD Analysis of the Proton Structure Function $F_2(x, Q^2)$ at HERA. H1 note, DESY, 1996. H1–96–039.

[23] M. Demoulin. VMEUA1MON Users Manual. Technical Report CERN-EF-UA1, CERN, 1988.

[24] J. Drees. In W. Pfeil, editor, *Proceedings of the 1988 International Symposium on Lepton and Photon Interactions at High Energies*, page 444, 1988.

[25] V.S. Fadin E.A. Kuraev, L.N. Lipatov. *Sov. J. Nucl. Phys.*, 45:199, 1977.

[26] J. Botts et al. *Phys. Lett.*, B(304):159, 1993.

[27] R. Brun et al. GEANT3 User's Guide. Technical Report DD/EE 84–1, CERN, 1987.

[28] Erik Evrard. MacHbook, an HBOOK version for the Macintosh. Technical report, Interuniversity Institute for High Energies, 1989.

[29] F. Charles, S. Reinshagen, R. Roosen, P. Van Esch. Photoproduction as background in Deep Inelastic Scattering at low x. H1 note, DESY, September 1994. H1–09/94–380.

[30] R.P. Feynman. *Phys. Rev. Lett.*, 23:1415, 1969.

[31] Manfred Fleischer. *Untersuchungen radiativer Ereignisse in der tief inelastischen ep-Streuung mit dem H1-Detektor bei HERA.* PhD thesis, Universität Hamburg, 1994.

[32] G. Parisi G. Altarelli. *Nucl. Phys.*, 126:297, 1977.

[33] G. Bernardi, W. Hildesheim. A detailed simulation of F_2 measurability at HERA. In W. Buchmüller and G. Ingelman (DESY), editor, *Physics at HERA—Proceedings of the Workshop*, pages 79–99, 1992.

[34] G. Ingelman. LEPTO version 6.1—The Lund Monte Carlo for Deep Inelastic Lepton-Nucleon Scattering. In W. Buchmüller and G. Ingelman (DESY), editor, *Physics at HERA—Proceedings of the Workshop*, page 1366, 1992.

[35] G.A. Schuler and H. Spiesberger. DJANGO: the interface for the event generators HERACLES and LEPTO. In W. Buchmüller and G. Ingelman (DESY), editor, *Physics at HERA—Proceedings of the Workshop*, pages 1419–1432, 1992.

[36] A. Glazov. The 1994 H1 F_2 structure function analysis of the nominal vertex data. Unpublished note.

[37] K. Golec Biernat. H1 note, DESY, 1993. H1–93–320.

[38] H1 Collaboration. Measurement of the Proton Structure Function $F_2(x, Q^2)$ in the low x Region at HERA. *Nuclear Physics*, B(407):515–535, 1993.

[39] H1 Collaboration. The H1 Detector at HERA. H1 note, DESY, July 1993. DESY 93–103.

[40] H1 Collaboration. Total photoproduction cross section measurement at HERA energies. *Physics Letters*, B(299):374–384, 1993.

[41] H1 Collaboration. A measurement of the proton structure function $F_2(x, Q^2)$. *Nucl. Phys. B*, B(439):471–502, 1995.

[42] F. Halzen and A.D. Martin. *Quarks & Leptons: An Introductory Course in Modern Particle Physics.* John Wiley & Sons, New York, 1984.

[43] W.J. Haynes. VMEXI_SSP, VMEtaxi System Software Package. Technical Report Version 1.0 Beta 2, DESY, 1989.

[44] P. Huet. *A VMEbus-Based Data Acuisition System for the Multiwire Proportional Chambers of the H1 Detector at the HERA Collider.* PhD thesis, Université Libre de Bruxelles, May 1993.

[45] N. Huot. *Estimation et rejection de l'empilement pour la mesure des fonctions de structure par les calorimetres de H1.* PhD thesis, Université de Paris VII, February 1992.

[46] M. Seman J. Bán, T. Kurča. Proposal for a separated electron and independent t_0 trigger for bemc. Technical report, IEP Košice, September 1990.

[47] Hans-Peter Kasselmann. *Untersuchungen zur Messung von Elektronen mit dem elektromagnetischen Rückwärtskalorimeter (BEMC) des HERA H1-Detektors.* PhD thesis, Universität Hamburg, 1994.

[48] K.C. Hoeger. Measurement of x, y, Q^2 in neutral current events. In W. Buchmüller and G. Ingelman (DESY), editor, *Physics at HERA—Proceedings of the Workshop*, pages 43–55, 1992.

[49] H. Krehbiel. The Fanout Card of the Subsystem Trigger Controller. Technical Report H1 Technical Report, DESY, 1989.

[50] H. Krehbiel. The Fast Card of the Subsystem Trigger Controller. Technical report, DESY, 1990.

[51] H. Krehbiel. The Extended Fanout Card of the H1 STC. Technical Report H1 Technical Report, DESY, 1991.

[52] H. Krehbiel. The Triggerbits Card of the H1 STC. Technical Report H1 Technical Report, DESY, 1992.

[53] Tibor Kurča. *The H1 Trigger for Neutral Current Deep Inelastic Scattering Events at Low Q^2.* PhD thesis, Universität Hamburg, 1994.

[54] S. Levonian. The H1 luminosity in 1994. Talk given at H1 collab. meeting December 1994.

[55] M. Glück, E. Reya, A. Voght. *Phys. Lett.*, B(306):391, 1992.

[56] Katharina Müller. *Measurement of the proton structure function F_2 at low Bjorken x at the H1 experiment.* PhD thesis, Universität Zürich, 1994.

[57] A. De Roeck N.H. Brook and A.T. Doyle. RAYPHOTON 2.0. In *Proceedings of the Workshop Physics at HERA*, volume 3, page 1453, 1992.

[58] J. Olszowska. The Slow Card of the Subsystem Trigger Controller. Technical Report H1 Technical Report, DESY, 1991.

[59] A. Panitch. Vertex reconstruction and BPC efficiency determinations for the 1993 structure function analysis. H1 note, IIHE, 1994. H1–08/94–373.

[60] Erich Peppel. *Messung der Protonenstrukturfunktion F_2 unter besonder Berücksichtung des H1-Rückwärtskalorimeters.* PhD thesis, Universität Hamburg, 1994.

[61] D.H. Perkins. *Introduction to High Energy Physics.* Addison Wesley Publishing Company Inc., 1987.

[62] Christian Pichler. *Untersuchungen zur Messung von Elektronen im äußeren Randbereich des elektromagnetischen Rückwärtskalorimeters (BEMC) des H1-Detektors bei HERA.* PhD thesis, Universität Hamburg, 1995.

[63] H. Plothow Besch. PDFLIB: A Library of all available Parton Density Functions of the Nucleon, the Pion and the Photon and the corresponding α_s Calculations. Technical Report PPE-/92–123, CERN, 1992.

[64] K. Prytz. *Phys. Lett.*, B(311):286, 1993.

[65] K. Prytz. *Phys. Lett.*, B(332):393, 1994.

[66] C. Quigg. *Gauge Theories of the Strong, Weak and Electromagnetic Interactions.* The Benjamin/Cummings Publishing Company, Inc., Menlo Park, California, 1983.

[67] R.E. Taylor, H.W. Kendall, J.I. Friedmann. *Rev. Mod. Phys.*, 63:573–615, 1991.

[68] P. Reimer. Calibration of the BEMC with a detailed H1SIM Monte Carlo Study. Unpublished, 1992.

[69] E.M. Riordan et al. SLAC-Pub 1634, 1975.

[70] S. Bentvelsen, J. Engelen, P. Kooijman. Reconstruction of (x, Q^2) and extraction of structure functions in neutral current scattering at HERA. In W. Buchmüller and G. Ingelman (DESY), editor, *Physics at HERA—Proceedings of the Workshop*, pages 23–42, 1992.

[71] A. Panitch S. Levonian. Treatment of the Proton Satellite Bunches in 1994 Data. H1 note, DESY, 1995. H1–95–454.

[72] T. Sjöstrand. PYTHIA at HERA. In W. Buchmüller and G. Ingelman (DESY), editor, *Physics at HERA—Proceedings of the Workshop*, pages 1405–1418, 1992.

[73] L.N. Lipatov V.N. Gribov. *Sov. J. Nucl. Phys.*, 15:438–675, 1972.

[74] W.J. Haynes. The H1 VME Based Data Acquisition System. In North-Holland, editor, *VMEbus IN RESEARCH*, pages 191–201, 1988.

[75] W.J. Haynes. Microprocessor-Based Data Acquisition Systems for Hera Experiments. *RAL-89-092*, 1989.

[76] Nicolas Wullf. *Tiefinelastische Elektron-Proton-Streuung bei kleinem x-Bjorken.* PhD thesis, Universität Hamburg, 1993.

[77] L.N. Lipatov Y.Y. Balitsky. *Sov. J. Nucl. Phys.*, 28:822, 1978.

[78] Zeus Collaboration. *submitted to Z. Phys. C*, (DESY 94-143), 1994.

List of Figures

List of Tables

Acknowledgement

This project would never have come to a good end without the help, support and advice of many people. In particular I would like to mention:

Prof. Dr. J. Lemonne, who raised my interest in high energy physics when I was still an undergraduate student, who initiated me in the wonderful world of elementary particles and who made it possible for me to start this work at the I.I.H.E.

Dr. Robert Roosen, who continually assisted me for the whole length of my stay at the I.I.H.E. I'm very grateful for his continuous support, at first in the early 'DAQ' days, but also later when my activitities moved towards physics analysis. I think I've learned a lot from his wisdom, rich scientific and human experience, but also from his ubiquitous critical questions.

Bill Haynes, who managed the early H1 DAQ team so well, and without whom H1 would never have logged one single event. It was a true pleasure working with and for him. Also the other 'early days' subsystem experts, who were–with me–the earliest habitants of the North Hall: Eckhard Elsen, Jörg Tutas, Frédéric Décamps, Claude Vallée, Scot Kolya, Sasha Usik, and Sasha Fomenko. The days together are unforgettable.

Philippe Huet, whom I worked and lived together with in Hamburg, to set up the MWPC DAQ system. His knowledge of high-tech electronics never ceased to impress me. It was also in those days that I met Dietmar Lewin and Albrecht Leuschner, who made my life in Hamburg much more enjoyable, and who raised my interest in the former G.D.R. I always looked forward to visit Berlin, with the knowledge to find so much hospitality in your homes.

My good friend Christophe Royon, who initiated me into the world of F_2 during the analysis of the 1992 data, and was always there also in later years to offer advice, assistance and support, but also whose friendship I'll never forget. It was in those days also that I met Witek Krasny, Jean-Francois Laporte and Marc Besançon from Saclay, it was a true pleasure to collaborate with you all. I will never forget those sunny days that I've spent in Saclay. Special thanks go to Witek, who accepted to be a member of my jury, and who after two years took up the subject of F_2 again to give advice during the completion of this document.

Greg Bernardi who welcomed me in the 1993 analysis team. And the whole Paris team: Ursula Bassler, Beatriz Gonzales-Pineiro, Damien Neyret, Marcel Goldberg and Khan Nguyen. Working under the glass pyramid in Paris was quite an experience.

Max Klein, who invited me to join his analysis team for the 1994 data, which eventually lead to the completion of this work. His experience was vital to finish this analysis within a reasonable amount of time. It was also a pleasure to be a guest in Zeuthen, whose H1 collaborators I've met years before, and whose hospitality is hard to beat. Thank you Peter Kostka, Thomas Naumann, Uta Stößlein and Helmut Kaufmann. And thank you in particular Sasha Glazov, without your incredible efforts this work wouldn't be ready.

There are many other people who I met at DESY and who made my life at DESY more pleasant. In particular I would like to thank Pavel Binko, for his friendship and

FPACK support, Sebastian Reinshagen, for many useful F_2 discussions, Jozef Ferencei, Erich Peppel and Manfred Fleischer for all the BEMC assistance, and many, many others.

Dr. Smain Kermiche and Dr. Hans-Peter Kasselmann, for the nice encapsulated postscript images, which I could borrow to illustrate this document.

Patrick Van Esch, with whom I shared the office in Brussels, and whose company made the last years extremely enjoyable, and for the many discussions—also outside the domain of physics. Arkadi Panitch who also spent quite some time with me working on F_2 in DESY and Zeuthen, for his valuable scripts in perl, which helped to digest the many megabytes of the H1-DSTs. Tom Heiremans and Marleen Goeman, for the many pleasant lunches when I was in Brussels for a change. Ludo Vanhelleputte, who taught me a lot of interesting computer wisdom, who was always ready to help when our binary 'friends' were unwilling, and who increased my quota to 80,000 Mbytes and later to infinite, otherwise this document would have never seen the light of the day.

Myriam Pins and Danielle Peymans, who helped me a lot in making nice drawings for this document.

All the other members of the I.I.H.E., who made my stay there for the last seven years a very pleasant and unforgetable experience.

All my new collegues at EUnet, whom I had the pleasure to work with for more than one year before this work was finally completed. They gave me constant moral support, and allowed me sufficient flexibility to find some time to continue to work on my thesis. In particular I would like to thank Wim Vink and my good friend Anthony Stone.

My parents, who saw me now and then between my regular foreign trips and I always found a warm home when I returned to Belgium.

And finally I would like to thank Marjon, the most elementary part(icle) in my life, for her continuous support and her patience during my many trips abroad.

Thank you, bedankt, danke, merci, ...